Searches for neutral Higgs bosons in final states with two tau leptons using the CMS detector

Adinda Maite de Wit

Imperial College London
Department of Physics

A dissertation submitted to Imperial College London
for the degree of Doctor of Philosophy

Abstract

The Compact Muon Solenoid (CMS) detector is a general-purpose detector located at the Large Hadron Collider at CERN. It was designed to test the predictions of the standard model and to search for the Higgs boson in addition to searches for new physics beyond the standard model. The analyses presented in this thesis are searches for neutral Higgs bosons with tau leptons in the final state. These searches use proton-proton collision data recorded by CMS during 2012, 2015 and 2016. The searches are performed in the context of the minimal supersymmetric standard model (MSSM). One of the analyses, using $19.7\,\mathrm{fb}^{-1}$ of data collected during 2012 at $\sqrt{s} = 8\,\mathrm{TeV}$, is a search for a heavy neutral Higgs boson decaying into two 125 GeV Higgs bosons with standard model-like properties, with two b-quarks and two tau leptons in the final state. The other analyses use $2.3\,\mathrm{fb}^{-1}$ of data collected during 2015 and $12.9\,\mathrm{fb}^{-1}$ of data collected during 2016, both at $\sqrt{s} = 13\,\mathrm{TeV}$. These are searches for neutral MSSM Higgs bosons in the mass range of 90 GeV–3.2 TeV directly decaying into pairs of tau leptons. No significant excess is observed in any of the searches. Upper limits at the 95% confidence level are set on the cross section times branching ratio for the production of Higgs bosons in the MSSM. In addition, limits are set in the m_{A}-$\tan\beta$ parameter space of several MSSM benchmark scenarios, and in the $\cos(\beta-\alpha)$-$\tan\beta$ parameter space of a two Higgs doublet model.

Declaration

I declare that the work in this thesis is mine. Figures and results taken from other sources include the appropriate reference in the text or figure caption. Figures labelled ‘CMS’ are sourced directly from CMS publications. The ‘CMS Preliminary’ label indicates figures which have been made public via a preliminary public document or a public website, but are not included in a publication in a peer-reviewed journal. Figures labelled ‘CMS’ or ‘CMS preliminary’, including those made by myself, include the relevant reference in the figure caption. Chapters 1–3 do not contain original work by myself, however they give information on the theoretical background, the CMS detector and the standard reconstruction algorithms used within the CMS collaboration which underpin my own work described in later chapters. The work for the $\mathrm{H} \to \mathrm{hh} \to \mathrm{bb}\tau\tau$ and $\mathrm{A/H} \to \tau\tau$ analyses presented in chapters 4 and 5 was carried out as part of the CMS $\mathrm{H} \to \tau\tau$ working group, and in collaboration with other members of the group. For the results of the $\mathrm{H} \to \mathrm{hh} \to \mathrm{bb}\tau\tau$ analysis I contributed to the data analysis of the $\mathrm{e}\tau_\mathrm{h}$ and $\mu\tau_\mathrm{h}$ final states of the di-tau pair, with studies of alternative $\mathrm{t\bar{t}}$ background rejection methods and other uses of the kinematic fit variable. These studies are not further discussed in this thesis. I was responsible for the statistical inference of the analyses in the $\mathrm{e}\tau_\mathrm{h}$, $\mu\tau_\mathrm{h}$ and $\tau_\mathrm{h}\tau_\mathrm{h}$ final states of the di-tau pair. This included the interpretation of the results in MSSM and 2HDM benchmark scenarios. The work is included in reference [1]. For the results of the $\mathrm{A/H} \to \tau\tau$ analysis I was responsible for all stages of the analysis, including the optimisation of object selection and event categorisation, as well as studies of background methods for the $\mathrm{e}\tau_\mathrm{h}$, $\mu\tau_\mathrm{h}$ and $\tau_\mathrm{h}\tau_\mathrm{h}$ final states in the public result, evaluation of systematic uncertainties in the $\mathrm{e}\tau_\mathrm{h}$, $\mu\tau_\mathrm{h}$, $\tau_\mathrm{h}\tau_\mathrm{h}$ and $\mathrm{e}\mu$ final states, and production of the statistical results, including model interpretations. This work is included in the most recent preliminary result [2], as well as a predating preliminary result using a smaller dataset [3]. The work on the combination of $\mathrm{A/H} \to \tau\tau$ analyses presented in chapter 6 has not been made public, and draws on the results of [2] and [3].

Adinda de Wit

Acknowledgements

I would like to thank Imperial College and the Imperial College HEP group for giving me the opportunity to carry out this research, and especially for the valuable experience of spending two years at CERN. Thanks to my supervisors, David Colling for helping secure this funding and his support, and Gavin Davies for many useful discussions and general advice. The work in this thesis would not have come to fruition without Rebecca, who taught me all the important aspects of doing an analysis as well as always being ready to discuss ideas, and I am very grateful to her for that. My thanks extend to Andrew in this regard, who was also always available to discuss physics and coding issues. I would also like to thank the people I've worked with in the CMS H $\rightarrow \tau\tau$ group, particularly those involved in the most recent MSSM result.

Thanks to my friends, nearby and far away, for all of the good times and laughter. Most importantly, I would like to thank those closest to me for their love: My mother, who is always there for me despite the fact I live so far away; my father, whose love of science I inherited and who would certainly be a little bit jealous of the computing power I get to play with on a daily basis; my sister, who always understands me as she's followed a similar path; and Andrew, for making the days so much brighter.

Adinda de Wit

Contents

List of figures **10**

List of tables **15**

1 Theory and motivation **17**

1.1 The standard model of particle physics 17

1.1.1 Fundamental particles and forces 17

1.1.2 The Higgs mechanism 19

1.2 Standard model Higgs boson measurements 22

1.3 Beyond the standard model 24

1.3.1 The Higgs sector of the MSSM 25

1.3.2 Two Higgs doublet models 29

1.4 MSSM benchmark scenarios 31

1.4.1 The $m_{\mathrm{h}}^{\mathrm{mod+}}$ scenario 31

1.4.2 MSSM scenarios at low $\tan\beta$ 32

1.5 Status of BSM Higgs boson searches 36

2 The LHC and the CMS experiment **38**

2.1 The LHC 38

2.2 The CMS detector 42

2.2.1 Tracker 43

2.2.2 Electromagnetic calorimeter 45

2.2.3 Hadron calorimeter 47

2.2.4 Muon system 48

2.2.5 Triggering and data processing 50

3 Object reconstruction **53**

3.1 Tracks and vertices 53

3.2 Electrons 55

3.3 Muons 57
3.4 Particle flow 58
3.5 Jets and b-tagging 60
  3.5.1 Jet energy corrections 61
  3.5.2 b-Tagging 62
3.6 Missing energy 64
  3.6.1 Recoil corrections 66
3.7 Hadronic taus 66

4 Search for H $\rightarrow$ hh $\rightarrow$ bb$\tau\tau$ 72
4.1 Datasets and Monte Carlo samples 73
4.2 Event selection and categorisation 74
  4.2.1 Event selection in the $\mu\tau_{\mathrm{h}}$ channel 74
  4.2.2 Event selection in the eτ_{h} channel 75
  4.2.3 Categorisation 75
4.3 Monte Carlo simulation-to-data correction factors 78
4.4 Discriminating variable 79
4.5 Background estimation 82
  4.5.1 $\mathrm{Z}/\gamma^* \rightarrow \tau\tau$ 83
  4.5.2 $\mathrm{t\bar{t}}$ 83
  4.5.3 W+jets 83
  4.5.4 QCD multijet 84
  4.5.5 Other backgrounds 84
4.6 Systematic uncertainties 84
  4.6.1 Normalisation uncertainties 85
  4.6.2 Shape uncertainties 86
4.7 Overview of A $\rightarrow$ Zh $\rightarrow$ $\ell\ell\tau\tau$ 87
4.8 Results 88
  4.8.1 Signal extraction 88
  4.8.2 Model-independent results 91
  4.8.3 Model-dependent results 95

5 Search for MSSM A/H $\rightarrow$ $\tau\tau$ 99
5.1 Datasets and Monte Carlo samples 99
5.2 Event selection and categorisation 100
  5.2.1 Pair selection and vetoes 101
  5.2.2 Event selection in the $\mu\tau_{\mathrm{h}}$ channel 102

5.2.3 Event selection in the eτ_h channel 107
5.2.4 Event selection in the $\tau_\mathrm{h}\tau_\mathrm{h}$ channel 109
5.2.5 Event selection in the eμ channel 110
5.2.6 Categorisation 111
5.3 Discriminating variable 113
5.4 Monte Carlo simulation-to-data correction factors 114
5.5 Background estimation 118
5.5.1 Generator matching 119
5.5.2 Z/γ^* → $\tau\tau$ 120
5.5.3 W+jets and QCD in the eτ_h and $\mu\tau_\mathrm{h}$ channels 121
5.5.4 QCD in the $\tau_\mathrm{h}\tau_\mathrm{h}$ and eμ channels 127
5.5.5 t$\bar{\mathrm{t}}$ 128
5.5.6 Other backgrounds 129
5.6 Systematic uncertainties 129
5.6.1 Normalisation uncertainties 129
5.6.2 Shape uncertainties 132
5.7 Signal extraction 134
5.7.1 Inclusion of control regions in the fit 134
5.7.2 Signal process profiling and 2D likelihood scans 135
5.7.3 MSSM vs SM hypothesis testing 135
5.8 Results 138
5.8.1 Model-independent results 138
5.8.2 Sensitivity to the SM Higgs boson 143
5.8.3 2D likelihood scans 143
5.8.4 Interpretations in MSSM benchmark scenarios 145

6 Combination of MSSM analyses **147**
6.1 Results from the 2015 analysis 147
6.2 Combination procedure 151
6.3 Results 154

7 Conclusions and outlook **157**

Bibliography **160**

List of acronyms **175**

A Event yields in the H → hh → bb$\tau\tau$ analysis **178**

B Systematic uncertainties in the MSSM A/H $\rightarrow \tau\tau$ analysis 180

C Event yields in the MSSM A/H $\rightarrow \tau\tau$ analysis 186

List of figures

1.1 Tree-level Feynman diagrams for the dominant Higgs boson production modes at the LHC. . . . 23

1.2 SM Higgs boson production cross sections at $\sqrt{s} = 13\,\mathrm{TeV}$ and SM Higgs boson branching ratios, for Higgs boson masses between 120 and 130 GeV. 24

1.3 Branching ratios of the H boson in the $m_{\mathrm{h}}^{\mathrm{mod+}}$ scenario. . . . 28

1.4 Tree-level Feynman diagrams of gluon fusion and b-associated production of neutral Higgs bosons in the MSSM. . . . 29

1.5 Inclusive production $\sigma\times\mathcal{B}$ for an example of a type-II 2HDM, for the H and A bosons. . . . 30

1.6 Production cross sections of gluon fusion and b-associated production of the H boson in the $m_{\mathrm{h}}^{\mathrm{mod+}}$ scenario. . . . 32

1.7 Branching ratios of the H and A bosons into $\tau\tau$. . . . 33

1.8 The mass of the light Higgs boson, m_{h}, as a function of m_{A} and $\tan\beta$ in the $m_{\mathrm{h}}^{\mathrm{mod+}}$ scenario and the low-$\tan\beta$ scenario. . . . 33

1.9 Branching ratios of H → hh and A → Zh in the low-$\tan\beta$ scenario. . . . 35

1.10 Summary of the interpretations of BSM Higgs boson searches using data up to the end of 2012 at CMS in the $m_{\mathrm{h}}^{\mathrm{mod+}}$ scenario and the hMSSM scenario. . . . 37

2.1 Schematic of the CERN accelerator complex. . . . 39

2.2 Total p-p cross section, and the cross sections for several processes studied at the LHC. . . . 40

2.3 Cumulative integrated luminosity delivered to CMS for p-p collisions at the LHC, separated by running year. . . . 41

2.4 A cutaway view of the CMS detector, indicating the different sub-components of the detector. . . . 42

2.5 Schematic of the CMS tracker in the r-z plane, indicating the positions of the pixel and strip detectors. . . . 44

2.6 Layout of the ECAL, indicating the positions of the different components. 46

2.7 Illustration of a quadrant of the HCAL, showing the different sub-systems of the detector. 47
2.8 Cross section of one quadrant of the CMS detector, indicating the positions of the different muon system components. 49
2.9 Schematic of the different components of the L1 trigger. 51

3.1 Resolution of the x and z coordinates of reconstructed primary vertices as a function of the scalar p_{T} sum of the associated tracks. 54
3.2 $\sigma_{i\eta,i\eta}$ and $1/E_{\mathrm{SC}} - 1/p_e$ for real and misidentified electrons at 8 TeV, for data and simulation. 56
3.3 The b-tagging scale factors and uncertainties for b-jets in the data sample collected during 2015 as a function of jet p_{T} for the medium working point of the CSVv2 discriminant. 64
3.4 $E_{\mathrm{T}}^{\mathrm{miss}}$ distributions comparing MVA $E_{\mathrm{T}}^{\mathrm{miss}}$ to PF $E_{\mathrm{T}}^{\mathrm{miss}}$ for $\mathrm{Z}/\gamma^* \rightarrow \mu\mu$ events, in a sample corresponding to $42\,\mathrm{pb}^{-1}$ of data collected at $\sqrt{s} = 13\,\mathrm{TeV}$. 65
3.5 Figures of the jet$\rightarrow\tau_{\mathrm{h}}$ fake rate in simulated QCD events versus τ_{h} identification efficiency for simulated $\mathrm{H} \rightarrow \tau\tau$ events, the τ_{h} identification efficiency for different working points of the anti-electron discriminator, and the $\mathrm{e} \rightarrow \tau_{\mathrm{h}}$ fake rate for different working points of the anti-electron discriminator. 71

4.1 m_{T} distributions in the $\mu\tau_{\mathrm{h}}$ and $\mathrm{e}\tau_{\mathrm{h}}$ channels. 76
4.2 Number of b-tagged jets in the two-jet selection of the $\mu\tau_{\mathrm{h}}$ and $\mathrm{e}\tau_{\mathrm{h}}$ channels. 77
4.3 Reconstructed di-tau invariant mass and di-jet invariant mass in the 2jet-2tag category of the $\mu\tau_{\mathrm{h}}$ channel. 78
4.4 Comparison of the reconstructed heavy Higgs boson mass using the kinematic fit in signal events with $m_{\mathrm{H}} = 300\,\mathrm{GeV}$ and $\mathrm{t\bar{t}}$ background events in the 2jet-1tag category of the $\mu\tau_{\mathrm{h}}$ channel. 82
4.5 The expected and observed upper limits at the 95 % CL on the $\sigma\times\mathcal{B}$ for the $\mathrm{A} \rightarrow \mathrm{Zh} \rightarrow \ell\ell\tau\tau$ process. 88
4.6 Distributions of $m_{\mathrm{H}}^{\mathrm{kinfit}}$ in the 2jet-0tag, 2jet-1tag and 2jet-2tag categories of the $\mu\tau_{\mathrm{h}}$ channel. 92
4.7 Distributions of $m_{\mathrm{H}}^{\mathrm{kinfit}}$ in the 2jet-0tag, 2jet-1tag and 2jet-2tag categories of the $\mathrm{e}\tau_{\mathrm{h}}$ channel. 93
4.8 Expected and observed upper limits at the 95% CL on $\sigma\times\mathcal{B}$ for the $\mathrm{H} \rightarrow \mathrm{hh} \rightarrow \mathrm{bb}\tau\tau$ process. 94

4.9 Search for H → hh → bb$\tau\tau$ and search for A → Zh → $\ell\ell\tau\tau$ interpreted in a type-II 2HDM, assuming $m_{\mathrm{A}} = m_{\mathrm{H}} = m_{\mathrm{H}^+} = 300\,\mathrm{GeV}$. 96
4.10 $\sigma\times\mathcal{B}$ of the H → hh → bb$\tau\tau$ process and the A → Zh → $\ell\ell\tau\tau$ process in the low-tan β MSSM scenario. The expected and observed 95% CL exclusion limits for the A → Zh → $\ell\ell\tau\tau$ analysis in the low tan β MSSM scenario have been overlaid. 97
4.11 Combination of the A → Zh → $\ell\ell\tau\tau$ and H → hh → bb$\tau\tau$ searches interpreted in a type-II 2HDM and in the low-tan β MSSM scenario. . . . 98

5.1 The p_{T} of the muon in the $\mu\tau_{\mathrm{h}}$ channel and η of the electron in the eτ_{h} channel, with the signal overlaid. 102
5.2 The $S/\sqrt{B}$ for Z/γ^* → $\tau\tau$ signal and the size of the error interval on the best-fit value of a maximum-likelihood fit to the Z/γ^* → $\tau\tau$ signal strength, for various isolation selections. 104
5.3 Pre-fit expected limit on $\sigma\times\mathcal{B}$ for the ggϕ production process with decay into $\tau\tau$ as a function of tau isolation working point and m_{T} selection, for two mass points. 106
5.4 Pre-fit expected limits on $\sigma\times\mathcal{B}$ for the ggϕ and bbϕ processes in the $\mu\tau_{\mathrm{h}}$ channel for an increasingly looser m_{T} selection and tau isolation working point. 106
5.5 Pre-fit expected limits on $\sigma\times\mathcal{B}$ in the $\mu\tau_{\mathrm{h}}$ channel for ggϕ and bbϕ production, comparing different hadronic tau p_{T} cuts. 107
5.6 Pre-fit expected limits on $\sigma\times\mathcal{B}$ in the eτ_{h} channel for ggϕ and bbϕ production for an increasingly looser m_{T} selection and tau isolation working point. 108
5.7 Pre-fit expected limits on $\sigma\times\mathcal{B}$ in the eτ_{h} channel for ggϕ and bbϕ production comparing different hadronic tau isolation cuts. 109
5.8 Expected upper limits for the ggϕ and bbϕ process in the $\tau_{\mathrm{h}}\tau_{\mathrm{h}}$ channel, comparing different hadronic tau isolation working points. 110
5.9 Reconstruction of the D_ζ variable and the D_ζ distribution in the eμ channel. 112
5.10 Number of jets and number of b-tagged jets in the $\mu\tau_{\mathrm{h}}$ channel, with the signal overlaid. 113
5.11 Total transverse mass distributions in the no b-tag category of the $\tau_{\mathrm{h}}\tau_{\mathrm{h}}$ channel for QCD and gluon fusion signal, and in the b-tag category of the eμ channel, for t$\bar{\mathrm{t}}$ and b-associated signal. 114

5.12 The $m_{\mathrm{T}}^{\mathrm{tot}}$ distribution in the $\mathrm{t\bar{t}}$ enriched control region, with and without applying top quark p_{T} reweighting. 116
5.13 The mis-modelling in the di-lepton p_{T} distribution as observed in $\mathrm{Z}/\gamma^{*} \to \mu\mu$ events, and the impact of applying the Drell-Yan shape reweighting on the total transverse mass distribution of the $\mathrm{Z}/\gamma^{*} \to \tau\tau$ background in the no b-tag category of the $\mathrm{e}\tau_{\mathrm{h}}$ channel. 117
5.14 The low $m_{\mathrm{T}}^{\mathrm{tot}}$ region in the no b-tag category of the $\mu\tau_{\mathrm{h}}$ channel and in the b-tag category of the $\mathrm{e}\mu$ channel. 119
5.15 Distribution of the transverse mass m_{T} in the $\mu\tau_{\mathrm{h}}$ channel, indicating the signal region and the high-m_{T} control region. 121
5.16 High-m_{T} control region in the no b-tag and b-tag categories of the $\mathrm{e}\tau_{\mathrm{h}}$ channel. 123
5.17 The visible mass distribution of the di-tau pair in the $\mu\tau_{\mathrm{h}}$ channel for the sideband near the signal region, before and after the maximum likelihood fit to $R_{\mathrm{QCD}}^{\mathrm{OS/SS}}$. 125
5.18 The visible mass distribution of the di-tau pair in the $\mu\tau_{\mathrm{h}}$ channel for the sideband further away from the signal region, before and after the maximum likelihood fit to $R_{\mathrm{QCD}}^{\mathrm{OS/SS}}$. 125
5.19 The visible mass distribution of the di-tau pair in the $\mathrm{e}\tau_{\mathrm{h}}$ channel for the sideband near the signal region, before and after the maximum likelihood fit to $R_{\mathrm{QCD}}^{\mathrm{OS/SS}}$. 126
5.20 The visible mass distribution of the di-tau pair in the $\mathrm{e}\tau_{\mathrm{h}}$ channel for the sideband further away from the signal region, before and after the maximum likelihood fit to $R_{\mathrm{QCD}}^{\mathrm{OS/SS}}$. 126
5.21 Impact of the high-p_{T} tau ID uncertainty in the no b-tag category of the $\tau_{\mathrm{h}}\tau_{\mathrm{h}}$ channel for a high-mass signal sample and the $\mathrm{Z}/\gamma^{*} \to \tau\tau$ background. 133
5.22 Distributions of the test statistic for the SM and MSSM hypotheses at three different points in the $m_{\mathrm{h}}^{\mathrm{mod+}}$ scenario. 138
5.23 Distributions of $m_{\mathrm{T}}^{\mathrm{tot}}$ in the no b-tag and b-tag categories of the $\mu\tau_{\mathrm{h}}$ channel. 140
5.24 Distributions of $m_{\mathrm{T}}^{\mathrm{tot}}$ in the no b-tag and b-tag categories of the $\mathrm{e}\tau_{\mathrm{h}}$ channel. 140
5.25 Distributions of $m_{\mathrm{T}}^{\mathrm{tot}}$ in the no b-tag and b-tag categories of the $\tau_{\mathrm{h}}\tau_{\mathrm{h}}$ channel. 141
5.26 Distributions of $m_{\mathrm{T}}^{\mathrm{tot}}$ in the no b-tag and b-tag categories of the $\mathrm{e}\mu$ channel. 141
5.27 Upper limits at the 95% CL for the gluon fusion production process and the b-associated production process, combining all final states and categories. 142

5.28 Comparison of expected upper limits at the 95% CL for gluon fusion and b-associated production per channel. 142
5.29 Upper limits at the 95% CL for the gluon fusion and b-associated production processes, with the 125 GeV SM Higgs boson included as one of the backgrounds. 143
5.30 2D likelihood scans showing the best-fit value for $\sigma\times\mathcal{B}$ of both the gluon fusion and b-associated production processes. 144
5.31 Exclusions in the $m_{\mathrm{h}}^{\mathrm{mod+}}$ scenario and the hMSSM scenario of the A/H $\rightarrow \tau\tau$ analysis. 146

6.1 Transverse component of the di-tau mass for the expected backgrounds and observed events in the no b-tag and b-tag categories of the $\mu\tau_{\mathrm{h}}$ channel. 148
6.2 Transverse component of the di-tau mass for the expected backgrounds and observed events in the no b-tag and b-tag categories of the $\mathrm{e}\tau_{\mathrm{h}}$ channel. 148
6.3 Transverse component of the di-tau mass for the expected backgrounds and observed events in the no b-tag and b-tag categories of the $\tau_{\mathrm{h}}\tau_{\mathrm{h}}$ channel. 149
6.4 Transverse component of the di-tau mass for the expected backgrounds and observed events in the no b-tag and b-tag categories of the $\mathrm{e}\mu$ channel. 149
6.5 Upper limits at the 95% CL for the gluon fusion and b-associated production process. 150
6.6 Expected upper limits at the 95% CL for the gluon fusion and b-associated production, comparing the combination of all channels with the per-channel limits. 151
6.7 Upper limits at the 95% CL for the gluon fusion and b-associated production process, obtained by combining all channels and categories of the 2015 and the 2016 analyses. 155
6.8 Comparison of the expected upper limits at the 95% CL for the gluon fusion and b-associated production process, comparing the 2015 and 2016 analyses with a combination. 155
6.9 Exclusions in the $m_{\mathrm{h}}^{\mathrm{mod+}}$ scenario and the hMSSM scenario of the combination of the 2015 and 2016 A/H $\rightarrow \tau\tau$ analyses. 156

7.1 The expected exclusion in the $m_{\mathrm{h}}^{\mathrm{mod+}}$ scenario at the 95% CL of the 2015 MSSM analysis, projected to integrated luminosities of 300 and 3000 fb^{-1}. 159

List of tables

1.1 The fundamental fermions. 18

1.2 Tree-level couplings in the MSSM, as multiplicative factors with respect to the couplings of the Higgs boson in the SM. 27

3.1 Summary of hadronic tau decay modes. 66

4.1 Couplings in the type-II 2HDM. 95

6.1 Correlations between nuisance parameters in the 2015 and 2016 analyses. 152

A.1 Number of events observed in data in the 2jet-0tag, 2jet-1tag and 2jet-2tag categories in the $\mu\tau_{\mathrm{h}}$ channel, compared with the background expectation. The signal expectations at $m_{\mathrm{H}} = 300\,\mathrm{GeV}$, $\tan\beta = 2$ are given for comparison. The uncertainties correspond to the post-fit systematic unceraintties, taking into account correlations between them. 178

A.2 Number of events observed in data in the 2jet-0tag, 2jet-1tag and 2jet-2tag categories in the $\mathrm{e}\tau_{\mathrm{h}}$ channel, compared with the background expectation. The signal expectations at $m_{\mathrm{H}} = 300\,\mathrm{GeV}$, $\tan\beta = 2$ are given for comparison. The uncertainties correspond to the post-fit systematic unceraintties, taking into account correlations between them. 179

B.1 Systematic uncertainties that affect the estimated number of signal or background events in the $\mu\tau_{\mathrm{h}}$ channel. 181

B.2 Systematic uncertainties that affect the estimated number of signal or background events in the $\mathrm{e}\tau_{\mathrm{h}}$ channel. 182

B.3 Systematic uncertainties that affect the estimated number of signal or background events in the $\tau_{\mathrm{h}}\tau_{\mathrm{h}}$ channel. 183

B.4 Systematic uncertainties that affect the estimated number of signal or background events in the $\mathrm{e}\mu$ channel. 184

B.5 Systematic uncertainties that affect the estimated number of background events in the $\mathrm{Z} \to \mu\mu$ channel. 185

C.1 Number of events observed in data in the b-tag and no b-tag categories in the $\mu\tau_{\mathrm{h}}$ compared with the background expectation. The signal expectation, for $m_{\mathrm{A}} = 1\,\mathrm{TeV}$ and $\tan\beta = 50$ in the $m_{\mathrm{h}}^{\mathrm{mod+}}$ scenario, is also shown. The uncertainties correspond to the post-fit systematic uncerainties, taking into account correlations between them. 187

C.2 Number of events observed in data in the b-tag and no b-tag categories in the $\mathrm{e}\tau_{\mathrm{h}}$ channel, compared with the background expectation. The signal expectation, for $m_{\mathrm{A}} = 1\,\mathrm{TeV}$ and $\tan\beta = 50$ in the $m_{\mathrm{h}}^{\mathrm{mod+}}$ scenario, is also shown. The uncertainties correspond to the post-fit systematic uncerainties, taking into account correlations between them. 187

C.3 Number of events observed in data in the b-tag and no b-tag categories in the $\tau_{\mathrm{h}}\tau_{\mathrm{h}}$ channel, compared with the background expectation. The signal expectation, for $m_{\mathrm{A}} = 1\,\mathrm{TeV}$ and $\tan\beta = 50$ in the $m_{\mathrm{h}}^{\mathrm{mod+}}$ scenario, is also shown. The uncertainties correspond to the post-fit systematic uncerainties, taking into account correlations between them. 188

C.4 Number of events observed in data in the b-tag and no b-tag categories in the and $\mathrm{e}\mu$ channel, compared with the background expectation. The signal expectation, for $m_{\mathrm{A}} = 1\,\mathrm{TeV}$ and $\tan\beta = 50$ in the $m_{\mathrm{h}}^{\mathrm{mod+}}$ scenario, is also shown. The uncertainties correspond to the post-fit systematic uncerainties, taking into account correlations between them. 188

Chapter 1

Theory and motivation

To understand and motivate the searches presented in chapters 4 and 5 it is important to understand the theory and phenomenology behind them. This chapter describes the standard model of particle physics, the motivations for supersymmetry and the phenomenology of Higgs sectors beyond the standard model.

1.1 The standard model of particle physics

The standard model (SM) of particle physics is a theory that describes the electromagnetic (EM), weak nuclear and strong nuclear forces, and the interaction of those forces with particles. The SM is a quantum field theory (QFT) in which matter particles are represented by spin-$\frac{1}{2}$ fermions, with the forces represented by spin-1 bosons.

1.1.1 Fundamental particles and forces

In the SM there are twelve fundamental fermions, six that interact via the strong nuclear force (quarks) and six that do not (leptons). Each of the fermions has an antiparticle with opposite quantum numbers. The quarks and leptons are divided into three generations, with corresponding particles from different generations sharing the same properties apart from their mass. The quarks and leptons are summarised in table 1.1.

The symmetries governing the forces in the SM imply the presence of spin-1 bosons which carry the forces. The gluon (g) mediates the strong nuclear force, while the EM force is mediated by the photon (γ), and the weak force by the $\mathrm{W}^{\pm}$ and Z bosons.

Table 1.1: The fundamental fermions.

	1$^{\text{st}}$ generation	**2$^{\text{nd}}$ generation**	**3$^{\text{rd}}$ generation**
		Quarks	
Charge: $+\frac{2}{3}$	up (u)	charm (c)	top (t)
Charge: -$\frac{1}{3}$	down (d)	strange (s)	bottom (b)
		Leptons	
Charge: -1	electron (e)	muon (μ)	tau (τ)
Charge: 0	electron neutrino (ν_{e})	muon neutrino (ν_{μ})	tau neutrino (ν_{τ})

The quantum number associated with the strong force is colour, which both the quarks and the gluons carry. Within the framework of QFT, the strong force is described by quantum chromodynamics (QCD), governed by an SU(3) (colour) symmetry. Characteristics of QCD include confinement, meaning quarks are always observed in bound states called hadrons, and asymptotic freedom [4, 5]. Due to asymptotic freedom the strong coupling strength decreases at high energy, or short distances, making the force weaker. A more detailed introduction to QCD can be found in reference [6].

The unification of the weak nuclear and EM forces, introduced in the 1960s by Glashow [7], Weinberg [8] and Salam [9], is a key component of the SM. The electroweak force is governed by an $\text{SU(2)}_{\text{L}}\times\text{U(1)}_{\text{Y}}$ symmetry and implies the presence of weak neutral currents.

The SU(2)_{L} part of the symmetry is built from the weak isospin generators $I_{1,2,3} = \frac{1}{2}\sigma_{1,2,3}$, where σ_i are the Pauli spin matrices. The U(1)_{Y} symmetry comes from the weak hypercharge generator Y, which is related to weak isospin and electric charge as

$$Q = I_3 + \frac{1}{2}Y. \tag{1.1}$$

The associated gauge fields are the three weak isospin fields W_{μ}^{i} and the weak hypercharge field B_{μ}. These four fields mix to form the physical γ, Z and $\text{W}^{\pm}$ states as

$$\text{W}_{\mu}^{\pm} = \frac{1}{\sqrt{2}}(\text{W}_{\mu}^{1} \mp i\text{W}_{\mu}^{2}), \tag{1.2}$$

$$\mathrm{A}_\mu = \mathrm{W}^3_\mu \sin\theta_W + \mathrm{B}_\mu \cos\theta_W, \tag{1.3}$$

$$\mathrm{Z}_\mu = \mathrm{W}^3_\mu \cos\theta_W - \mathrm{B}_\mu \sin\theta_W. \tag{1.4}$$

In these equations A_μ is the photon field and Z_μ the Z field. The weak mixing angle θ_W is related to the weak (g) and electromagnetic (g') coupling constants as

$$\begin{aligned} & g\sin\theta_W = g'\cos\theta_W \\ \Rightarrow & \sin\theta_W = \frac{g'}{\sqrt{g^2+g'^2}} \text{ and } \cos\theta_W = \frac{g}{\sqrt{g^2+g'^2}}. \end{aligned} \tag{1.5}$$

Neutral weak-current interactions were discovered in 1973 at the Gargamelle bubble chamber experiment at CERN [10]. This discovery was followed ten years later by the discovery of the $\mathrm{W}^\pm$ [11, 12] and Z [13, 14] bosons by the UA1 and UA2 Collaborations at CERN, confirming the predictions from electroweak unification. It should be noted that the weak force only couples to the left-handed parts of fermion states, and so is maximally parity violating.

An issue with electroweak theory is that the gauge invariance of the Lagrangian would be broken by the addition of mass terms of the form $-\frac{1}{2}m^2\mathrm{Z}_\mu\mathrm{Z}^\mu$ for the gauge bosons. However, the W and Z bosons are known to be massive. A similar problem exists for fermions, as they are known to have mass but again the introduction of mass terms would break the gauge invariance of the Lagrangian. To be able to introduce mass terms electroweak symmetry must be broken. In the SM this happens via the Higgs mechanism.

1.1.2 The Higgs mechanism

The mechanism of electroweak symmetry breaking, the Higgs mechanism, was proposed in the 1960s by Englert and Brout [15], Higgs [16–18] and Guralnik, Hagen and Kibble [19]. The idea is to add a field that is symmetric under gauge transformations, but has a non-zero vacuum expectation value and thus breaks the symmetry spontaneously. According to Goldstone's theorem [20, 21] a consequence of spontaneous symmetry breaking is the appearance of a massless scalar (Goldstone boson) for each broken generator.

The simplest field that needs to be added to break electroweak symmetry is a complex doublet,

$$\Phi = \begin{pmatrix} \phi^+ \\ \phi^0 \end{pmatrix}. \tag{1.6}$$

The corresponding Lagrangian is of the form

$$\begin{aligned} \mathcal{L}_{\text{Higgs}} &= -(D_\mu\Phi)^\dagger(D^\mu\Phi) - V(\Phi^\dagger\Phi), \text{ with} \\ V &= \lambda(\Phi^\dagger\Phi - \frac{\mu_{\text{SM}}^2}{2\lambda})^2, \end{aligned} \tag{1.7}$$

where λ and μ_{SM}^2 are two real parameters. The parameter λ is a quartic coupling strength modifier, and it will later be shown that μ_{SM} is a mass parameter. For the vacuum to be stable λ must be positive, and for spontaneous symmetry breaking μ_{SM}^2 is also required to be positive.

Under a local SU(2)×U(1) transformation, the field transforms as,

$$\begin{pmatrix} \phi^+ \\ \phi^0 \end{pmatrix} = \exp\{\frac{i}{2}(\vec{\theta}\cdot\vec{\sigma} + \rho)\} \begin{pmatrix} \phi^+ \\ \phi^0 \end{pmatrix}, \tag{1.8}$$

where $\vec{\theta}$ and ρ are phase transformations which are functions of the space-time coordinates. The covariant derivative associated with such a transformation is

$$D_\mu = \partial_\mu - \frac{i}{2}g\vec{\mathrm{W}}_\mu\cdot\vec{\sigma} - \frac{i}{2}g'\mathrm{B}_\mu. \tag{1.9}$$

In the vacuum state, $V(\Phi^\dagger\Phi) = 0$, $\Phi^\dagger\Phi = \frac{\mu_{\text{SM}}^2}{2\lambda}$ and so Φ has to be non-zero. Now choosing $\phi^+ = 0$ and taking ϕ^0 to be real, this means:

$$\langle 0|\Phi|0\rangle = \begin{pmatrix} 0 \\ \frac{v}{\sqrt{2}} \end{pmatrix}, \tag{1.10}$$

where v is a real parameter, $v^2 \equiv \frac{\mu_{\text{SM}}^2}{\lambda}$.

Considering infinitesimal fluctuations around the vacuum state, it can be shown that the only remaining generator that leaves the field invariant is $I_3 + \frac{Y}{2}$, the generator of the U(1) group. Denoting the remaining, broken, generators as $\vec{b}$ and parameterising the field as an expansion around the vacuum state gives

$$\Phi = \exp\{\frac{i}{\sqrt{2}v}\vec{\theta}\cdot\vec{b}\}\begin{pmatrix} 0 \\ \frac{1}{\sqrt{2}}(v+\mathrm{H}) \end{pmatrix}. \tag{1.11}$$

By choosing an appropriate gauge the Goldstone bosons $\vec{\theta}$ can be eliminated. They become the longitudinal degrees of freedom of the $\mathrm{W}^{\pm}$ and Z bosons. This then leaves

$$\Phi = \begin{pmatrix} 0 \\ \frac{1}{\sqrt{2}}(v+\mathrm{H}) \end{pmatrix}. \tag{1.12}$$

Substituting this into the Lagrangian of equation 1.7, and using the definitions of $\mathrm{W}^{\pm}_{\mu}$ and Z_{μ} from equations 1.2–1.4, the Lagrangian becomes

$$\begin{aligned}\mathcal{L}_{\mathrm{Higgs}} = -\frac{1}{2}\partial_{\mu}\mathrm{H}\partial^{\mu}\mathrm{H} - \frac{g^2v^2}{4}\mathrm{W}^{-}_{\mu}\mathrm{W}^{\mu+} - \frac{g^2+g'^2}{8}v^2\mathrm{Z}_{\mu}\mathrm{Z}^{\mu} - \mu^2_{\mathrm{SM}}\mathrm{H}^2 + \\ \text{terms of at least } \mathcal{O}(3) \text{ in the fields.}\end{aligned} \tag{1.13}$$

This Lagrangian contains mass terms for the $\mathrm{W}^{\pm}$ and Z bosons, with $m_{\mathrm{W}} = \frac{gv}{2}$ and $m_{\mathrm{Z}} = \frac{1}{2}v\sqrt{g^2+g'^2}$. Using equation 1.5 it can be seen that these two masses are related as $\frac{m_{\mathrm{W}}}{m_{\mathrm{Z}}} = \cos\theta_W$. The remaining mass term is for the Higgs field H, $M_{\mathrm{H}} = \sqrt{2\mu^2_{\mathrm{SM}}}$. It is denoted M_{H} to avoid confusion with the mass of the heavy scalar H boson in the minimal supersymmetric standard model (MSSM), m_{H}, which will be introduced in section 1.3.1. Note that the photon does not acquire a mass.

Using these developments it is also possible to add mass terms for the fermions through Yukawa couplings between the fermion and Higgs fields, which are of the form

$$\lambda_f(\bar{\psi_L}\Phi\psi_R + \bar{\psi_R}\Phi\psi_L). \tag{1.14}$$

The parameter λ_f is a coupling constant specific to each fermion, $\lambda_f \propto m_f$. This means that heavier fermions couple more strongly to the Higgs field.

1.2 Standard model Higgs boson measurements

The mass of the Higgs boson is a free parameter in the SM, and so a large range of possible masses needed to be covered in Higgs boson searches. Searches for the Higgs boson at the Large Electron-Positron (LEP) collider did not lead to its observation. However, masses below 114.4 GeV were excluded at the 95% confidence level (CL) [22], providing a lower search limit. Subsequent searches at the Tevatron also did not lead to the discovery of the Higgs boson, but did exclude an additional mass range of 140–186 GeV at the 95% CL [23].

On the fourth of July 2012 the ATLAS and CMS Collaborations announced the discovery of a boson with a mass of around 125 GeV [24, 25]. The discovery was based on the observation of excesses in the search for $\mathrm{H} \rightarrow \gamma\gamma$ and $\mathrm{H} \rightarrow \mathrm{ZZ} \rightarrow 4\ell$, with a significance above 5σ. More data were collected and analysed during the remainder of 2012, and subsequent studies of its properties, such as spin, parity [26, 27] and couplings to other particles, increased the confidence in the compatibility of this new state with the SM Higgs boson. The most precise measurement of the mass of the Higgs boson, $M_{\mathrm{H}} = 125.09 \pm 0.21\ (\mathrm{stat}) \pm 0.11\ (\mathrm{syst})\,\mathrm{GeV}$, comes from the ATLAS and CMS combined mass measurement using the full dataset collected up to the end of 2012 [28]. The combined ATLAS and CMS production and decay rate measurements, using the same dataset, show very good agreement with the SM predictions [29]. In addition, the $\mathrm{H} \rightarrow \tau\tau$ decay was observed with a significance of 5.5σ through this combination. The individual searches by the ATLAS and CMS Collaborations resulted in observed significances of 4.5σ [30] and 3.2σ [31] for this process, respectively.

Figure 1.1 shows Feynman diagrams of the dominant Higgs boson production modes at the LHC. The production cross sections for each mode, shown in figure 1.2a, show that gluon fusion production is by far dominant. The other modes shown have cross sections at least an order of magnitude smaller, but are of importance due to their topologies. Tagging the additional leptons or jets in the final states of these production modes can reduce the size of the SM background.

Figure 1.2b shows that the branching ratios of $\mathrm{H} \rightarrow \gamma\gamma$ and $\mathrm{H} \rightarrow \mathrm{ZZ}$, the two discovery channels, are smaller than the branching ratios into many other final states. These two channels are thus not sensitive as a result of the size of their branching ratios, but rather

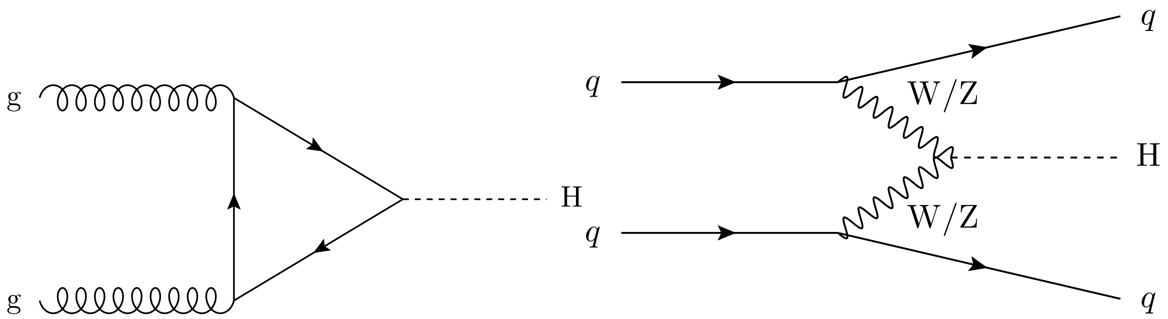

(a) Gluon fusion

(b) Vector boson fusion

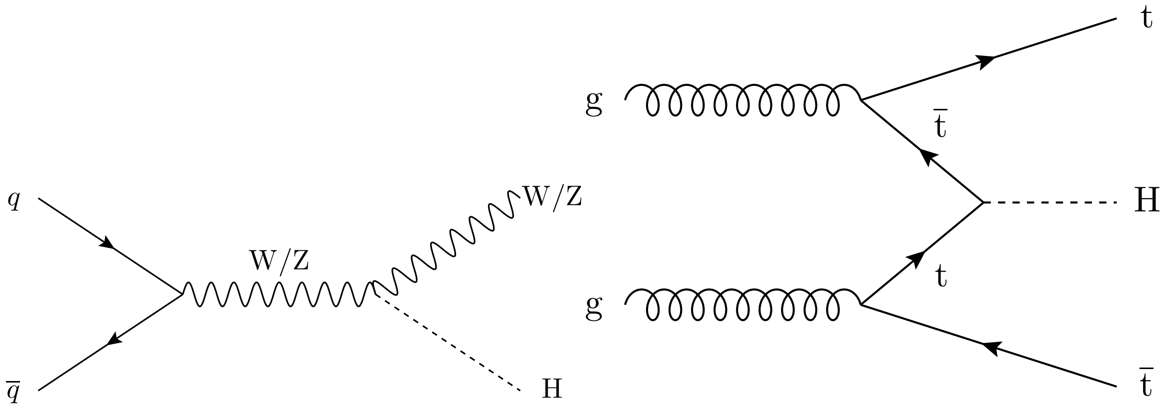

(c) W/Z associated production

(d) $t\bar{t}$ associated production

Figure 1.1: Tree-level Feynman diagrams for the dominant Higgs boson production modes at the LHC.

due to the small backgrounds in these analyses as well as the excellent photon and lepton energy resolution the detectors provide.

Since the restart of the LHC in 2015, SM Higgs boson measurements, and searches for the SM Higgs boson in decay channels not previously established, have already been performed. The decay into $\gamma\gamma$ has been re-established [33, 34], as has the decay into ZZ $\rightarrow 4\ell$ [35, 36], and measurements of H $\rightarrow$ WW have been performed [37, 38]. Establishing evidence for the decay of H $\rightarrow$ bb [39, 40] and of H $\rightarrow \mu\mu$ [41] is still to be achieved. Finally, searches for ttH production, which are important to directly probe the top-Higgs coupling, have also been carried out [42–45]. As more data are collected studies at the LHC will continue to test the compatibility of the Higgs boson with the SM.

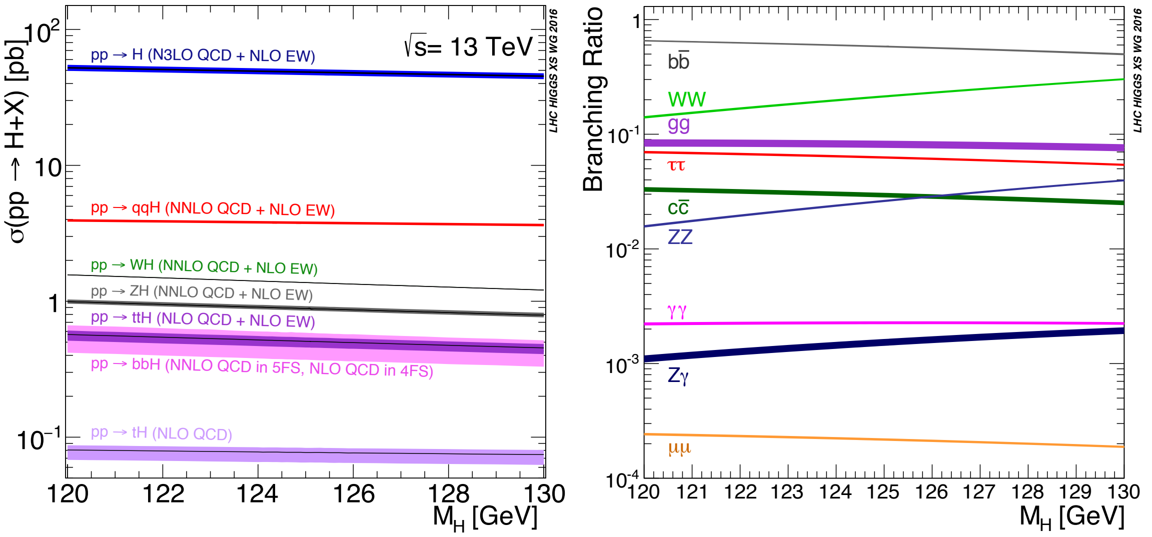

(a) SM Higgs boson production cross sections **(b)** SM Higgs boson branching ratios

Figure 1.2: (a) SM Higgs boson production cross sections at $\sqrt{s} = 13\,\mathrm{TeV}$ and (b) SM Higgs boson branching ratios, for Higgs boson masses between 120 and 130 GeV [32].

1.3 Beyond the standard model

The SM has been successfully tested to high accuracy [46]. However, some issues remain that cannot be addressed by the SM alone. For example, it does not provide a candidate for dark matter, which is estimated to make up 25% of the matter-energy density in the universe [47]. In addition, the running coupling constants of the electroweak and strong forces do not intersect at a common energy scale [48]. Another problem is that the force of gravity does not appear in the SM [49].

These points aside, the most important issue concerning the Higgs sector of the SM is the hierarchy problem [50]. The SM is accepted to be an effective field theory that describes the elementary particles and their interactions well, up to an energy scale Λ beyond which it breaks down. This is the energy scale at which new physics must enter. It is known that $\Lambda \leq \mathcal{O}(10^{19})$, the Planck scale, as quantum gravitational effects start to become important in that region. The energy scale Λ enters the corrections due to fermion and boson loops to the Higgs boson mass quadratically [51]:

$$\begin{aligned} M^2_{\mathrm{H_{SM}}} &= (M_{\mathrm{H}})^2_0 + \Delta M^2_{\mathrm{H}}, \\ \Delta M^2_{\mathrm{H}} &\sim \mathcal{O}(\Lambda^2). \end{aligned} \tag{1.15}$$

Thus, assuming that there is no new physics all the way up to the Planck scale, the observation $M_{\mathrm{H}} = 125\,\mathrm{GeV}$ would only be compatible with Λ of order 10^{19} GeV if there was extreme fine-tuning of the bare Higgs boson mass $(M_{\mathrm{H}})_0^2$.

Many beyond the standard model (BSM) theories that can address the hierarchy problem, and some of the other issues that were mentioned, have been developed. One of the most popular of these theories is supersymmetry (SUSY) [50], which postulates that there is a symmetry between bosons and fermions. This means every fermionic SM particle has a bosonic superpartner (sfermion, for scalar fermion) and every bosonic SM particle has a fermionic superpartner (boson name + 'ino', e.g. higgsino, Wino).

If this symmetry is unbroken the SUSY particles must have the same mass as their SM partners. However, if that had been the case such particles would have been detected a long time ago. The only possibility is then that SUSY is a broken symmetry and the superpartners are heavier than their SM equivalents. It is important to note that the fermion and boson loops contribute to the Higgs boson mass corrections with opposite sign, and so the symmetry between bosons and fermions allows for the cancellation of ΔM_{H}^2 terms. The cancellation would be exact if SUSY were unbroken, but because this is not the case the cancellation is not complete. Therefore if the SUSY breaking scale, where new particles should be found, is much larger than a few TeV further fine-tuning of the bare Higgs boson mass would be required [50, 51]. Apart from solving the hierarchy problem, SUSY addresses some of the other aforementioned issues. The lightest SUSY particle would be a candidate for dark matter if it were stable [50]. On top of that, SUSY allows the electroweak and strong coupling constants to intersect at a common energy scale of $\mathcal{O}(10^{16}\,\mathrm{GeV})$ [48].

The simplest supersymmetric extension of the SM, the MSSM [50], only adds the minimum number of particles and fields required to formulate a supersymmetric theory.

1.3.1 The Higgs sector of the MSSM

At least two Higgs doublets are required in the Higgs sector of the MSSM, and so in its simplest form two complex Higgs doublets are added [51],

$$\Phi_d = \begin{pmatrix} \phi_d^0 \\ \phi_d^- \end{pmatrix} \text{ and } \Phi_u = \begin{pmatrix} \phi_u^+ \\ \phi_u^0 \end{pmatrix}. \tag{1.16}$$

Note that ϕ_d^0 couples exclusively to down-type fermions, and ϕ_u^0 couples exclusively to up-type fermions. Electroweak symmetry is broken as in the SM case and minimising the potential associated with the two Higgs doublets gives,

$$\langle 0|\Phi_d|0\rangle = \begin{pmatrix} v_d \\ 0 \end{pmatrix} \text{ and } \langle 0|\Phi_u|0\rangle = \begin{pmatrix} 0 \\ v_u \end{pmatrix}. \tag{1.17}$$

This can be used to define

$$\tan\beta \equiv \frac{v_u}{v_d}. \tag{1.18}$$

Of the eight degrees of freedom due to the introduction of two complex doublets, three become longitudinal states of the $\mathrm{W}^\pm$ and Z bosons. The remaining five degrees of freedom lead to five physical Higgs bosons: a charged Higgs boson pair $\mathrm{H}^\pm$, the neutral pseudoscalar A and the neutral scalars h and H. These arise from the mixing of the fields as:

$$\mathrm{H}^+ = \phi_u^+ \cos\beta + \phi_d^{-\dagger} \sin\beta, \tag{1.19}$$

$$\mathrm{H}^- = \phi_u^{+\dagger} \cos\beta + \phi_d^- \sin\beta, \tag{1.20}$$

$$\mathrm{A} = \sqrt{2}(\mathrm{Im}\phi_d^0 \sin\beta + \mathrm{Im}\phi_u^0 \cos\beta), \tag{1.21}$$

$$\mathrm{h} = -(\sqrt{2}\mathrm{Re}\phi_d^0 - v_d)\sin\alpha + (\sqrt{s}\mathrm{Re}\phi_u^0 - v_u)\cos\alpha, \tag{1.22}$$

$$\mathrm{H} = (\sqrt{2}\mathrm{Re}\phi_d^0 - v_d)\cos\alpha + (\sqrt{2}\mathrm{Re}\phi_u^0 - v_u)\sin\alpha. \tag{1.23}$$

These mixtures depend on $\tan\beta$ and the mixing angle α which is found by diagonalising the neutral scalar Higgs squared-mass matrix,

$$\mathcal{M}^2_{\mathrm{tree}} = \begin{pmatrix} m_\mathrm{A}^2 \sin\beta^2 + m_\mathrm{Z}^2 \cos^2\beta & -(m_\mathrm{A}^2 + m_\mathrm{Z}^2)\sin\beta\cos\beta \\ -(m_\mathrm{A}^2 + m_\mathrm{Z}^2)\sin\beta\cos\beta & m_\mathrm{A}^2\cos^2\beta + m_\mathrm{Z}^2\sin^2\beta \end{pmatrix}, \tag{1.24}$$

of which H and h are the eigenstates. As the self-interactions of the Higgs fields are not independent parameters, at tree level the MSSM Higgs sector is determined by two free parameters, $\tan\beta$ and one of the Higgs boson masses, conventionally chosen as m_A. The masses of the neutral scalars H and h are the eigenvalues of $\mathcal{M}^2_{\mathrm{tree}}$,

$$m^2_{\mathrm{H,h}} = \frac{1}{2}[m_\mathrm{A}^2 + m_\mathrm{Z}^2 \pm \sqrt{(m_\mathrm{A}^2 + m_\mathrm{Z}^2)^2 - 4m_\mathrm{Z}^2 m_\mathrm{A}^2 \cos^2 2\beta}\ ]. \tag{1.25}$$

The masses of the charged Higgs bosons are

$$m_{\mathrm{H}^{\pm}}^2 = m_{\mathrm{A}}^2 + m_{\mathrm{W}}^2. \tag{1.26}$$

A consequence of equation 1.25 is a tree-level upper bound on the mass of the light Higgs boson,

$$m_{\mathrm{h}} \leq m_{\mathrm{Z}}, \tag{1.27}$$

and a constraint on α,

$$\cos^2(\beta - \alpha) = \frac{m_{\mathrm{h}}^2(m_{\mathrm{Z}}^2 - m_{\mathrm{h}}^2)}{m_{\mathrm{A}}^2(m_{\mathrm{H}}^2 - m_{\mathrm{h}}^2)}. \tag{1.28}$$

The requirement that m_{h} be less than the mass of the Z boson, 91.2 GeV, seems problematic at first, as it is known that there is a Higgs state with a mass of 125 GeV. However, the tree-level masses and couplings of the Higgs bosons in the MSSM can be significantly altered by radiative corrections. The dominant effect is from incomplete cancellation of the stop- and top-loop corrections. This can increase the mass of the light Higgs boson up to a maximum of 135 GeV.

The tree-level couplings of the neutral Higgs bosons to bosons and fermions are modified with respect to the couplings of the Higgs boson in the SM by the multiplicative factors given in table 1.2 [32].

Table 1.2: Tree-level couplings in the MSSM, as multiplicative factors with respect to the couplings of the Higgs boson in the SM.

Particle	Coupling to bosons	Coupling to up-type quarks	Coupling to down-type quarks and leptons
A	0	$\cot\beta$	$\tan\beta$
H	$\cos(\beta - \alpha)$	$\frac{\sin\alpha}{\sin\beta}$	$\frac{\cos\alpha}{\cos\beta}$
h	$\sin(\beta - \alpha)$	$\frac{\cos\alpha}{\sin\beta}$	$-\frac{\sin\alpha}{\cos\beta}$

In the *decoupling limit*, when $m_{\mathrm{A}} \gg m_{\mathrm{Z}}$ and $\cos(\beta - \alpha)$ tends to zero, the mixing angle $\alpha \approx \beta - \pi/2$. This reduces the couplings in table 1.2 to the SM couplings for the h boson, with negligible couplings to bosons for the two remaining neutral Higgs bosons;

couplings to down-type quarks and leptons enhanced by a factor $\tan\beta$; and couplings to up-type quarks enhanced by a factor $\frac{1}{\tan\beta}$. This motivates the choice of decay into $\tau\tau$ as a search channel for the neutral Higgs bosons in the MSSM. Figure 1.3 shows the branching ratios of the H boson in the $m_{\rm h}^{\rm mod+}$ scenario which will be discussed in more detail in section 1.4.1. The branching ratio into di-tau pairs is large for $\tan\beta = 30$. The branching ratios of the A boson follow a similar pattern.

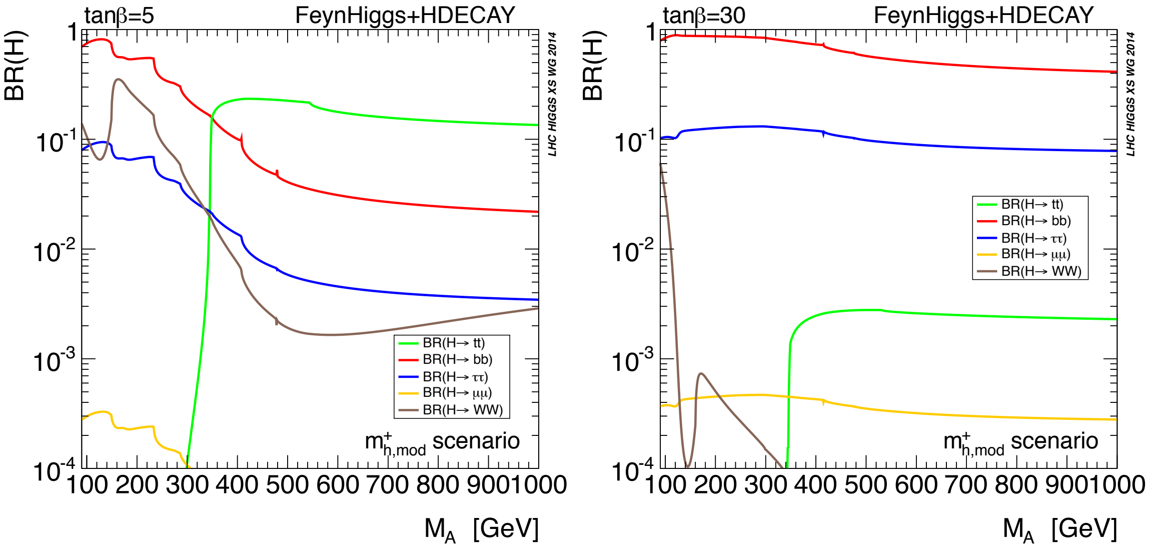

(a) $\tan\beta$=5 **(b)** $\tan\beta$=30

Figure 1.3: Branching ratios of the H boson in the $m_{\rm h}^{\rm mod+}$ scenario, at (a) $\tan\beta$=5 and (b) $\tan\beta$=30. The branching ratio into $\tau\tau$ (blue), $\rm b\bar{b}$ (red) and $\mu\mu$ (yellow) is enhanced at high $\tan\beta$, while the branching ratio into WW (brown) and $\rm t\bar{t}$ (green) is reduced [52].

The dominant neutral MSSM Higgs boson production processes at hadron colliders are slightly different from the SM Higgs boson production processes. Because the pseudoscalar A does not couple to the vector bosons, and in the decoupling limit the coupling of H to vector bosons is suppressed with respect to the SM expectation, vector boson fusion (VBF) and W or Z associated production (WH or ZH) are not as important as for the production of the SM Higgs boson. As in the SM, gluon fusion production is the dominant production mode at low $\tan\beta$. An example tree-level Feynman diagram for gluon fusion production, which proceeds via a quark loop, is given in figure 1.4a. At low $\tan\beta$ values this loop is dominated by top quarks, while at high $\tan\beta$ the b-quark loop dominates. This is a result of the enhanced coupling to down-type fermions at high $\tan\beta$. Due to the negative top-bottom loop interference effect the gluon fusion cross section decreases with increasing $\tan\beta$ up to around $\tan\beta = 3$, where the cross section starts to increase with increasing $\tan\beta$ again.

Another consequence of the enhanced couplings to down-type fermions at high $\tan\beta$ is the dominance of b-associated production, where the Higgs boson is produced through bottom quark fusion. The tree-level Feynman diagram for this process is shown in figure 1.4b.

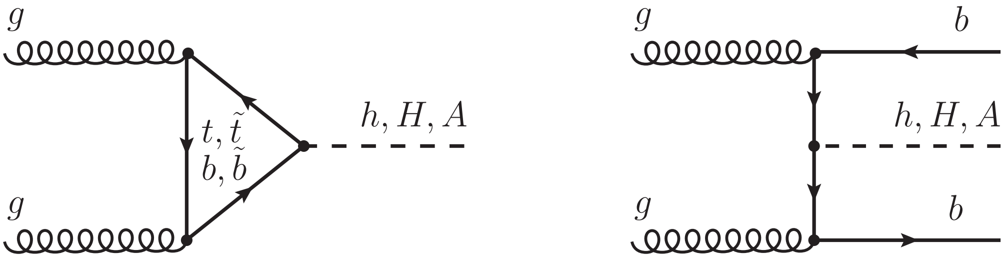

(a) Gluon fusion production **(b)** b-Associated production

Figure 1.4: Tree-level Feynman diagrams of (a) gluon fusion production and (b) b-associated production of neutral Higgs bosons in the MSSM. The squarks in the gluon fusion production loop do not contribute to the production of the A boson.

1.3.2 Two Higgs doublet models

A different approach, also leading to an extended Higgs sector with respect to the SM, is found in two Higgs doublet models (2HDMs) [53, 54]. As the name suggests 2HDMs are a generic class of models in which there is not one, but two Higgs doublets. The addition of a second Higgs doublet cannot just be motivated by SUSY, but also by other models. An important point is that despite the presence of a second Higgs doublet, there are no explicit SUSY particles in the 2HDM.

There are several different types of 2HDM, all distinguished by the couplings of the different Higgs states to bosons and fermions. In its most general form, there are nine free parameters in the potential of a CP-conserving 2HDM. These are taken as $\tan\beta$ and the mixing angle α, already discussed in the context of the MSSM, the masses of the five Higgs bosons, and quartic couplings appearing in the potential. The most studied of the 2HDMs, the type-II 2HDM, has a structure very similar to the MSSM Higgs sector. The tree-level couplings of the neutral Higgs bosons to vector bosons and fermions are the same as the tree-level MSSM couplings in table 1.2.

The behaviour of the 2HDM couplings in the *alignment limit*, where $\cos(\beta - \alpha) = 0$, differs from that of the MSSM couplings. In particular, in the alignment limit of the 2HDM the decays A → Zh and H → hh vanish. This is due to the fact that these couplings are proportional to $\cos(\beta - \alpha)$ and there are no corrections from SUSY particles to make the branching ratios non-zero.

The inclusive cross section times branching ratio ($\sigma\times\mathcal{B}$) for production of an H boson and decays into various final states is shown in figure 1.5a for an example of a type-II 2HDM, for two values of $\tan\beta$. Figure 1.5b shows the inclusive $\sigma\times\mathcal{B}$ for production and decay of an A boson in the same type-II 2HDM example, at two values of $\tan\beta$. At low $\tan\beta$ the $\sigma\times\mathcal{B}$ for H → hh production and decay and A → Zh production and decay are enhanced for $250 \leq m_{\mathrm{H}} \leq 350\,\mathrm{GeV}$ and $220 \leq m_{\mathrm{A}} \leq 350\,\mathrm{GeV}$, respectively.

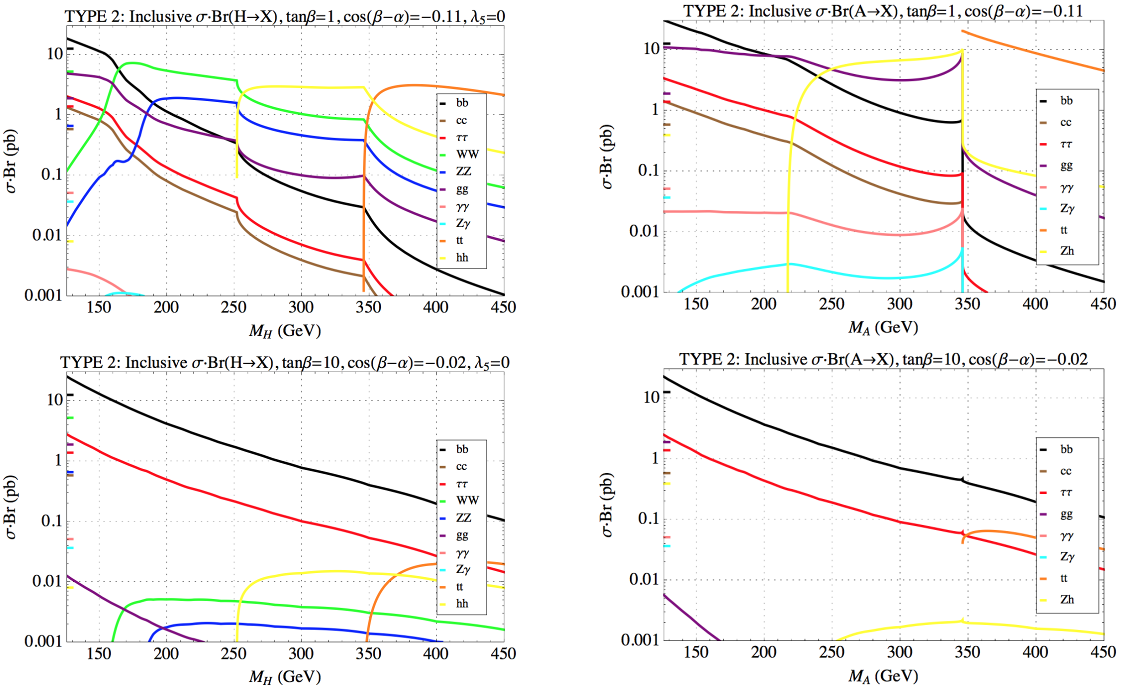

(a) H boson

(b) A boson

Figure 1.5: Inclusive production $\sigma\times\mathcal{B}$ for an example of a type-II 2HDM, for (a) the H boson and (b) the A boson. The top figures use $\tan\beta$=1 and $\cos(\beta - \alpha) = -0.11$, the bottom figures are made for $\tan\beta$=10 and $\cos(\beta - \alpha) = -0.02$. At low $\tan\beta$ the H → hh and A → Zh decays are enhanced for masses up to 350 GeV [54].

1.4 MSSM benchmark scenarios

Because the MSSM contains a large number of SUSY-breaking parameters that affect the Higgs sector, it is usual to define benchmark scenarios in which the only free parameters are m_{A} and $\tan\beta$. In these scenarios the SUSY parameters entering in the radiative corrections are fixed.

The parameters that need to be fixed in the benchmark scenarios are the SUSY breaking scale M_{SUSY}, which is also the mass scale of the third generation squarks; the higgsino mass parameter μ_{MSSM}; the U(1) and SU(2) gaugino mass parameters, M_1 and M_2; the masses of the stau, $m_{\tilde{\ell}_3}$, and the gluino, $m_{\tilde{g}}$; the trilinear couplings of the stops, sbottoms and staus to the Higgs field (A_{t}, A_{b} and A_{τ}); and the stop, sbottom and stau mixing parameters (X_{t}, X_{b} and X_{τ}).

Some of these parameters can be related to each other. For example, X_{t}, X_{b} and X_{τ} can be expressed as:

$$\begin{aligned} X_{\mathrm{t}} &= A_{\mathrm{t}} - \mu_{\mathrm{MSSM}} \cot\beta, \\ X_{\mathrm{b}} &= A_{\mathrm{b}} - \mu_{\mathrm{MSSM}} \tan\beta, \\ X_{\tau} &= A_{\tau} - \mu_{\mathrm{MSSM}} \tan\beta. \end{aligned} \tag{1.29}$$

In addition, M_1 is fixed via the unification relation,

$$M_1 = \frac{5}{3} M_2 \tan{\theta_W}^2. \tag{1.30}$$

Some additional parameters which only have a small effect on the MSSM Higgs boson sector are fixed to values compatible with exclusion limits from direct searches in all benchmark scenarios. The masses of the first and second generation squarks are set to 1.5 TeV, and the masses of the first and second generation sleptons to 500 GeV. The trilinear couplings of the first and second generation squarks and sleptons are taken to be zero.

1.4.1 The $m_{\mathrm{h}}^{\mathrm{mod+}}$ scenario

The $m_{\mathrm{h}}^{\mathrm{mod+}}$ scenario [55] is a modification of the $m_{\mathrm{h}}^{\mathrm{max}}$ scenario [56]. The $m_{\mathrm{h}}^{\mathrm{max}}$ scenario, which was used for interpretations of MSSM Higgs boson searches at LEP and the Tevatron, allows the mass of the light Higgs boson to reach the highest a-priori expected value of around 135 GeV for high m_A. There is only a small area of the m_A-$\tan\beta$ plane in this scenario where the mass of the light Higgs boson is compatible with the observed 125 GeV state. The modifications to the parameters of the $m_\mathrm{h}^\mathrm{max}$ scenario address this issue. In the $m_\mathrm{h}^\mathrm{mod+}$ scenario M_SUSY is chosen to be 1 TeV. The stop mixing parameter is positive, $X_\mathrm{t} = 1.5 M_\mathrm{SUSY}$. The remaining parameters are set as $\mu_\mathrm{MSSM} = 200\,\mathrm{GeV}$, $m_{\tilde{g}} = 1.5\,\mathrm{TeV}$, $m_{\tilde{\ell}_3} = 1\,\mathrm{TeV}$, and $A_\mathrm{b} = A_\mathrm{t} = A_\tau$.

Figure 1.6 shows the cross sections of gluon fusion and b-associated production of the H boson in the $m_\mathrm{h}^\mathrm{mod+}$ scenario. Gluon fusion production dominates at low $\tan\beta$, while b-associated production has a larger cross section at high $\tan\beta$. The behaviour of the production cross sections of the A boson is similar.

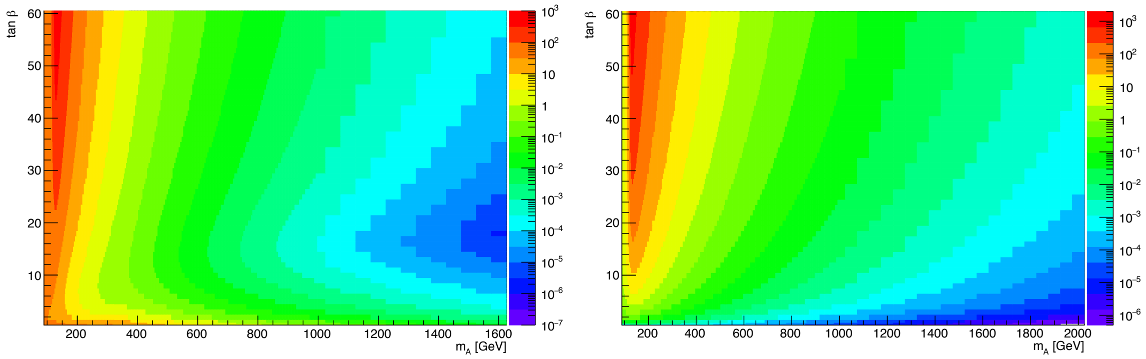

(a) $\sigma(\mathrm{gg} \to \mathrm{H})$ (pb) **(b)** $\sigma(\mathrm{gg} \to \mathrm{bbH})$ (pb)

Figure 1.6: Production cross section of (a) gluon fusion production and (b) b-associated production of the H boson in the $m_\mathrm{h}^\mathrm{mod+}$ scenario. The gluon fusion production cross section is larger at low $\tan\beta$, while the b-associated production cross section is larger at high $\tan\beta$. These values are based on the calculations in reference [57].

Figure 1.7 shows the branching ratios of the H and A bosons into $\tau\tau$. The branching ratios into $\tau\tau$ are enhanced, especially at high $\tan\beta$, showing how this decay channel is useful for MSSM Higgs boson searches.

1.4.2 MSSM scenarios at low $\tan\beta$

The mass of the light Higgs boson in the MSSM is said to be compatible with 125 GeV if the light Higgs boson mass lies within ±3 GeV of 125 GeV. This mass window corresponds to the theoretical uncertainty on the MSSM prediction for m_h. A large area of the m_A-$\tan\beta$ plane in the $m_\mathrm{h}^\mathrm{mod+}$ scenario contains a light Higgs boson with a mass compatible with 125 GeV. However, at low values of $\tan\beta$ this is not the case. This is illustrated in

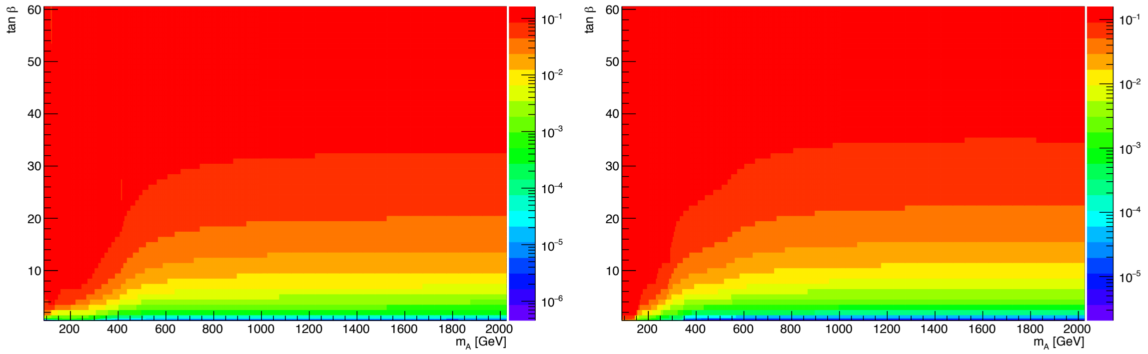

(a) $\mathcal{B}(\mathrm{H} \rightarrow \tau\tau)$ **(b)** $\mathcal{B}(\mathrm{A} \rightarrow \tau\tau)$

Figure 1.7: Branching ratios of (a) the H boson and (b) the A boson into $\tau\tau$. The branching ratios into $\tau\tau$ are enhanced at high $\tan\beta$. These values are based on the calculations in reference [57].

figure 1.8a, where the mass of the light Higgs boson in the $m_\mathrm{h}^\mathrm{mod+}$ scenario is shown. The low $\tan\beta$ regime can be re-opened if M_SUSY is allowed to be greater than 3 TeV [58].

Two approaches for the definition of an MSSM scenario that gives access to the low $\tan\beta$ region have been developed, they will be discussed in the next sections.

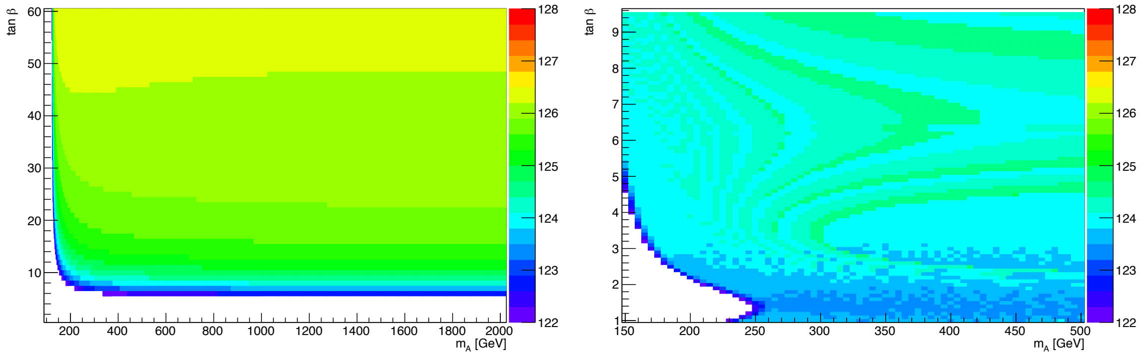

(a) $m_\mathrm{h}^\mathrm{mod+}$ scenario **(b)** Low-$\tan\beta$ scenario

Figure 1.8: The mass of the light Higgs boson, m_h, in GeV as a function of m_A and $\tan\beta$ in (a) the $m_\mathrm{h}^\mathrm{mod+}$ scenario and (b) the low-$\tan\beta$ scenario. The white areas indicate masses lower than 122 GeV. The figures show that the mass of the light Higgs boson is compatible with 125 GeV over a large part of the m_A-$\tan\beta$ plane in the $m_\mathrm{h}^\mathrm{mod+}$ scenario, except at low $\tan\beta$. In the low-$\tan\beta$ scenario the mass of the light Higgs boson is compatible with 125 GeV nearly everywhere. These values are based on the calculations in reference [57].

The low-tan β scenario

In the low-tan β scenario [59, 60], the SUSY parameters entering the radiative corrections are tuned to obtain a light Higgs boson mass of around 125 GeV in most of the m_{A}-tan β plane considered. Figure 1.8b shows that, apart from in a corner of tan β = 1–4 and m_{A} = 150–250 GeV, m_{h} is compatible with 125 GeV.

To obtain $m_{\mathrm{h}} \approx 125$ GeV over a large part of the parameter space, M_{SUSY} is not fixed but varies between a few TeV and 100 TeV, while varying the parameter X_{t} as:

$$\begin{aligned} \tan\beta \leq 2 : \frac{X_{\mathrm{t}}}{M_{\mathrm{SUSY}}} &= 2, \\ 2 < \tan\beta \leq 8.6 : \frac{X_{\mathrm{t}}}{M_{\mathrm{SUSY}}} &= 0.0375\tan^2\beta - 0.7\tan\beta + 3.25, \\ 8.6 < \tan\beta : \frac{X_{\mathrm{t}}}{M_{\mathrm{SUSY}}} &= 0. \end{aligned} \tag{1.31}$$

The other trilinear couplings are set to 2 TeV, with μ_{MSSM} set to 1.5 TeV and M_2 to 2 TeV.

The branching ratios of H → hh and A → Zh in the low-tan β scenario are shown in figure 1.9. For both decay channels there are areas in the m_{A}-tan β plane where the branching ratio is enhanced, indicating how analyses targeting such processes can be sensitive in this scenario.

The hMSSM scenario

The hMSSM scenario [61, 62] uses a different approach, in which $m_{\mathrm{h}} = 125$ GeV by construction.

One of the assumptions of the hMSSM is that the mass matrix for the neutral CP-even states can be decomposed as,

$$\mathcal{M}^2_{\phi} = \mathcal{M}^2_{\mathrm{tree}} + \begin{pmatrix} \Delta\mathcal{M}^2_{11} & \Delta\mathcal{M}^2_{12} \\ \Delta\mathcal{M}^2_{12} & \Delta\mathcal{M}^2_{22} \end{pmatrix}, \tag{1.32}$$

where the $\Delta\mathcal{M}^2_{ij}$ are the radiative corrections. The second assumption is that only $\Delta\mathcal{M}^2_{22}$ needs to be taken into account, as this is the element that involves the stop-top correction and so $\Delta\mathcal{M}^2_{22} \gg \Delta\mathcal{M}^2_{12}, \Delta\mathcal{M}^2_{11}$. Finally, all SUSY particles are assumed to be heavy

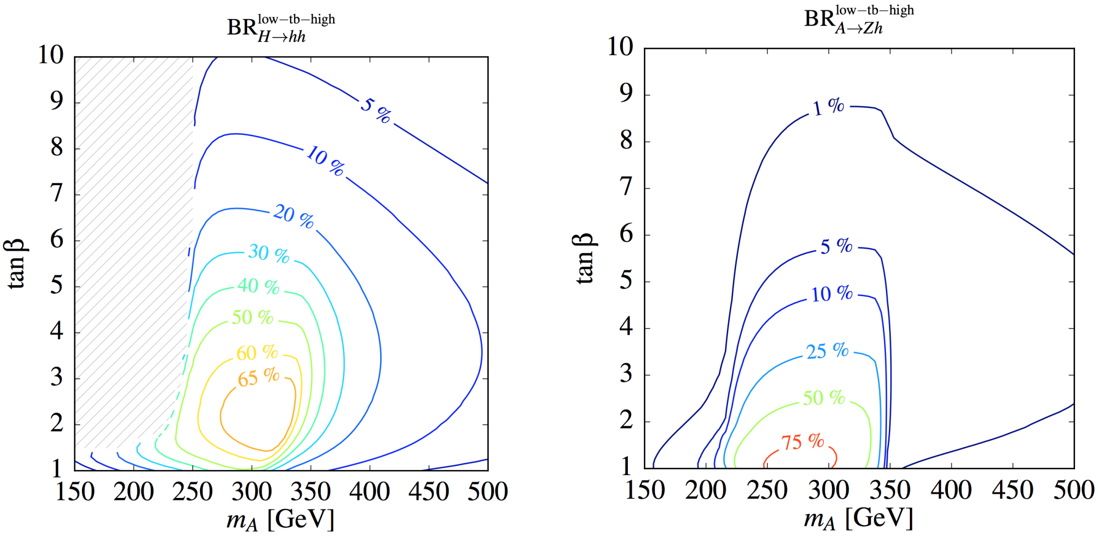

(a) H → hh **(b)** A → Zh

Figure 1.9: Branching ratios of (a) H → hh and (b) A → Zh in the low-$\tan\beta$ scenario, indicating areas where both are significantly enhanced [60].

enough not to be detected at the LHC and apart from effects on the mass matrix, the effects on the Higgs sector can be neglected.

Using these assumptions the lightest eigenvalue of the mass matrix can be inverted to get:

$$\Delta\mathcal{M}^2_{22} = \frac{m_\mathrm{h}^2(m_\mathrm{A}^2 + m_\mathrm{Z}^2 - m_\mathrm{h}^2) - m_\mathrm{A}^2 m_\mathrm{Z}^2 \cos^2 2\beta}{m_\mathrm{Z}^2\cos^2\beta + m_\mathrm{A}^2\sin^2\beta - m_\mathrm{h}^2}. \tag{1.33}$$

This can be used to write,

$$\begin{aligned} m_\mathrm{H}^2 &= \frac{(m_\mathrm{A}^2 + m_\mathrm{Z}^2 - m_\mathrm{h}^2)(m_\mathrm{Z}^2\cos^2\beta + m_\mathrm{A}^2\sin^2\beta - m_\mathrm{A}^2 m_\mathrm{Z}^2\cos^2 2\beta)}{m_\mathrm{Z}^2\cos^2\beta + m_\mathrm{A}^2\sin^2\beta - m_\mathrm{h}^2}, \\ \tan\alpha &= -\frac{(m_\mathrm{Z}^2 + m_\mathrm{A}^2)\cos\beta\sin\beta}{m_\mathrm{Z}^2\cos^2\beta + m_\mathrm{A}^2\sin^2\beta - m_\mathrm{h}^2}. \end{aligned} \tag{1.34}$$

Combining this with the H-hh coupling,

$$\lambda_\mathrm{Hhh} = \lambda_\mathrm{Hhh,tree} + 3\frac{\Delta\mathcal{M}^2_{22}\sin\alpha}{m_\mathrm{Z}^2\sin\beta}\cos^2\alpha, \tag{1.35}$$

gives enough information to determine the cross sections and branching ratios of all of the five Higgs bosons as a function of m_{A} and $\tan\beta$. The scenario is only well defined in regions where the denominator in equations 1.33 and 1.34, $m_{\mathrm{Z}}^2\cos^2\beta + m_{\mathrm{A}}^2\sin^2\beta - m_{\mathrm{h}}^2$, is non-zero. This leads to a minimum accessible m_{A} value of m_{h} at high $\tan\beta$, and a minimum accessible m_{A} of around 151 GeV for $\tan\beta$=1. In addition, the scenario can be formulated, but is not strictly valid, for values of $\tan\beta$ upwards of ten [63]. The reason for this is that direct higher order SUSY corrections to down-type fermion couplings and corrections due to SUSY particles in loops become relevant above $\tan\beta$=10, but these are omitted in the hMSSM approach.

The production cross sections of the H and A bosons are qualitatively similar to those in other MSSM scenarios. Gluon fusion is dominant at low $\tan\beta$, with b-associated production being more important at high $\tan\beta$.

The branching ratios of the H and A bosons into $\tau\tau$ follow a similar pattern as in other MSSM scenarios, with large branching ratios at high $\tan\beta$.

1.5 Status of BSM Higgs boson searches

With the data collected by the LHC experiments up to the end of 2012 many searches for BSM Higgs bosons were performed. Figure 1.10 shows the interpretations of different searches performed with the CMS detector during this period in the $m_{\mathrm{h}}^{\mathrm{mod+}}$ (figure 1.10a) and hMSSM (figure 1.10b) scenarios. The direct search for heavier Higgs bosons decaying into pairs of tau leptons sets the most stringent limits at high $\tan\beta$, with searches for heavy Higgs bosons decaying to bb and to $\mu\mu$ both excluding smaller parts of the high-$\tan\beta$ region. Searches for heavy Higgs bosons decaying to WW and ZZ are able to exclude part of the low-$\tan\beta$ region. In the hMSSM scenario searches for H $\to$ hh and A $\to$ Zh can exclude a small area at low $\tan\beta$ and between m_{A} = 250–350 GeV. The red exclusion contour in figure 1.10b is the reinterpretation of the H $\to$ hh $\to$ bb$\tau\tau$ analysis presented in chapter 4.

Since the restart of the LHC in 2015 searches for A/H $\to$ $\tau\tau$, setting more stringent limits than those shown in figure 1.10, have been performed with the CMS detector. The results of these searches will be presented in chapter 5. Similar searches have been performed by ATLAS [64]. Neutral BSM Higgs bosons are being searched for in other channels too, with some results for decays into tt [65], ZZ [35, 36], and WW [66] already public. In addition, searches for charged Higgs bosons [67–69] and di-Higgs searches [70–75], both in various final states, have been performed.

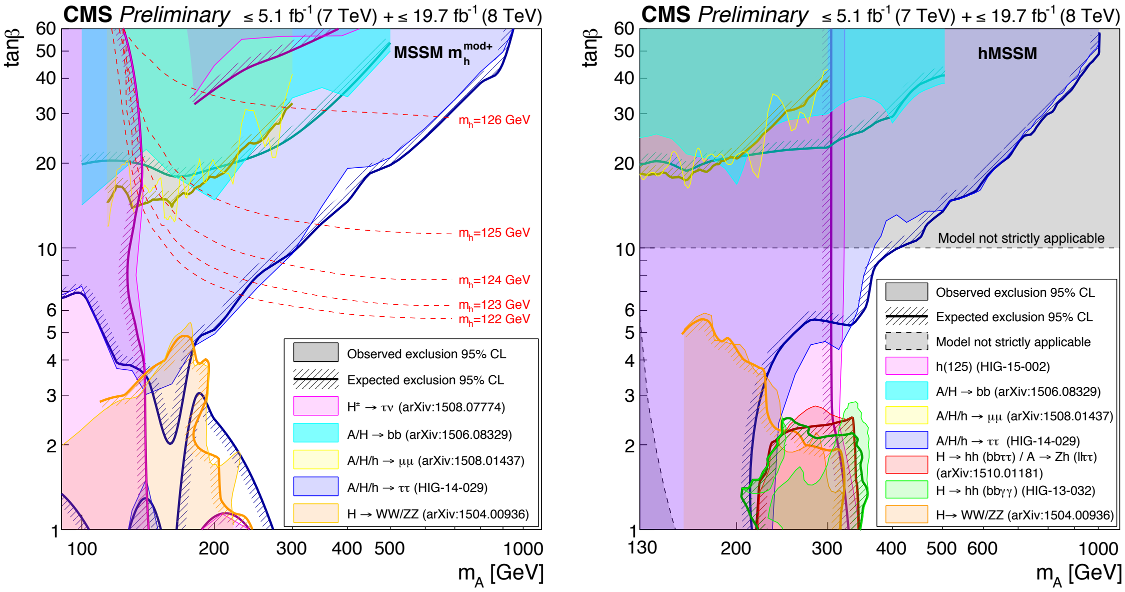

(a) $m_{\mathrm{h}}^{\mathrm{mod+}}$ scenario

(b) hMSSM scenario

Figure 1.10: Summary of the interpretations of BSM Higgs boson searches at CMS using data collected up to the end of 2012 in (a) the $m_{\mathrm{h}}^{\mathrm{mod+}}$ and (b) the hMSSM scenario. The different coloured areas indicate the observed and expected exclusion from different searches in these scenarios. The results from MSSM Higgs boson searches with decays into tau leptons are shown in blue and exclude more of the parameter space than any of the other searches. The MSSM Higgs to bb (cyan) and Higgs to $\mu\mu$ (yellow) searches are also sensitive in part of the high-$\tan\beta$ region, with searches for Higgs to WW or ZZ (orange) providing exclusion power at low $\tan\beta$ and low mass. In the $m_{\mathrm{h}}^{\mathrm{mod+}}$ scenario the charged Higgs to $\tau\nu$ search (magenta) excludes the low mass region for all values of $\tan\beta$. Masses below around 300 GeV in the hMSSM scenario are excluded instead by constraints from SM Higgs boson measurements (magenta). In this scenario small areas of the low-$\tan\beta$ region are also excluded by the searches for $\mathrm{H} \to \mathrm{hh} \to \mathrm{bb}\tau\tau$ and $\mathrm{A} \to \mathrm{Zh} \to \ell\ell\tau\tau$ (red) and the search for $\mathrm{H} \to \mathrm{hh} \to \mathrm{bb}\gamma\gamma$ [63].

Chapter 2

The LHC and the CMS experiment

2.1 The LHC

The Large Hadron Collider (LHC) [76] is a 26.7 km long synchrotron hadron accelerator and collider below the surface of the Franco-Swiss border near Geneva. It is installed in the tunnel that previously hosted the Large Electron-Positron (LEP) accelerator [77] that was operated by the European Organisation for Nuclear Research (CERN) between 1989 and 2000.

The LHC was designed to collide two beams of protons at centre-of-mass energies ($\sqrt{s}$) of up to 14 TeV. It therefore consists of two rings in which the beams of protons are individually accelerated. In addition to colliding beams of protons, the LHC is also used for proton-lead and lead-lead collisions.

The LHC does not operate on its own: the protons are fed into it via a chain of accelerators. Figure 2.1 shows a schematic of the CERN accelerator complex. Protons originate from hydrogen gas, where electrons are stripped off the hydrogen atoms using an electric field. The protons then pass through an injector chain which increases the energy of the protons in several steps. After the protons are created from the hydrogen gas they are accelerated to an energy of 50 MeV in the Linac 2 linear accelerator. They are then passed on to the Proton Synchrotron Booster (PSB) which accelerates the protons until they reach an energy of 1.4 GeV. The next accelerator in the chain, the Proton Synchrotron (PS), further accelerates the protons to 25 GeV, with the Super Proton Synchrotron (SPS) bringing the energy up to 450 GeV. When this energy has been reached the protons are injected into the LHC in two counter-rotating beams. In the LHC ring the beams are further accelerated to the required centre-of-mass energy by eight radio frequency (RF)

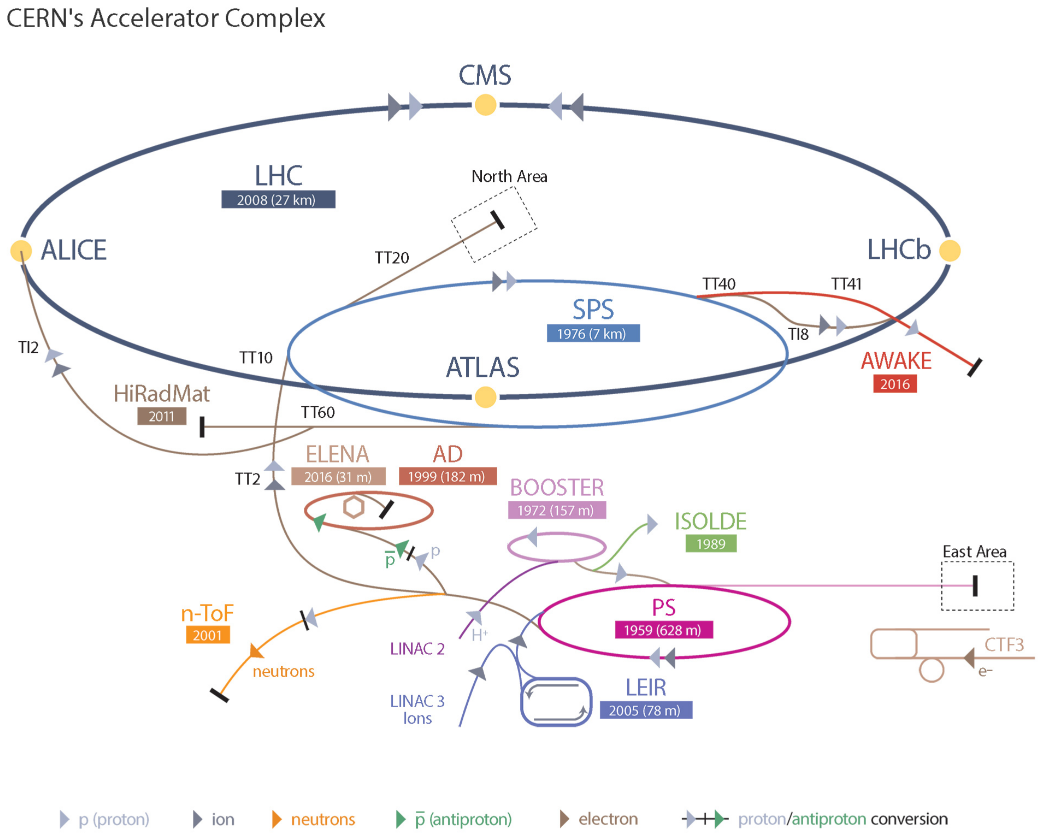

Figure 2.1: Schematic of the CERN accelerator complex [78].

cavities. At design operation the beams consist of 2808 proton bunches each made up of $\mathcal{O}(10^{11})$ protons, spaced 25 ns apart. The beams are kept in circulation using 1232 niobium-titanium superconducting dipole magnets, cooled to operate at a temperature of 1.9 K and generating magnetic fields of up to 8.4 T. The beams collide at four points around the LHC ring, where the collisions are recorded by the ATLAS [79], CMS [80], ALICE [81], and LHCb [82] detectors.

The processes the LHC was built to study have a small cross section compared with the total proton-proton (p-p) inelastic cross section, as seen from figure 2.2. For example, the production cross section of the SM Higgs boson is 9–10 orders of magnitude smaller than the total p-p cross section. In order to be able to study these relatively rare processes the LHC operates at high instantaneous luminosity, defined as

$$\mathcal{L} = \frac{N_b^2 n_b f_{\mathrm{rev}} \gamma}{4\pi \epsilon_n \beta^*} F, \tag{2.1}$$

where N_b is the number of protons per bunch, n_b the number of bunches per beam, f_{rev} the revolution frequency, γ the Lorentz factor, ϵ_n the normalised beam emittance, β^* the β-function at the interaction point and F a reduction factor due to the crossing angle.

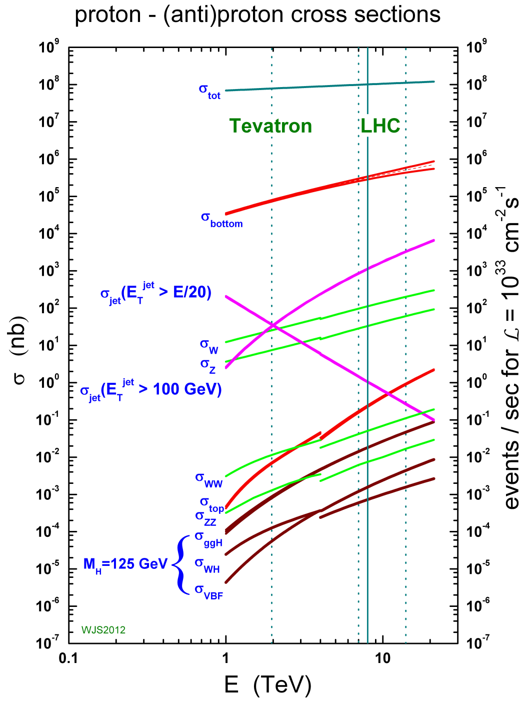

Figure 2.2: Total p-p cross section, σ^{tot}, and the cross sections for several processes studied at the LHC as a function of $\sqrt{s}$ [83]. The cross sections of these processes are often many orders of magnitude smaller than the total p-p cross section.

The LHC began its first physics run in May 2010, colliding protons at $\sqrt{s} = 7\,\text{TeV}$, and continued operation until the end of 2012. This period is known collectively as LHC Run 1. After this the two-year Long Shutdown 1 (LS1) was used to upgrade the LHC and the detectors for collisions at a $\sqrt{s}$ of 13–14 TeV. In April 2015 the LHC restarted with collisions at $\sqrt{s} = 13\,\text{TeV}$, marking the start of Run 2. The integrated luminosity delivered to the Compact Muon Solenoid (CMS) experiment, separated by running year, is shown in figure 2.3.

The data-taking efficiency of CMS is not 100%, as parts of the detector might be switched off while collisions are ongoing. In 2012 the data-taking efficiency was 93.5%, in 2015 it was 90.3% and in 2016 it was 92.0%. Only a subset of the recorded data is used for analysis. Data are certified as good for use in analyses if it is known that all relevant sub-detectors were functioning correctly. In 2012 the certification efficiency was 90.4%,

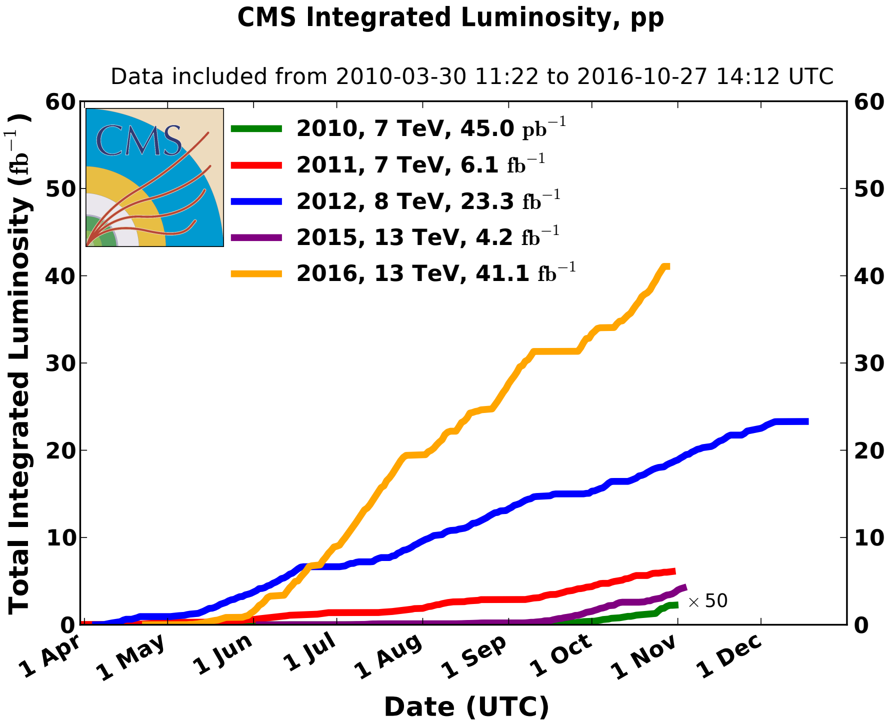

Figure 2.3: Cumulative integrated luminosity delivered to CMS for p-p collisions at the LHC, separated by running year [84].

meaning all sub-detectors were working well for a dataset corresponding to 19.7 fb^{-1}. Due to cryogenic issues the certification efficiency with the magnet operating at 3.8 T was 60.4% in 2015, leading to 2.3 fb^{-1} of analysable data for which the full detector was operational. An additional 0.6 fb^{-1} was taken with the CMS magnet switched off. For the full 2016 p-p running period the certification efficiency was 95.0%, resulting in 35.9 fb^{-1} of data marked good for use in analyses.

The LHC was designed for p-p collisions with a nominal peak luminosity of $10^{34}\,\mathrm{cm}^{-2}\,\mathrm{s}^{-1}$. In 2012 peak luminosities of $7.7 \times 10^{33}\,\mathrm{cm}^{-2}\,\mathrm{s}^{-1}$ were reached, with the peak luminosity in 2015 being $5.1 \times 10^{33}\,\mathrm{cm}^{-2}\,\mathrm{s}^{-1}$. Since July 2016 the LHC has been operating at instantaneous luminosities upwards of the design luminosity, with peak luminosities of $1.5 \times 10^{34}\,\mathrm{cm}^{-2}\,\mathrm{s}^{-1}$ reached in October 2016 [84].

Multiple p-p collisions per bunch crossing are likely to occur due to the high operating luminosity. Additional interactions on top of events of interest are referred to as pileup. The average number of interactions per bunch crossing was 21 in 2012 [84]. The average number of interactions per bunch crossing was lower than this at the start of Run 2, with an average of 14 interactions per bunch crossing for the data collected during 2015 [3]. In the data-taking period up to August 2016 the average number of interactions per bunch crossing increased to 24 [2].

2.2 The CMS detector

To meet the demands of the LHC physics programme, the CMS detector was designed to have a high sensitivity in searches for new physics at the TeV scale and to be able to function in the challenging high-luminosity environment. The detector is 21.6 m long, 14.6 m in diameter, and weighs 12 500 tonnes [80]. It consists of several sub-detectors, arranged parallel to the beam axis in the barrel region and perpendicular to it in the endcaps, as illustrated in figure 2.4.

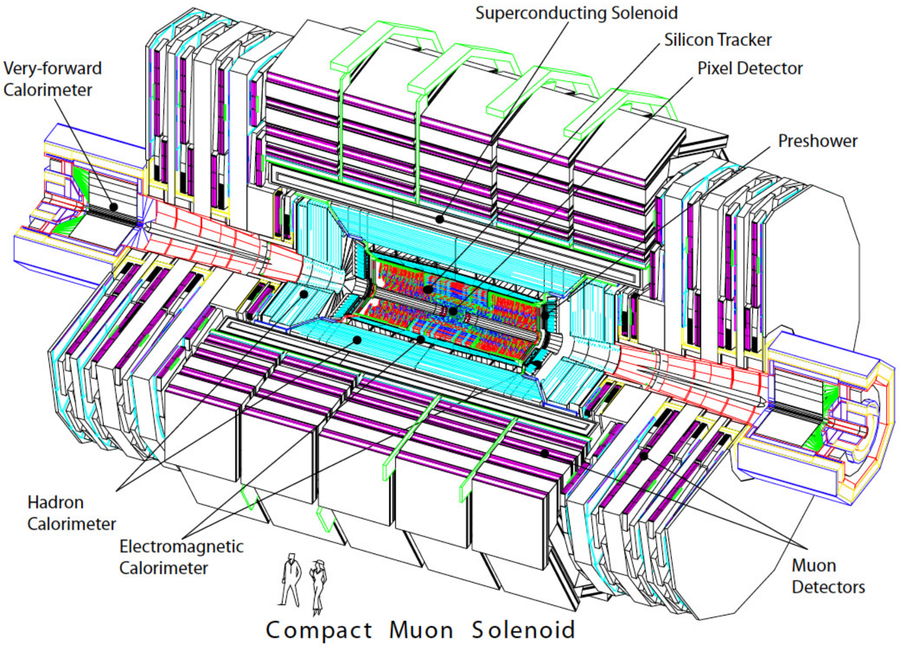

Figure 2.4: A cutaway view of the CMS detector [80], indicating the different sub-components of the detector.

The silicon tracker, a cylinder 5.8 m in length and 2.6 m in diameter, surrounds the interaction point. The tracker is surrounded by the lead-tungstate electromagnetic calorimeter (ECAL), which is enclosed by the brass scintillator hadron calorimeter (HCAL). The tracking and calorimeter systems are surrounded by a superconducting solenoid, 13 m long, 6 m in diameter and operating at 3.8 T. Charged particles are bent in this magnetic field, allowing for precise measurement of their momentum. Gaseous muon detectors are embedded in the iron return yoke of the solenoid.

For the measurement of physical quantities CMS uses a coordinate system with the origin centred at the nominal collision point inside the experiment. The y axis points vertically upward, the x axis points radially inward toward the centre of the LHC ring. The z axis points along the beam direction. As such the transverse momentum and energy, p_T and E_T, are defined by the x- and y-components of the momentum and energy. The azimuthal angle ϕ is measured in the x-y plane with respect to the x axis and the polar angle θ is measured with respect to the z axis. A coordinate more frequently used than the polar angle is the pseudorapidity $\eta = -\ln\left[\tan\frac{\theta}{2}\right]$. Distances in the η-ϕ plane are given as $\Delta R = \sqrt{(\Delta\eta)^2 + (\Delta\phi)^2}$.

The subsystems of the CMS detector will be described in more detail in the next sections.

2.2.1 Tracker

The tracker [80] is the sub-detector closest to the interaction point. It is used for accurate reconstruction of charged particle trajectories and the precise reconstruction of primary (collision) and secondary vertices, the latter being important for the identification of the in-flight decays of heavy-flavour particles. This means a small impact parameter resolution needs to be achieved, for which a highly granular system is required. Due to the large number of particles emerging from each collision, on average 1000 per bunch crossing at design operation, the system also needs to be able to respond quickly in order to reconstruct trajectories accurately. At the same time, this large particle flux calls for a radiation-hard design that is able to survive in this harsh environment for a long period of time. These requirements motivate the use of a silicon tracking system.

In a silicon tracking system the positions of particles are recorded via the creation of drifting electron-hole pairs. When a charged particle passes through the silicon an electron-hole pair is created, which drift under an applied electric field and produce a current that can be read out.

The tracker, providing coverage up to $|\eta| < 2.5$, consists of several different components. A schematic of the tracking detector, indicating the locations of these components, is given in figure 2.5. The pixel detector is the closest to the interaction point. It is composed of 66 million silicon pixels, each $100\,\mu\mathrm{m} \times 150\,\mu\mathrm{m}$ in size. The choice of this pixel size is driven by the desired spatial resolution, which is 15–20 µm in the r-ϕ and z directions. Such a precise resolution allows for 3D vertex reconstruction. The pixel detector consists of three layers of pixels in the barrel region, with two pixel disks placed in the endcap region at either side. The barrel layers sit at radii of 4.4, 7.3 and 10.2 cm and extend out to $z = \pm 26.5$ cm. The disks are placed at $z = \pm 34.5$ cm and $z = \pm 46.5$cm. With this layout the pixel tracker can provide three precise position measurements along each charged particle trajectory.

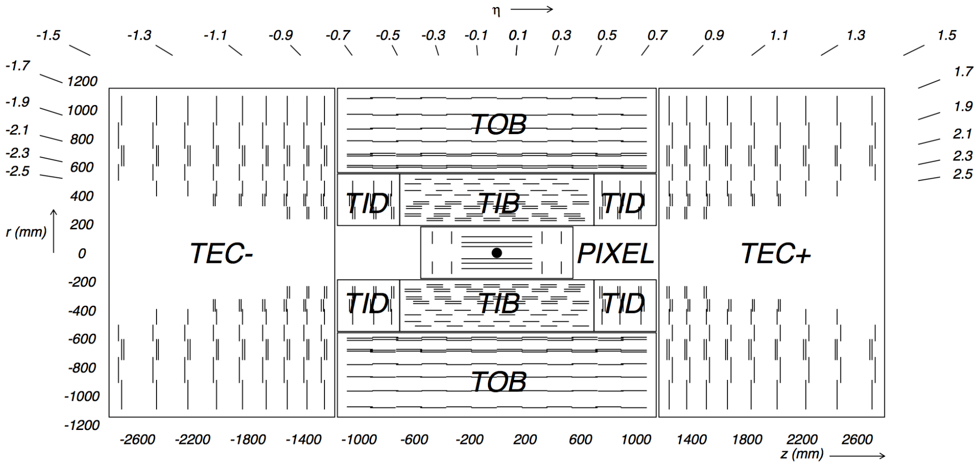

Figure 2.5: Schematic of the CMS tracker in the r-z plane, indicating the positions of the pixel and strip detectors [80]. Each line on the figure represents a detector module.

Around the pixel detector the tracking system is made up of a silicon strip detector divided into four sub-systems. The first part of the silicon strip tracker consists of the tracker inner barrel (TIB) and tracker inner disk (TID), providing four layers of silicon strip detectors in the barrel plus three disks at both ends. These two systems extend out up to a radius of 55 cm. The barrel layers and disks each consist of silicon strips which are 10 cm long, 80–141 µm wide and 320 µm thick. The TIB and TID provide four measurements of the r-ϕ position with a resolution of 23–35 µm. The TIB and TID are surrounded by the tracker outer barrel (TOB), which consists of six layers of silicon strip sensors extending up to an outer radius of 116 cm and up to $z = \pm 118$ cm. The strips in the TOB are 500 µm thick, around 25 cm long and 122–183 µm wide providing six measurements of r and ϕ, with a resolution of 35–53 µm. Beyond the z range covered by the TOB, coverage is provided by the tracker endcap (TEC), consisting of nine disks of strips. In the TEC the strip thickness ranges from 320–500 µm and the the strip width ranges from 97–184 µm. This part of the system provides up to nine ϕ measurements.

Some of the strip modules in the detector carry a second strip detector module mounted back-to-back with a stereo angle of 100 mrad, in order to provide measurements of the z coordinate in the barrel. This is achieved with a resolution of 230–530 µm.

The pixel tracker was upgraded during the extended year-end technical stop in late 2016-early 2017. This upgrade was needed to maintain the performance of the tracker as the pileup increases throughout the remainder of Run 2 [85].

2.2.2 Electromagnetic calorimeter

The ECAL [80] is a hermetic homogeneous calorimeter made of nearly 76 000 lead tungstate ($PbWO_4$) crystals. It has very good energy resolution, is highly granular and has a fast response, all qualities which are needed to be able to detect $H \rightarrow \gamma\gamma$ decays.

The choice of lead tungstate crystals is motivated by the radiation-hardness of the material in combination with its short radiation length, small Molière radius and short scintillation decay time. With a radiation length of 0.89 cm and a Molière radius of 2.2 cm, lead tungstate crystals allow for the construction of a compact, highly granular ECAL. The ECAL is required to be compact for it to fit inside the bore of the magnet. The lead tungstate crystals satisfy the requirements imposed by the LHC operating parameters as 80% of the light from the crystals is emitted within 25 ns, which is the time between two bunch crossings at design operation.

When a high energy electron or photon enters a crystal it starts a shower producing a cascade of lower energy particles. Electrons lose energy through bremsstrahlung, with photons undergoing e^+e^- pair production. The shower continues until the photon energy drops below the e^+e^- pair production threshold, and ionisation starts to dominate for electrons. The shower excites the atoms in the lead-tungstate crystals, which then emit scintillation light that is converted to a current by the photodetectors. To record the light of the crystals amplifying photodetectors need to be used, with avalanche photodiodes used in the barrel region, and vacuum phototriodes employed in the endcaps. As the crystals are 25.8 radiation lengths long, most of the shower is contained inside them.

Figure 2.6 shows a schematic of the ECAL, indicating the sub-systems it is made up of. The ECAL barrel (EB) covers the pseudorapidity range up to $|\eta| < 1.479$, with crystals of 0.0174×0.0174 in η-ϕ. The ECAL endcaps (EEs) provide coverage beyond the range of the EB, up to $|\eta| < 3.0$. Each endcap is divided into two halves. The preshower detectors, which are sampling calorimeters placed in front of the endcaps, cover a range of $1.653 < |\eta| < 2.6$. The main use of the preshower detectors is to identify neutral pions decaying to two photons in the endcaps. Additionally, they aid in the identification of electrons and improve the resolution of the position determination. Each of the two preshower detectors consists of two layers of lead radiators to initiate the shower, with silicon sensors placed after each layer of radiators to measure the deposited energy. The total thickness of the preshower is three radiation lengths.

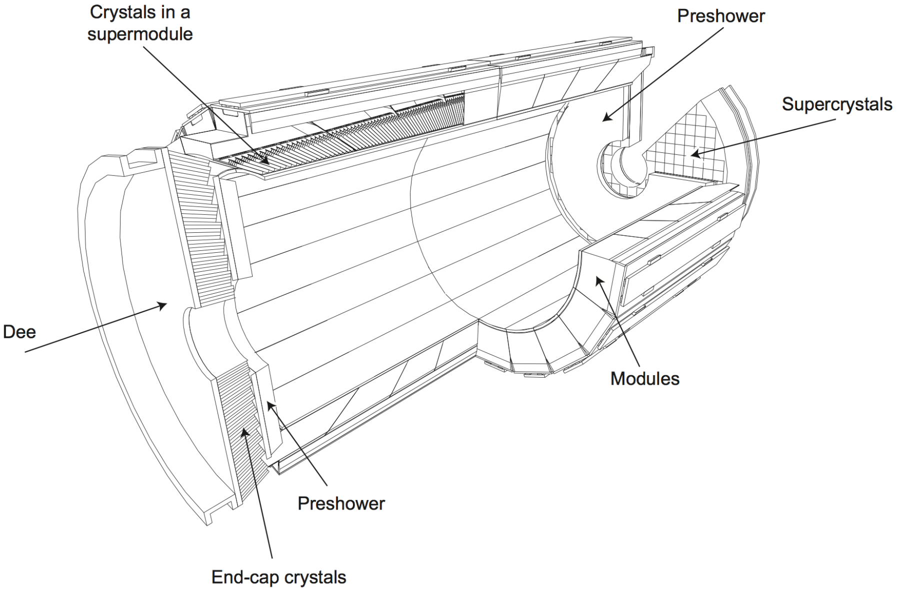

Figure 2.6: Layout of the ECAL, indicating the position of the different components [80].

To preserve the energy resolution the crystals and photodetectors need to be kept stable within $18 \pm 0.05^{\circ}$C as the number of scintillation photons emitted by the crystals, and the amplification of the photodetectors, are temperature dependent. This nominal operating temperature is ensured by supplying the detector with water at the same temperature.

The energy resolution of the ECAL can be parameterised as

$$\frac{\sigma}{E} = \frac{S}{\sqrt{E}} \oplus \frac{N}{E} \oplus C, \tag{2.2}$$

where S is the stochastic term, N the noise term and C the constant term. The stochastic term arises from fluctuations in lateral shower containment and fluctuations in the scintillation yield, the noise term is due to noise from the electronics and additional particles in the event, and the constant term comes from crystal-to-crystal intercalibration errors, the non-uniformity of the longitudinal response and energy leakage from the back of the crystals.

The values of S, N and C have been measured in an electron test-beam, without a magnetic field or material in front of the ECAL, as $S = 0.028\,\mathrm{GeV}^{\frac{1}{2}}$, $N = 0.12\,\mathrm{GeV}$ and $C = 0.003$.

2.2.3 Hadron calorimeter

The ECAL is surrounded by the HCAL [80], which is needed for the measurement of the energies of strongly interacting particles. As the ECAL extends out to a radius of 1.77 m and the magnet coil starts at a radius of 2.95 m, space for the HCAL inside the magnet coil is limited. The HCAL design takes this into account by placing part of the calorimeter outside the magnet coil. An illustration of a quadrant of the HCAL, indicating the positions of the sub-systems, is shown in figure 2.7.

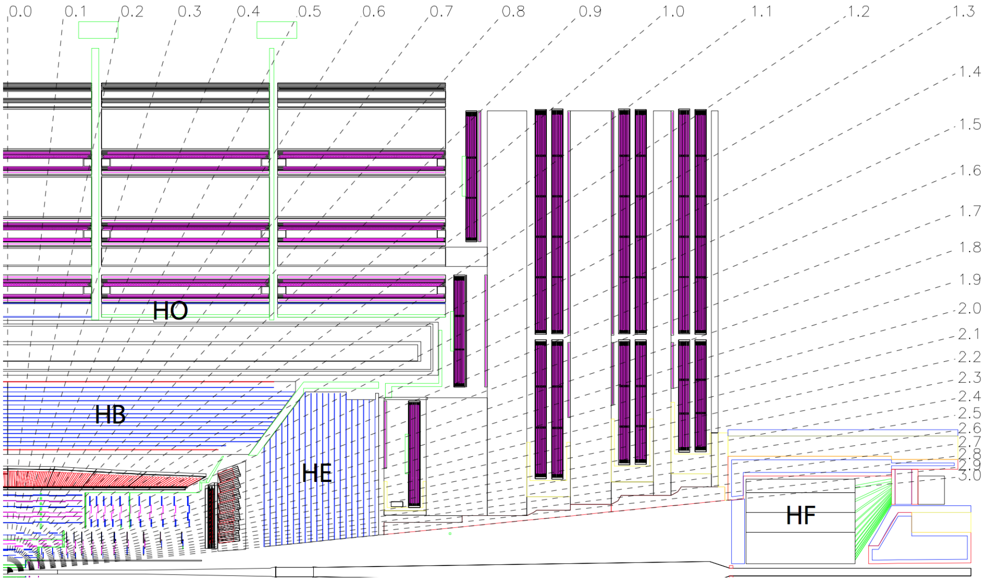

Figure 2.7: Illustration of a quadrant of the HCAL, showing the different sub-systems of the detector [80].

In the barrel region the hadron barrel calorimeter (HB) provides coverage up to $|\eta| < 1.3$. Beyond this η range the hadron endcap calorimeter (HE) covers the region up to $|\eta| < 3$. The HB and HE are sampling calorimeters made of brass absorber plates with tiles of plastic scintillator as the active material. The brass used as absorber fits the constraints imposed by the environment due to its short interaction length of 16.42 cm and the fact that it is non-magnetic. The tiles of scintillator are 0.087 × 0.087 in η-ϕ for $|\eta| < 1.6$ and 0.17 × 0.17 in η-ϕ beyond this range. The light from each tile is collected with a wavelength-shifting fibre, which is read out using hybrid photodiodes.

In the barrel the HCAL has a thickness of between 5.82 and 10.6 interaction lengths, which is not sufficient to identify, for example, late-starting showers. The hadron outer calorimeter (HO), sitting outside of the magnet and using the coil as an additional absorber, extends the thickness to at least 11.8 interaction lengths. As in the HB the active material of the HO consists of plastic scintillator tiles which roughly map the granularity of the tiles in the HB, and are read out via the same mechanism.

The hadron forward calorimeter (HF), providing coverage in the very forward region, is subjected to large radiation doses. This means an extremely radiation-hard active material is needed. For this reason quartz fibres are used. These fibres are embedded in a steel absorber structure. Charged particles from the shower initiated in the steel generate Cherenkov light in the quartz fibres, which is read out by photomultiplier tubes.

The energy resolution of the HCAL for single charged pions was measured in a test beam [86] and can be parameterised as

$$\frac{\sigma}{E} = \frac{S}{\sqrt{E}} \oplus C, \tag{2.3}$$

where S is the stochastic term, found to be 94.3% and C is the constant term, measured to be 8.4%.

During LS1 the photomultiplier tubes of the HF were upgraded. The photomultiplier tubes and read-out systems of other parts of the HCAL will be upgraded in stages over the next few years [87].

2.2.4 Muon system

Accurate muon identification is one of the requirements of the CMS experiment. High muon identification efficiency and precise muon momentum resolution are key to the success of the experiment, as muons are very important for the detection of $\mathrm{H} \to \mathrm{ZZ} \to 4\ell$ decays. In addition to that, muons appear in the final states of many of the BSM signatures the experiment is searching for.

The CMS muon system [80] is composed of three sub-systems which are all necessary to ensure the identification requirements can be met. The muon system is located outside of the magnet coil, interspersed in the iron return yoke of the solenoid. In the barrel of the detector the drift tube chambers (DTs) provide coverage for $|\eta| < 1.2$, with the cathode strip chambers (CSCs) covering the $0.9 < |\eta| < 2.4$ region. The resistive plate chambers (RPCs), covering the same regions as both the DTs and CSCs, are used as a dedicated triggering system.

A cross section of one quadrant of the detector, indicating the positions of the DTs, CSCs and RPCs, is shown in figure 2.8. The top of the fourth muon endcap station as shown in this figure was added during LS1 [88], providing additional layers of CSCs and RPCs.

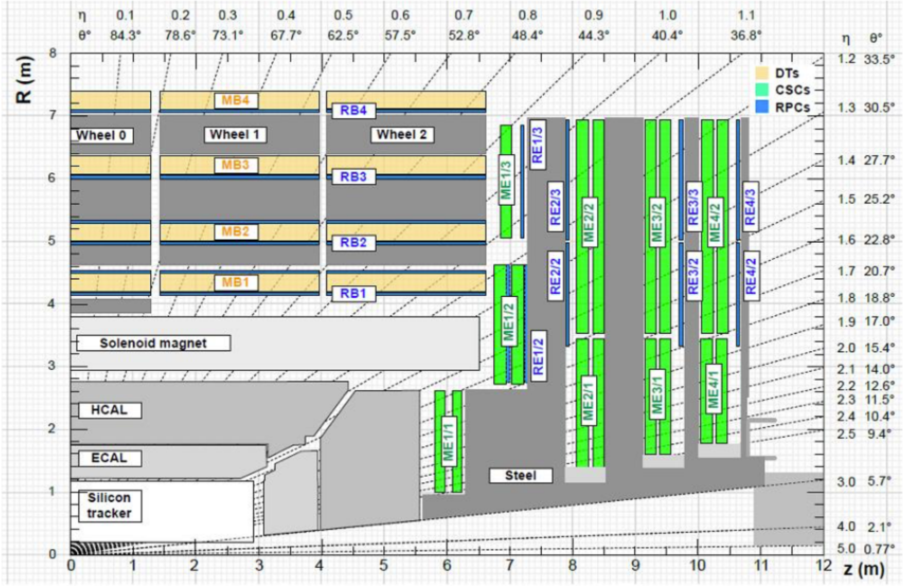

Figure 2.8: Cross section of one quadrant of the CMS detector, indicating the positions of the different muon system components [88]. The fourth muon endcap stations were extended during LS1; in Run 1 only the lower part existed.

The DTs consist of layers of drift cells which have a cross section of 4.2 cm × 1.3 cm and are 2.4 m long. The cells are filled with a mixture of argon gas and carbon dioxide gas. Muons passing through the chamber ionise the gas, freeing electrons which drift towards the anode wire running along the centre of the tube-shaped cell. This gives rise to an electric signal. There are four drift tube stations in each wedge of the detector, each in turn consisting of 8 to 12 layers of drift tubes. Some of these layers are oriented parallel to the beam line, providing a measurement of ϕ. There are also layers oriented orthogonal to the beam line, which give a measurement of the z coordinate. Measurements of the spatial resolution were made during p-p running in 2010. The spatial resolution of the DTs is 80–120 µm per chamber for measurements in the ϕ direction, while the resolution of the z measurement is 130–400 µm [89].

In the endcaps, where both the muon rate and the radiation levels are higher, the CSCs provide measurements of the muon track. These detectors are radiation hard, and have a fast response and fine segmentation. Each of the CSC modules is a wedge-shaped multi-wire proportional chamber with six gaseous chambers bounded by cathode plates. Sensitive strips are placed on these plates in the radial direction, to measure the muon coordinate in the r–ϕ plane. Anode wires between the cathode planes run along the ϕ direction and provide a measurement of η. The resolution of the r–ϕ measurement is 40–120 µm [89].

In addition to the DTs and CSCs, the RPCs provide coverage for $|\eta| < 1.6$. These are made up of parallel plates, forming the anode and cathode, with a gas gap in between. Ionisation of the gas due to the passing muons is read out using aluminium strips running parallel to the beam axis. The position resolution of the RPCs is poorer than that of the DTs and CSCs, but their time response is very fast. As a result of this the RPCs are used as an independent muon trigger which can correctly identify the beam crossing from which the muon originated.

To obtain precise muon momentum resolution, information from the tracker hits has to be combined with measurements in the muon stations. The momentum resolution of the muon system alone is 9% for muons with p_{T} up to 200 GeV, and varies with η between 15–40% for muons with p_{T} of 1 TeV [80].

2.2.5 Triggering and data processing

When the LHC is operating under design conditions, protons are collided at a rate of 40 MHz. This rate is too high for the data acquisition (DAQ) system to read out every event. In addition this high collision rate produces such a large number of events that it would not be feasible to write every single event, with a size of around 1 MB, to tape. Therefore, a trigger system is used to select events of interest, which reduces the rate at which events are stored to $\mathcal{O}(1\ \mathrm{kHz})$.

The trigger system consists of two stages: the level-1 (L1) trigger and the high-level trigger (HLT). The L1 trigger only makes use of front-end electronics and reduces the event rate from 40 MHz to around 100 kHz. The HLT runs on a computer farm with around 13 000 CPU cores [90]. During LS1 and the year-end technical stop at the end of 2015 the L1 trigger was replaced by a completely upgraded system [91], which provides, amongst other things, improved object isolation, hadronic tau identification, muon p_T resolution and jet finding with respect to the system used during Run 1. An overview of the data flow in the L1 trigger is given in figure 2.9.

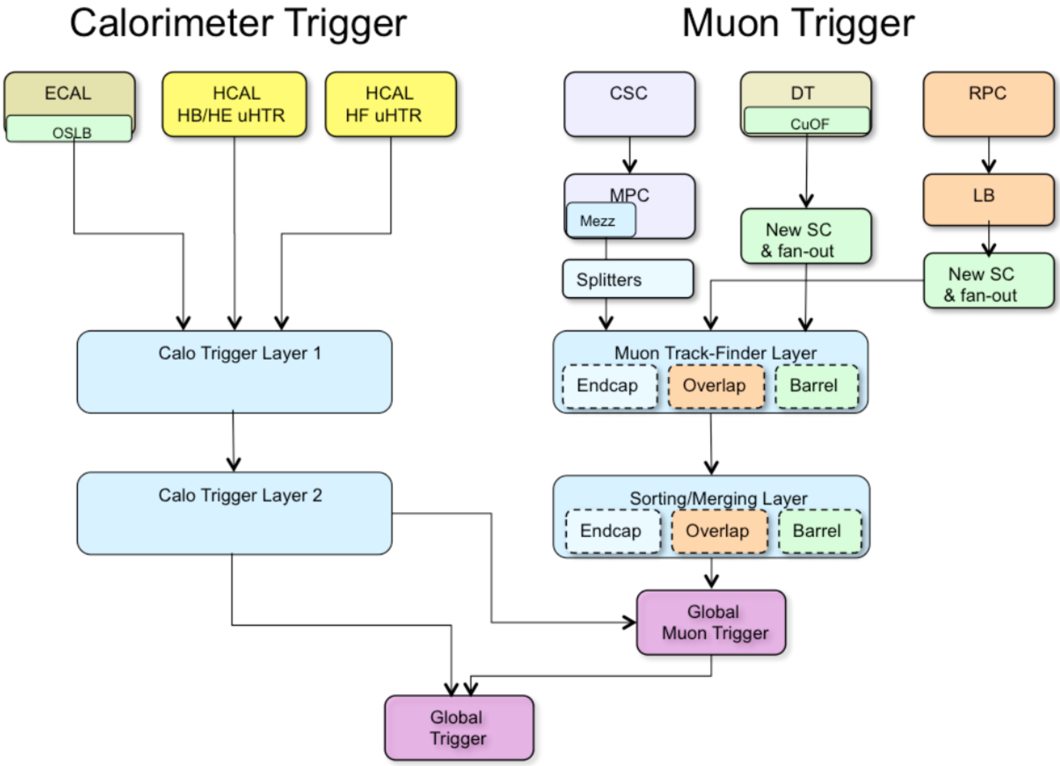

Figure 2.9: Schematic of the different components of the L1 trigger [91].

The L1 trigger only makes use of information from the calorimeters and the muon systems. The calorimeter trigger starts from HCAL and ECAL energy deposits, which are fed to the first layer of the trigger, where it makes use of a time-multiplexed system. The first trigger layer maps onto slices of the detector, receiving data from many bunch crossings. These data are passed on to the second layer of the trigger in a way that bundles data from a single bunch crossing, but different slices of the detector, to be processed on one node in the second layer of the trigger. In this step basic object identification is performed based on the energy deposits, so that a sorted list of the best candidates can be passed to the global trigger. The trigger employed during Run 1, and the first year of Run 2, did not use time-multiplexing. Instead, information from different regions of the detector was processed independently.

Hits in the muon chambers are read out and passed to the track finder layer of the muon trigger, which combines information from the CSC, DT and RPC systems in regions of η-ϕ. In further layers of the muon trigger the information from different regions is combined, until finally the global muon trigger can return a sorted list of the best muon candidates to the global trigger. The global trigger combines the information from the calorimeter and muon triggers to make a decision on whether the event should be sent to the HLT or whether it should be discarded. A decision has to be made within 3.2 µs, the maximum time during which data can be stored in the L1 trigger before being lost.

The HLT, running on CPU nodes, makes use of the full information from the detector, including tracker hits. This means particles can be more accurately identified and their momentum is more precisely known. The algorithms used in the HLT are usually simpler versions of those used in the full offline reconstruction. During the 2012 run of the LHC the HLT operated with an output capacity of around 1 kHz. For Run 2 this has been increased. In August 2016 the HLT output rate was 1.2 kHz for immediate data processing, with an additional 0.6 kHz saved as raw data to be reconstructed and analysed when more processing power is available [2].

While the trigger system reduces the rate substantially, several petabytes of collision data are stored by CMS each year, on top of large sets of simulated events. To make these large amounts of data easily accessible for analysis, CMS and the other LHC experiments make use of the Worldwide LHC Computing Grid (WLCG) [92]. The WLCG pools the resources of computer centres at universities and research laboratories associated with LHC experiments, based on a system of tiers. The Tier 0, at CERN and the Wigner Research Centre for Physics in Budapest, performs the full reconstruction and saves a copy of the data to tape. Datasets are copied to at least one Tier 1 centre, from where data can be distributed to Tier 2 centres. The Tier 2 centres are located at over 150 universities and research institutes around the world, providing resources for analysis of the datasets to all researchers associated with the experiment.

Chapter 3

Object reconstruction

In this chapter the reconstruction of the physics objects necessary for performing searches with taus in the final state with CMS will be discussed. Section 3.1 details the algorithms used to reconstruct charged particle tracks in the inner tracker, with section 3.2 describing how these tracks are combined with ECAL energy deposits to reconstruct electrons. The reconstruction of muons by the combination of tracks in the inner tracker with hits in the muon chambers will be discussed in section 3.3. Section 3.4 describes the particle flow (PF) algorithm, which uses information from all sub-detectors in CMS to reconstruct all stable particles. PF is of particular importance for the reconstruction of jets, missing transverse energy and hadronically decaying taus as detailed in sections 3.5, 3.6 and 3.7 respectively.

3.1 Tracks and vertices

To reconstruct the trajectories of charged particles, and therefore their momenta and positions, from the hits they leave in the inner tracker the combinatorial track finder (CTF) algorithm is used [93]. This algorithm performs four steps. First, initial estimates of the parameters of the trajectory are given by track seeds, made out of the hits found in two or three layers of the inner tracker. These track seeds are extrapolated using a Kalman filter (KF) [94], which extrapolates the seeding trajectories along the expected flight path of a charged particle. Any additional matched hits found along this extrapolated trajectory are added to the track. After the extrapolation has reached the final tracker layers the KF is run again, now with the full set of hits that have been found in the previous step. This provides the best estimate of the track parameters. Finally, tracks that fail a set of quality criteria are rejected.

These four steps are repeated six times. After each iteration the hits associated with reconstructed tracks are removed and the settings of the algorithm updated, in order to reconstruct as many tracks as possible. The tracking efficiency for muons and pions was measured in p-p collisions at $\sqrt{s} = 7\,\text{TeV}$ and found to be $> 98.5\%$ for tracks with $p_{\mathrm{T}} > 500\,\text{MeV}$ and $> 99\%$ for tracks with $p_{\mathrm{T}} > 2\,\text{GeV}$ [95].

Primary vertices are reconstructed by clustering tracks that are compatible with having originated from the same vertex, then fitting these tracks for the position of the vertex. The clustering is performed using the deterministic annealing (DA) algorithm [96], which identifies the most probable vertex candidates and assigns tracks to them. Vertex candidates with at least two associated tracks are fitted using an adaptive vertex fitter [97] to determine the best estimate of the vertex position. The $\mathrm{H} \to \mathrm{hh} \to \mathrm{bb}\tau\tau$ and $\mathrm{A/H} \to \tau\tau$ analyses, described in chapters 4 and 5, take the primary vertex of the hard scatter to be the reconstructed vertex with the largest scalar p_{T} sum of the associated tracks.

The resolutions of the x and z coordinates of the primary vertex were measured in collisions at $\sqrt{s} = 13\,\text{TeV}$ and depend strongly on the number of tracks associated with the vertex, as figure 3.1 shows.

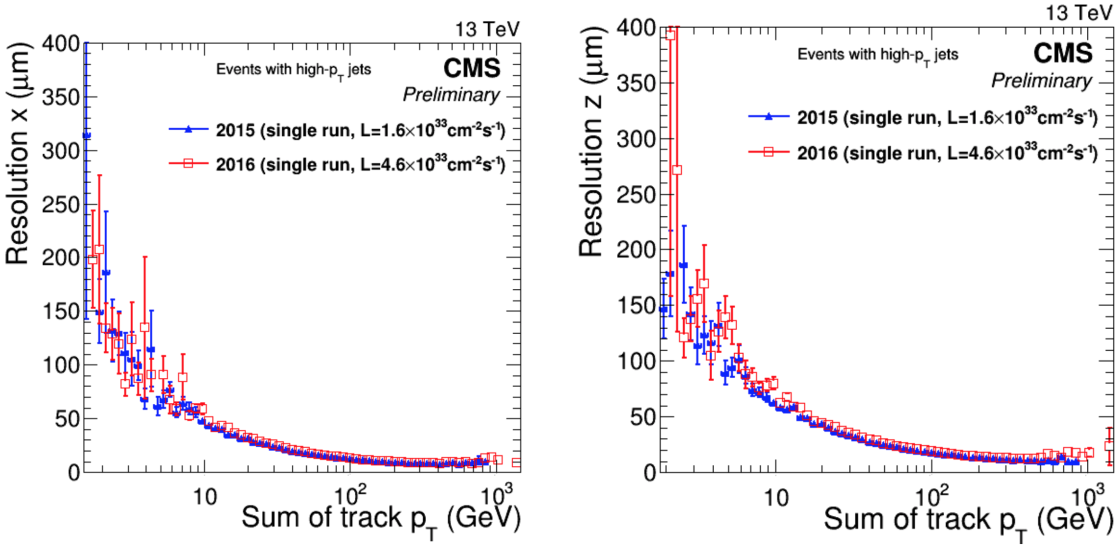

(a) Resolution in x

(b) Resolution in z

Figure 3.1: Resolution of (a) the x coordinate and (b) the z coordinate of reconstructed primary vertices as a function of the scalar p_{T} sum of the associated tracks, measured in 2015 (blue triangles) and 2016 (red squares). The resolution improves with higher scalar p_{T} sum of the associated tracks, which corresponds to larger numbers of tracks [98].

3.2 Electrons

Electrons are reconstructed by combining tracks from the inner tracker with energy deposits in the ECAL. A standalone electron reconstruction algorithm [99] complements the PF approach that will be described in section 3.4. Depending on the thickness of the intervening material, electrons lose up to an average of 86% of their energy due to bremsstrahlung before reaching the ECAL. To accurately reconstruct the energy of the electron it is important to capture the energy of the bremsstrahlung photons, which are spread in the ϕ direction due to the magnetic field. To achieve this, "supercluster" algorithms are used. In these algorithms the clustering is performed by defining a seed crystal as the crystal containing a local energy maximum above a certain threshold. In the barrel, arrays of 5×1 crystals in $\eta \times \phi$ are then added to the cluster, stepping sideways in both directions in ϕ within a range of approximately ± 0.3 rad. Contiguous clusters are merged into superclusters as long as each cluster satisfies a minimum energy deposit. In the endcaps arrays of 5×5 crystals are merged into superclusters within a range in η of ± 0.07 and a range in ϕ of ± 0.3 rad.

Due to the radiation of bremsstrahlung photons in the tracker, the change in curvature of the electron track can be large. Therefore a dedicated tracking algorithm is used, with better performance than the CTF for this particular case. For high-p_{T} electrons the best efficiency is reached by the use of an ECAL-based track seeding algorithm [99]. This algorithm extrapolates the position and energy of the supercluster to the first layers of the tracker to determine the approximate area where the tracker seeds should be. Once the tracker seeds have been found they are extrapolated and smoothed using the gaussian sum filter (GSF) [100] instead of the KF, which approximates the non-Gaussian energy loss in each layer by a combination of Gaussian distributions rather than the single Gaussian used in the KF.

For a particle to be identified as an electron it must also be reconstructed as an electron by the PF algorithm, and must in addition pass more advanced identification criteria based on some of the variables used in the standalone electron reconstruction. This provides separation power from backgrounds such as photon conversions, jets misidentified as electrons, or electrons from b- and c-quark decays. Both a cut-based algorithm and an algorithm based on boosted decision trees (BDTs) are available. For the selection of electrons in the analyses presented in later chapters the BDT-based algorithm is used, with exceptions for the loose identification criteria required for vetoing electrons. The variables used in this BDT include:

- Cluster shape variables, such as $\sigma_{i\eta,i\eta}$, the energy-weighted width of the supercluster in units of η crystals (illustrated in figure 3.2a).
- Track quality variables.
- Distances in η and ϕ between the supercluster and the associated track.
- Energy ratios and energy-momentum ratios in the region of the supercluster, including $1/E_{\mathrm{SC}} - 1/p_{\mathrm{e}}$, where E_{SC} is the energy in the supercluster and p_{e} the momentum of the electron track (illustrated in figure 3.2b).

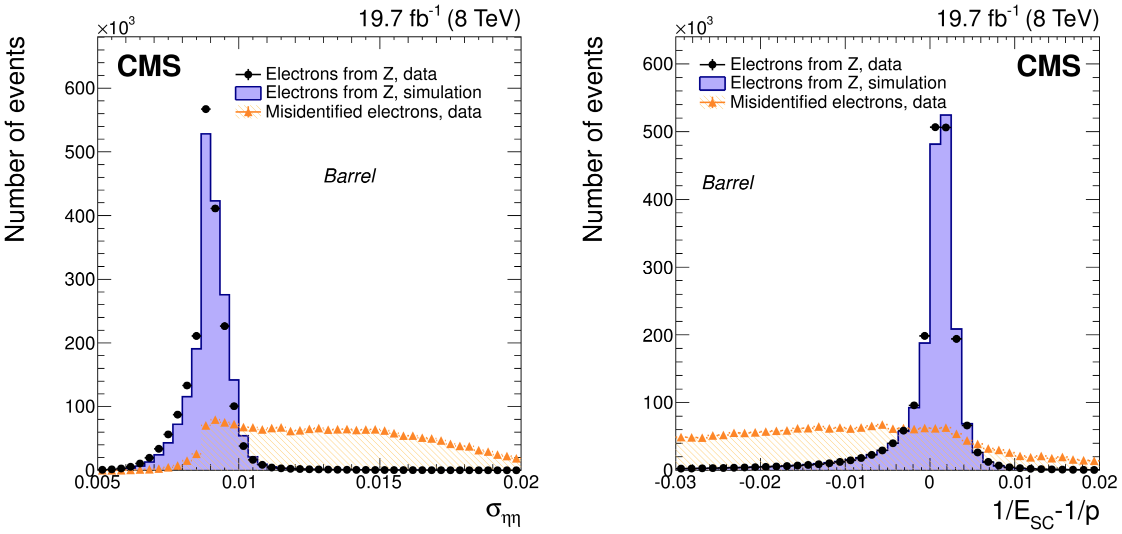

(a) $\sigma_{i\eta,i\eta}$ **(b)** $1/E_{\mathrm{SC}} - 1/p_e$

Figure 3.2: (a) $\sigma_{i\eta,i\eta}$ and (b) $1/E_{\mathrm{SC}} - 1/p_e$ for real (black points) and misidentified (yellow triangles) electrons in a dataset corresponding to $19.7\,\mathrm{fb}^{-1}$ taken at $\sqrt{s} = 8\,\mathrm{TeV}$, overlaid on the distributions for simulated real electrons in purple [99].

The identification requirements discussed up to now reduce the backgrounds from misidentified electrons, but do not eliminate them completely. If jets are misidentified as electrons, or an electron resulting from a heavy-flavour decay is identified, the electron is not isolated. Therefore requirements on the electron isolation can reduce these backgrounds even further. Different isolation definitions are used in CMS. The default, which is used for the analyses presented in later chapters, is a combined relative isolation variable defined as [31]:

$$I_{\text{rel}} = \frac{\Sigma p_{\text{T}}^{\text{charged}} + \max(\Sigma E_{\text{T}}^{\text{neutral}} + \Sigma E_{\text{T}}^{\text{photon}} - \Delta\beta \Sigma E_{\text{T}}^{\text{PU}}, 0)}{p_{\text{T}}^{e}}, \tag{3.1}$$

where the p_{T} and E_{T} sums are taken within a cone in η-ϕ around the direction of the electron of size $\Delta R = 0.4$ during Run 1 and $\Delta R = 0.3$ during Run 2 [2]. The sum over ${p_{\text{T}}}^{\text{charged}}$ corresponds to the p_{T} of all charged hadrons associated with the primary vertex. The ${E_{\text{T}}}^{\text{neutral}}$ and ${E_{\text{T}}}^{\text{photon}}$ sums run over all neutral hadronic energy and photon energy. The contribution from neutral particles due to pileup needs to be subtracted from the sum of these two terms. It is estimated as the sum of charged hadronic p_{T} for hadrons not associated with the primary vertex, multiplied by a $\Delta\beta$ factor of $\frac{1}{2}$. This factor is the average ratio of neutral to charged particles, which is measured in jets by studying the fraction of energy carried by charged and neutral constituents [101].

3.3 Muons

Muons are reconstructed by combining tracks in the inner tracker with tracks from the muon system [102]. Two complementary approaches are used: “global” and “tracker” muon reconstruction. The former starts from tracks reconstructed in the muon system and searches for a matching tracker track, then reapplies the KF to the combination of hits in the muon system and inner tracker. Conversely, the tracker muon reconstruction starts from tracks in the inner tracker which pass requirements on p_{T} to be considered a muon candidate track. The trajectory is then extrapolated to the muon systems and considered a muon if at least one muon segment, a track stub in the DTs or CSCs, is found. Due to the requirement of a single muon segment this method is more efficient than the global muon reconstruction for muons with p_{T} smaller than 5 GeV [102]. For muons with p_{T} greater than 200 GeV, the momentum resolution is improved by the global muon reconstruction [103].

The muon momentum resolution was measured in p-p collisions at $\sqrt{s} = 7\,\text{TeV}$ for muons with p_{T} up to 100 GeV and found to range from 1–6% depending on detector region. For muons with p_{T} between 100 GeV and 1 TeV the momentum resolution was determined to be better than 10% in the barrel region using cosmic rays [102].

For global muon reconstruction the non-muon backgrounds are small, though there can be a small contamination from hadronic showers not fully contained in the HCAL. A larger contribution is expected from real muons originating from, for example, decays of hadrons. These backgrounds can be reduced by applying additional identification criteria.

For the A/H $\rightarrow \tau\tau$ analysis, "medium" muon requirements were applied [2]. These requirements include:

- Reconstruction by either the global or tracker muon reconstruction algorithms.
- Requirements on track quality, and compatibility between the tracker track and the muon system track.
- Selection on the segment compatibility, a weight between 0 and 1 which is a measure of the compatibility of a track with the muon track segments in the muon stations it has crossed.
- Requirements on the maximum kink in the tracker track in any of the layers of the tracker, to suppress in-flight decays.

In the H $\rightarrow$ hh $\rightarrow$ bb$\tau\tau$ analysis, where Run 1 data were used, muons were required to pass "tight" identification requirements [102]. In addition to having to be reconstructed by the global muon algorithm, selections are made on the χ^2 per degrees of freedom of the track fit, number of hits of the inner track in different tracker layers and number of muon segments the inner track is matched to.

As described for electrons in section 3.2, placing isolation requirements on muons will also reduce backgrounds from misidentified jets and heavy-flavour decays. The isolation variable used for muons is very similar to the one described for electrons in equation 3.1, however the cone around the direction of the muon was chosen as $\Delta R = 0.4$ during both Run 1 and Run 2.

3.4 Particle flow

All stable particles are reconstructed and identified using the PF algorithm [101,104,105], which combines the information from all of the different subdetectors of CMS. This makes the identification of particles, and determination of their position and momentum, as precise as possible. All of these particles are then used to build, for example, jets, hadronically decaying taus and missing transverse energy $E_{\mathrm{T}}^{\mathrm{miss}}$, which will be discussed in subsequent sections.

The PF algorithm starts from charged particle tracks measured by the inner tracker, muon tracks measured in the muon system, and energy deposits in the calorimeters. These energy deposits are combined using a clustering algorithm, so that stable neutral particles can be identified and separated from charged hadrons, and in addition electrons and all bremsstrahlung photons can be reconstructed. Clustering is performed separately in the ECAL barrel, ECAL endcaps, first and second preshower layers, HCAL barrel and HCAL endcaps, with no clustering employed in the HF. The clustering algorithm used for PF starts from cluster seeds, calorimeter cells with local energy maxima. Topological clusters are built by merging neighbouring cells into the cluster, provided that the cells being merged in contain a certain minimum energy. The threshold is 800 MeV in the HCAL and two standard deviations above the expected noise level in the ECAL, meaning 80 MeV in the barrel and up to 300 MeV in the endcaps. Cell energies can be shared between multiple PF clusters, depending on the distance between a cell and the centre of the cluster.

Any given particle will usually give rise to multiple PF elements in the different subdetectors. To provide full reconstruction of each particle, and avoid double counting, the next step in the PF algorithm is to link the different elements. This is achieved by defining a distance parameter between any two PF elements in the event, which quantifies the link quality. Directly and indirectly linked elements are considered as input blocks to the reconstruction and identification algorithm. Links between charged tracks and calorimeter clusters are established by extrapolating the track from its last measured tracker hit to the preshower layers, the ECAL and the HCAL. If the extrapolated track position is within the boundaries of the cluster, plus the size of one cell in each direction to account for gaps between cells and multiple scattering, the track is said to be linked to the calorimeter cluster. The link distance parameter is taken as the distance ΔR between the position of the cluster and the position of the track. Tangents to tracks are also extrapolated to the ECAL from the interaction points between the track and each tracker layer, and clusters can be linked to the track as a possible bremsstrahlung photon if the extrapolated tangent position is within the boundaries of the cluster. Links between calorimeter clusters are made when the cluster position in the more granular calorimeter is within the cluster of the less granular calorimeter, with the link distance again defined as the ΔR between the positions of the two clusters. To determine links between charged tracks in the inner tracker and a muon track in the muon system, a global fit between the two tracks is performed, where the link is accepted if requirements on the maximum χ^2 of this fit are met. This χ^2 also determines the distance parameter.

For each block, particles are identified following a sequence of tests. Firstly, if there is a link between a tracker track and a muon system track, a PF muon is identified if the combined tracker and muon system momentum is compatible with the tracker-only momentum. The muon track is removed from the block before the next step of the algorithm.

Secondly, tracks are refitted with the GSF and the compatibility of the track with the already linked ECAL clusters is assessed using BDTs which take several variables into account. If the candidate passes, it is identified as a PF electron and the track and ECAL clusters are removed from the block.

After this, remaining tracks lead to charged hadrons. The track is given the momentum from the track fit, assuming the mass of a charged pion. If the energy measured in the calorimeters is compatible with the momentum assigned to the track, a charged hadron is identified and the momentum redefined by fitting the tracker and calorimeter measurements. If the energy of the calorimeter clusters linked to the track is significantly larger than the charged particle momentum from the track fit, additional overlapping neutral particles are identified. If the difference between the tracker momentum and the calorimeter energy is larger than the total energy registered in associated ECAL clusters, a PF photon with energy equal to the total ECAL energy is created. Any remaining momentum difference is assigned to a PF neutral hadron. If the momentum difference is smaller than the energy registered in associated ECAL clusters the energy difference is only associated with a PF photon. Finally, any remaining ECAL clusters not linked to a track give rise to PF photons, with any HCAL clusters not linked to tracks giving rise to neutral PF hadrons.

3.5 Jets and b-tagging

Many quarks and gluons are produced in the collisions at the LHC, fragmenting and hadronising and forming collimated jets of particles. These particle jets need to be combined into single objects so the properties of the original particles can be measured.

The particles identified by the PF algorithm are clustered into jets using the anti-k_{T} algorithm [106] as implemented in `FastJet` version 3.0.1 [107]. Jet clustering algorithms define distance parameters d_{ij}, denoting the distance between object (particle or cluster of particles) i and object j, and d_{iB} denoting the distance between object i and the beam.

The smallest of these distances is determined and if this is a distance between an object i and an object j, objects i and j are combined. If the smallest distance is a d_{iB}, object i is called a jet and removed from the list of objects. In the anti-k_T algorithm these distance parameters are defined as:

$$\begin{aligned} d_{ij} &= \min(p_{\mathrm{T},i}^{-2}, p_{\mathrm{T},j}^{-2})\frac{\Delta_{ij}^2}{R^2} \\ d_{iB} &= p_\mathrm{T}^{-2}, \end{aligned} \tag{3.2}$$

where $\Delta_{ij} = \sqrt{(y_i - y_j)^2 + (\phi_i - \phi_j)^2}$ is the distance between the objects i and j in rapidity-azimuthal angle space. The radius parameter R was chosen as 0.5 during Run 1 [108] and as 0.4 during Run 2 [109]. This algorithm is collinear- and infrared-safe, which means that the number of jets is not affected by the emission of soft collinear gluons or parton splitting. To reject badly reconstructed jets and fake jets due to noise, clustered jets are required to pass loose identification requirements [109, 110]. These requirements are based on the charged and neutral particle multiplicities in the jet, as well as on the fraction of jet energy carried by different PF particle types.

Several methods exist for reducing the effects of pileup particles on the jet energy and substructure. For the A/H $\to \tau\tau$ analysis a charged hadron subtraction (CHS) technique [109] is employed, which means charged hadronic PF candidates not associated with the primary vertex are not considered in the jet clustering. For the H $\to$ hh $\to$ bb$\tau\tau$ analysis a dedicated identification algorithm [111] based on vertex information and jet shape information was used to reject jets due to pileup.

3.5.1 Jet energy corrections

The energy measured for a jet in the detector is usually different from the true particle jet at hadron level. A correction [108] is applied to both jets in data and jets in Monte Carlo (MC) simulation to match the measured and true energies as

$$p_\mu^\mathrm{corr} = (\mathrm{C}_\mathrm{offset}(p_\mathrm{T}^\mathrm{raw}) \cdot \mathrm{C}_\mathrm{rel}(p'_\mathrm{T}, \eta) \cdot \mathrm{C}_\mathrm{abs}(p''_\mathrm{T})) \cdot p_\mu^\mathrm{raw}. \tag{3.3}$$

In this equation $\mathrm{C}_\mathrm{offset}$ is an offset correction, C_rel a relative residual correction factor and C_abs an absolute scale correction factor. The corrections are applied in sequence with p'_T the p_T of the jet after applying the offset correction and p''_T the p_T of the jet after all of the preceding corrections.

The offset correction C_{offset} estimates and subtracts the additional energy not associated with the hard scatter, including contributions from electronics noise and pileup. This is estimated on an event-by-event basis based on the average p_{T} density per unit area ρ and the area of the jet A [112]. The factor ρ includes contributions from pileup, electronics noise and the underlying event (UE) of the hard interaction. The last of these should not be corrected for and therefore the average expected contribution from the underlying event $\rho_{<\mathrm{UE}>}$ is subtracted from ρ.

A di-jet p_{T}-balancing technique [108] is used to measure the response of a jet at any η relative to the jet energy response in the region $|\eta| < 1.3$, such that the relative residual correction factor makes the response flat as a function of η. This is achieved by requiring a reference jet in the central region of the detector ($|\eta| < 1.3$), where the response is flat, and a probe jet at any η value. The relative response, in bins of η and p_{T}, is determined by averaging the balancing function $\frac{p_{\mathrm{T}}^{\text{probe}} - p_{\mathrm{T}}^{\text{reference}}}{p_{\mathrm{T}}^{\text{average}}}$.

The absolute energy scale correction factor is designed to make the response uniform in p_{T}. It is measured using the missing transverse energy projection fraction (MPF) method [108] using samples of γ+jets and Z+jets events. This method relies on the fact that the events used for the measurement have no intrinsic missing energy, and so any measured $E_{\mathrm{T}}^{\text{miss}}$ is used to calibrate the p_{T} response of jets in the event.

The uncertainty on the jet energy scale is propagated through to analyses. It is driven by uncertainties in the energy density used for pileup subtraction, the photon energy scale, and the extrapolation required in the MPF method [108].

3.5.2 b-Tagging

As jets due to b-quark hadronisation are an important signature for many analyses at the LHC it is important to identify such jets correctly. Because b-hadrons have a relatively long lifetime, $\tau \approx 1.5$ ps [46], they travel for around $c\tau \approx 450\,\mu\mathrm{m}$ before decaying. This means they produce a displaced secondary decay vertex in the inner tracker. Algorithms for tagging b-jets usually rely on the information from these secondary vertices. For the $\mathrm{H} \to \mathrm{hh} \to \mathrm{bb}\tau\tau$ analysis the combined secondary vertex (CSV) algorithm [113] has been used, with the upgraded CSVv2 version of the algorithm [114] used for the $\mathrm{A/H} \to \tau\tau$ analysis. The CSV algorithm takes PF jets with $p_{\mathrm{T}} > 20\,\mathrm{GeV}$ and $|\eta| < 2.4$ as input and uses a likelihood-based discriminator to determine whether a jet is likely due to b-quark hadronisation or not. For this algorithm, secondary vertices are reconstructed from high-purity tracks within a cone of $\Delta R = 0.3$ around the jet axis, with quality cuts applied to reduce contamination from decays of long-lived particles or particles due to interactions with the detector material. Information from the resulting secondary vertices is combined with information from the tracks associated with the jet into a likelihood ratio.

The CSVv2 algorithm as improved for Run 2 uses an inclusive vertex finder (IVF) algorithm to reconstruct secondary vertices [115]. Instead of using only tracks near the jet, in this algorithm all reconstructed tracks in the event which are displaced from the primary vertex are used. In addition, the algorithm makes use of a multilayer perceptron to combine the variables instead of constructing a likelihood ratio from the input variables [114]. This allows for the addition of extra variables to discriminate between b-jets and other jets. Once the discriminator has been constructed, loose, medium and tight working points can be determined as a minimum requirement on the discriminator such that the probability of misidentifying light-flavour jets with $p_{\mathrm{T}} > 30\,\mathrm{GeV}$ is around 10%, 1% and 0.1% respectively [113, 114].

Because not all of the input variables to the CSV algorithm are perfectly modelled in simulation, the b-tagging efficiency for different jet flavours is different in data and MC simulation. Scale factors can be determined as the ratio of tagging efficiencies between the two, which are applied to the simulated events in order to match the data. The measurement of the tagging efficiency for genuine b-jets is based on samples containing a muon overlapping with the jet, making use of the $\approx 11\%$ semileptonic branching fraction of b-hadrons. This measurement can be complemented by measurements from samples with the kinematic signatures of $\mathrm{t\bar{t}}$ production, making use of the large $\mathrm{t} \rightarrow \mathrm{Wb}$ branching ratio.

Systematic uncertainties in the scale factors arise from, amongst other things, pileup modelling in simulation, gluon splitting into $\mathrm{b\bar{b}}$ pairs, track mismeasurement, and uncertainties in the fractions of different jet types. Figure 3.3 shows the b-tagging scale factors, and associated uncertainties, for the medium working point of the CSVv2 discriminator in the 2015 data sample.

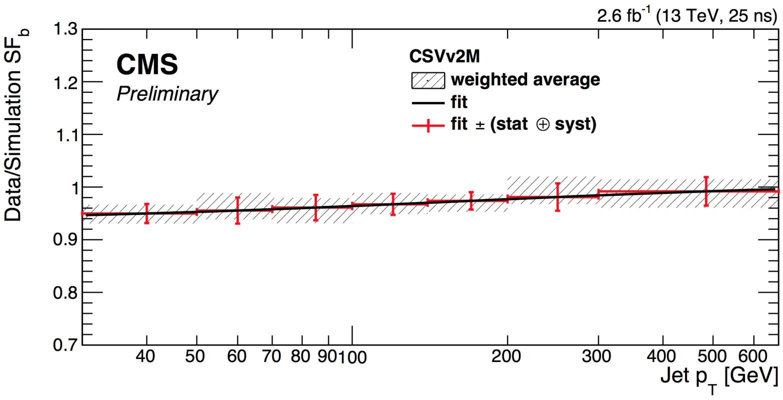

Figure 3.3: The b-tagging scale factors and uncertainties for b-jets in the data sample collected during 2015 as a function of jet p_{T} for the medium working point of the CSVv2 discriminant [114].

3.6 Missing energy

The CMS detector is able to detect most stable and long-lived particles, however, neutrinos and hypothetical neutral weakly interacting particles travel straight through the detector without being recorded. These particles will give rise to an energy imbalance in the transverse plane, and so their presence can be inferred from missing transverse energy, $E_{\mathrm{T}}^{\mathrm{miss}}$, in the event.

The $E_{\mathrm{T}}^{\mathrm{miss}}$ is defined as $-\Sigma\vec{p}_{\mathrm{T}}$, where the sum runs over all final-state particles and jets in the event. This quantity can be mismeasured due to detector inefficiencies, calorimeter energy thresholds and the nonlinearity of the calorimeter response for hadronic particles. Therefore, to increase the accuracy of the $E_{\mathrm{T}}^{\mathrm{miss}}$ measurement the jet energy corrections are propagated as

$$\vec{E}_{\mathrm{T}}^{\mathrm{miss,\ corr}} = \vec{E}_{\mathrm{T}}^{\mathrm{miss}} - \Sigma_{jets}(\vec{p}_{\mathrm{T,jet}}^{\,\mathrm{corr}} - \vec{p}_{\mathrm{T,jet}}), \tag{3.4}$$

where ‘corr’ refers to the corrected values. The $E_{\mathrm{T}}^{\mathrm{miss}}$ can also be mismeasured due to pileup interactions, and an improved measurement of the $E_{\mathrm{T}}^{\mathrm{miss}}$ at high pileup can be obtained by using the MVA $E_{\mathrm{T}}^{\mathrm{miss}}$ algorithm, used for $E_{\mathrm{T}}^{\mathrm{miss}}$ reconstruction in the $\mathrm{H} \to \mathrm{hh} \to \mathrm{bb}\tau\tau$ and $\mathrm{A/H} \to \tau\tau$ analyses. This algorithm computes a correction to the hadronic recoil $\vec{u}_{\mathrm{T}}$ reconstructed from PF particles

$$\vec{u}_{\mathrm{T}} = \vec{E}_{\mathrm{T}}^{\mathrm{miss}} - \Sigma\vec{p}_{\mathrm{T}}^{\,\mathrm{lep}}, \tag{3.5}$$

where $\Sigma\vec{p}_{\mathrm{T}}^{\mathrm{lep}}$ corresponds to the vectorial sum of the transverse momenta of the constituents selected as the di-tau candidate.

Two BDTs trained on $Z/\gamma^* \rightarrow \mu\mu$ events are used to compute this correction. The first one corrects the direction of the hadronic recoil, and the second one uses a data sample with the corrected recoil direction to compute a correction to the magnitude of the hadronic recoil. This BDT regression uses the magnitude of the hadronic recoil, its azimuthal angle and the scalar p_{T} sum of all PF particles for several different $E_{\mathrm{T}}^{\mathrm{miss}}$ definitions [116] as input. Figure 3.4 shows the performance of the MVA $E_{\mathrm{T}}^{\mathrm{miss}}$ in data collected at $\sqrt{s} = 13\,\mathrm{TeV}$ compared with the PF $E_{\mathrm{T}}^{\mathrm{miss}}$. Figure 3.4a indicates the lower MVA $E_{\mathrm{T}}^{\mathrm{miss}}$ values for events without genuine $E_{\mathrm{T}}^{\mathrm{miss}}$and figure 3.4b shows the improved resolution at high pileup.

In the process of calculating the corrections to the hadronic recoil using the MVA $E_{\mathrm{T}}^{\mathrm{miss}}$ algorithm, an event-by-event estimator of the likelihood that the $E_{\mathrm{T}}^{\mathrm{miss}}$ is due to unseen objects rather than induced by mismeasurement of jet energy is also determined [116].

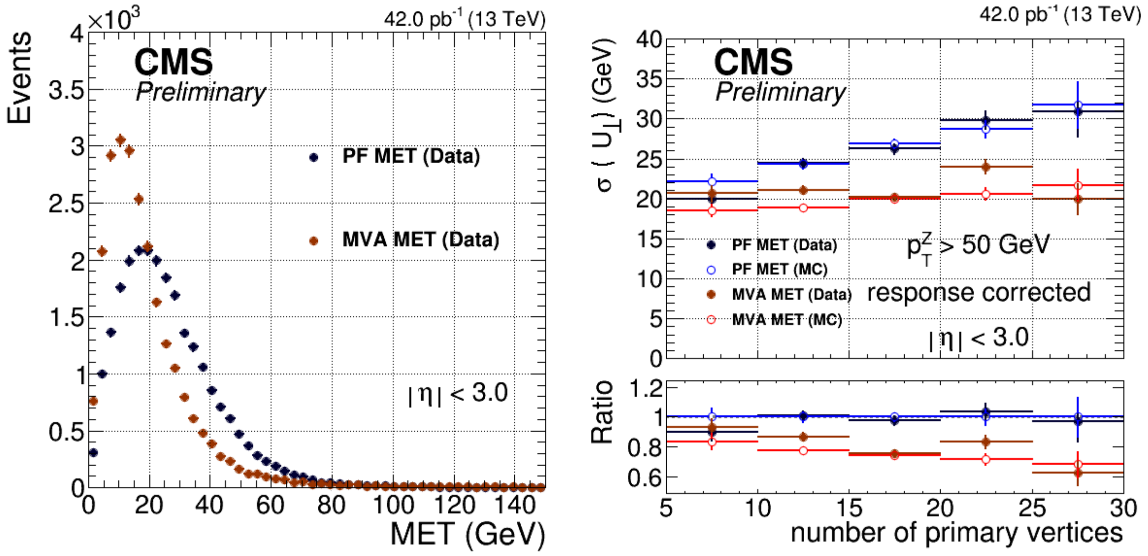

(a) $E_{\mathrm{T}}^{\mathrm{miss}}$ distribution in $Z/\gamma^* \rightarrow \mu\mu$ events

(b) $E_{\mathrm{T}}^{\mathrm{miss}}$ resolution

Figure 3.4: (a) $E_{\mathrm{T}}^{\mathrm{miss}}$ distributions comparing MVA $E_{\mathrm{T}}^{\mathrm{miss}}$ (brown circles) to PF $E_{\mathrm{T}}^{\mathrm{miss}}$ (black circles) for $Z/\gamma^* \rightarrow \mu\mu$ events, which contain no genuine $E_{\mathrm{T}}^{\mathrm{miss}}$, in a sample corresponding to $42\,\mathrm{pb}^{-1}$ of data collected at $\sqrt{s} = 13\,\mathrm{TeV}$. The $E_{\mathrm{T}}^{\mathrm{miss}}$ values for MVA $E_{\mathrm{T}}^{\mathrm{miss}}$ are lower than for PF $E_{\mathrm{T}}^{\mathrm{miss}}$. (b) The $E_{\mathrm{T}}^{\mathrm{miss}}$ resolution for PF $E_{\mathrm{T}}^{\mathrm{miss}}$ in blue and MVA $E_{\mathrm{T}}^{\mathrm{miss}}$ in red/brown circles, as a function of number of vertices. The MVA $E_{\mathrm{T}}^{\mathrm{miss}}$ resolution is more stable with increased pileup [117].

3.6.1 Recoil corrections

To correct for the mis-modelling of $E_{\mathrm{T}}^{\mathrm{miss}}$ in simulated events, recoil corrections are determined. The hadronic recoil $\vec{u}_{\mathrm{T}} = \vec{E}_{\mathrm{T}}^{\mathrm{miss}} - \Sigma\vec{p}_{\mathrm{T}}^{\,\mathrm{leptons}/\nu}$ is projected onto the axes parallel, $u_{\parallel}$, and perpendicular, $u_{\perp}$, to the p_{T} of the boson producing the leptons and neutrinos. For the H $\rightarrow$ hh $\rightarrow$ bb$\tau\tau$ and A/H $\rightarrow$ $\tau\tau$ analyses it is measured in Z/γ^{*} $\rightarrow$ $\mu\mu$ events, where no neutrinos are present. Distributions of $u_{\parallel}$ and $u_{\perp}$ are fitted both in data and simulated events, using convolutions of gaussians. Corrections are then applied to the simulation as

$$u'_{\parallel,\perp} = < u_{\parallel,\perp} >_{\mathrm{data}} + (u_{\parallel,\perp} - < u_{\parallel,\perp} >_{\mathrm{MC}}) \cdot \frac{\sigma_{\mathrm{Data}}}{\sigma_{\mathrm{MC}}}. \tag{3.6}$$

3.7 Hadronic taus

Taus are unstable particles and they decay before reaching the detector. In 17.4% of cases they decay to muons and neutrinos, with an additional 17.8% decaying to electrons plus neutrinos. The remaining 64.8% decay hadronically. Hadronically decaying taus, τ_{h}, are characterised by narrow jets containing either one or three charged particles ($\pi^{\pm}, K^{\pm}$) and zero, one, or two neutral pions. An overview of the most common decay modes is given in table 3.1.

Table 3.1: Summary of hadronic tau decay modes, indicating the branching fraction, and intermediate resonances where relevant [46].

Decay mode	**Resonance**	**Branching fraction [%]**
$\tau^{\pm} \rightarrow \mathrm{h}^{\pm}\nu_{\tau}$		11.5%
$\tau^{\pm} \rightarrow \mathrm{h}^{\pm}\pi^{0}\ \nu_{\tau}$	$\rho(770)$	26.0%
$\tau^{\pm} \rightarrow \mathrm{h}^{\pm}\pi^{0}\ \pi^{0}\ \nu_{\tau}$	$\mathrm{a}_1(1260)$	9.5%
$\tau^{\pm} \rightarrow \mathrm{h}^{\pm}\mathrm{h}^{\mp}\mathrm{h}^{\pm}\nu_{\tau}$	$\mathrm{a}_1(1260)$	9.8%
$\tau^{\pm} \rightarrow \mathrm{h}^{\pm}\mathrm{h}^{\mp}\mathrm{h}^{\pm}\pi^{0}\ \nu_{\tau}$		4.8%
Other modes with hadrons		3.2%
Total		64.8%

Hadronic tau decays are reconstructed using the “hadrons plus strips” (HPS) algorithm [118, 119], which is seeded by jets clustered from PF candidates, using the anti-

k_T algorithm with a distance parameter $\Delta R = 0.5$ in Run 1 and $\Delta R = 0.4$ in Run 2. As table 3.1 shows, 62% of hadronic tau decays contain at least one π^0 in the final state. There is a large probability that photons from $\pi^0 \to \gamma\gamma$ decays will convert to $\mathrm{e}^+\mathrm{e}^-$ pairs, which are bent in the magnetic field and therefore cause showers dispersed in the ϕ direction in the ECAL. Therefore, to reconstruct the energy deposits π^0 candidates leave in the ECAL, the photon and electron constituents of the jet that seeds the τ_h reconstruction are clustered into strips. The electron or photon with the highest p_T that is not yet included in a strip is used to build a new strip. The η and ϕ of this candidate determine the initial position of the strip, the next highest p_T electron or photon within an $\eta \times \phi$ window centered on the strip location is added to the strip and the position is recomputed as the energy-weighted average of the electron and photon constituents in the strip. This procedure is repeated until there are no more electrons or photons with $p_\mathrm{T} > 0.5\,\mathrm{GeV}$ within the strip window. During Run 1 the strip window had a fixed size of 0.05×0.2 in $\eta \times \phi$, while in the algorithm used during Run 2 the strip size is dynamically allocated. The width of the strip in η and ϕ is varied based on the p_T or E_T to be added to the strip and on the energy the strip already has, as

$$\begin{aligned} \Delta\eta &= 0.2 \cdot p_{\mathrm{T,e}/\gamma}^{-0.66} + 0.2 \cdot p_{\mathrm{T,strip}}^{-0.66} \\ \Delta\phi &= 0.35 \cdot p_{\mathrm{T,e}/\gamma}^{-0.71} + 0.35 \cdot p_{\mathrm{T,strip}}^{-0.71}, \end{aligned} \tag{3.7}$$

where $p_{\mathrm{T,e}/\gamma}$ is the transverse momentum of the candidate to be added to the strip and $p_{\mathrm{T,strip}}$ is the transverse momentum of the strip before merging a new candidate in.
In addition, the strip size is bounded as $0.05 < \Delta\eta < 0.15$ and $0.05 < \Delta\phi < 0.3$ [119].

If the $\Sigma\, p_\mathrm{T}$ of the strip is at least 2.5 GeV it is considered as a π^0 candidate. To reconstruct hadronic taus, charged particles and strips are combined into different signatures which are said to be compatible with a certain decay mode if the selection listed below is satisfied. The charged particles and strips are required to be within the signal cone $R_\mathrm{sig} = \frac{3.0}{p_\mathrm{T}[\mathrm{GeV}]}$, bounded by $0.05 < R_\mathrm{sig} < 0.1$. If a candidate satisfies more than one of the hypotheses the one that maximises the p_T is retained. The decay modes considered for reconstructing hadronic taus are:

- **One prong + 0 π^0:** One charged particle, no strips.
- **One prong + 1 π^0:** One charged particle and one strip with tau mass requirement $0.3 < m_\tau < 1.3\sqrt{p_\mathrm{T}/100}\,\mathrm{GeV}$, with this upper limit on the mass at least 1.3 GeV and at most 4.2 GeV.

- **One prong + 2 π^0:** One charged particle and two strips. The tau mass should be $0.4 < m_\tau < 1.2\sqrt{p_\mathrm{T}/100}$ GeV, with the upper limit on the mass at least 1.2 GeV and at most 4.0 GeV.
- **Three prong + 0 π^0:** Three charged particles with mass $0.8 < m_\tau < 1.5$ GeV. The tracks are required to originate within $\Delta z < 0.4$ cm of the same vertex, and their total charge is required to be ± 1.

The three prong + 1 π^0 decay mode, which would reconstruct the $\tau^\pm \to \mathrm{h}^\pm \mathrm{h}^\mp \mathrm{h}^\pm \pi^0\ \nu_\tau$ decay, suffers from large contamination by jets and is therefore not considered.

Requiring the reconstructed τ_h to be isolated reduces the jet $\to \tau_\mathrm{h}$ fake rate. Isolation discriminators can be defined using the isolation sum,

$$I_\tau = \Sigma p_\mathrm{T}^\mathrm{charged}(d_Z < 0.2\ \mathrm{cm}) + \max(0, \Sigma p_\mathrm{T}^\gamma - \Delta\beta \Sigma p_\mathrm{T}^\mathrm{charged}(d_Z > 0.2\ \mathrm{cm})), \tag{3.8}$$

where the first term denotes the sum of the transverse momenta of all charged particles not part of the identified τ_h. Only particles with $p_\mathrm{T} > 0.5$ GeV within a cone of $\Delta R = 0.5$ centred around the direction of the τ_h are taken into account and the charged particle tracks are required to be compatible with having originated from the τ_h production vertex. This is achieved by requiring the longitudinal impact parameter with respect to the primary vertex to be $d_z < 0.2$ cm. The second term of equation 3.8 denotes the sum of the transverse momenta of photons with $p_\mathrm{T} > 0.5$ GeV within a cone of $\Delta R = 0.5$ centred around the direction of the τ_h. The effect of pileup on this term is accounted for by subtracting the sum of the momenta of charged particles with $p_\mathrm{T} > 0.5$ GeV, within a cone of $\Delta R = 0.8$ around the direction of the hadronic tau and tracks not compatible with having originated from the production vertex of the hadronic tau, multiplied by a $\Delta\beta$ factor of 0.2. This factor accounts for the fraction of neutral to charged energy. To determine it, the photon energy sum discussed above is fitted as a function of the quantity $\Sigma p_\mathrm{T}^\mathrm{charged}(d_Z > 0.2\ \mathrm{cm})$. The slope of this linear fit is taken as the $\Delta\beta$ factor.

In addition to the isolation sum, a requirement on the sum of transverse momenta of electrons and photons included in strips but which are located outside of the signal cone,

$$p_\mathrm{T}^\text{strip, outer} = \Sigma p_\mathrm{T}^{\mathrm{e}/\gamma}(\Delta R > R_\mathrm{sig}) < 0.10 \cdot p_\mathrm{T}^\tau, \tag{3.9}$$

can be made. An MVA τ_{h} isolation discriminator combines isolation variables with tau lifetime information into a BDT to discriminate between τ_{h} decays and quark and gluon jets. The variables used as inputs are:

- Isolation sums of charged and neutral particles, in addition to the isolation sums in equations 3.8 and 3.9.
- Track-related variables: the impact parameters, quality of the track, information about decay vertices.
- Information about photons: the momentum-weighted ΔR, $\Delta\eta$ and $\Delta\phi$ of photons in strips inside or outside the signal cone, in addition to the number of signal and isolation photons found.
- τ_{h}-related variables: the reconstructed decay mode and τ_{h} kinematics.
- The ratio of the total electromagnetic energy to the total energy within the τ_{h} signal cone.

Figure 3.5a compares the τ_{h} identification efficiency with the jet → τ_{h} fake rate for different working points of the MVA isolation discriminator, as well as the cut-based isolation discriminator based on the isolation sum and $p_{\mathrm{T}}^{\mathrm{strip,outer}}$. The MVA-based discriminator performs better than the cut-based discriminator alone.

In order to reduce the $\mathrm{e} \to \tau_{\mathrm{h}}$ and $\mu \to \tau_{\mathrm{h}}$ fake rates, anti-electron and anti-muon discriminators are used. The anti-electron discriminator is a BDT-based discriminator trained using the following input variables:

- Kinematic variables of the τ_{h} candidate and the GSF track, plus the visible mass of the τ_{h} candidate.
- Energy and momentum ratios: the fraction of electromagnetic energy, plus the ECAL and HCAL energy relative to track momentum.
- Photon-related variables: the momentum-weighted $\Delta\eta$ and $\Delta\phi$ between photons, the fraction of the τ_{h} energy carried by photons, the ratio of the energies of bremsstrahlung photons measured in the ECAL and the tracker, and the number of photons found in strips.
- Information on the quality of the track.

Five working points are provided, ranging from very loose to very tight. The τ_h efficiency and e $\rightarrow \tau_\mathrm{h}$ fake rate for the various working points are shown in figures 3.5b and 3.5c, respectively.

The anti-muon discriminator is a cut-based discriminant, for which a loose and a tight working point are provided. It is based on variables such as the number of track segments found in various parts of the muon system around the direction of the τ_h, and comparisons of calorimeter energy with the momentum of the leading τ_h track.

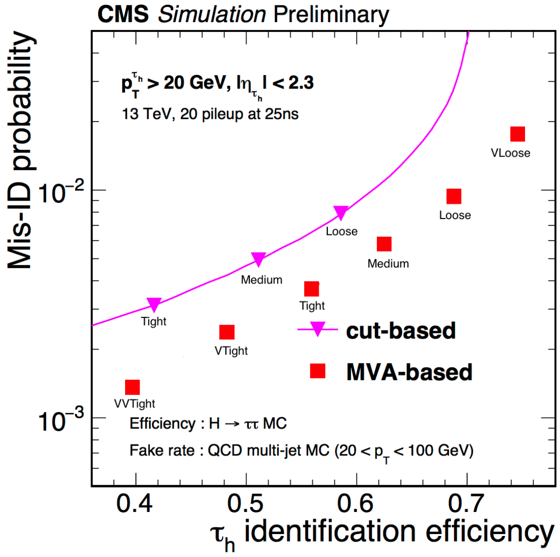

(a) Isolation performance

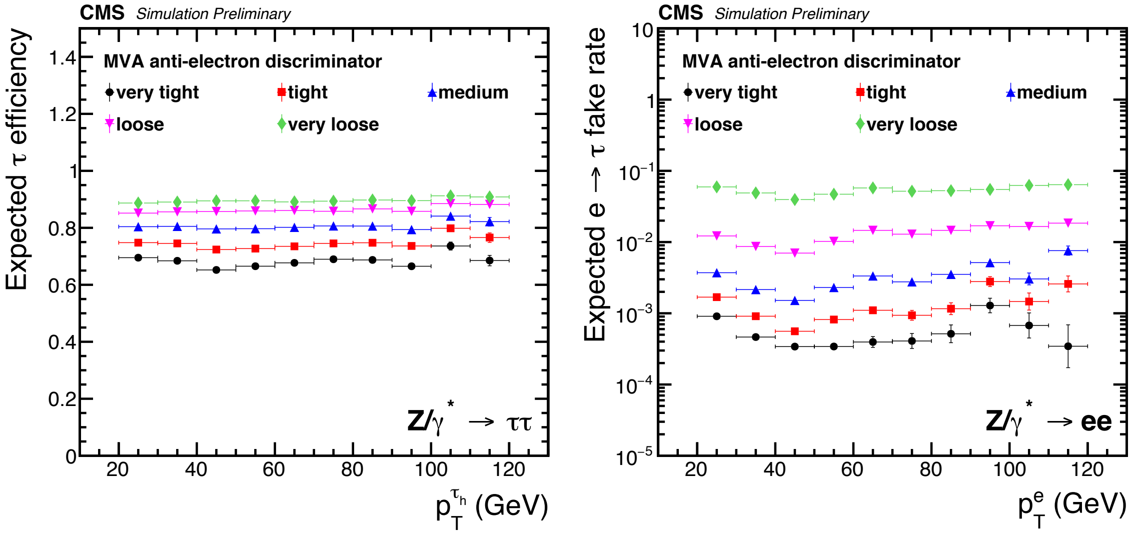

(b) Real τ_h efficiency for anti-e discriminator **(c)** e $\rightarrow \tau_h$ fake rate for the anti-e discriminator

Figure 3.5: (a) The jet$\rightarrow\tau_h$ fake rate in simulated QCD multijet events versus τ_h identification efficiency for simulated H $\rightarrow \tau\tau$ events, comparing the MVA-based isolation discriminator in red with the cut-based isolation discriminator in pink. Tighter working points give lower hadronic tau identification efficiencies and lower fake rates, and for the same τ_h identification efficiency the fake rate from the MVA-based discriminator is lower than from the cut-based discriminator. Figure adapted from [119]. (b) The τ_h identification efficiency in simulated $Z/\gamma^* \rightarrow \tau\tau$ events for different working points of the anti-electron discriminator as a function of the p_T of the τ_h, and (c) the e $\rightarrow \tau_h$ fake rate in simulated $Z/\gamma^* \rightarrow$ ee events for different working points of the anti-electron discriminator, as a function of the p_T of the electron [119]. Note that the efficiencies and fake rates are fully derived from simulation and serve to give an indication of the efficiencies of the different working points relative to each other.

Chapter 4

Search for H → hh → bb$\tau\tau$

The discovery of the 125 GeV Higgs boson by the ATLAS and CMS Collaborations in 2012 [24, 25] has opened up new possibilities for probing the Higgs sector beyond the SM. As discussed in chapter 1, in some MSSM scenarios and some more generic type-II 2HDMs, a heavy neutral Higgs boson H can decay to a pair of 125 GeV Higgs bosons for low values of $\tan\beta$, probing a region of parameter space not yet excluded by the stringent existing limits. In regions where the decay H → hh is enhanced, the A → Zh decay also has a large branching ratio, indicating the usefulness of both channels for probing the low $\tan\beta$ region. The bb$\tau\tau$ final state is chosen for the combination of the large h(125) → bb branching ratio and the cleaner h(125) → $\tau\tau$ final state.

In this chapter the search for a heavy Higgs boson decaying to a pair of 125 GeV Higgs bosons, with one of these Higgs bosons decaying to a pair of b-jets and the other decaying to a pair of tau leptons, is discussed. In this analysis, which uses a dataset corresponding to 19.8 fb^{-1} collected during the 2012 p-p running period of the LHC, the eτ_{h}, $\mu\tau_{\mathrm{h}}$ and $\tau_{\mathrm{h}}\tau_{\mathrm{h}}$ final states of the di-tau pair are studied; these final states are referred to as channels. The results of this search are model-independent upper limits on the heavy Higgs production cross section times branching ratio ($\sigma\times\mathcal{B}$) into h(125)h(125)→ bb$\tau\tau$, for which all three channels are combined. The eτ_{h} and $\mu\tau_{\mathrm{h}}$ channels will be described in this chapter. The $\tau_{\mathrm{h}}\tau_{\mathrm{h}}$ channel will not be covered, although the limits shown in section 4.8 will include this final state. In addition the results are interpreted in the context of the MSSM and a type-II 2HDM. These interpretations are made in combination with the results of a search for A → Zh → $\ell\ell\tau\tau$ [1]. For these results I contributed to the analysis of the eτ_{h} and $\mu\tau_{\mathrm{h}}$ channels, studying alternative t$\bar{\mathrm{t}}$ background rejection methods and other uses of the kinmeatic fit variable which are not further discussed. My main contribution was the statistical inference for the H → hh analysis, which included limit setting and performing the model interpretations of the H → hh and A → Zh analyses, plus their combination. Both searches, and their interpretations, are detailed in reference [1].

4.1 Datasets and Monte Carlo samples

The dataset used for this analysis corresponds to the full dataset collected by the CMS experiment during the 2012 p-p running period of the LHC. Signal and background events are generated using several different MC event generators. With the exception of the embedded samples described later in this section, all of these simulated samples are centrally produced for use by all CMS analyses. The `MadGraph` [120] matrix element generator is used to generate samples of W+jets, $Z/\gamma^* \rightarrow \ell\ell$, $t\bar{t}$ and ZZ, WZ and WW events. In addition to samples with a mixture of jet multiplicities ('inclusive' samples), samples binned in jet multiplicity are used for the W+jets and $Z/\gamma^* \rightarrow \ell\ell$ backgrounds. This increases the number of simulated background events in regions with multiple jets, which are important for this analysis due to the presence of b-jets in the final state. The samples binned in jet multiplicity are combined with the inclusive samples such that the fraction of events with each jet multiplicity is preserved.

Single top samples are produced with the `POWHEG` [121, 122] generator. Samples of gg → H → hh → bb$\tau\tau$ are generated in steps of 10 GeV between m_{H}= 260 − 350 GeV using `PYTHIA 6` [123]. The maximum mass is 350 GeV because for the interpretation of a resonance as a Higgs boson the decay H → $t\bar{t}$ starts to dominate beyond this mass. In all of the samples `TAUOLA` [124] is used to decay the tau leptons, and parton showering and hadronisation are modelled using `PYTHIA 6` [123]. Minimum bias events generated using `PYTHIA 6` are added to all MC samples to model additional interactions. The MC samples are then reweighted so that the pileup distribution matches the pileup distribution in data. The detector response to the final simulated particles is modelled using a `GEANT4`-based [125] detector simulation.

To better model the $Z/\gamma^* \rightarrow \tau\tau$ background an embedding technique is used [31]. In this method, $Z/\gamma^* \rightarrow \mu\mu$ events are selected in data and the muons are replaced by simulated taus. `TAUOLA` is used to decay the taus, with the final state particles passed through the detector simulation. Tracks in the inner tracking system, hits in the muon systems and energy deposits in the calorimeters due to the simulated taus are combined with the remains of the $Z/\gamma^* \rightarrow \mu\mu$ event after the detector signals of the two muons originating from the Z boson have been removed. This technique is also applied to a simulated $\mathrm{t\bar{t}}$ sample to estimate the $\mathrm{t\bar{t}}$ contamination in the $\mathrm{Z}/\gamma^* \rightarrow \mu\mu$ embedded sample.

4.2 Event selection and categorisation

This section gives an overview of the event selection; a detailed description of the physics objects used in this analysis is given in chapter 3.

4.2.1 Event selection in the $\mu\tau_\mathrm{h}$ channel

The first step of event selection in the $\mu\tau_\mathrm{h}$ channel is a trigger which requires only a muon at L1. At the level of the HLT a hadronic tau, reconstructed using a simpler version of the PF algorithm, is also required. Loose isolation requirements are applied to this hadronic tau, and loose ID and isolation requirements are applied to the muon at this stage.

In the offline event selection, an oppositely charged $\mu\tau_\mathrm{h}$ pair is required, separated by $\Delta R > 0.5$. The muon is required to have a p_T of at least 20 GeV and $|\eta| < 2.1$, and should be compatible with originating from the primary vertex. This means the transverse and longitudinal impact parameters with respect to the primary vertex, d_{xy} and d_z, must be smaller than 0.045 cm and 0.2 cm respectively. Tight muon identification criteria and a tight isolation requirement, $I^{\mu}_{\mathrm{rel}} < 0.1$, are applied. The hadronic tau must have a p_T of at least 20 GeV, $|\eta| < 2.3$, and must have $d_z < 0.2$ cm. It is required to pass the decay mode finding identification from the HPS algorithm. Additionally, the isolation sum (equation 3.8) is required to be at most 1.5 GeV. To reject $\mathrm{e}/\mu \rightarrow \tau_\mathrm{h}$ fakes, and to reduce the contribution of $\mathrm{Z}/\gamma^* \rightarrow \mu\mu$ background events, the hadronic tau is also required to pass the tight working point of the anti-muon discriminator and the loose working point of the cut-based anti-electron discriminator.

After this selection there is still a chance that more than one possible $\mu\tau_\mathrm{h}$ pair exists in the event. If this is the case the combination with largest ${p_\mathrm{T}}^{\mu} + {p_\mathrm{T}}^{\tau_\mathrm{h}}$ is chosen. In order to reduce the $\mathrm{Z}/\gamma^* \rightarrow \mu\mu$ background further, in cases where the reconstructed hadronic tau originates from a misidentified jet, the event is rejected if an opposite-charge pair of lower p_T (at least 15 GeV) muons, passing looser ID and isolation requirements than the signal muon, can be formed. Additional vetoes, requiring exactly one muon and exactly zero electrons to pass $p_\mathrm{T} > 10$ GeV and loose ID and isolation requirements, are applied to prevent overlap with other channels and to reduce the di-boson background.

In addition to the requirements on the di-tau pair, at least two jets with $p_{\mathrm{T}} > 20\,\mathrm{GeV}$ are required. No b-tagging requirements are applied at this stage; these will be discussed in more detail in section 4.2.3.

4.2.2 Event selection in the eτ_{h} channel

Events in the eτ_{h} channel are selected using a trigger which requires an electron at L1, and both an electron and a hadronic tau in the HLT. The hadronic tau is reconstructed in a similar way as for the trigger in the $\mu\tau_{\mathrm{h}}$ channel, and loose ID and isolation requirements are also applied to the electron at this stage.

After the trigger selection, an oppositely charged eτ_{h} pair is required, again separated by $\Delta R > 0.5$. The electron should have a p_{T} of at least 24 GeV, $|\eta| < 2.1$, and should satisfy $d_{xy} < 0.045\,\mathrm{cm}$ and $d_{z} < 0.2\,\mathrm{cm}$. The electron must pass the tight working point of the electron MVA ID discriminator, and the relative isolation is required to be $I^{\mathrm{e}}_{\mathrm{rel}} < 0.1$. The requirements placed on the hadronic tau are similar to those required in the $\mu\tau_{\mathrm{h}}$ channel, apart from the anti-muon discriminator, where the loose working point is required, and the anti-electron discriminator, where the medium working point of the MVA discriminator is required.

If there is more than one possible eτ_{h} pair, the pair with the largest ${p_{\mathrm{T}}}^{\mathrm{e}}+{p_{\mathrm{T}}}^{\tau_{\mathrm{h}}}$ is taken. Similar additional vetoes as in the $\mu\tau_{\mathrm{h}}$ channel are applied. The event is rejected if an opposite-charge pair of electrons with $p_{\mathrm{T}} > 15\,\mathrm{GeV}$, passing looser ID and isolation requirements than the signal electron requirements, can be formed. To prevent overlap with other channels and to reduce the di-boson background, events that have more than one electron or at least one muon passing $p_{\mathrm{T}} > 10\,\mathrm{GeV}$ and loose ID and isolation requirements are rejected.

In addition to the requirements on the di-tau pair, at least two jets with $p_{\mathrm{T}} > 20\,\mathrm{GeV}$ are required.

4.2.3 Categorisation

In both channels a selection on the transverse mass, m_{T}, between the electron or muon and missing transverse energy, defined as,

$$m_{\mathrm{T}} = \sqrt{2 p_{\mathrm{T}} E_{\mathrm{T}}^{\mathrm{miss}} (1 - \cos \Delta\phi)}\,, \tag{4.1}$$

is applied. In this equation p_{T} is the transverse momentum of the electron or muon, and $\Delta\phi$ the azimuthal angle between this light lepton and the missing transverse energy. The m_{T} distributions for the eτ_{h} and $\mu\tau_{\mathrm{h}}$ channels, using the selections as described in sections 4.2.1 and 4.2.2, are shown in figure 4.1.

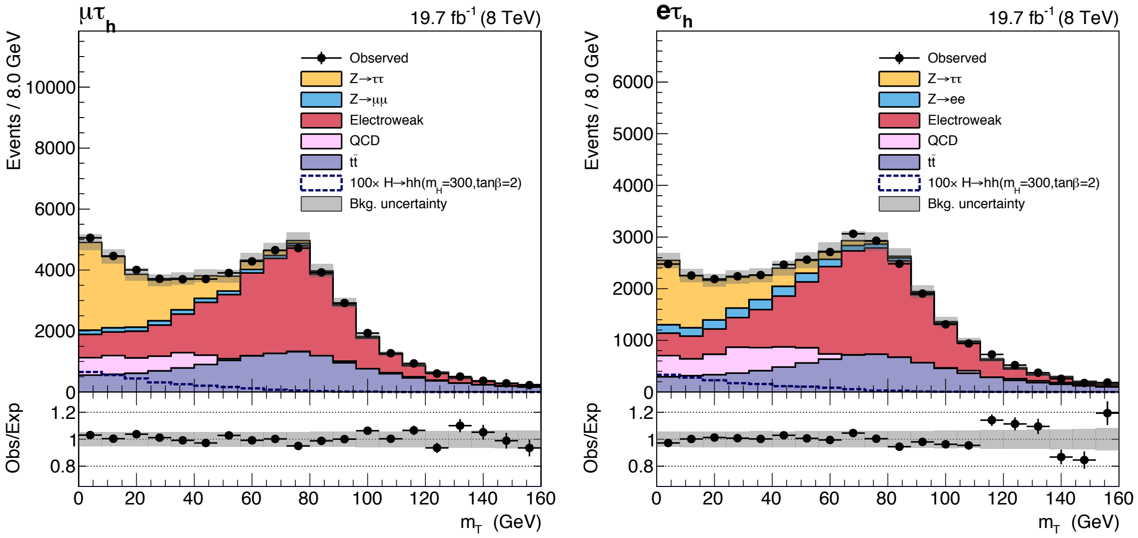

(a) $\mu\tau_{\mathrm{h}}$ channel

(b) eτ_{h} channel

Figure 4.1: m_{T} distributions in the (a) $\mu\tau_{\mathrm{h}}$ and (b) eτ_{h} channels. The signal at $m_{\mathrm{H}} = 300\,\mathrm{GeV}$ and $\tan\beta = 2$ in the MSSM low-$\tan\beta$ scenario, multiplied by a factor of 100, is overlaid.

This quantity is required to be smaller than 30 GeV in both channels. In events where the missing energy and the light lepton are oriented back-to-back, m_{T} is large, whereas it is closer to zero when the two are aligned. In W $\rightarrow \ell\nu$ events, as the W boson is very heavy, the lepton and neutrino are more likely to be emitted back-to-back, and therefore m_{T} will be large. For Z/γ^* $\rightarrow \tau\tau$ and h $\rightarrow \tau\tau$ events, the neutrinos in the $\tau \rightarrow \ell\nu\nu$ decay are more likely to travel in the same direction as the visible decay products of the tau, due to the smaller mass of the τ compared with the W boson. Therefore requiring the transverse mass to be less than 30 GeV reduces the W+jets background. This effect is also visible in figure 4.1, where the W+jets and the much smaller di-boson and single-top backgrounds are combined into the "electroweak" background contribution, drawn in red.

After applying the m_{T} selection, events are divided into three categories to maximise sensitivity to the signal: 2jet-0tag (at least two jets, none of which are b-tagged), 2jet-1tag (at least two jets, exactly one of which is b-tagged), 2jet-2tag (at least two jets, at least two of which are b-tagged). Jets are considered b-tagged if they pass the medium working point of the CSV b-tagging discriminator. The typical b-tagging efficiency at this working point is 70% [126]. The 2jet-0tag category does not collect much of the signal and is dominated by backgrounds, and the 2jet-2tag category is the most sensitive to signal. Figure 4.2, which shows the number of b-tagged jets in the two-jet selection of the $\mu\tau_\mathrm{h}$ and $\mathrm{e}\tau_\mathrm{h}$ channels, illustrates this.

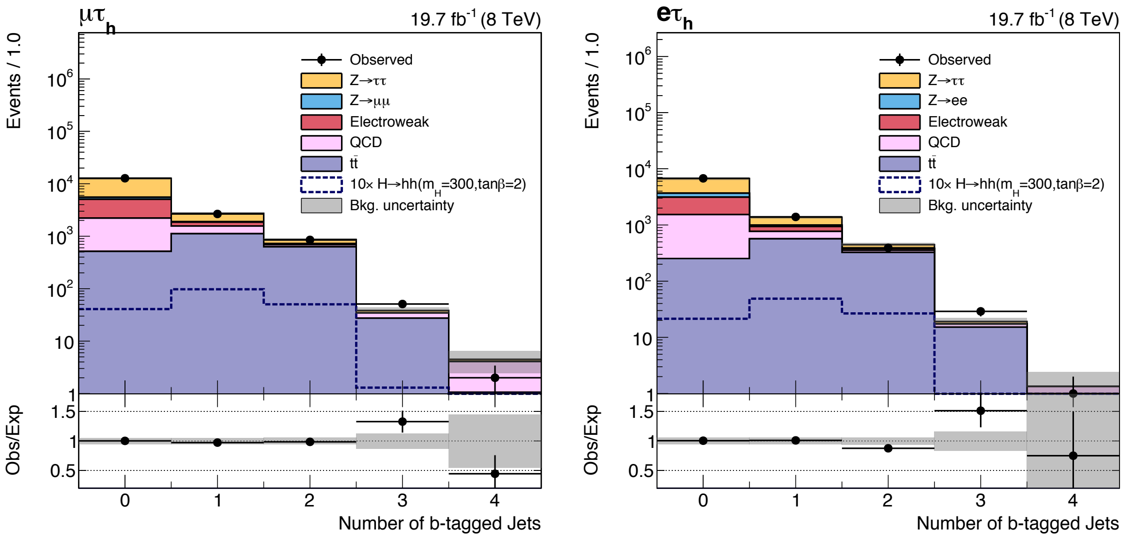

(a) $\mu\tau_\mathrm{h}$ channel **(b)** $\mathrm{e}\tau_\mathrm{h}$ channel

Figure 4.2: Number of b-tagged jets in the two-jet selection of the (a) $\mu\tau_\mathrm{h}$ and (b) $\mathrm{e}\tau_\mathrm{h}$ channels. The signal at $m_\mathrm{H} = 300\,\mathrm{GeV}$ and $\tan\beta = 2$ in the MSSM low-$\tan\beta$ scenario, multiplied by a factor of 10, is overlaid.

In signal events the di-tau pair and di-jet pair are the decay products of a 125 GeV Higgs boson, and therefore their invariant masses should be close to 125 GeV. To reduce background contributions from events where the di-tau or di-jet mass is not compatible with 125 GeV, requirements are made on m_{jj}, the di-jet invariant mass, and on $m_{\tau\tau}$, the di-tau invariant mass as reconstructed using the `SVFit` algorithm [25,127]. This algorithm provides a likelihood-based estimate of the di-tau mass using the visible decay products of the taus and the reconstructed $E_\mathrm{T}^\mathrm{miss}$. The use of this algorithm greatly improves the separation between $\mathrm{Z} \to \tau\tau$ and $\mathrm{H} \to \tau\tau$ events, which is of great importance for the SM $\mathrm{H} \to \tau\tau$ analysis [25]. By requiring $70 < m_{jj} < 150\,\mathrm{GeV}$ and $90 < m_{\tau\tau} < 150\,\mathrm{GeV}$, a large number of background events can be rejected, while retaining most of the signal. This is illustrated in figure 4.3 for the 2jet-2tag category.

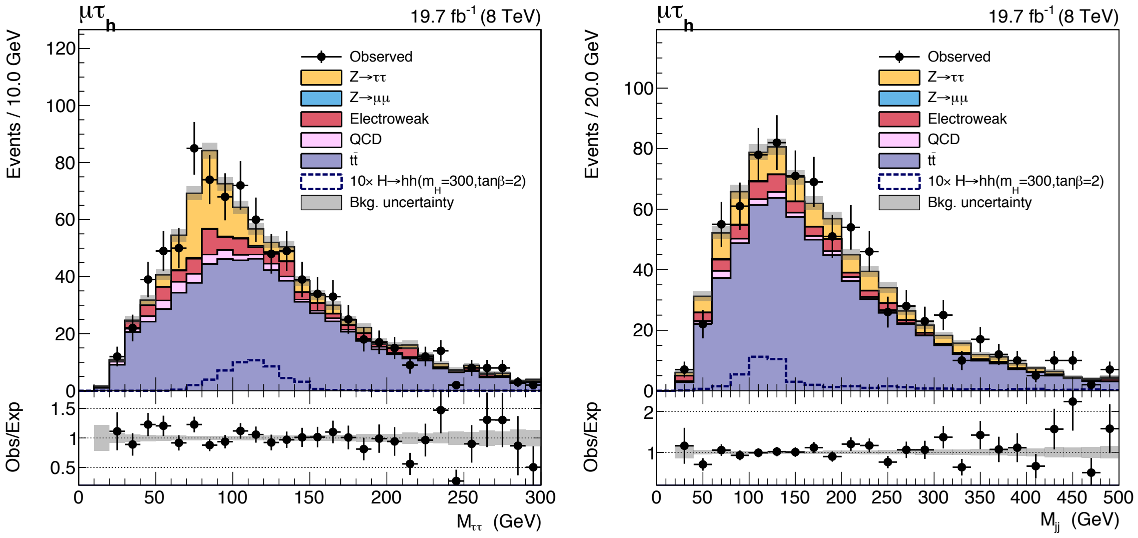

(a) $m_{\tau\tau}$ **(b)** m_{jj}

Figure 4.3: (a) Reconstructed di-tau invariant mass and (b) di-jet invariant mass in the 2jet-2tag category of the $\mu\tau_\mathrm{h}$ channel. The signal for a heavy Higgs boson H with mass $m_\mathrm{H} = 300\,\mathrm{GeV}$ at $\tan\beta = 2$ in the low-$\tan\beta$ MSSM scenario, multiplied by a factor 10, is overlaid. The signal peaks at around 125 GeV in both variables.

4.3 Monte Carlo simulation-to-data correction factors

Simulated samples are used for the estimation of some of the backgrounds and the signal, and it is therefore important to correct for any mis-modelling. The MC simulation-to-data correction factors used for this are estimated in dedicated control regions.

Identification, isolation, and trigger efficiencies are measured for electrons, muons and hadronic taus in data and simulated events. The difference between the efficiencies in data and simulated events are applied to simulated events as a scale factor $\mathrm{SF} = \frac{\epsilon_\mathrm{Data}}{\epsilon_\mathrm{MC}}$.

For electrons and muons these efficiencies are measured using a tag-and-probe method using Z → ee and Z → $\mu\mu$ events, respectively. The hadronic tau identification, isolation and trigger efficiencies are measured via a similar method that makes use of $\mathrm{Z} \to \tau\tau \to \mu\tau_\mathrm{h}$ events.

The energy scale for hadronic taus is determined by fitting the mass of the hadronic tau candidate in $\mathrm{Z} \to \tau\tau \to \mu\tau_\mathrm{h}$ events. This fit is performed separately for each hadronic tau decay mode to obtain an energy scaling that is applied to reconstructed hadronic taus matched to simulated hadronic tau decays in simulation.

In the eτ_{h} channel a scale factor is applied to the Z/γ^{*} $\rightarrow$ ee background to correct for differences in the e $\rightarrow$ τ_{h} fake rate between data and simulation. This scale factor is derived separately for the 1-prong + $0\pi^{0}$ and 1-prong + at least one π^{0} decay modes by fitting the visible mass of the eτ_{h} pair in events passing the selection of the eτ_{h} channel as described in section 4.2.2, but with the two-jet requirement removed.

Differences in $E_{\mathrm{T}}^{\mathrm{miss}}$ resolution and response between data and simulation are accounted for by applying recoil corrections to Z/γ^{*} $\rightarrow$ $\ell\ell$, W+jets and signal simulation. Section 3.6.1 gives more details on how these corrections are derived.

To correct for the differences in b-tagging efficiency and light jet mis-tagging rates between data and simulation, p_{T}-and η-dependent scale factors are derived using the method described in reference [126]. There are separate scale factors for b-/c-jets and light jets.

In this analysis the "promote-demote" method is used to apply these scale factors. In this method a demotion or promotion probability is assigned to every jet as:

$$\begin{aligned} P(\text{demote}) &= 1 - \text{SF for SF} < 1 \\ P(\text{promote}) &= \frac{(\text{SF}-1)(\epsilon_{\text{MC}}-1)}{\text{SF}} \text{ for SF} > 1, \end{aligned} \tag{4.2}$$

where 'SF' is the scale factor mentioned above, and ϵ_{MC} is the b-tagging efficiency in simulated events for the type of jet (light, b- or c-) under consideration.

4.4 Discriminating variable

The variable of interest in this analysis is the mass of the heavy Higgs boson H. This can be reconstructed as the four-body mass of the two jets and the two taus. A more accurate result can be obtained by using a kinematic fitting procedure that makes use of the 125 GeV mass constraint on the di-tau and di-jet candidates.

In a kinematic fit constraints are made on the event kinematics, in the case of this analysis these constraints are $m(\tau_1, \tau_2) = m_{\mathrm{h}} = 125\,\mathrm{GeV}$ and $m(\mathrm{j}_1, \mathrm{j}_2) = m_{\mathrm{h}} = 125\,\mathrm{GeV}$. The kinematic observables related to the hadronic taus and jets are varied within their uncertainties to fulfil these constraints. A χ^{2} cost term is introduced for each observable that is varied with respect to the measurement; the aim of the fit is to minimise the sum of these χ^2 terms.

For jets, the reconstructed direction in η and ϕ is assumed to be measured accurately in comparison with their energy. Therefore only their energy is varied in the fit. In addition, we assume that uncertainties in the energy measurement directly translate to uncertainties in the momentum measurement, and therefore $\vec{\beta} = \vec{p}/E$ is also kept constant.

Before the fit, the mass constraint gives:

$$\begin{aligned} m_{\mathrm{h}}^2 &= E_{\mathrm{h}}^2 - \vec{p_{\mathrm{h}}}^2 = (E_{\mathrm{j1}} + E_{\mathrm{j2}})^2 - (\vec{p_{\mathrm{j1}}} + \vec{p_{\mathrm{j2}}})^2 \\ &= 2E_{\mathrm{j1}}E_{\mathrm{j2}} + m_{\mathrm{j1}}^2 + m_{\mathrm{j2}}^2 - 2\vec{p_{\mathrm{j1}}}\vec{p_{\mathrm{j2}}} \\ &= m_{\mathrm{j1}}^2 + m_{\mathrm{j2}}^2 - 2E_{\mathrm{j1}}E_{\mathrm{j2}}(1 - \vec{\beta_{\mathrm{j1}}}\vec{\beta_{\mathrm{j2}}}) \\ &\Rightarrow (1 - \vec{\beta_{\mathrm{j1}}}\vec{\beta_{\mathrm{j2}}}) = \frac{m_{\mathrm{h}}^2 - m_{\mathrm{j1}}^2 - m_{\mathrm{j2}}^2}{2E_{\mathrm{j1}}E_{\mathrm{j2}}}. \end{aligned} \tag{4.3}$$

When varying the energy of the first jet in the fit, equation 4.3 can be rewritten to derive an expression for the updated energy of the second jet. Using $\mathcal{A} = (1 - \vec{\beta_{\mathrm{j1}}}\vec{\beta_{\mathrm{j2}}})$ and

$$\gamma = \frac{1}{1-\beta^2} \Rightarrow \gamma^2 = \frac{1}{1-\beta^2} = \frac{1}{1-p^2/E^2} = \frac{E^2}{m^2}, \tag{4.4}$$

we get:

$$\begin{aligned} m_{\mathrm{h}}^2 &= m_{\mathrm{j1}}^2 + m_{\mathrm{j2}}^2 - 2E_{\mathrm{j1}}E_{\mathrm{j2}}(1 - \vec{\beta_{\mathrm{j1}}}\vec{\beta_{\mathrm{j2}}}) \\ &= m_{\mathrm{j1}}^2 + \frac{E_{\mathrm{j2,fit}}^2}{\gamma_{\mathrm{j2}}^2} + 2\mathcal{A}E_{\mathrm{j1}}E_{\mathrm{j2,fit}} \\ \Rightarrow E_{\mathrm{j2}}^{\mathrm{fit}} &= \frac{(-2E_{\mathrm{j1}}\mathcal{A} + \sqrt{4E_{\mathrm{j1}}^2\mathcal{A} - 4(m_{\mathrm{j1}}^2 - m_{\mathrm{h}}^2)\gamma_{\mathrm{j2}}^{-2}})\gamma_{\mathrm{j2}}^2}{2} \\ &= -E_{\mathrm{j1}}\mathcal{A}\gamma_{\mathrm{j2}}^2 + \sqrt{E_{\mathrm{j1}}^2\mathcal{A}\gamma_{\mathrm{j2}}^4 - (m_{\mathrm{j1}}^2 - m_{\mathrm{h}}^2)\gamma_{\mathrm{j2}}^2} \\ &\Rightarrow E_{\mathrm{j2}}^{\mathrm{fit}} = E_{\mathrm{j1}}\mathcal{A}\gamma_{\mathrm{j2}}^2(-1 + \sqrt{1 + \frac{m_{\mathrm{h}}^2 - m_{\mathrm{j1}}^2}{E_{\mathrm{j1}}^2\mathcal{A}\gamma_{\mathrm{j2}}^2}}). \end{aligned} \tag{4.5}$$

The fitting procedure additionally modifies the masses of the jets as

$$m_{\mathrm{j}_{1,2}}^{\mathrm{fit}} = m_{\mathrm{j1,2}}\frac{E_{\mathrm{j1,2}}^{\mathrm{fit}}}{E_{\mathrm{j1,2}}}. \tag{4.6}$$

The χ^2 term for each jet is calculated as $\chi^2_{\mathrm{j1,2}} = \frac{E^{\mathrm{fit}}_{\mathrm{j1,2}} - E^{\mathrm{meas}}_{\mathrm{j1,2}}}{\sigma_{\mathrm{j1,2}}}$, where 'meas' denotes the measured value and 'fit' the value given by the fit.

For taus only the visible decay products are measured. Assuming these point in the same direction as the original tau, a similar procedure as for the jets can be employed to constrain the energy of the second tau when varying the energy of the first tau in the fit. The masses of the taus are kept fixed at m_τ throughout the procedure.

Due to the missing energy associated with the tau decays, additional constraints on the fit have to be used to reconstruct the correct tau energies. This is done by enforcing that the heavy Higgs boson recoil from the fit is close to the reconstructed recoil.

The measured recoil is

$$\vec{p}^{\,\mathrm{meas}}_{\mathrm{T,recoil}} = -\vec{p}^{\,\mathrm{meas}}_{\mathrm{T,H}} = -\vec{p}^{\,\mathrm{meas}}_{\mathrm{T,miss}} - \vec{p}^{\,\mathrm{meas}}_{\mathrm{T,j1}} - \vec{p}^{\,\mathrm{meas}}_{\mathrm{T,j2}} - \vec{p}^{\,\mathrm{meas}}_{\mathrm{T},\tau_1^{\mathrm{vis}}} - \vec{p}^{\,\mathrm{meas}}_{\mathrm{T},\tau_2^{\mathrm{vis}}}, \tag{4.7}$$

and the recoil from the fit is,

$$\vec{p}^{\,\mathrm{fit}}_{\mathrm{T,recoil}} = -\vec{p}^{\,\mathrm{fit}}_{\mathrm{T,H}} = -\vec{p}^{\,\mathrm{fit}}_{\mathrm{T,j1}} - \vec{p}^{\,\mathrm{fit}}_{\mathrm{T,j2}} - \vec{p}^{\,\mathrm{fit}}_{\mathrm{T},\tau_1} - \vec{p}^{\,\mathrm{fit}}_{\mathrm{T},\tau_2}. \tag{4.8}$$

A χ^2 corresponding to the agreement between the fitted and measured recoil is reconstructed as

$$\chi^2_{\mathrm{recoil}} = (\vec{p}^{\,\mathrm{fit}}_{\mathrm{T,recoil}} - \vec{p}^{\,\mathrm{meas}}_{\mathrm{T,recoil}})^T V^{-1}_{\mathrm{recoil}} (\vec{p}^{\,\mathrm{fit}}_{\mathrm{T,recoil}} - \vec{p}^{\,\mathrm{meas}}_{\mathrm{T,recoil}}), \tag{4.9}$$

where the covariance matrix V_{recoil} of the recoil vector is estimated as

$$V_{\mathrm{recoil}} = V_{\vec{p}_{\mathrm{T,miss}}} - V_{\mathrm{j1}} - V_{\mathrm{j2}}, \tag{4.10}$$

from the covariance matrices of the jets and the covariance matrix of the missing transverse momentum. The latter is estimated in the process of determining the MVA $E_{\mathrm{T}}^{\mathrm{miss}}$, while the covariance matrices of the jets can be written in terms of the position, momentum, and energy resolution of the jets. The total χ^2 term that needs to be minimised in the fit can then be written as

$$\chi^2 = \chi^2_{\mathrm{j1}} + \chi^2_{\mathrm{j2}} + \chi^2_{\mathrm{recoil}}. \tag{4.11}$$

The results of the kinematic fit are the tau and jet four-vectors with their energies and momenta set to the best fit values found for them in the fit. These can then be added together to find the mass of the heavy Higgs boson as reconstructed by the kinematic fit.

As illustrated in figure 4.4a the use of the kinematic fit greatly improves the resolution of the reconstructed heavy Higgs boson mass in signal events, when compared with the simple four-body mass reconstruction. It also shifts the mean of the distribution closer to the true value. It is also insightful to make such a comparison for the $\mathrm{t\bar{t}}$ background, which is the dominant background in the most signal-sensitive categories as shown in figure 4.3. This comparison between four-body mass and kinematic fit mass for $\mathrm{t\bar{t}}$ events is shown in figure 4.4b. This figure shows that the mass distribution for background events is less affected by the kinematic fit, although due to the invariant mass constraint the minimum of the reconstructed mass distribution is forced to 250 GeV.

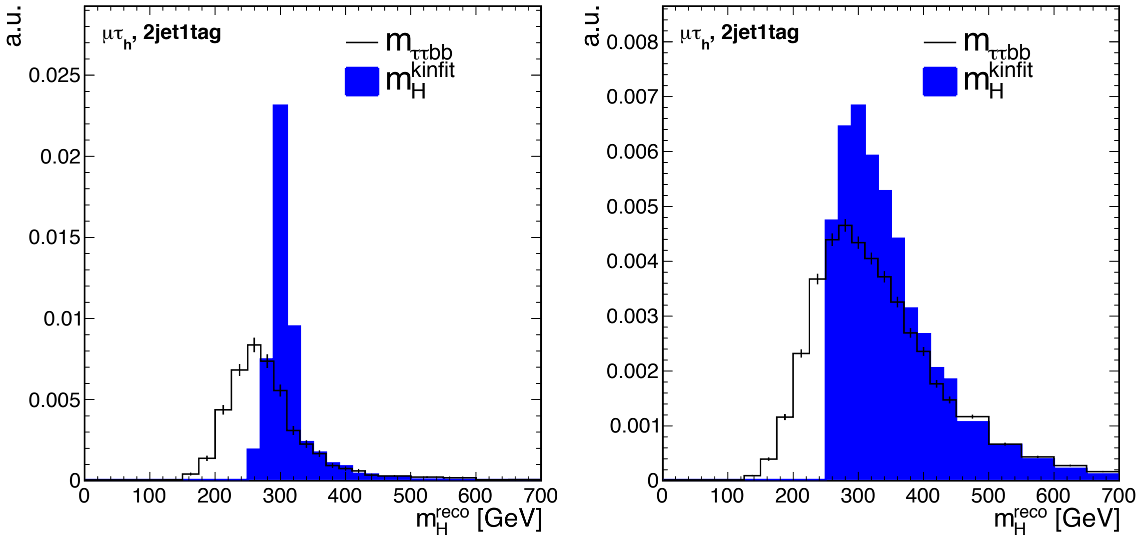

(a) Signal **(b)** $\mathrm{t\bar{t}}$ background

Figure 4.4: Comparison of the reconstructed heavy Higgs boson mass using the kinematic fit (blue) and four-body mass without use of the kinematic fit (black) in (a) signal events with $m_{\mathrm{H}} = 300$ GeV and (b) $\mathrm{t\bar{t}}$ background events in the 2jet-1tag category of the $\mu\tau_{\mathrm{h}}$ channel. The kinematic fit greatly improves the resolution and accuracy of the mean of the mass distribution in signal events.

4.5 Background estimation

To estimate the shape and yield of backgrounds in this analysis, data-driven techniques are used where possible.

4.5.1 $Z/\gamma^* \rightarrow \tau\tau$

The $Z/\gamma^* \rightarrow \tau\tau$ background is estimated using the embedded samples described in section 4.1. The yield of $Z/\gamma^* \rightarrow \tau\tau$ in each category is evaluated in two steps. In the first step the total yield after the initial event selection, before subdividing into categories, is evaluated in the simulated $Z/\gamma^* \rightarrow \tau\tau$ sample. In the second step the yield obtained in the first step is scaled by the efficiency with which such events pass the category selection in the embedded sample. The shape of the $Z/\gamma^* \rightarrow \tau\tau$ background is taken from the embedded sample after applying the full category selection. The contamination from the $t\bar{t}$ background in the embedded sample is evaluated using the dedicated $t\bar{t}$ embedded sample. This contribution is subtracted from the $Z/\gamma^* \rightarrow \tau\tau$ background.

4.5.2 $t\bar{t}$

The $t\bar{t}$ shape and normalisation are both estimated using simulation. These are checked against data in dedicated control regions. One such control region uses the $e\mu$ final state of the di-tau pair. A correction factor is estimated in this control region and applied to the yield estimate from simulation in the signal region. The resulting scale factor is 1.033 ± 0.013 (stat.) $\pm\, 0.088$ (syst.). The statistical and systematic uncertainties are added in quadrature to give a 9% uncertainty, which is applied to the $t\bar{t}$ process.

4.5.3 W+jets

The W+jets background is greatly reduced by requiring m_T to be less than 30 GeV. To estimate the remaining contribution in the signal region a sideband with m_T greater than 70 GeV is used in the 2jet-0tag and 2jet-1tag categories. Contributions from other backgrounds are subtracted from the data in this region, and a high-m_T to low-m_T extrapolation factor is determined from the W+jets simulation. The yield in the signal region is given by the data yield in the high-m_T sideband, with other backgrounds subtracted, multiplied by this extrapolation factor. In the 2jet-2tag category, a slightly different high-m_T sideband of 60–120 GeV is used as above 120 GeV the $t\bar{t}$ background dominates over W+jets. The method of extrapolating this yield estimate into the signal region is otherwise analogous.

The shape of the W+jets distribution is taken from the simulation. To increase the number of events for this estimate, the b-tagging definition in the 2jet-1tag and 2jet-2tag categories is relaxed from the medium to the loose working point for the purpose of shape estimation.

4.5.4 QCD multijet

A fully data-driven method is used to estimate the QCD background. Here, di-tau candidates of the same sign, which otherwise pass the signal region selection, are used. The contributions from other backgrounds in this same-sign (SS) region are subtracted from the number of data events obtained. As the contributions from opposite-sign (OS) and same-sign QCD are not exactly the same an OS/SS ratio is applied to the same-sign region data yield with other backgrounds subtracted. The OS/SS ratio is measured using data with the electron or muon isolation requirements inverted.

For the 2jet-0tag and 2jet-1tag categories the yield is taken directly from the same-sign subtracted data multiplied by the OS/SS ratio. In the 2jet-2tag category the number of available events is too low for this, so another sideband is defined in which the electron or muon isolation requirement is inverted. This sideband is then used to determine an extrapolation factor from events with two jets to events passing the 2jet-2tag category selection. This extrapolation factor is then applied to a QCD estimate as described above, but using the two-jet selection only, to obtain the yield in the 2jet-2tag category.

The shapes in all categories are taken from same-sign data with the electron or muon isolation inverted. For the 2jet-1tag and 2jet-2tag categories, in addition to inverting the light lepton isolation requirements, the category definition is relaxed to obtain the shapes. For the purposes of QCD shape estimation, jets are considered b-tagged if they pass the loose b-tagging working point.

4.5.5 Other backgrounds

The remaining backgrounds of $Z/\gamma^* \rightarrow \ell\ell$, di-boson and single-top events are small. Both shapes and normalisations are estimated using simulated samples. Dedicated $e \rightarrow \tau_h$ fake rate corrections, described in section 4.3, are applied to adjust the $Z/\gamma^* \rightarrow ee$ normalisation. The $\mu \rightarrow \tau_h$ fake rate correction was found to be close to 1 and therefore the $Z/\gamma^* \rightarrow \mu\mu$ normalisation is not subject to such an additional correction factor.

4.6 Systematic uncertainties

Two types of systematic uncertainties are considered: normalisation uncertainties and shape uncertainties. Normalisation uncertainties affect only the yield of a process, while shape uncertainties affect both the yield of a process and the shape of the kinematic fit mass distribution. Section 4.8.1 describes how these uncertainties are taken into account in the final result.

4.6.1 Normalisation uncertainties

Luminosity uncertainty

The uncertainty in the luminosity measurement amounts to 2.6% [128] for data collected during 2012. This uncertainty is applied to all processes in which the normalisation is estimated using simulation.

Identification, isolation and trigger efficiencies

A systematic uncertainty in the efficiency measurements for the leptons is derived by combining the separate uncertainties in these measurements in quadrature. For electrons and muons this leads to a 2% uncertainty. For hadronic taus a 6% uncertainty is measured on the tau identification efficiency, with an additional uncertainty of 3% for the tau legs of the triggers [1]. The identification, isolation and trigger efficiency measurement uncertainties are applied to all processes for which the normalisation is estimated using simulation.

e → τ_h and $\mu \rightarrow \tau_h$ fake rates

The uncertainty in both the e → τ_h fake rate measurement and the $\mu \rightarrow \tau_h$ fake rate measurement is 30% [31]. The central value of the $\mu \rightarrow \tau_h$ fake rate correction is close to 1, which is why it is not applied, but the uncertainty is taken into account.

b-Tag scale factors

The b-tag scale factors are varied within their uncertainties, as described in reference [113], to determine the effect on the yields of each process. Both a b-tagging uncertainty and a light jet mis-tagging uncertainty are obtained by considering the percentage by which these backgrounds change when the scale factors are varied within their uncertainty. The b-tagging efficiency uncertainty amounts to 1–10% for most processes in most categories, except for the 2jet-2tag category where a 70% uncertainty applies to the W+jets background. This uncertainty is large because in this category there is a significant amount of $t\bar{t}$ in the control region used for the W+jets estimate. A 10% change in the $t\bar{t}$ yield causes the W+jets yield to vary by this amount. The light jet mis-tagging rate uncertainty varies between 1–5% for all processes in all channels.

$E_{\mathrm{T}}^{\mathrm{miss}}$ resolution and response

Uncertainties in the $E_{\mathrm{T}}^{\mathrm{miss}}$ resolution and response are estimated by varying the recoil correction parameters within their estimated uncertainties. This leads to a 1–10% uncertainty, depending on the category and process considered.

Background normalisation

- $Z/\gamma^* \rightarrow \tau\tau$: The inclusive normalisation of the embedded samples has a 3.3% uncertainty, which is derived from combining the estimated normalisation uncertainty on the embedded samples themselves and the uncertainty on the $t\bar{t}$ embedded samples. In addition, an uncertainty of 5–6% for extrapolation from the inclusive selection to the category selection is applied.
- $Z/\gamma^* \rightarrow \ell\ell$: As this is a very small background after requiring two jets, the uncertainty on this estimate is derived from the statistical uncertainty on the yield estimate, which varies between 20–90%.
- $t\bar{t}$: The uncertainty in the measured $t\bar{t}$ scale factor 9%.
- Di-boson and single top: The combined uncertainty in the di-boson and single-top cross sections is 15% [129, 130].
- W+jets: As the W+jets yield is estimated from a high-m_{T} sideband in data, the uncertainty in this yield estimate is primarily due to the number of events available in the control region. The uncertainty ranges from 10% in the 2jet-0tag category to 100% in the 2jet-2tag category.
- QCD: The QCD normalisation uncertainty is obtained by adding the statistical uncertainty on the data-subtracted same-sign region in quadrature with the 10% uncertainty on the OS/SS ratio. This yields a 20% uncertainty in the 2jet-0tag category, a 40% uncertainty in the 2jet-1tag category and a 60–100% uncertainty in the 2jet-2tag category.

4.6.2 Shape uncertainties

Tau energy scale

The energy of hadronically decaying taus is varied up and down by a 3% uncertainty [31]. As this directly affects the kinematic fit mass distribution this uncertainty is then applied as a shape uncertainty.

Jet energy scale

The uncertainty in the jet energy corrections are applied by shifting the jet energy up and down by the p_{T}-and η-dependent uncertainty [108]. Again, as this affects the shape of the kinematic fit mass distribution this uncertainty is applied as a shape uncertainty.

4.7 Overview of A $\rightarrow$ Zh $\rightarrow$ $\ell\ell\tau\tau$

In this section a summary of the A $\rightarrow$ Zh $\rightarrow$ $\ell\ell\tau\tau$ analysis [1], which is combined with the analysis described so far for the purpose of model interpretations, is given.

The search for A $\rightarrow$ Zh $\rightarrow$ $\ell\ell\tau\tau$ also uses the full dataset collected by the CMS experiment during the 2012 p-p running period of the LHC. In this search the $\mu\mu$ and ee final states of the Z boson and the eμ, eτ_{h}, $\mu\tau_{\mathrm{h}}$ and $\tau_{\mathrm{h}}\tau_{\mathrm{h}}$ channels of the h $\rightarrow$ $\tau\tau$ decay are considered, leading to a total of eight final states.

First the Z candidate is chosen as a pair of isolated electrons or muons, with opposite charge, and invariant mass between 60–120 GeV. If there is more than one possible pair, the pair with invariant mass closest to the Z boson mass is chosen. The h $\rightarrow$ $\tau\tau$ decay is chosen by selecting an oppositely charged pair of isolated particles in the four channels mentioned above. To ensure no overlap between different final states is possible, events with additional electrons or muons satisfying the p_{T} and η requirements are discarded.

To reject some of the backgrounds from misidentified leptons and ZZ production, a requirement is made on the scalar sum of the visible transverse momenta of the two tau candidates from the h $\rightarrow$ $\tau\tau$ decay. This selection changes by final state and has been chosen to optimise the analysis sensitivity to an A $\rightarrow$ Zh signal with m_{A} = 220–350 GeV. Furthermore, $\mathrm{t\bar{t}}$ events are discarded by rejecting events with at least one b-tagged jet.

Remaining backgrounds from ZZ, tri-boson and $\mathrm{t\bar{t}}$ +Z production are estimated using simulation. Backgrounds from Z+jets and WZ+jets events, with at least one misidentified lepton, are estimated from control regions in data.

For signal extraction the mass of the A boson, m_{A}, is used. This mass is reconstructed by combining the four-vector of the Z boson candidate with the four-vector of the h candidate as obtained by using the `SVFit` algorithm. The expected and observed upper limits at the 95% CL, for all $\ell\ell\tau\tau$ final states combined, is shown in figure 4.5.

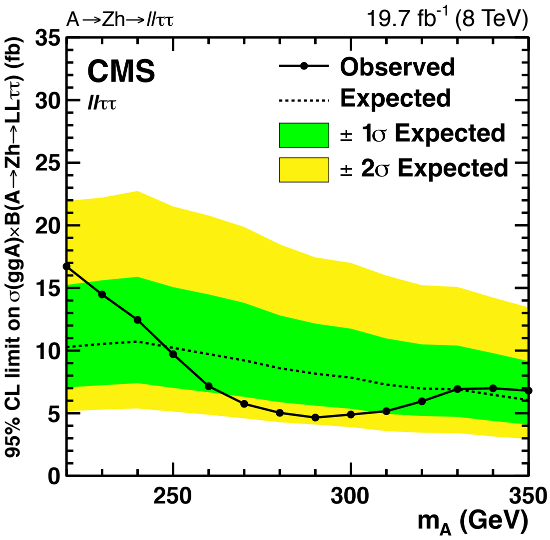

Figure 4.5: The expected (dashed) and observed (solid) upper limits at the 95% CL on the $\sigma \times \mathcal{B}$ for the A → Zh → $\ell\ell\tau\tau$ process. The green and yellow bands indicate the $\pm 1\sigma$ and $\pm 2\sigma$ probability intervals on the expected limit [1].

More detail on this analysis can be found in reference [1]. Systematic uncertainties are also applied in the A → Zh → $\ell\ell\tau\tau$ analysis. For the purpose of combining the results with the H → hh → bb$\tau\tau$ search, some of these are correlated between the two analyses. This applies to the luminosity uncertainty and the uncertainties in the b-tagging efficiency and the light jet mis-tagging rate.

4.8 Results

4.8.1 Signal extraction

The kinematic fit mass $m_{\mathrm{H}}^{\mathrm{kinfit}}$ is used as the discriminating variable in the H → hh analysis. For each channel and category the compatibility of the $m_{\mathrm{H}}^{\mathrm{kinfit}}$ distribution of the observed data with the expected background distribution can be assessed. All bins of the $m_{\mathrm{H}}^{\mathrm{kinfit}}$ distribution are used to perform a shape analysis. The statistical methods used are recommended by the LHC Higgs Combination Group [131] and are used for all Higgs analyses in ATLAS and CMS.

The likelihood function for data, whether observed or pseudo-data, is constructed as

$$\mathcal{L}(\mathrm{data}|\mu,\theta) = \Pi_i \mathrm{Poisson}(n_i|(\mu \cdot s_i(\theta) + b_i(\theta))) \cdot p(\tilde{\theta}|\theta), \tag{4.12}$$

where $\mathrm{Poisson}(n_i|(\mu \cdot s_i(\theta) + b_i(\theta)))$ is given by

$$\mathrm{Poisson}(n_i|(\mu \cdot s_i(\theta) + b_i(\theta))) = \frac{(\mu \cdot s_i(\theta) + b_i(\theta))^{n_i})}{n_i!} e^{-(\mu \cdot s_i(\theta) + b_i(\theta))}, \tag{4.13}$$

with n_i the number of data events in bin i.

The first factor in equation 4.12 runs over all bins of the $m_{\mathrm{H}}^{\mathrm{kinfit}}$ distribution in all channels and categories. The parameter s represents the number of expected signal events in each bin, and b the number of expected background events. These are functions of θ, the full set of nuisance parameters. The signal strength modifier μ can represent different quantities depending on the normalisation of the signal expectation. In the case of the H → hh → bb$\tau\tau$ analysis the signal is normalised to 1 pb, so the signal strength modifier represents the $\sigma \times \mathcal{B}$ of a possible signal.

The second factor in equation 4.12, $p(\tilde{\theta}|\theta)$, represents the full set of probability density functions of the uncertainties on the nominal values of the nuisance parameters $\tilde{\theta}$. Each nuisance parameter represents a systematic uncertainty as discussed in section 4.6. The functional form of the probability density function depends on the type of systematic uncertainty. Normalisation uncertainties are applied with log-normal constraints, which ensures that the process yields can never become negative, and therefore unphysical, in the fit. Shape uncertainties are accounted for using a vertical template morphing technique [132]. For each nuisance parameter that affects the shape of the fitted distribution, two additional templates corresponding to the quantity varied by $\pm 1\sigma$ are generated. A nuisance parameter is added to the likelihood model with a gaussian constraint to smoothly interpolate between the nominal and $\pm 1\sigma$ templates. Limitations in the number of events used to construct the shape templates are accounted for by the Barlow-Beeston method [133], in which each of the bins of each shape template is allowed to vary within its statistical uncertainty, independent of the other bins.

To compare the data with the background-only and signal-plus-background hypotheses, a test statistic q_μ can be defined. This is a single number that is used to distinguish between the two hypotheses. The test statistic used for LHC Higgs analyses, known as the profile likelihood, is given by

$$q_\mu = -2\ln \frac{\mathcal{L}(\mathrm{data}|\mu, \hat{\theta}_\mu)}{\mathcal{L}(\mathrm{data}|\hat{\mu}, \hat{\theta})}, \tag{4.14}$$

where $0 \leq \hat{\mu} \leq \mu$ is required for setting upper limits.

In this equation μ is the signal strength modifier being tested, $\hat{\theta}_\mu$ denotes the values of the nuisance parameters which maximise the likelihood for that particular μ, while $\hat{\mu}$ and $\hat{\theta}$ are the values of the signal strength modifier and the nuisance parameters which give the global maximum of the likelihood. The requirements on μ ensure that the signal strength is non-negative and that a one-sided confidence interval is constructed so as not to allow the observation of a signal with strength $\hat{\mu} > \mu$ to cause rejection of the signal hypothesis.

The probabilities of finding a value q_μ at least as large as the observed value q_μ^{obs}, assuming the signal-plus-background hypothesis and assuming the background-only hypothesis, are given by

$$p_\mu = P(q_\mu \geq q_\mu^{\text{obs}}|\text{s+b}) = \int_{q_\mu^{\text{obs}}}^{\infty} f(q_\mu|\mu, \hat{\theta}_\mu^{\text{obs}}) dq_\mu, \tag{4.15}$$

and

$$1 - p_b = P(q_\mu \geq q_\mu^{\text{obs}}|\text{b}) = \int_{q_\mu^{\text{obs}}}^{\infty} f(q_\mu|0, \hat{\theta}_0^{\text{obs}}) dq_\mu, \tag{4.16}$$

where $f(q_\mu|\mu, \hat{\theta}_\mu)$ and $f(q_\mu|0, \hat{\theta}_0)$ are the probability density functions of q_μ under the signal-plus-background and background-only hypotheses.

Using this, CL_s is defined as

$$\text{CL}_s(\mu) = \frac{\text{CL}_{s+b}}{\text{CL}_b} = \frac{p_\mu}{1 - p_b}. \tag{4.17}$$

The value of μ for which CL_s equals α is referred to as the upper limit on μ at confidence level (CL) $1 - \alpha$. Upper limits at the LHC are generally quoted at the 95% CL. The use of CL_s to set exclusion limits is referred to as the modified frequentist approach [134].

The distributions $f(q_\mu|\mu, \hat{\theta}_\mu)$ and $f(q_\mu|0, \hat{\theta}_0)$ are determined using toy MC datasets. These datasets are generated from the signal-plus-background or background-only expectations respectively. To generate each toy dataset the nuisance parameters are fixed to their best-fit values as found in the fit to the observed data. The number of events in each bin in the toy dataset is set using poisson fluctuations around the expectation in that bin, and the effect of systematic uncertainties is taken into account by sampling a set of pseudo measurements $\tilde{\theta}'$ for each toy, based on the probability density function $p(\tilde{\theta}|\theta)$. The probability density function of q_μ under the relevant hypothesis (signal-plus-background or background-only) can by found be accumulating a large number of toy datasets and evaluating q_μ for each of them.

This method of generating toy MC datasets can be computationally intensive. In the limit of a large number of events $f(q_\mu)$ follows a known formula [135]. This formula, known as the asymptotic approximation, allows for the calculation of the observed limit as well as the median and $\pm 1\sigma$ and $\pm 2\sigma$ expected limits using the properties of the Asimov dataset: a dataset in which the observation in each bin exactly matches the predictions of the model. This method is used for the analysis described in this chapter, removing the need to generate toy datasets.

4.8.2 Model-independent results

The $m_{\mathrm{H}}^{\mathrm{kinfit}}$ distributions in all categories of the $\mu\tau_{\mathrm{h}}$ and eτ_{h} channels, after the fit to the observed data has been performed, are shown in figures 4.6 and 4.7 respectively. The numbers of observed events, compared with the background expectation, are given in appendix A.

None of these distributions show hints of an excess of observed events above the background expectation. The model-independent expected and observed upper limits at the 95% CL on $\sigma\times\mathcal{B}$ are shown in figure 4.8a, with figure 4.8b showing the expected limit per channel. These figures include the contribution from the $\tau_{\mathrm{h}}\tau_{\mathrm{h}}$ channel not described in this chapter. The expected upper limit on the H $\rightarrow$ hh $\rightarrow$ bb$\tau\tau$ process is around 0.3 pb, the observed ranges from 0.2 pb at low mass to 0.4 pb at high mass. The $\mu\tau_{\mathrm{h}}$ channel is the most sensitive at masses lower than 320 GeV, with the $\tau_{\mathrm{h}}\tau_{\mathrm{h}}$ channel being the most sensitive beyond this mass point. The eτ_{h} channel is always less sensitive than the $\mu\tau_{\mathrm{h}}$ channel, but at low mass it is still more sensitive than the $\tau_{\mathrm{h}}\tau_{\mathrm{h}}$ channel.

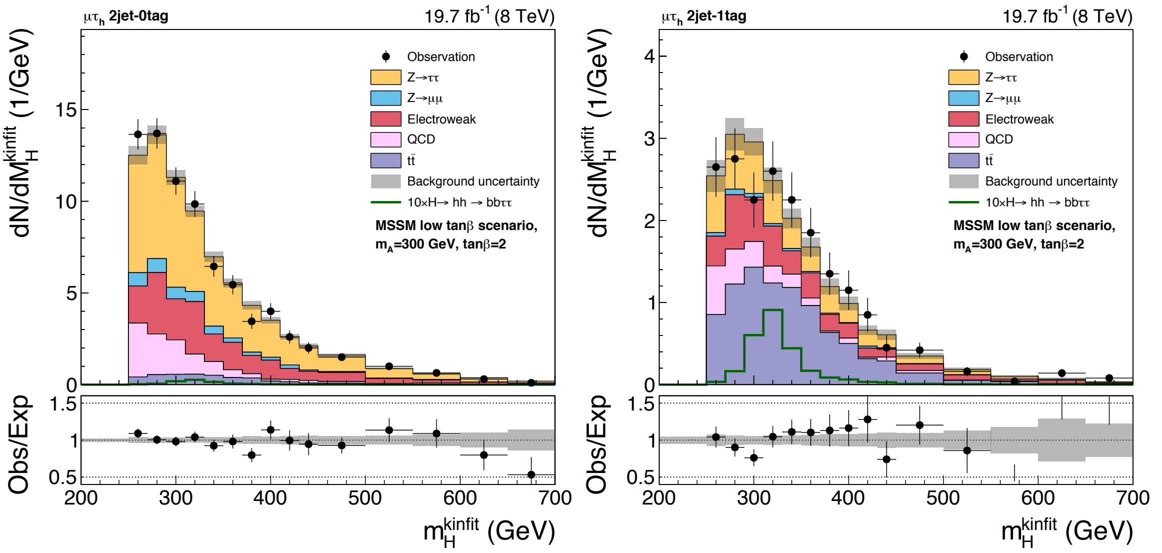

(a) 2jet-0tag **(b)** 2jet-1tag

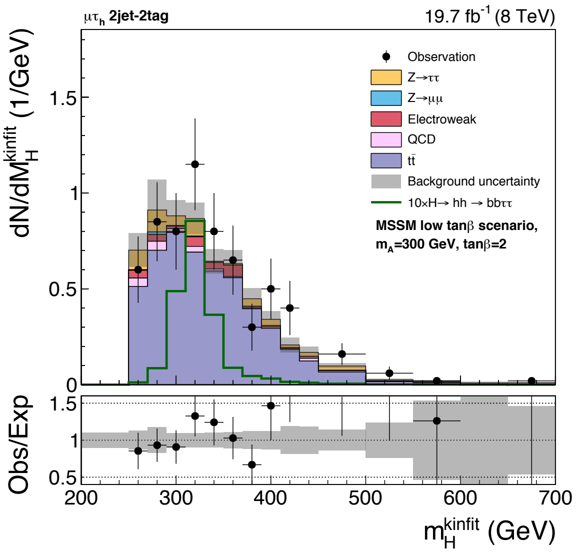

(c) 2jet-2tag

Figure 4.6: Distributions of $m_{\mathrm{H}}^{\mathrm{kinfit}}$ in the (a) 2jet-0tag, (b) 2jet-1tag and (c) 2jet-2tag categories of the $\mu\tau_{\mathrm{h}}$ channel. The H → hh → bb$\tau\tau$ signal for $m_{\mathrm{A}} = 300\,\mathrm{GeV}$ at $\tan\beta = 2$ in the low-$\tan\beta$ MSSM scenario, multiplied by 10, is also overlaid. Note that at low $\tan\beta$ $m_{\mathrm{A}} \neq m_{\mathrm{H}}$, at the point in the MSSM scenario that is considered m_{H} is around around 316 GeV.

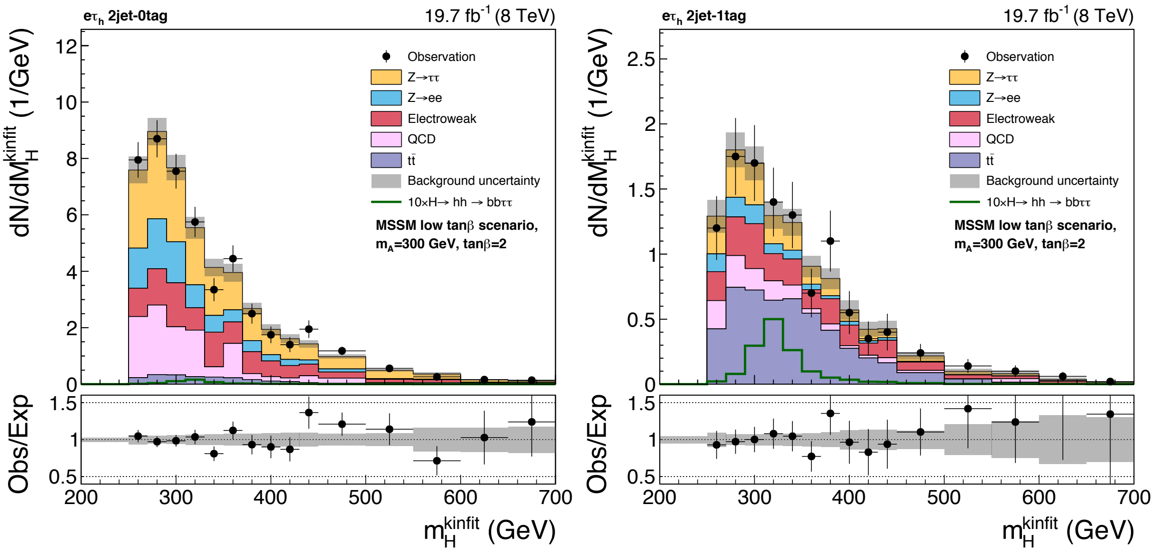

(a) 2jet-0tag **(b)** 2jet-1tag

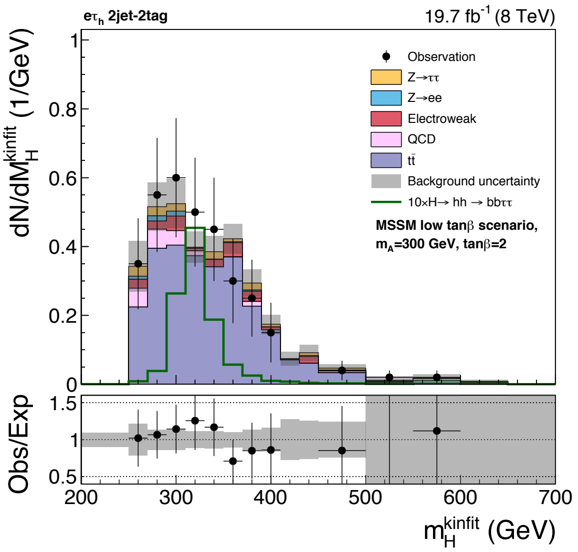

(c) 2jet-2tag

Figure 4.7: Distributions of $m_{\mathrm{H}}^{\mathrm{kinfit}}$ in the (a) 2jet-0tag, (b) 2jet-1tag and (c) 2jet-2tag categories of the eτ_{h} channel. The H → hh → bb$\tau\tau$ signal for $m_{\mathrm{A}} = 300\,\mathrm{GeV}$ at $\tan\beta = 2$ in the low-$\tan\beta$ MSSM scenario, multiplied by 10, is also overlaid. Note that at this low value of $\tan\beta$ $m_{\mathrm{A}} \neq m_{\mathrm{H}}$, in this case m_{H} is around 316 GeV.

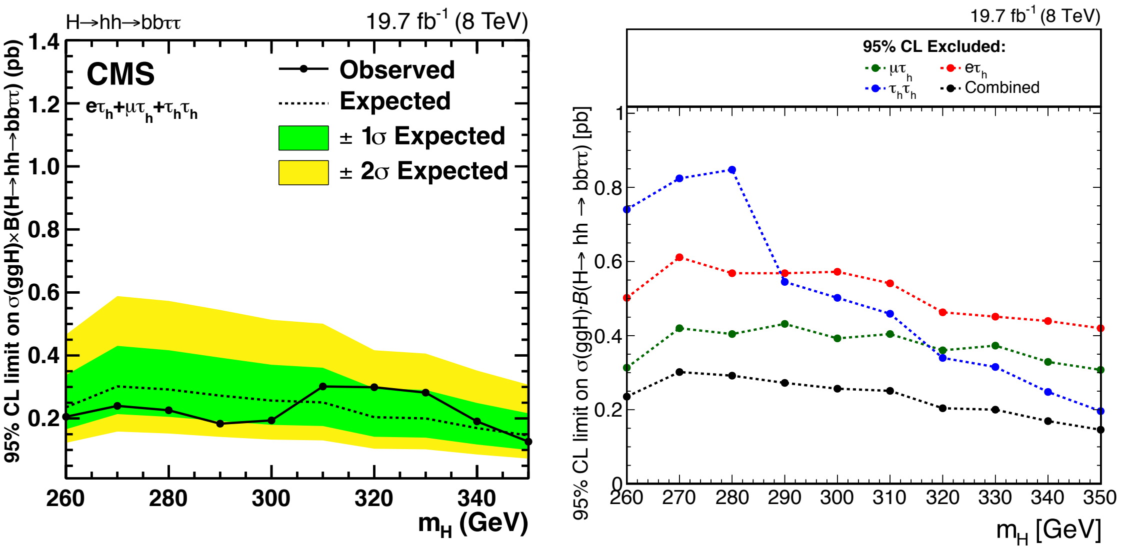

(a) (b)

Figure 4.8: Expected and observed upper limits at the 95% CL on $\sigma\times\mathcal{B}$ for the $\mathrm{H} \rightarrow \mathrm{hh} \rightarrow \mathrm{bb}\tau\tau$ process. In (a) the three final states of $\mathrm{e}\tau_\mathrm{h}$, $\mu\tau_\mathrm{h}$ and $\tau_\mathrm{h}\tau_\mathrm{h}$ are combined. The green and yellow bands indicate the $\pm1\sigma$ and $\pm2\sigma$ probability intervals on the expected limit [1]. (b) Shows the expected upper limits at the 95% CL on $\sigma\times\mathcal{B}$ for the $\mathrm{H} \rightarrow \mathrm{hh} \rightarrow \mathrm{bb}\tau\tau$ process, separated by channel. The blue line shows the limit for the $\tau_\mathrm{h}\tau_\mathrm{h}$ channel, the green line for the $\mu\tau_\mathrm{h}$ channel, the red line for the $\mathrm{e}\tau_\mathrm{h}$ channel and the black line the limit for all three channels combined. Up to around $m_\mathrm{H} = 320\,\mathrm{GeV}$ the $\mu\tau_\mathrm{h}$ channel is the most sensitive, with the $\tau_\mathrm{h}\tau_\mathrm{h}$ channel being more sensitive at higher masses.

4.8.3 Model-dependent results

The results of the analysis are interpreted in two scenarios, a type-II 2HDM and the low-tan β MSSM scenario, both discussed in chapter 1.

Interpretation in a type-II 2HDM

As discussed in section 1.3.2, a 2HDM has more free parameters than a particular MSSM benchmark scenario. To leave just two free parameters, it is enough to fix the masses of the five Higgs bosons and take the quartic couplings to be zero. For the interpretation shown here the assumption that $m_{\mathrm{A}} = m_{\mathrm{H}} = m_{\mathrm{H}^+} = 300\,\mathrm{GeV}$ is made. The couplings of the Higgs bosons to quarks and leptons, and of the heavy Higgs bosons to other particles, are defined by α and β, as in table 4.1.

Table 4.1: Couplings in the type-II 2HDM.

Decay	**Coupling**
h $\rightarrow$ up-type quarks	SM coupling $\times \frac{\cos\alpha}{\sin\beta}$
h $\rightarrow$ down-type quarks, leptons	SM coupling $\times -\frac{\sin\alpha}{\cos\beta}$
H $\rightarrow$ hh	$\sim \cos(\beta-\alpha)\times$ terms containing masses, mixing angles, quartic couplings
A $\rightarrow$ Zh	$\sim \cos(\beta-\alpha)$

The interpretations are made in the $\cos(\beta-\alpha)$-tan β plane. Figure 4.9 shows the observed and expected exclusion at the 95% CL for the H $\rightarrow$ hh and A $\rightarrow$ Zh analyses, overlaid on the $\sigma\times\mathcal{B}$. The exclusion contours have some interesting features, most of which can be explained by the couplings in table 4.1. When $\cos(\beta-\alpha)$=0, in the alignment limit, the couplings of all particles are exactly SM-like. This is reflected in the H $\rightarrow$ hh and A $\rightarrow$ Zh branching ratios, which both vanish as $\cos(\beta-\alpha)$ approaches zero. This leads to the corridor of non-exclusion down the centre of the graphs in figure 4.9. Additionally, as the coupling of the h to pairs of b-quarks or tau leptons is proportional to $\frac{\sin\alpha}{\cos\beta}$, the branching ratios of H $\rightarrow$ hh $\rightarrow$ bb$\tau\tau$ and A $\rightarrow$ Zh $\rightarrow$ $\ell\ell\tau\tau$ vanish when $\alpha = 0$, leading to the corridor of non-exclusion at $\cos(\beta-\alpha) > 0$ and low tan β in the A $\rightarrow$ Zh figure. A similar corridor is starting to become visible in the $\sigma\times\mathcal{B}$ structure of the H $\rightarrow$ hh interpretation, but the analysis is not yet sensitive enough to actually observe it.

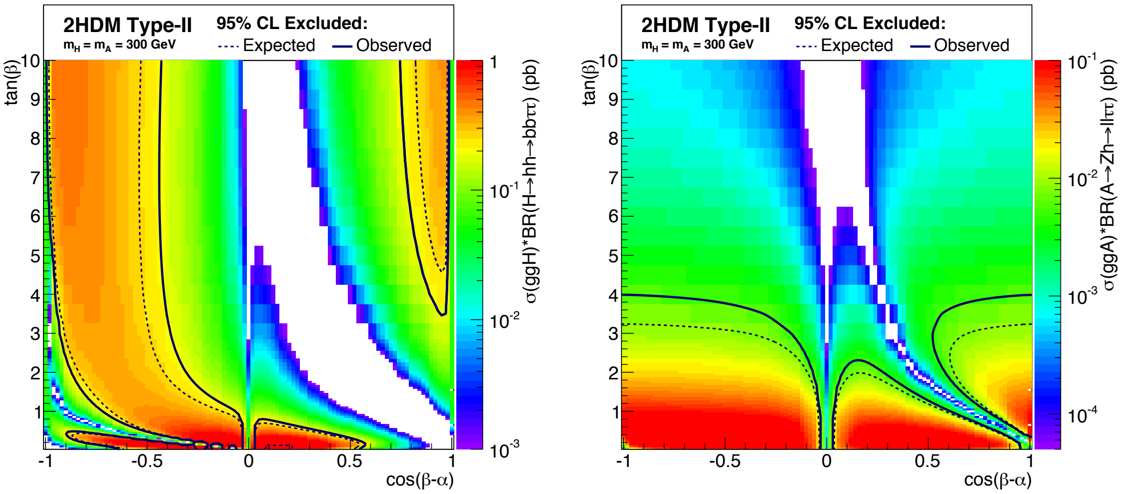

(a) H → hh → bb$\tau\tau$ **(b)** A → Zh → $\ell\ell\tau\tau$

Figure 4.9: Search for (a) H → hh → bb$\tau\tau$ and (b) A → Zh → $\ell\ell\tau\tau$ interpreted in a type-II 2HDM, assuming $m_{\mathrm{A}} = m_{\mathrm{H}} = m_{\mathrm{H}^+} = 300\,\mathrm{GeV}$. The expected (dashed line) and observed (solid line) exclusion contours at the 95% CL are overlaid on the $\sigma\times\mathcal{B}$ of the searched-for process. Regions of the $\cos(\beta-\alpha)$-$\tan\beta$ plane where the $\sigma\times\mathcal{B}$ is larger than the model-independent upper limit set for $m_{\mathrm{H}} = 300\,\mathrm{GeV}$ (see figures 4.5 and 4.8) are excluded.

A combined interpretation of both analyses in this model is presented in figure 4.11a. Some of the features discussed earlier in this section are also visible in this combined interpretation.

Interpretation in the low-tan β MSSM scenario

The low-tan β MSSM scenario, as discussed in section 1.4.2, is an MSSM scenario that has been adapted to allow $m_{\mathrm{h}} = 125 \pm 3\,\mathrm{GeV}$ for $\tan\beta$ values as low as 1.

Figure 4.10a shows the $\sigma\times\mathcal{B}$ of the H → hh → bb$\tau\tau$ process in the low-tan β MSSM scenario. Comparing these values to the expected and observed upper limits in figure 4.8 we can see that the $\sigma\times\mathcal{B}$ in this model is, with the exception of a few very small areas, lower than the upper limits set by this analysis. This analysis on its own is, therefore, not sensitive enough to exclude any of the m_{A}-$\tan\beta$ region in this model. Note that at low $\tan\beta$, $m_{\mathrm{A}} \neq m_{\mathrm{H}}$, and therefore m_{H} is not in the studied range of 260–350 GeV everywhere in the m_{A}-$\tan\beta$ plane shown here.

The A → Zh → $\ell\ell\tau\tau$ analysis on the other hand can exclude parts of the m_{A}-tan β region in this model. The expected and observed exclusion contours at the 95% CL are overlaid on the $\sigma\times\mathcal{B}$ for this process in the low-tan β MSSM scenario in figure 4.10b. The sharp drop in $\sigma\times\mathcal{B}$, and therefore exclusion, near $m_{\mathrm{A}} = 350\,\mathrm{GeV}$ arises from the fact that near this mass the decay A → t$\bar{\mathrm{t}}$ becomes kinematically allowed, resulting in a reduction of the A → Zh branching ratio.

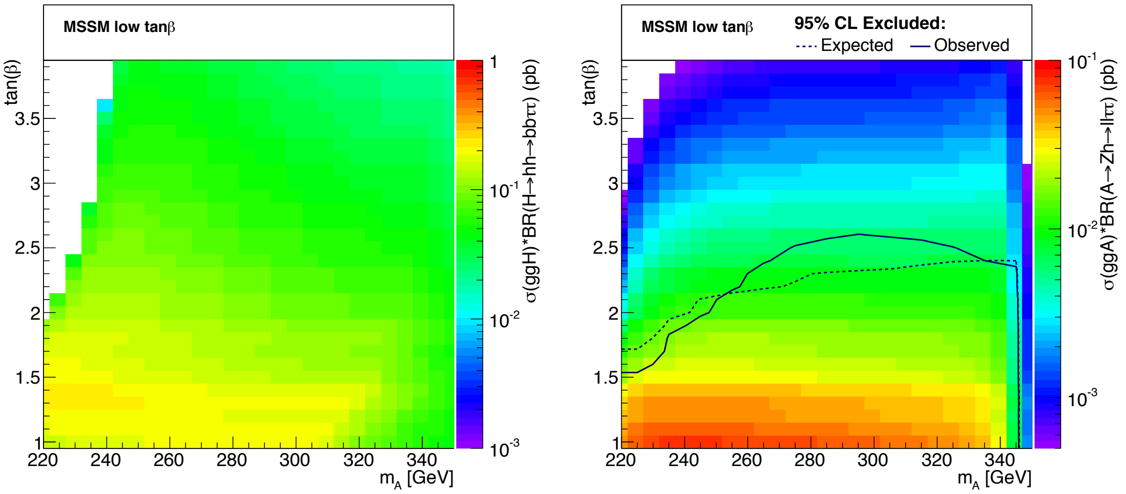

(a) H → hh → bb$\tau\tau$ **(b)** A → Zh → $\ell\ell\tau\tau$

Figure 4.10: The $\sigma\times\mathcal{B}$ of (a) the H → hh → bb$\tau\tau$ process and (b) the A → Zh → $\ell\ell\tau\tau$ process in the low-tan β MSSM scenario. In (b) the expected and observed 95% CL exclusion limits for the A → Zh → $\ell\ell\tau\tau$ analysis in the low-tan β MSSM scenario have been overlaid on the $\sigma\times\mathcal{B}$. Areas where the $\sigma\times\mathcal{B}$ is larger than the upper limits in figure 4.5 are excluded. The exclusion rapidly drops off at $m_{\mathrm{A}} = 350\,\mathrm{GeV}$ due to the turn-on of the A → t$\bar{\mathrm{t}}$ process. No expected and observed exclusion contours have been overlaid on (a) as the $\sigma\times\mathcal{B}$ is smaller than the upper limits set in figure 4.8.

The combined interpretation of both analyses in this model is presented in figure 4.11b. By combining the two analyses a slightly larger amount of the m_{A}-tan β plane can be excluded than using the A → Zh → $\ell\ell\tau\tau$ analysis alone. The features described for figure 4.10b are also visible in this figure. In a small region of phase space, at low m_{A} and low tan β, this scenario predicts a light Higgs boson mass that is not compatible with $125 \pm 3\,\mathrm{GeV}$. This region is therefore excluded, as indicated by the red band.

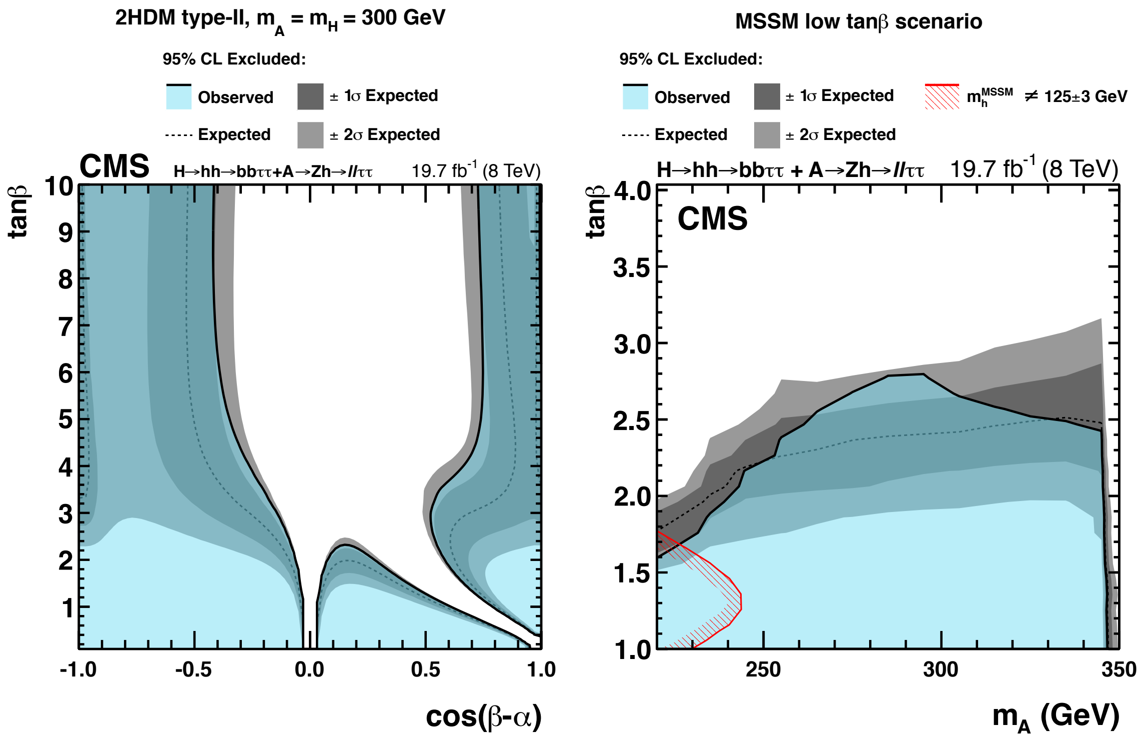

(a) type-II 2HDM **(b)** low-tan β MSSM scenario

Figure 4.11: Combination of the A → Zh → $\ell\ell\tau\tau$ and H → hh → bb$\tau\tau$ searches interpreted in (a) a type-II 2HDM assuming $m_{\mathrm{H}} = m_{\mathrm{A}} = m_{\mathrm{H}^+} = 300\,\mathrm{GeV}$ and (b) in the low-tan β MSSM scenario. The blue shaded area bounded by the solid black line indicates the observed excluded region at 95% CL. The dashed black line indicates the expected exclusion, with the grey bands showing the $\pm 1\sigma$ and $\pm 2\sigma$ probability intervals on the expected exclusion [1]. The area bounded by the red line is the region of phase space where $m_{\mathrm{h}} \neq 125 \pm 3\,\mathrm{GeV}$ and is therefore excluded.

Chapter 5

Search for MSSM A/H $\rightarrow \tau\tau$

In this chapter the search for neutral Higgs bosons H or A decaying to a pair of tau leptons is discussed. The results presented here correspond to those from an analysis performed on a dataset collected during the first half of the 2016 p-p running period of the LHC [2]. The $e\tau_{h}$, $\mu\tau_{h}$, $\tau_{h}\tau_{h}$ and $e\mu$ final states of the di-tau pair were studied. The results of this search are model-independent upper limits on $\sigma\times\mathcal{B}$ of H or A production in the gluon fusion ($gg\phi$) and b-associated ($bb\phi$) production modes and decay into $\tau\tau$. In addition to the upper limits on $\sigma\times\mathcal{B}$ of these two processes, the results are interpreted in MSSM benchmark scenarios. A very similar analysis, not described in detail here, was performed on a dataset corresponding to $2.3\,\mathrm{fb}^{-1}$ collected at $\sqrt{s} = 13\,\mathrm{TeV}$ during the 2015 LHC p-p running period. More information can be found in reference [3].

For the analysis described in this chapter, as well as the 2015 analysis, I was responsible for all stages of the analysis. This included optimisation of object selection and categorisation, as well as studies of background methods for the $\mu\tau_{h}$, $e\tau_{h}$ and $\tau_{h}\tau_{h}$ channels, evaluation of systematic uncertainties in all four channels, and production of the statistical results, including model interpretations.

5.1 Datasets and Monte Carlo samples

The dataset used for this analysis corresponds to an integrated luminosity of $12.9\,\mathrm{fb}^{-1}$ collected at a centre-of-mass energy of $13\,\mathrm{TeV}$ during the first half of the 2016 p-p running period of the LHC.

Signal and background events are generated using various MC event generators. All of these simulated samples are centrally produced for use by all CMS analyses. Signal samples for the gg $\rightarrow \phi$ and gg $\rightarrow$ bbϕ production processes of the H or A bosons are generated using `PYTHIA 8.1` [136]. These samples are produced for a range of masses between 90 GeV and 3.2 TeV. This range is slightly wider than the range in which MSSM Higgs sector benchmark computations are available, 90 GeV–2 TeV, and improves on the mass range of 90 GeV to 1 TeV that was studied during Run 1 in the context of BSM Higgs searches. SM Higgs boson signal samples are used for the interpretation of the analysis results in MSSM benchmark scenarios. These samples are generated using `POWHEG` [121, 122, 137].

Single-top and $\mathrm{t\bar{t}}$ background samples are generated using `POWHEG`, while for the generation of di-boson background samples `MadGraph5_aMC@NLO` [138] is used. W+jets and $\mathrm{Z}/\gamma^* \rightarrow ll$ backgrounds are generated with the `MadGraph 5` [120] matrix element generator. Samples containing both a mixture of jet multiplicities (‘inclusive’ samples) and samples with one, two, three or four jets (‘exclusive’ samples) are generated. These exclusive samples increase the available number of background events with higher jet multiplicities. The ‘inclusive’ and ‘exclusive’ samples are reweighted before they are combined so that the fraction of events with each jet multiplicity is the same as in the inclusive sample only. The W+γ background samples, only included in the eμ channel, are generated either with `MadGraph 5` or with `MadGraph5_aMC@NLO`.

Parton showering and hadronisation are modelled using `PYTHIA 8.1` for all samples, and minimum-bias events generated with `PYTHIA 8.1` are added to all MC samples to model additional interactions. A reweighting is then applied to the MC samples to make the pileup distribution match the pileup distribution observed in data.

5.2 Event selection and categorisation

In this section an overview of the event selection, and how it was optimised, is given. More detailed information on how the objects used are reconstructed, and a more in-depth description of the identification criteria, is given in chapter 3.

The basis of the event selection is to identify $\mu\tau_\mathrm{h}$, $\mathrm{e}\tau_\mathrm{h}$, $\tau_\mathrm{h}\tau_\mathrm{h}$ and eμ pairs. Events are selected first by using a trigger, followed by additional selection criteria. For the $\mathrm{e}\tau_\mathrm{h}$ and $\mu\tau_\mathrm{h}$ channels, events are selected by only triggering on the electron or muon. While the lepton + hadronic tau cross-triggers that are also available allow for a 3 GeV (6 GeV) lower p_T threshold on the muon (electron), the benefit of using such a trigger is small:

most of the signals at high mass, the region of interest in this analysis, have higher p_{T} electrons and muons. This is illustrated in figure 5.1a, which shows the p_{T} of muons in the $\mu\tau_{\mathrm{h}}$ channel. The signal is overlaid, with a normalisation of 4000 times its $\sigma\times\mathcal{B}$ at $m_{\mathrm{A}} = 1\,\mathrm{TeV}$ and $\tan\beta = 50$ in the $m_{\mathrm{h}}^{\mathrm{mod+}}$ scenario. In the eμ channel two dedicated electron-muon cross-triggers are used. These have significantly lower p_{T} cuts on the two leptons than the single lepton triggers. For the $\tau_{\mathrm{h}}\tau_{\mathrm{h}}$ channel a di-tau trigger is used.

Because the triggers involving electrons or muons reach their maximum efficiency as a function of p_{T} quickly, the offline p_{T} cut on the electrons and muons is 1 GeV above the p_{T} threshold of the trigger. The hadronic tau efficiency turns on much more slowly, and therefore the offline p_{T} cut on the hadronic taus in the $\tau_{\mathrm{h}}\tau_{\mathrm{h}}$ channel is 5 GeV above the trigger p_{T} threshold. In addition, a requirement is made on the η of the electrons, muons and hadronic taus. This selection is driven by the η range covered by the tracker and so the range that is used for the reconstruction of the particles. For some of the channels the trigger that is used is restricted in η. If that is the case the cut is chosen to be the same as the trigger restrictions. As an illustration figure 5.1b shows the η distribution for electrons in the eτ_{h} channel, again with the signal overlaid. The signal peaks in the central η region.

Other selections include cuts on the transverse and longitudinal impact parameters d_{xy} and d_z, which ensure that the particle is likely to have originated from the primary vertex. This reduces the number of selected particles which come from pileup interactions. Additional identification and isolation criteria are also applied; these will be discussed in sections 5.2.1–5.2.5. The optimisation of some of the selections will also be discussed there. Note that the optimisations are all based on the dataset collected during the 2015 p-p running period of the LHC, which corresponds to an integrated luminosity of $2.3\,\mathrm{fb}^{-1}$.

5.2.1 Pair selection and vetoes

After applying trigger requirements, identification criteria and kinematic cuts, more than one possible candidate pair can exist. If this is the case the pair with the two most isolated candidates is chosen, as isolated candidates are less likely to be jets mis-reconstructed as leptons or hadronic taus.

To prevent overlap with other channels, events are rejected if there are muons or electrons, other than those in the selected pair, with $p_{\mathrm{T}} > 10\,\mathrm{GeV}$ and passing loose ID and isolation

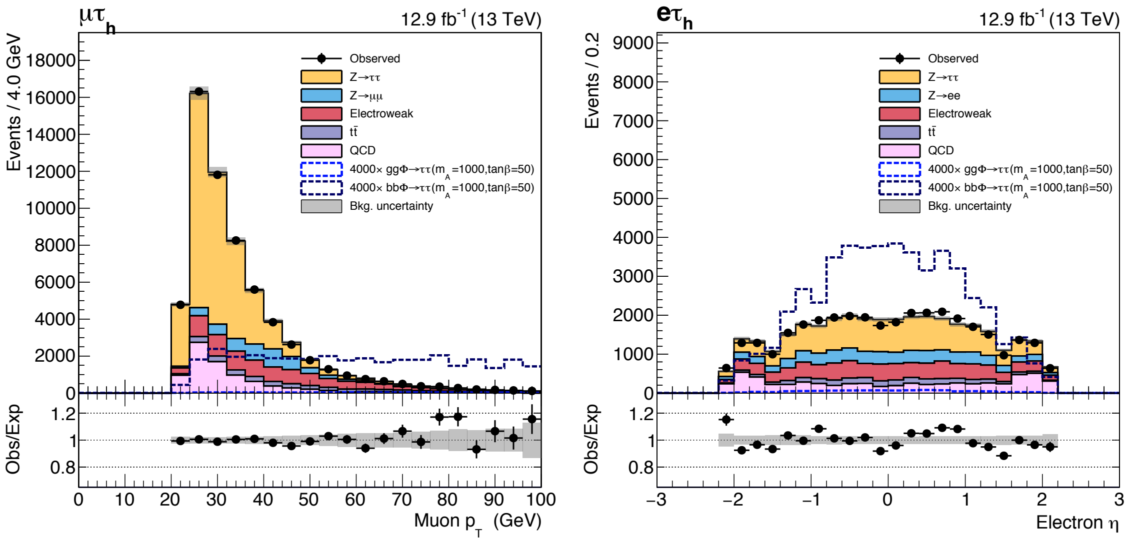

(a) Muon p_T **(b)** Electron η

Figure 5.1: (a) The p_T of the muon in the $\mu\tau_\mathrm{h}$ channel and (b) η of the electron in the $\mathrm{e}\tau_\mathrm{h}$ channel. The gluon fusion (dashed blue line) and b-associated (dashed purple line) signals are overlaid. The signals are normalised to 4000 times their $\sigma \times \mathcal{B}$ at $m_\mathrm{A} = 1\,\mathrm{TeV}$ and $\tan\beta = 50$ in the $m_\mathrm{h}^{\mathrm{mod}+}$ scenario.

requirements. This also reduces backgrounds from di-boson events. The application of these vetoes means that the selection of the pair with the two most isolated candidates is only important where hadronic taus are concerned, for if there were additional electrons (muons) the event would not pass the electron (muon) veto. In addition to these extra electron and muon vetoes, $\mathrm{Z}/\gamma^* \rightarrow \mathrm{ee}$ events are reduced in the $\mathrm{e}\tau_\mathrm{h}$ channel by rejecting events where an opposite-sign pair of electrons of $p_\mathrm{T} > 15\,\mathrm{GeV}$ and passing very loose ID and isolation requirements can be formed. In the $\mu\tau_\mathrm{h}$ channel the contribution from $\mathrm{Z}/\gamma^* \rightarrow \mu\mu$ events is reduced in a similar fashion.

5.2.2 Event selection in the $\mu\tau_\mathrm{h}$ channel

The trigger only requires a muon at L1, to which loose identification and isolation criteria are applied at the level of the HLT.

The offline event selection requires an oppositely charged muon and hadronically decaying tau, which are separated by $\Delta R > 0.5$. The muon is required to have $p_\mathrm{T} > 23\,\mathrm{GeV}$, and $|\eta| < 2.1$. Additional "medium" identification requirements are placed on the muon, and the impact parameters must satisfy $d_{xy} < 0.045\,\mathrm{cm}$ and $d_z < 0.2\,\mathrm{cm}$. The muon is also required to be isolated, with $I^{\mu}_{\mathrm{rel}} < 0.15$, where the isolation variable is calculated using a cone size of $\Delta R = 0.4$.

The hadronic tau needs to have $p_{\mathrm{T}} > 30\,\mathrm{GeV}$ and $|\eta| < 2.3$. It is required to be reconstructed by the HPS algorithm and to pass the medium working point of the MVA isolation discriminator. The impact parameter d_z is required to be less than 0.2 cm. Finally the hadronic tau is required to satisfy the very loose working point of the anti-electron discriminator and the tight working point of the anti-muon discriminator.

The selection on the relative isolation of the muon is chosen after comparing the performance of several isolation variables, using different relative isolation selections. This was based on a simple $\mu\tau_{\mathrm{h}}$ channel event selection as described above, with only the isolation being varied. The selection was optimised based on two figures of merit, both of which consider $\mathrm{Z}/\gamma^* \rightarrow \tau\tau$, instead of the Higgs processes, as the signal. The first figure of merit used is the number of signal events divided by the square root of the number of background events, $S/\sqrt{B}$, after the selection. The aim is to identify the isolation selection that maximises $S/\sqrt{B}$. The second figure of merit is the uncertainty interval on the best-fit value for a maximum-likelihood fit to the $\mathrm{Z}/\gamma^* \rightarrow \tau\tau$ signal strength, which should be minimised by the choice of isolation selection.

The isolation variables studied include the $\Delta\beta$ corrected isolation variable analogous to the one given for electrons in equation 3.1 with isolation cone sizes of 0.3 and 0.4 in ΔR. In addition to this a very similar variable, which does not just consider charged PF hadrons but also electrons and muons in the isolation sum, is considered. This variable is also studied for cone sizes of 0.3 and 0.4. Finally, a relative isolation variable based solely on the p_{T} of tracks from the primary vertex,

$$I_{\mathrm{trk}} = \frac{\Sigma p_{\mathrm{T}}^{\mathrm{trkPV}}}{p_{\mathrm{T}}^{\mu}}, \tag{5.1}$$

where 'trkPV' refers to tracks from the primary vertex which are within a cone of $\Delta R = 0.3$ of the muon, is studied. The $S/\sqrt{B}$ for the different isolation variables is shown in figure 5.2a, with the size of the error interval from the maximum-likelihood fit to the $\mathrm{Z}/\gamma^* \rightarrow \tau\tau$ signal strength shown in 5.2b. Both figures of merit do not change significantly when varying the isolation requirements meaning that this analysis is not so sensitive to fake, non-isolated muons. The choice of isolation variable, $\Delta\beta$ corrected isolation as in equation 3.1 with a cone size of $\Delta R = 0.4$, is therefore driven mostly by simplicity and consistency with other CMS analyses.

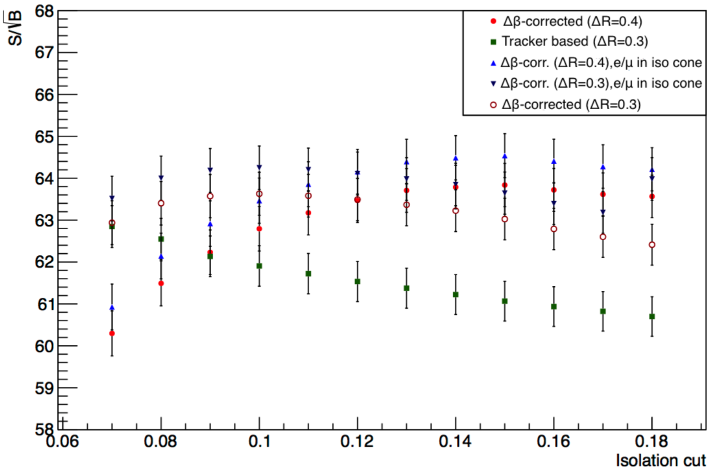

(a) $S/\sqrt{B}$

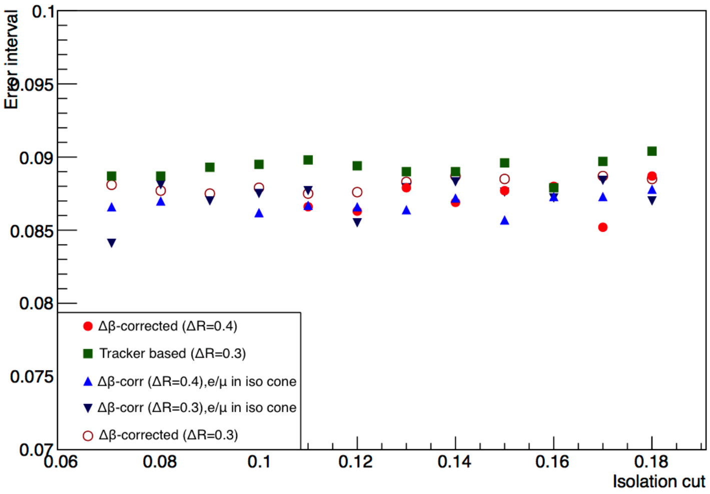

(b) Size of error interval

Figure 5.2: (a) The $S/\sqrt{B}$ for $Z/\gamma^* \rightarrow \tau\tau$ signal and (b) the size of the error interval on the best-fit value of a maximum-likelihood fit to the $Z/\gamma^* \rightarrow \tau\tau$ signal strength, for various selections of the $\Delta\beta$-corrected isolation variable with a cone size of $\Delta R = 0.4$ (solid circles) and $\Delta R = 0.3$ (open circles), the $\Delta\beta$-corrected isolation variable including electrons and muons in the isolation sum, for a cone size of $\Delta R = 0.4$ (upward facing triangles) and $\Delta R = 0.3$ (downward facing triangles) and the tracker-based relative isolation (solid squares).

A topological selection on the m_T variable, introduced in section 4.2.3, is made on events in the $\mu\tau_\mathrm{h}$ channel. This selection and the choice of hadronic tau isolation working point provide two competing effects and therefore they are optimised simultaneously. The “pre-fit” expected upper limits, determined without the fit to the real observed data, on $\sigma\times\mathcal{B}$ for both ggϕ and bbϕ production with decay into $\tau\tau$ at several mass points in the 90 GeV–3.2 TeV range are used as a figure of merit. Because of the use of such a wide range of signal masses, it is not possible to choose a selection that is optimal for every mass point. This is illustrated in figure 5.3: figure 5.3a shows the upper limit on $\sigma\times\mathcal{B}$ for the gluon fusion production process, for a mass $m_\phi = 160\,\mathrm{GeV}$, with figure 5.3b showing this upper limit for $m_\phi = 2.9\,\mathrm{TeV}$. Figure 5.4 shows the effect of gradually loosening the m_T and hadronic tau isolation working point selections on both the ggϕ and bbϕ production processes.

These figures show that looser selections are preferred for higher masses. This behaviour can be explained by considering the function of each of the selections. Tightening the hadronic tau isolation working point reduces the selection of fake taus and increases the proportion of backgrounds which contain real hadronic taus. The m_T selection reduces the W+jets background. As the backgrounds are concentrated at the lower end of the spectrum of mass-like discriminating variables, such tighter selections are preferred where signal and backgrounds overlap. For higher masses the backgrounds are lower in the region where the signal peaks, and there is more benefit to loosening the selection to increase the signal efficiency than to keep the tighter selection to reduce an already low background. The selection was optimised for masses around 800 GeV–1 TeV, by using the medium hadronic tau isolation working point and a selection on $m_\mathrm{T} < 40\,\mathrm{GeV}$.

The choice of the hadronic tau p_T selection is driven by the effect on the low mass region: raising the p_T selection by 10 GeV from the minimum of 20 GeV does not affect the sensitivity of the analysis for high mass points, while recovering some of the loss of loosening the tau isolation working point and m_T cut. The reason for this is that when using $p_\mathrm{T} > 30\,\mathrm{GeV}$ the loss of background events exceeds the loss of signal events. The effect of the increased hadronic tau p_T selection on the upper limits for the ggϕ production process is shown in figure 5.5a, and on the bbϕ production process in figure 5.5b. At low mass the improvement in the ggϕ limits obtained by increasing the p_T selection is sizeable; for bbϕ events the effect is much less pronounced.

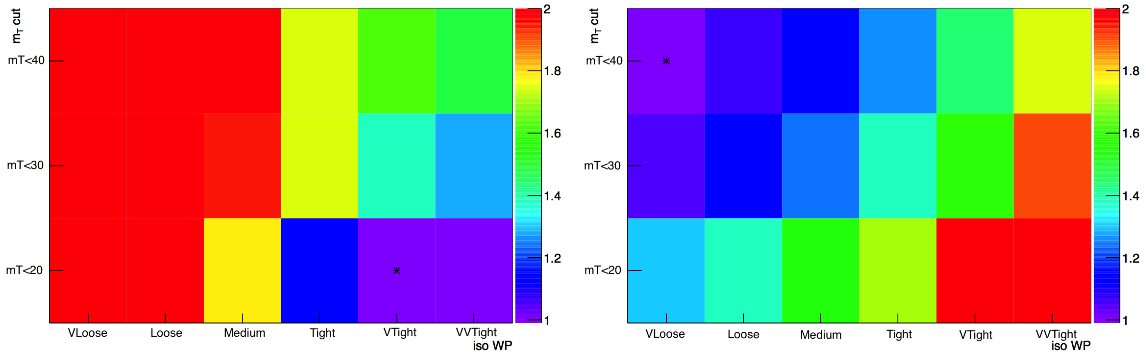

(a) $m_\phi = 160\,\text{GeV}$ **(b)** $m_\phi = 2.9\,\text{TeV}$

Figure 5.3: Pre-fit expected limit on $\sigma{\times}\mathcal{B}$ for the gg$\phi \to \tau\tau$ process, as a function of the tau isolation working point (from very loose to very very tight) and of the m_{T} selection from $m_{\text{T}} < 20\,\text{GeV}$ to $m_{\text{T}} < 40\,\text{GeV}$, normalised to the best limit in the plane, indicated by the asterisk. This is shown for (a) $m_\phi = 160\,\text{GeV}$ and (b) $m_\phi = 2.9\,\text{TeV}$. The most optimal combination of m_{T} selection and hadronic tau isolation working point varies, with looser selections preferred at higher mass.

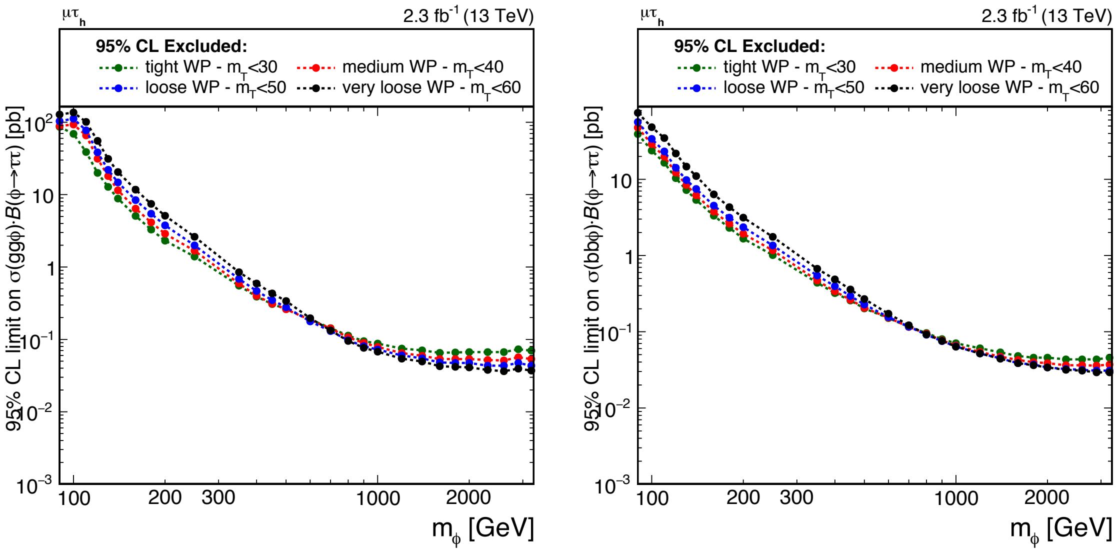

(a) ggϕ **(b)** bbϕ

Figure 5.4: Pre-fit expected limits on $\sigma{\times}\mathcal{B}$ in the $\mu\tau_{\text{h}}$ channel for (a) ggϕ and (b) bbϕ production, for an increasingly looser m_{T} selection and tau isolation working point, starting at the tight working point and $m_{\text{T}} < 30\,\text{GeV}$ in green, the medium working point and $m_{\text{T}} < 40\,\text{GeV}$ in red, the loose working point and $m_{\text{T}} < 50\,\text{GeV}$ in blue and the very loose working point and $m_{\text{T}} < 60\,\text{GeV}$ in black. Loosening the tau isolation working point and m_{T} selection improves the limits at higher mass and degrades them at low mass.

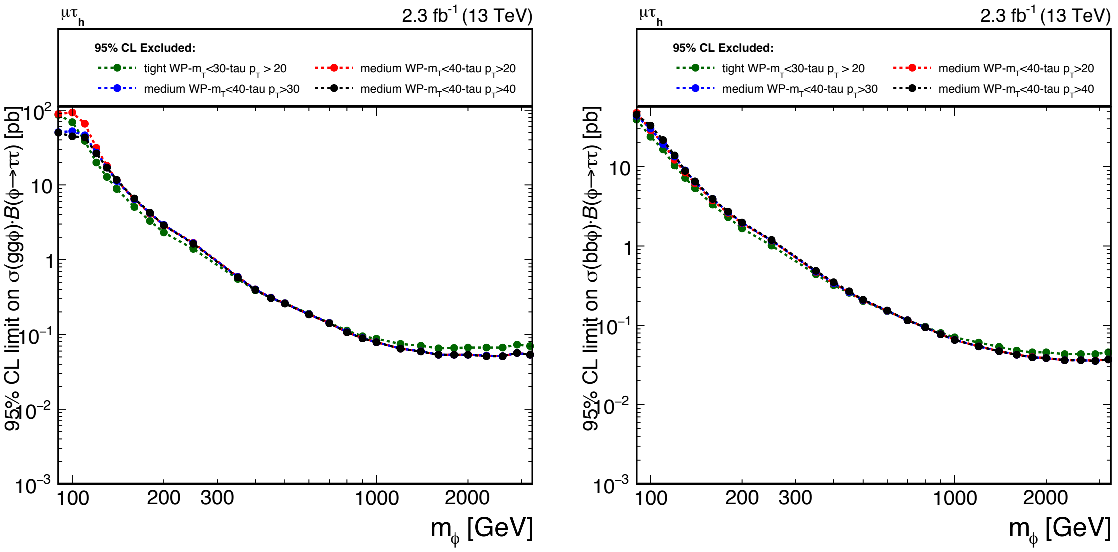

(a) ggϕ **(b)** bbϕ

Figure 5.5: Pre-fit expected limits on $\sigma \times \mathcal{B}$ in the $\mu\tau_\mathrm{h}$ channel for (a) ggϕ production and (b) bbϕ production. The limits when using the medium hadronic tau isolation working point and $m_\mathrm{T} < 40\,\mathrm{GeV}$ selection using a minimum hadronic tau p_T selection of 20 GeV (red circles), 30 GeV (blue circles) and 40 GeV (black circles) are shown. The green circles show the limits using the tight tau isolation working point and $m_\mathrm{T} < 30\,\mathrm{GeV}$. The limits on the gg$\phi$ production process improve at low masses when increasing the minimum hadronic tau p_T selection, the effect on the bbϕ production process is less pronounced.

5.2.3 Event selection in the eτ_h channel

For the selection of events in the eτ_h channel, the first step is a trigger that only requires an electron at L1. Loose ID and isolation criteria are applied to the electron with the HLT.

The offline event selection requires an oppositely charged electron and hadronically decaying tau, which are separated by $\Delta R > 0.5$. The electron is required to have $p_\mathrm{T} > 26\,\mathrm{GeV}$ and $|\eta| < 2.1$. The impact parameters are required to satisfy $d_{xy} < 0.045\,\mathrm{cm}$ and $d_z < 0.2\,\mathrm{cm}$, and the electron must pass additional identification criteria. The chosen working point of the MVA identification discriminator was designed to select electrons from $\mathrm{Z}/\gamma^* \to \mathrm{ee}$ events with 80% efficiency. In addition the electron needs to be isolated, $I^\mathrm{e}_\mathrm{rel} < 0.1$, with the relative isolation variable calculated with a cone size of 0.3.

The hadronic tau is required to have $p_\mathrm{T} > 30\,\mathrm{GeV}$, $|\eta| < 2.3$, to be reconstructed by the HPS algorithm and to pass the medium working point of the MVA isolation discriminator.

The impact parameter d_z of the hadronic tau must be less than 0.2 cm. Finally, the hadronic tau must pass the tight working point of the anti-electron discriminator and the loose working point of the anti-muon discriminator.

Analogously to the muons, it was found that the analysis is not highly sensitive to the choice of electron isolation variable and cut value. A topological selection on the m_{T} variable is also made in this channel to reject W+jets events. The value of $m_{\mathrm{T}} < 50\,\mathrm{GeV}$ that is used is obtained by performing a simultaneous optimisation of the m_{T} selection and hadronic tau isolation working point. The same considerations as for the $\mu\tau_{\mathrm{h}}$ channel apply, as illustrated in figure 5.6. The choice of the hadronic tau p_{T} selection of 30 GeV is made to recover some of the sensitivity lost at low mass by using looser m_{T} and hadronic tau isolation criteria. This is illustrated in figure 5.7.

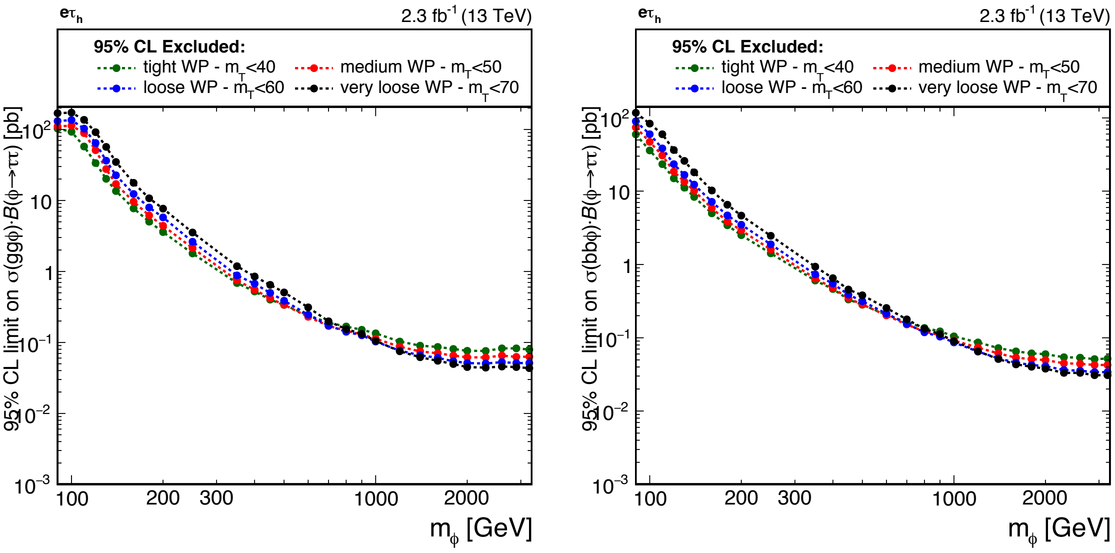

(a) ggϕ **(b)** bbϕ

Figure 5.6: Pre-fit expected limits on $\sigma\times\mathcal{B}$ in the eτ_{h} channel for (a) ggϕ and (b) bbϕ production, for an increasingly looser m_{T} selection and tau isolation working point, starting at the tight working point and $m_{\mathrm{T}} < 40\,\mathrm{GeV}$ in green, the medium working point and $m_{\mathrm{T}} < 50\,\mathrm{GeV}$ in red, the loose working point and $m_{\mathrm{T}} < 60\,\mathrm{GeV}$ in blue and the very loose working point and $m_{\mathrm{T}} < 70\,\mathrm{GeV}$ in black. Loosening the tau isolation working point and m_{T} selection improves the limits at higher mass and degrades them at low mass.

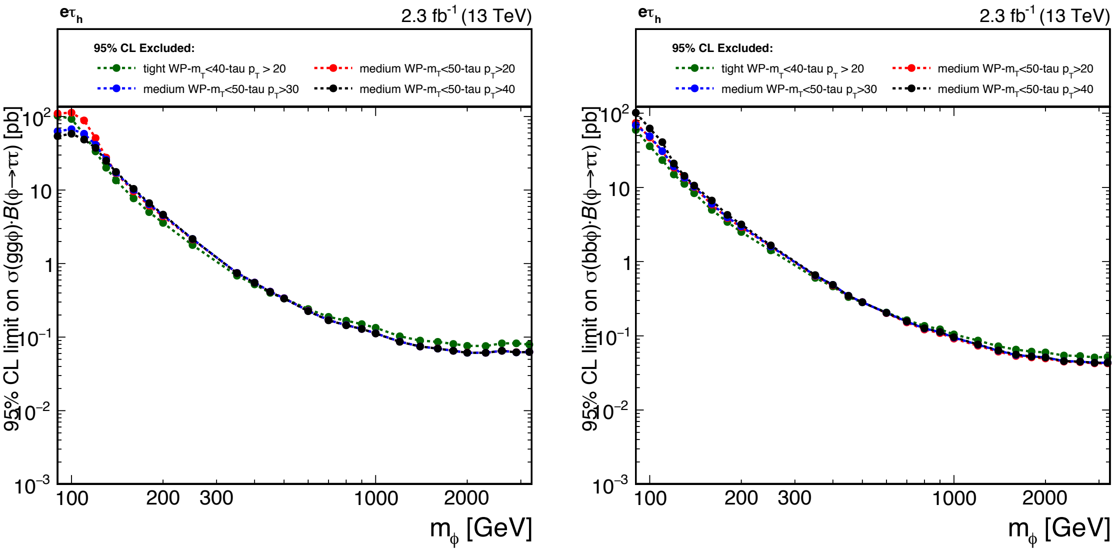

(a) ggϕ **(b)** bbϕ

Figure 5.7: Pre-fit expected limits on $\sigma\times\mathcal{B}$ in the eτ_h channel for (a) ggϕ production and (b) bbϕ production. The limits using the medium hadronic tau isolation working point and $m_\mathrm{T} < 40$ GeV selection using a minimum hadronic tau p_T cut of 20 GeV (red circles), 30 GeV (blue circles) and 40 GeV (black circles) are shown. The green circles show the limits using the tight tau isolation working point and $m_\mathrm{T} < 40$ GeV. The limits on the ggϕ production process improve at low masses when increasing the hadronic tau p_T cut, the effect on the bbϕ production process is less pronounced.

5.2.4 Event selection in the $\tau_\mathrm{h}\tau_\mathrm{h}$ channel

The trigger in the $\tau_\mathrm{h}\tau_\mathrm{h}$ channel requires two hadronic taus at L1 to which loose identification and isolation criteria are applied in the HLT.

The offline event selection requires both hadronic taus to be oppositely charged, separated by $\Delta R > 0.5$, to have $p_\mathrm{T} > 40$ GeV and to satisfy $|\eta| < 2.1$. Both taus need to be reconstructed by the HPS algorithm, and their impact parameter d_z must be less than 0.2 cm. Both taus need to pass the tight working point of the isolation discriminator, the very loose working point of the anti-electron discriminator and the loose working point of the anti-muon discriminator. The tight working point of the isolation discriminator is chosen such that the selection is near-optimal at high mass, while not losing too much sensitivity in the low to intermediate mass range. This is illustrated in figure 5.8a for the ggϕ process and in figure 5.8b for the bbϕ process.

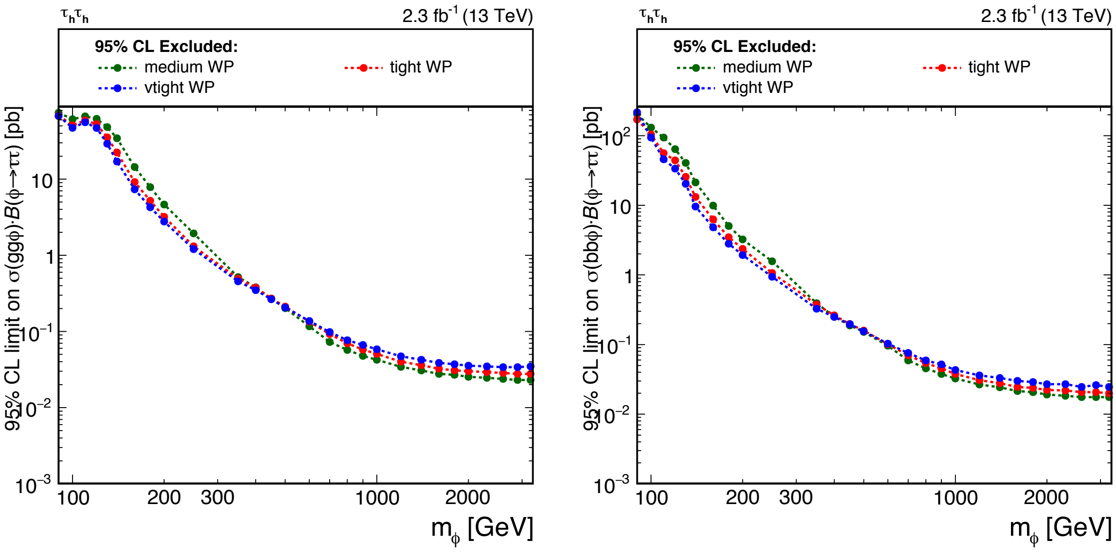

(a) ggϕ **(b)** bbϕ

Figure 5.8: Expected upper limits for (a) the ggϕ process and (b) the bbϕ process in the $\tau_\mathrm{h}\tau_\mathrm{h}$ channel, using the medium (green), tight (red) and very tight (blue) working point of the tau isolation discriminator. The pattern is similar to that in the eτ_h and $\mu\tau_\mathrm{h}$ channels, with looser selections preferred at high mass.

5.2.5 Event selection in the eμ channel

Events in the eμ channel are first selected by two triggers that both require an electron and muon at L1 and apply loose ID and isolation requirements to these objects in the HLT. The p_T requirements on the electron and muon are different in the two triggers, thus using the combination of the two improves the signal efficiency.

Offline, the electron and muon are required to be oppositely charged and separated by $\Delta R > 0.3$. The electron needs to have $p_\mathrm{T} > 13\,\mathrm{GeV}$ and $|\eta| < 2.5$. As in the eτ_h channel the impact parameters have to satisfy $d_{xy} < 0.045\,\mathrm{cm}$ and $d_z < 0.2\,\mathrm{cm}$. The same selection on the MVA identification discriminator as in the eτ_h channel is applied. The electron also needs to be isolated, $I^{\mathrm{e}}_{\mathrm{rel}} < 0.15$, where the relative isolation variable is calculated with a cone size of 0.3.

The muon needs to have $p_\mathrm{T} > 10\,\mathrm{GeV}$, $|\eta| < 2.4$ and its impact parameters need to be $d_{xy} < 0.045\,\mathrm{cm}$ and $d_z < 0.2\,\mathrm{cm}$. In addition to these requirements the muon must pass the "medium" identification criteria and be isolated with $I^{\mu}_{\mathrm{rel}} < 0.2$, where the relative isolation variable is calculated using a cone size of 0.4.

Because a combination of triggers is used, one with electron $p_{\mathrm{T}} > 23\,\mathrm{GeV}$ and muon $p_{\mathrm{T}} > 8\,\mathrm{GeV}$ and one with muon $p_{\mathrm{T}} > 23\,\mathrm{GeV}$ and electron $p_{\mathrm{T}} > 13\,\mathrm{GeV}$, the object firing the higher p_{T} trigger leg needs to have a transverse momentum of at least 24 GeV on top of the requirements already discussed. This avoids events in the lower part of the trigger turn-on curve being selected.

In addition to the selection described so far, a topological selection is made on the D_ζ variable [139],

$$\begin{aligned} &D_\zeta = P_\zeta^{\mathrm{miss}} - 0.85 P_\zeta^{\mathrm{vis}}, \\ &\text{where } P_\zeta^{\mathrm{miss}} = \vec{E}_{\mathrm{T}}^{\mathrm{miss}} \cdot \frac{\vec{\zeta}}{|\vec{\zeta}|} \text{ and } P_\zeta^{\mathrm{vis}} = (\vec{p}_{\mathrm{T},1}^{\,\mathrm{vis}} + \vec{p}_{\mathrm{T},2}^{\,\mathrm{vis}}) \cdot \frac{\vec{\zeta}}{|\vec{\zeta}|}. \end{aligned} \tag{5.2}$$

This means D_ζ is defined as the projection of the transverse momenta of the visible tau decay products plus missing energy, $p_{\mathrm{T}}+E_{\mathrm{T}}^{\mathrm{miss}}$, onto the axis $\vec{\zeta}$, minus the projection of only the transverse momenta of the visible tau decay products onto this axis. The axis $\vec{\zeta}$ is the axis that bisects the directions $\vec{p}_{\mathrm{T},1}^{\,\mathrm{vis}}$ and $\vec{p}_{\mathrm{T},2}^{\,\mathrm{vis}}$ of the visible decay products in the transverse plane. This definition is illustrated in figure 5.9a. In $\mathrm{Z}/\gamma^* \to \tau\tau$ and $\mathrm{A/H} \to \tau\tau$ events, the neutrinos from the $\tau \to \ell\nu\nu$ decay are more likely to travel in the same direction as the visible decay products of the tau. This means the missing energy is not expected to point in the opposite direction of the momentum sum of the visible tau decay products, making D_ζ more likely to be positive. In decays of di-boson, $\mathrm{t\bar{t}}$ and W+jets events, leptons and neutrinos are more likely to be emitted back-to-back and therefore D_ζ is not preferentially positive. Figure 5.9b shows the D_ζ distribution for $\mathrm{e}\mu$ events. The selection used, $D_\zeta > -20\,\mathrm{GeV}$, rejects $\mathrm{t\bar{t}}$, W+jets and di-boson events.

5.2.6 Categorisation

As the analysis targets both the gluon fusion and the b-associated production modes, the sensitivity to the signal can be increased by categorising based on the number of b-tagged jets in the event. Jets are considered b-tagged if they pass the medium working point of the CSVv2 discriminator; the typical b-tagging efficiency at this working point is 69% [114].

Figure 5.10a shows the number of jets in the $\mu\tau_{\mathrm{h}}$ channel, with figure 5.10b showing the number of b-tagged jets in that channel. The gluon fusion and b-associated signals are overlaid on these distributions, normalised to 100 times their $\sigma\times\mathcal{B}$ at $m_{\mathrm{A}} = 1\,\mathrm{TeV}$

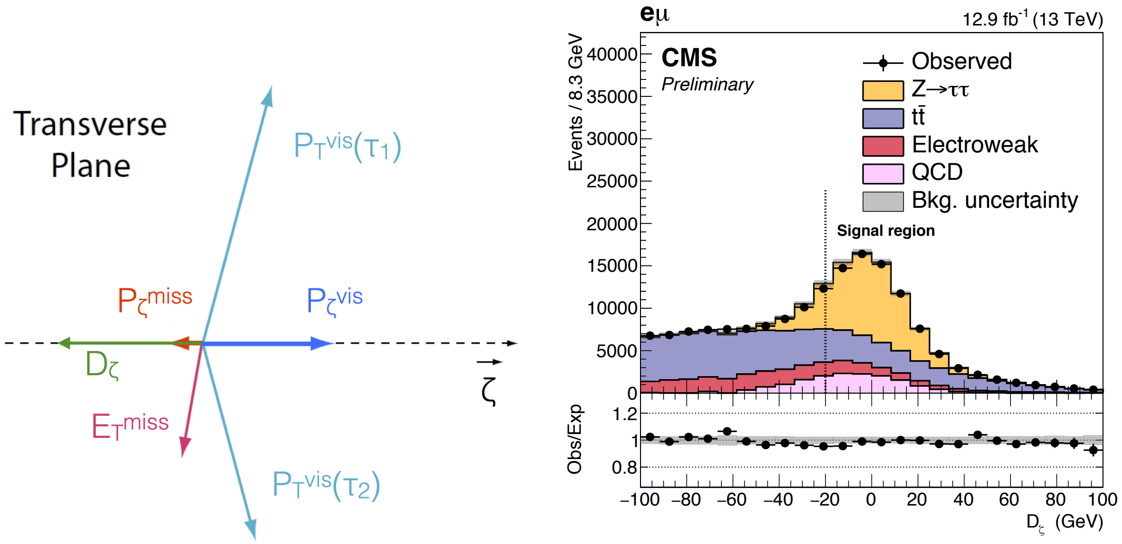

(a) Reconstruction of D_ζ **(b)** D_ζ distribution in eμ channel

Figure 5.9: (a) Reconstruction of D_ζ (adapted from [139]) and (b) D_ζ distribution in the eμ channel [2]. The events shown in (b) were selected according to the requirements described in this section.

and $\tan\beta = 50$ in the $m_{\mathrm{h}}^{\mathrm{mod}+}$ scenario. The distribution of the gluon fusion signal in figure 5.10b shows that the vast majority of these signal events do not have any b-tagged jets. To target this production mode a category which requires no b-tagged jets can be used. The same figure also shows that the majority of bbϕ signal events do not have any b-tagged jets: either the b-jets in these events are too soft, or they do not pass the b-tagging requirements. This means that the category which requires no b-tagged jets is also sensitive to some of the bbϕ signal. To target the remainder of the bbϕ signal, another category with at least one b-tagged jet is defined. The bbϕ signal in figure 5.10b shows that there is not such a large proportion of events with more than one b-tagged jet. Figure 5.10a shows that the t$\bar{\mathrm{t}}$ background starts to become larger for events with more than one jet. The definition of the category that targets the bbϕ signal is therefore chosen with the inclusion of a jet veto, such that the region where the t$\bar{\mathrm{t}}$ background becomes larger is excluded, while retaining a large proportion of the bbϕ signal.

In summary, the two categories are defined as:

- **No b-tag**: No b-tagged jets. This category targets the ggϕ production mode but is also sensitive to some of the bbϕ signal.

- **B-tag**: At least one b-tagged jet, at most one jet with $p_{\mathrm{T}} > 30\,\mathrm{GeV}$. This second requirement, the jet veto, reduces the $\mathrm{t\bar{t}}$ background. Due to the lower p_{T} requirement considered for b-tagging compared with the requirement for the jet veto, it is still possible for there to be more than one b-tagged jet in the event.

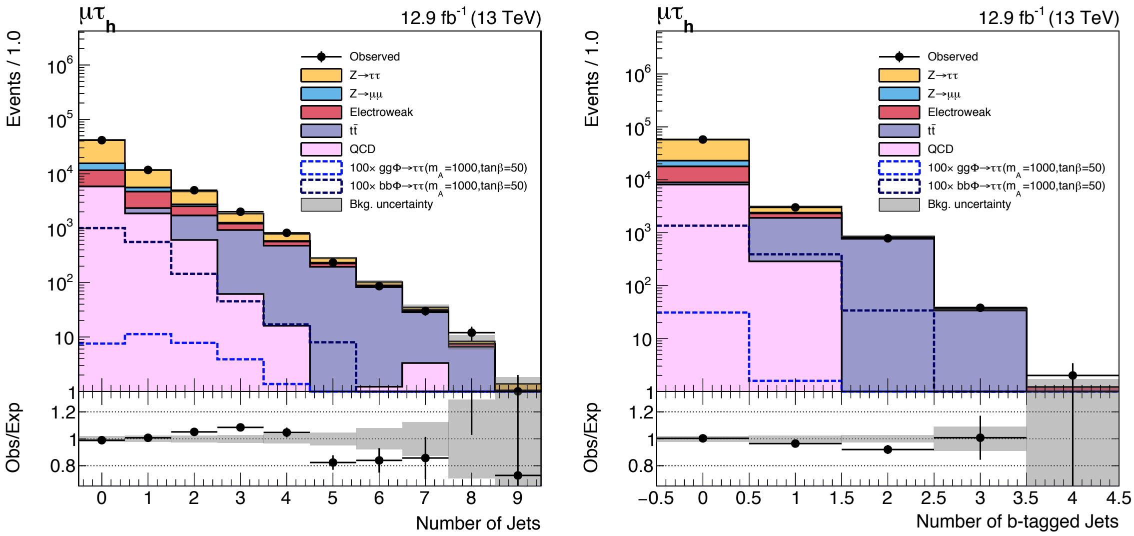

(a) Number of jets

(b) Number of b-tagged jets

Figure 5.10: (a) Number of jets and (b) number of b-tagged jets in the $\mu\tau_{\mathrm{h}}$ channel. The gluon fusion signal (dashed blue line) and b-associated signal (dashed purple line) are overlaid on the expected background distribution. The signals are normalised to 100 times their $\sigma\times\mathcal{B}$ at $m_{\mathrm{A}} = 1\,\mathrm{TeV}$ and $\tan\beta = 50$ in the $m_{\mathrm{h}}^{\mathrm{mod+}}$ scenario. The signal-sensitive bins motivate the choice of categories. The events shown in these figures were selected according to the requirements described in section 5.2.2.

5.3 Discriminating variable

The discriminating variable used for signal extraction is the total transverse mass,

$$m_{\mathrm{T}}^{\mathrm{tot}} = \sqrt{(m_{\mathrm{T}}(E_{\mathrm{T}}^{\mathrm{miss}}, \tau_1^{\mathrm{vis}}))^2 + (m_{\mathrm{T}}(E_{\mathrm{T}}^{\mathrm{miss}}, \tau_2^{\mathrm{vis}}))^2 + (m_{\mathrm{T}}(\tau_1^{\mathrm{vis}}, \tau_2^{\mathrm{vis}}))^2}\,, \tag{5.3}$$

where $m_{\mathrm{T}}(1,2)$ is defined as,

$$m_{\mathrm{T}}(1,2) = \sqrt{2p_{\mathrm{T},1}p_{\mathrm{T},2}(1-\cos{(\Delta\phi(1,2))})}\,. \tag{5.4}$$

This means that $m_{\mathrm{T}}(E_{\mathrm{T}}^{\mathrm{miss}}, \tau_1^{\mathrm{vis}})$ is equivalent to the m_{T} defined for the $\mathrm{e}\tau_{\mathrm{h}}$ and $\mu\tau_{\mathrm{h}}$ channels in equation 4.1. The $m_{\mathrm{T}}^{\mathrm{tot}}$ variable provides good separation between signal and QCD multijet events in the eτ_h, $\mu\tau_\mathrm{h}$ and $\tau_\mathrm{h}\tau_\mathrm{h}$ channels, and between signal and $\mathrm{t\bar{t}}$ events in the eμ channel. These are some of the major backgrounds and thus good separation between these processes and the signal is important for the sensitivity of the analysis. The separation between signal and backgrounds is illustrated in figure 5.11. Figure 5.11a shows the total transverse mass distribution of the QCD background in the no b-tag category of the $\tau_\mathrm{h}\tau_\mathrm{h}$ channel with the gluon fusion signal at 400 GeV, 1 TeV and 2 TeV overlaid. Figure 5.11b shows the total transverse mass distribution of the $\mathrm{t\bar{t}}$ background in the b-tag category of the eμ channel with the b-associated production signal at the same three masses overlaid.

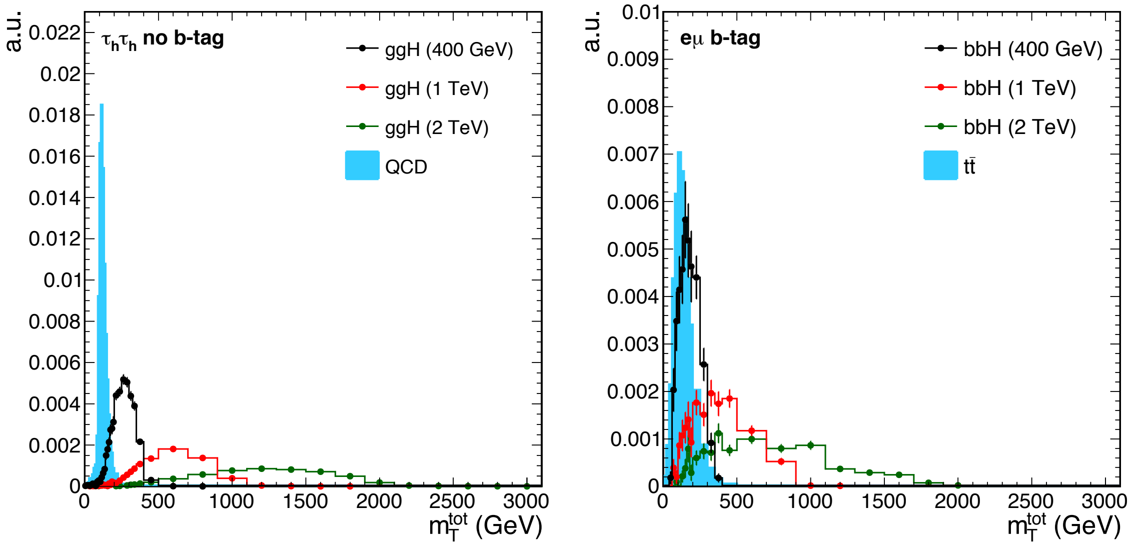

(a) QCD and signal in $\tau_\mathrm{h}\tau_\mathrm{h}$ no b-tag **(b)** $\mathrm{t\bar{t}}$ and signal in eμ b-tag

Figure 5.11: Total transverse mass distributions in (a) the no b-tag category of the $\tau_\mathrm{h}\tau_\mathrm{h}$ channel, for QCD and gluon fusion signal at 400 GeV, 1 TeV and 2 TeV and (b) in the b-tag category of the eμ channel, for $\mathrm{t\bar{t}}$ and b-associated signal at 400 GeV, 1 TeV and 2 TeV. The total transverse mass variable separates the signal and these backgrounds well.

5.4 Monte Carlo simulation-to-data correction factors

Because simulated samples are used for the signal prediction, and to estimate some of the backgrounds, it is important to correct for possible mis-modelling with respect to the data. Dedicated control regions are used to derive the MC simulation-to-data correction factors that are applied to the simulated samples. Where efficiencies are involved this scale factor is derived by measuring the efficiency in data and in simulation and constructing the scale factor as $\mathrm{SF} = \frac{\epsilon_\mathrm{Data}}{\epsilon_\mathrm{MC}}$.

Tracking efficiency

A discrepancy between the track reconstruction efficiency in data and simulation for electrons and muons was found. It is corrected for using η-dependent scale factors.

Electron, muon and tau identification and isolation

Identification and isolation efficiencies in data and simulation are measured for electrons, muons and hadronic taus. A tag-and-probe method using $\mathrm{Z} \to \mathrm{ee}$ ($\mathrm{Z} \to \mu\mu$) events is used to measure the efficiencies for electrons (muons). The hadronic tau identification and isolation efficiency is measured using a tag-and-probe method making use of $\mathrm{Z} \to \tau\tau \to \mu\tau_{\mathrm{h}}$ events.

Trigger efficiency

The electron, muon and hadronic tau trigger efficiencies are also measured using tag-and-probe methods with the types of events as described for the identification and isolation efficiencies. Because no trigger simulation is applied to the simulated samples, the efficiency ϵ_{Data} is simply applied to the simulated events. Because two electron-muon cross-triggers are used to select events in the $\mathrm{e}\mu$ channel, the efficiencies of the different cross-trigger legs need to be combined. With one of the cross-triggers having a minimum p_{T} of 23 GeV on the muon leg and 12 GeV on the electron leg, and the other having a minimum p_{T} of 23 GeV on the electron leg and 8 GeV on the muon leg, the combined efficiency of the two triggers becomes:

$$\begin{aligned}\epsilon_{\mathrm{Data}} = \epsilon_{\mathrm{Data}}(\mathrm{Mu23}) \cdot \epsilon_{\mathrm{Data}}(\mathrm{Ele12}) + \epsilon_{\mathrm{Data}}(\mathrm{Mu8}) \cdot \epsilon_{\mathrm{Data}}(\mathrm{Ele23}) \\ -\epsilon_{\mathrm{Data}}(\mathrm{Mu23}) \cdot \epsilon_{\mathrm{Data}}(\mathrm{Ele23}).\end{aligned} \tag{5.5}$$

e → τ_{h} fake rate and $\mu \to \tau_{\mathrm{h}}$ fake rate

The $\mathrm{e} \to \tau_{\mathrm{h}}$ and $\mu \to \tau_{\mathrm{h}}$ fake rates, after applying the anti-electron and anti-muon discriminators, are measured using a tag-and-probe method with $\mathrm{Z} \to \mathrm{ee}$ and $\mathrm{Z} \to \mu\mu$ events. Scale factors, applied to simulated events where the tau is faked by an electron or muon, are derived as the ratio between the fake rate in data and the fake rate in simulation.

$E_{\mathrm{T}}^{\mathrm{miss}}$ recoil corrections

Differences in $E_{\mathrm{T}}^{\mathrm{miss}}$ resolution and response between data and simulation are accounted for by the application of recoil corrections to signal, W+jets and $\mathrm{Z}/\gamma^* \to \tau\tau$ events. More detail about these corrections is given in section 3.6.1.

Top quark p_{T} reweighting

A reweighting which was derived during Run 1 to better match the top quark p_{T} distribution in simulation to that observed in data is applied to $\mathrm{t\bar{t}}$ events [140]. Despite the fact that the correction was derived during Run 1, it still improves the agreement with data in a $\mathrm{t\bar{t}}$ enriched control region in the $\mathrm{e}\mu$ channel, defined as $E_{\mathrm{T}}^{\mathrm{miss}} > 80\,\mathrm{GeV}$ and $D_\zeta < -20\,\mathrm{GeV}$. This is illustrated in figure 5.12.

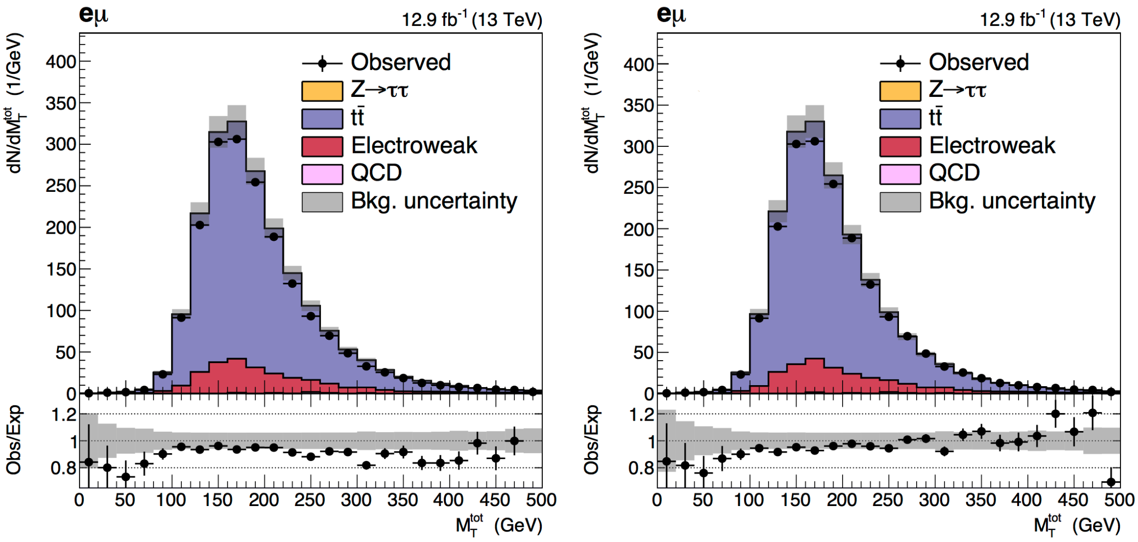

(a) Without top quark p_{T} reweighting (b) With top quark p_{T} reweighting

Figure 5.12: The $m_{\mathrm{T}}^{\mathrm{tot}}$ distribution in the $\mathrm{t\bar{t}}$ enriched control region $E_{\mathrm{T}}^{\mathrm{miss}} > 80\,\mathrm{GeV}$ and $D_\zeta < -20\,\mathrm{GeV}$ in the $\mathrm{e}\mu$ channel, (a) without applying the top quark p_{T} reweighting and (b) with the top quark p_{T} reweighting. The uncertainty band includes the statistical uncertainty as well as a 6% $\mathrm{t\bar{t}}$ cross section uncertainty. The remaining disagreement between data and simulation after applying the reweighting is covered by an associated systematic uncertainty which is further discussed in section 5.6.2.

b-Tag scale factors

To correct for the difference in b-tagging efficiency and light jet mis-tagging rates between data and simulation, p_{T}- and η-dependent scale factors are derived as described in reference [114]. They are applied using the promote-demote method as outlined in equation 4.2.

Drell-Yan shape reweighting

As the MC generator used for the $Z/\gamma^* \rightarrow \tau\tau$ estimate does not model the data well for events with high di-lepton mass and high p_T, a reweighting is applied to correct for this. These weights are derived in bins of di-lepton mass and p_T using $Z/\gamma^* \rightarrow \mu\mu$ events in data in such a way that they do not change the overall Drell-Yan normalisation. The weights are then applied to the $Z/\gamma^* \rightarrow \tau\tau$ and $Z/\gamma^* \rightarrow \ell\ell$ background processes. The mis-modelling can be seen in figure 5.13a, which shows the observed data and expected background distribution of the di-lepton p_T in $Z/\gamma^* \rightarrow \mu\mu$ events. The overall effect of the reweighting, which is derived based on the events shown in figure 5.13a, on the $Z/\gamma^* \rightarrow \tau\tau$ background shape in the no b-tag category of the $e\tau_\mathrm{h}$ channel is shown in figure 5.13b. While the correction factor can be up to 20% this figure shows that the total effect on the $Z/\gamma^* \rightarrow \tau\tau$ background distribution is small.

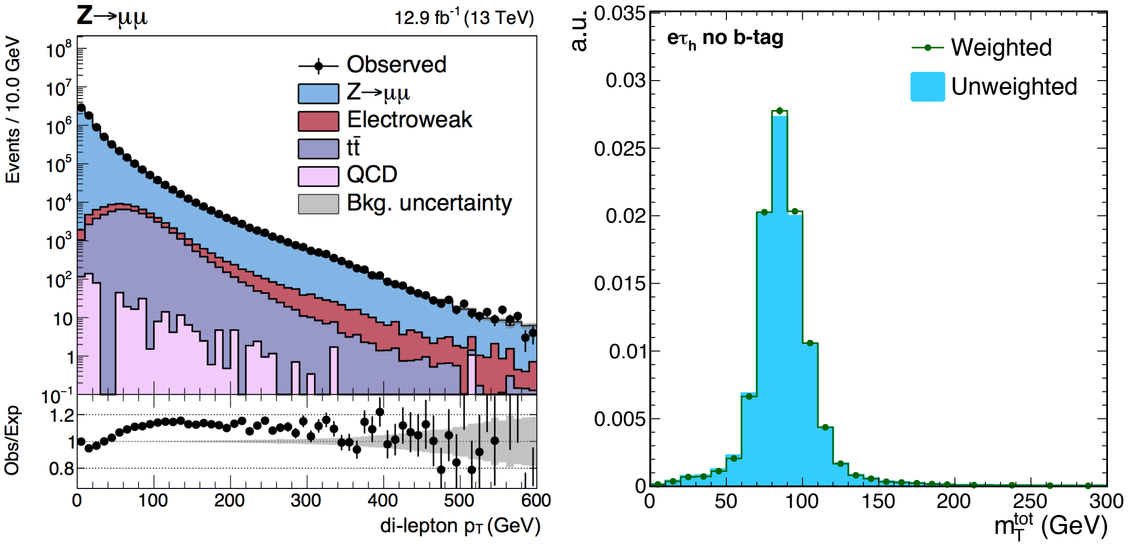

(a) $Z/\gamma^* \rightarrow \mu\mu$ events

(b) Effect of Drell-Yan shape reweighting on $Z/\gamma^* \rightarrow \tau\tau$ background

Figure 5.13: (a) The mis-modelling in the di-lepton p_T distribution as observed in $Z/\gamma^* \rightarrow \mu\mu$ events, used to derive the correction and (b) the impact of applying the Drell-Yan shape reweighting on the total transverse mass distribution of the $Z/\gamma^* \rightarrow \tau\tau$ background in the no b-tag category of the $e\tau_\mathrm{h}$ channel. The events shown in (a) were selected by requiring two oppositely charged muons, passing kinematic cuts, identification and isolation requirements equivalent to the selections applied to muons as described in section 5.2.2.

5.5 Background estimation

There are several backgrounds in this analysis, and the different final states can have different background compositions. Consider figure 5.14a, which shows the low $m_{\mathrm{T}}^{\mathrm{tot}}$ region in the no b-tag category of the $\mu\tau_{\mathrm{h}}$ channel and figure 5.14b, which shows the low $m_{\mathrm{T}}^{\mathrm{tot}}$ region in the b-tag category of the $\mathrm{e}\mu$ channel. These regions are where the backgrounds are concentrated and it is therefore easier to see the different contributions. $\mathrm{Z}/\gamma^{*} \rightarrow \tau\tau$ is a background in all four channels as it has two real taus in the final state, like the signal being searched for. Smaller backgrounds from $\mathrm{Z}/\gamma^{*} \rightarrow \ell\ell$ decays also play a role, especially in the $\mu\tau_{\mathrm{h}}$ and $\mathrm{e}\tau_{\mathrm{h}}$ channels where such events might pass the selection if, for example, one of the leptons or a jet is mis-reconstructed as a hadronic tau. Production of QCD multijet events, labelled 'QCD' in figure 5.14, is a background when two jets are mis-reconstructed as the two tau candidates. As is visible in figure 5.14b, the $\mathrm{t}\bar{\mathrm{t}}$ background is particularly important in the b-tag category. This is because top quarks virtually always decay as $\mathrm{t} \rightarrow \mathrm{Wb}$, and so such events nearly always contain b-jets. The decay products of one or both of the W bosons, and additional jets in the event, can then form $\mathrm{e}\tau_{\mathrm{h}}$, $\mu\tau_{\mathrm{h}}$, $\tau_{\mathrm{h}}\tau_{\mathrm{h}}$ and $\mathrm{e}\mu$ pairs.

The W+jets process is a background in the $\mathrm{e}\tau_{\mathrm{h}}$ and $\mu\tau_{\mathrm{h}}$ channels when the lepton from the W boson decay and a jet mis-reconstructed as a hadronic tau form a pair. In the $\tau_{\mathrm{h}}\tau_{\mathrm{h}}$ channel it is a background when one τ_{h} originates from a $\mathrm{W} \rightarrow \tau\nu$ decay and the other from an additional jet in the event being mis-reconstruced as a hadronic tau. In the $\mathrm{e}\mu$ channel an additional lepton would have to originate from one of the jets, and so in this channel this background is smaller. The di-boson and single-top backgrounds are small in all channels. In all figures in this chapter the di-boson and single-top backgrounds are drawn together with the W+jets background and labelled collectively as the 'Electroweak' component.

To estimate these backgrounds a mixture of data-driven methods and predictions from simulation is employed. The QCD background is estimated using data-driven techniques in all four channels. In the $\mu\tau_{\mathrm{h}}$ and $\mathrm{e}\tau_{\mathrm{h}}$ channels the W+jets background yield is also estimated using data-driven techniques. The control regions used for the estimation of QCD and W+jets in the $\mathrm{e}\tau_{\mathrm{h}}$ and $\mu\tau_{\mathrm{h}}$ channels are included in a simultaneous fit with the signal region to obtain the final results. More detail on this is given in section 5.7.1. In the $\mathrm{e}\mu$ and $\tau_{\mathrm{h}}\tau_{\mathrm{h}}$ channels the W+jets background is estimated using simulation. The $\mathrm{Z}/\gamma^{*} \rightarrow \tau\tau$ and $\mathrm{Z}/\gamma^{*} \rightarrow \ell\ell$ backgrounds are estimated using simulation for all four

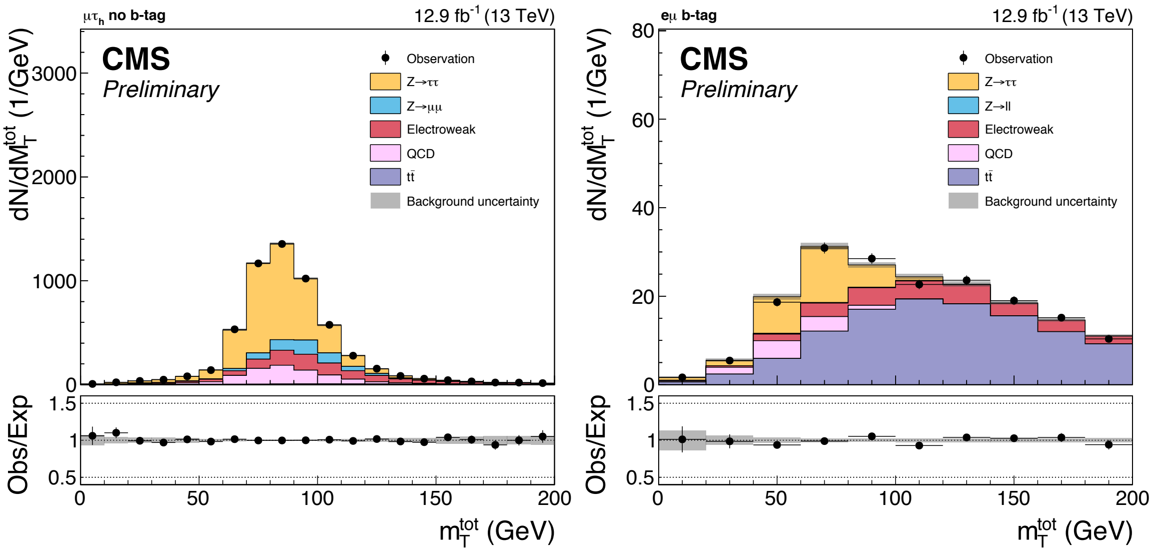

(a) $\mu\tau_{\mathrm{h}}$ no b-tag **(b)** eμ b-tag

Figure 5.14: The low $m_{\mathrm{T}}^{\mathrm{tot}}$ region in (a) the no b-tag category of the $\mu\tau_{\mathrm{h}}$ channel and (b) the b-tag category of the eμ channel. This low $m_{\mathrm{T}}^{\mathrm{tot}}$ region is where the backgrounds are concentrated [141].

channels. A $\mathrm{Z}/\gamma^* \rightarrow \mu\mu$ control region is considered in a simultaneous fit with the signal region to correct and constrain the $\mathrm{Z}/\gamma^* \rightarrow \tau\tau$ normalisation. The $\mathrm{t\bar{t}}$, di-boson and single-top backgrounds are estimated using simulation, with cross-checks in control regions in data. The rest of this section describes the background estimation methods in more detail.

5.5.1 Generator matching

For backgrounds estimated from simulation, it can be beneficial to split a background process into different components that are allowed to vary independently, and be subject to different systematic uncertainties, in the fit to data. Taking the $\mu\tau_{\mathrm{h}}$ channel as an example, a sample of Drell-Yan events will contain $\mathrm{Z}/\gamma^* \rightarrow \tau\tau$ events, where one of the taus decays hadronically and the other tau decays to a muon, but also $\mathrm{Z}/\gamma^* \rightarrow \mu\mu$ events where one of the muons fakes a tau. Similarly, $\mathrm{t\bar{t}}$ background events can be split into those with genuine taus, and those where a jet fakes a hadronic tau. In such cases dividing events from the same production process into separate components based on generator information allows for a correct treatment of systematic uncertainties.

To determine the simulated particle that a reconstructed electron, muon, or hadronic tau originates from, reconstructed objects are matched to a set of simulated objects within a cone of $\Delta R = 0.2$. Five categories of simulated object are considered for matching: prompt electrons and muons, that is electrons and muons not originating from a hadron, tau or muon decay; electrons and muons from tau decays; and simulated hadronic taus. These simulated hadronic taus are built by summing the four-momenta of the visible decay products of the simulated tau lepton.

If there is at least one simulated object within a cone of $\Delta R = 0.2$ around the direction of the reconstructed object, the simulated object nearest the reconstructed particle is chosen as the one the reconstructed particle is matched to. If there are no simulated objects in the cone at all the reconstructed object is said to have originated from a jet.

The type of simulated object matched to a reconstructed particle is used to perform the splitting of background samples. In what follows, it is indicated where this procedure is used.

5.5.2 $Z/\gamma^* \rightarrow \tau\tau$

For all channels, both the shape and normalisation of the $Z/\gamma^* \rightarrow \tau\tau$ background are estimated from the Drell-Yan simulation. For the $\mu\tau_h$ and $e\tau_h$ channels, events in which the reconstructed hadronic tau is matched to a simulated hadronic tau are considered part of the $Z/\gamma^* \rightarrow \tau\tau$ background. In the $\tau_h\tau_h$ channel both reconstructed hadronic taus are required to be matched to a simulated hadronic tau. In the $e\mu$ channel the $Z/\gamma^* \rightarrow \tau\tau$ component of the Drell-Yan background is taken as those events where the reconstructed electron is not matched to a simulated prompt electron and the reconstructed muon is not matched to a prompt muon. Events in the Drell-Yan simulation that do not satisfy the generator matching requirements are considered as the much smaller $Z/\gamma^* \rightarrow \ell\ell$ background.

5.5.3 W+jets and QCD in the eτ_h and $\mu\tau_\mathrm{h}$ channels

A data-driven approach is used for the estimation of both the W+jets and QCD backgrounds in the eτ_h and $\mu\tau_\mathrm{h}$ channels. The estimates of the normalisations of the two backgrounds are tied together due to the presence of some QCD contamination in the W+jets-dominated control region. The shape of the W+jets background is taken from simulation. The QCD shape is taken from same-sign data, that is, events selected in observed data with the opposite charge requirement on the di-tau pair inverted but otherwise identical cuts to the signal region. Contributions from other backgrounds in this region are subtracted.

W+jets normalisation

The W+jets normalisation is derived using a high-m_T control region, where selected events are required to satisfy $m_\mathrm{T} > 70\,\mathrm{GeV}$. The W+jets contribution in this region is enhanced, however there is still some contamination from QCD events. This is visible in figure 5.15 which shows the m_T distribution in the $\mu\tau_\mathrm{h}$ channel, indicating the signal region and the high-m_T control region.

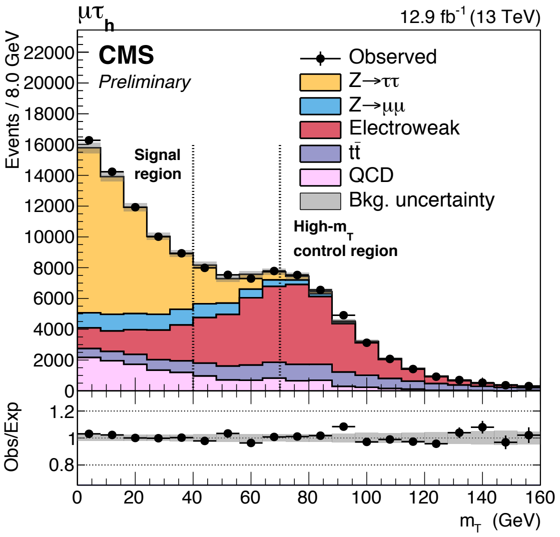

Figure 5.15: Distribution of the transverse mass m_T in the $\mu\tau_\mathrm{h}$ channel, indicating the signal region and the high-m_T control region. This distribution is shown before dividing the events into categories [2].

Because of this contribution from QCD events in the high-m_T region we can construct two equations relating the QCD and W+jets yields to the observed data. One of the equations relates these yields in the opposite-sign high-m_T region, the other relates them in the same-sign high-m_T region. Additionally relating the opposite-sign yields to the same-sign yields using the ratios of opposite-sign to same-sign QCD and W+jets events gives enough information to solve these equations for the yield of same-sign W+jets events. Writing the yield of process x in region y as N_x^y, this means, for $m_\mathrm{T} > 70\,\mathrm{GeV}$:

$$\begin{aligned}
N_\mathrm{data}^\text{SS, high m_T} - N_\mathrm{other}^\text{SS, high m_T} &= N_\mathrm{QCD}^\text{SS, high m_T} + N_\mathrm{W}^\text{SS, high m_T} \\
N_\mathrm{data}^\text{OS, high m_T} - N_\mathrm{other}^\text{OS, high m_T} &= N_\mathrm{QCD}^\text{OS, high m_T} + N_\mathrm{W}^\text{OS, high m_T} \\
&= R_\mathrm{QCD}^\mathrm{OS/SS} \cdot N_\mathrm{QCD}^\text{SS, high m_T} + R_\mathrm{W}^\mathrm{OS/SS} \cdot N_\mathrm{W}^\text{SS, high m_T}
\end{aligned}$$

$$\Rightarrow N_\mathrm{W}^\text{SS, high m_T} = \frac{N_\mathrm{data}^\text{OS, high m_T} - N_\mathrm{other}^\text{OS, high m_T} - R_\mathrm{QCD}^\mathrm{OS/SS} \cdot (N_\mathrm{data}^\text{SS, high m_T} - N_\mathrm{other}^\text{SS, high m_T})}{R_\mathrm{W}^\mathrm{OS/SS} - R_\mathrm{QCD}^\mathrm{OS/SS}}, \tag{5.6}$$

where $R_\mathrm{W}^\mathrm{OS/SS}$ is the ratio between opposite-sign and same-sign W+jets events and $R_\mathrm{QCD}^\mathrm{OS/SS}$ the ratio between opposite-sign and same-sign QCD events. Using equation 5.6, the number of W+jets events in the opposite-sign, high-m_T region is given by $R_\mathrm{W}^\mathrm{OS/SS} \cdot N_\mathrm{W}^\text{SS, high m_T}$. This is extrapolated to the number of W+jets events in the signal region at low m_T as:

$$N_\mathrm{W}^\text{OS, low m_T} = \frac{N_\mathrm{W,MC}^\text{OS, low m_T}}{N_\mathrm{W,MC}^\text{OS, high m_T}} \cdot R_\mathrm{W}^\mathrm{OS/SS} \cdot N_\mathrm{W}^\text{SS, high m_T}, \tag{5.7}$$

which means the estimate of the number of W+jets events in the opposite-sign, high-m_T, region is multiplied by a high-m_T to low-m_T extrapolation factor determined from simulation.

The use of the method presented relies on knowledge of $R_\mathrm{W}^\mathrm{OS/SS}$ and $R_\mathrm{QCD}^\mathrm{OS/SS}$, and on these two ratios not being too similar to each other. The ratio $R_\mathrm{QCD}^\mathrm{OS/SS}$ is measured in an anti-isolated control region in data; this measurement is described later in this section. $R_\mathrm{W}^\mathrm{OS/SS}$ is taken from the W+jets simulation, and is found to be between 4 and 5, while $R_\mathrm{QCD}^\mathrm{OS/SS}$ is close to 1.

The method described so far works well in the no b-tag categories, but in the b-tag category of both channels the $\mathrm{t\bar{t}}$ background dominates. This is illustrated in figure 5.16, where the high-m_T region in the no b-tag category, figure 5.16a, is compared with the high-m_T region in the b-tag category, figure 5.16b, of the $\mathrm{e}\tau_\mathrm{h}$ channel. It is clear that the $\mathrm{t\bar{t}}$ background is much larger than the W+jets background in the b-tag high-m_T control region. For this reason the estimate of the number of W+jets events in this category is made with a relaxed category selection where the b-tagging requirement itself is removed, but the jet requirements remain. Events with at least one jet with $p_{\mathrm{T}} > 20\,\mathrm{GeV}$ and with $|\eta| < 2.4$, but at most one jet with $p_{\mathrm{T}} > 30\,\mathrm{GeV}$ and $|\eta| < 4.7$, are therefore selected. The final W+jets estimate in the b-tag category signal region is determined by the estimate given by the number of W+jets events estimated in this one-jet selection, multiplied by an extrapolation factor $N_{\mathrm{W,MC}}^{\mathrm{OS,low}\ m_{\mathrm{T}},\mathrm{b\text{-}tag\ category}} / N_{\mathrm{W,MC}}^{\mathrm{OS,\ low}\ m_{\mathrm{T}},\mathrm{one\text{-}jet\ selection}}$.

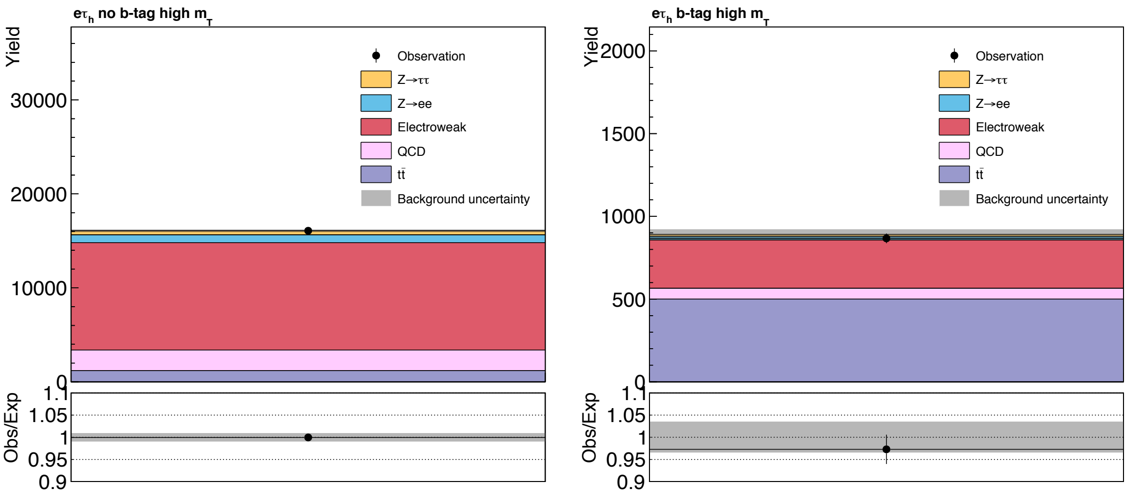

(a) No b-tag (b) B-tag

Figure 5.16: High-m_{T} control region in the (a) no b-tag and (b) b-tag categories of the $\mathrm{e}\tau_{\mathrm{h}}$ channel. In the no b-tag category the W+jets background, drawn together with the small di-boson plus single-top backgrounds as the 'electroweak' background component, dominates. In the b-tag category the $\mathrm{t\bar{t}}$ background is larger than the W+jets background.

QCD OS/SS ratio

The ratio of opposite-sign to same-sign QCD events, $R_{\mathrm{QCD}}^{\mathrm{OS/SS}}$, is measured in two anti-isolated sidebands by performing a fit to the distribution of the visible mass of the di-tau pair in opposite-sign events. The QCD template, which is taken from same-sign events assuming $R_{\mathrm{QCD}}^{\mathrm{OS/SS}} = 1$ is treated as the signal, and a binned maximum likelihood fit to $R_{\mathrm{QCD}}^{\mathrm{OS/SS}}$ is performed while allowing the other backgrounds to float within reasonable normalisation uncertainties. Of the two sidebands used, one is nearer the signal region, $0.15 < I_{\mathrm{rel}}^{\mu} < 0.25$ for the $\mu\tau_{\mathrm{h}}$ channel and $0.1 < I_{\mathrm{rel}}^{\mathrm{e}} < 0.2$ for the $\mathrm{e}\tau_{\mathrm{h}}$ channel, and one further away, $0.25 < I_{\mathrm{rel}}^{\mu} < 0.5$ for the $\mu\tau_{\mathrm{h}}$ channel and $0.2 < I_{\mathrm{rel}}^{\mathrm{e}} < 0.5$ for the $\mathrm{e}\tau_{\mathrm{h}}$ channel. The results of the fits, performed before the categorisation of events into the b-tag and no b-tag categories, are shown in figures 5.17 and 5.18 for the $\mu\tau_{\mathrm{h}}$ channel and in figures 5.19 and 5.20 for the $\mathrm{e}\tau_{\mathrm{h}}$ channel. The value of $R_{\mathrm{QCD}}^{\mathrm{OS/SS}}$ is found to be consistent between the two sidebands within 10% (1%) in the $\mathrm{e}\tau_{\mathrm{h}}$ ($\mu\tau_{\mathrm{h}}$) channel. Adding this uncertainty in quadrature to the uncertainty on the fit in the sidebands nearest the signal region gives an overall uncertainty of 12% in the $\mathrm{e}\tau_{\mathrm{h}}$ channel and 4% in the $\mu\tau_{\mathrm{h}}$ channel. The same fits can be performed in the no b-tag and b-tag categories to test if $R_{\mathrm{QCD}}^{\mathrm{OS/SS}}$ varies with the category selection, however it is found that the fit is not stable in the b-tag category due to the small number of events. The uncertainty on the ratio is increased for the b-tag category to cover the differences. The uncertainties are already large enough to cover differences between the inclusive $R_{\mathrm{QCD}}^{\mathrm{OS/SS}}$ and the fits as performed in the no b-tag category. Therefore $R_{\mathrm{QCD}}^{\mathrm{OS/SS}}$ in the $\mu\tau_{\mathrm{h}}$ channel is taken to be 1.18 in both the b-tag and the no b-tag category, with a 60% uncertainty in the b-tag category and a 4% uncertainty in the no b-tag category. In the $\mathrm{e}\tau_{\mathrm{h}}$ channel $R_{\mathrm{QCD}}^{\mathrm{OS/SS}}$ is taken to be 1.02 with a 60% uncertainty in the b-tag category and a 12% uncertainty in the no b-tag category.

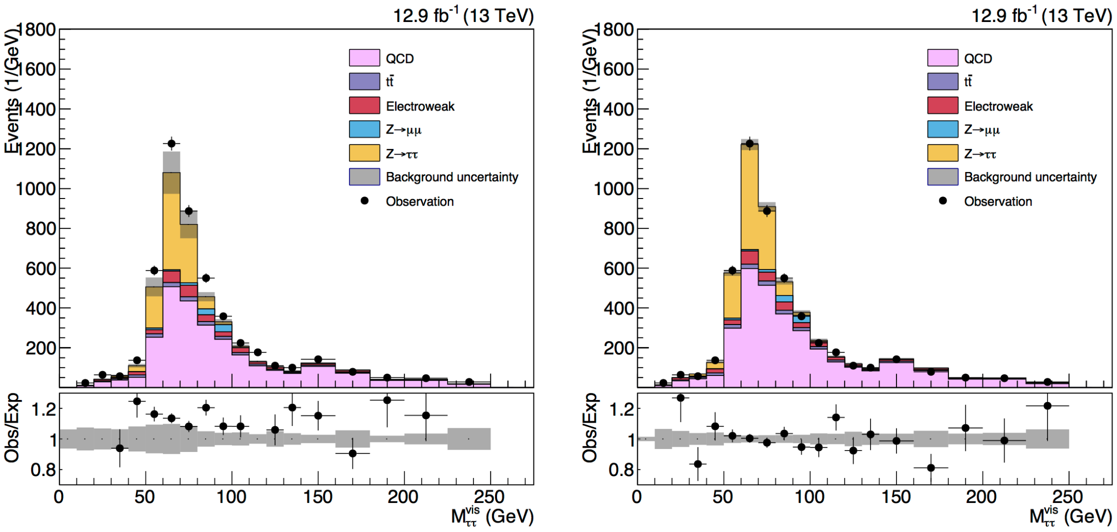

(a) Pre-fit distribution **(b)** Post-fit distribution

Figure 5.17: The visible mass distribution of the di-tau pair in the $\mu\tau_{\mathrm{h}}$ channel for the sideband near the signal region, (a) before the maximum likelihood fit to $R_{\mathrm{QCD}}^{\mathrm{OS/SS}}$ and (b) after the fit. The resulting value of $R_{\mathrm{QCD}}^{\mathrm{OS/SS}}$ is 1.18 ± 0.04.

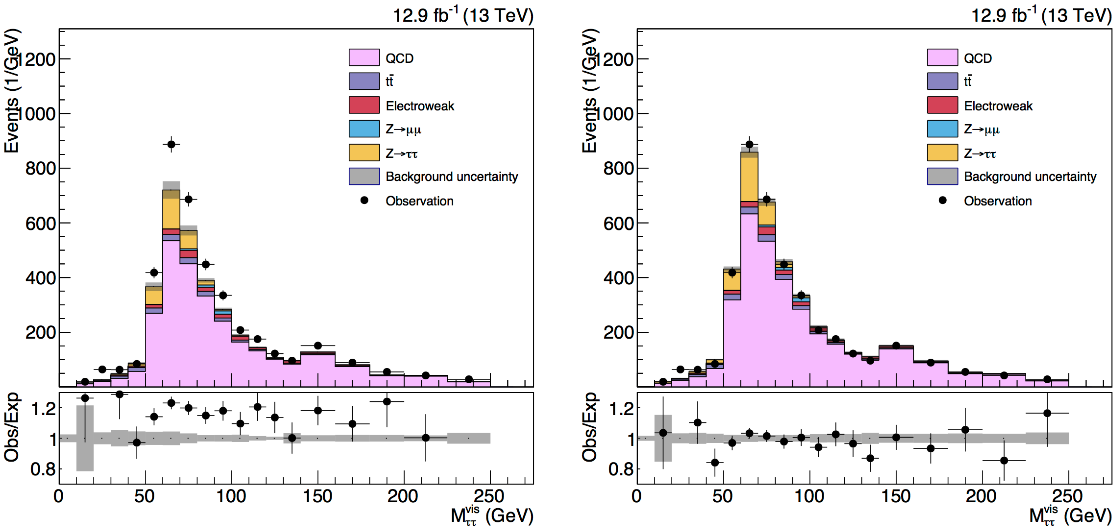

(a) Pre-fit distribution **(b)** Post-fit distribution

Figure 5.18: The visible mass distribution of the di-tau pair in the $\mu\tau_{\mathrm{h}}$ channel for the sideband further away from the signal region, (a) before the maximum likelihood fit to $R_{\mathrm{QCD}}^{\mathrm{OS/SS}}$ (b) after the fit. The resulting value of $R_{\mathrm{QCD}}^{\mathrm{OS/SS}}$ is 1.18 ± 0.04.

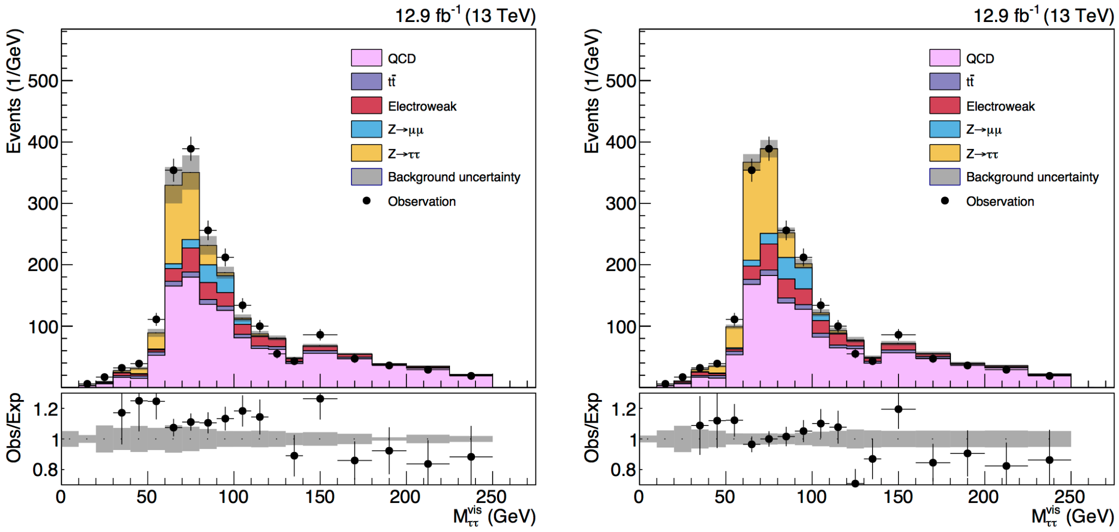

(a) Pre-fit distribution **(b)** Post-fit distribution

Figure 5.19: The visible mass distribution of the di-tau pair in the eτ_h channel for the sideband near the signal region, (a) before the maximum likelihood fit to $R_{\text{QCD}}^{\text{OS/SS}}$ and (b) after the fit. The resulting value of $R_{\text{QCD}}^{\text{OS/SS}}$ is 1.02 ± 0.06.

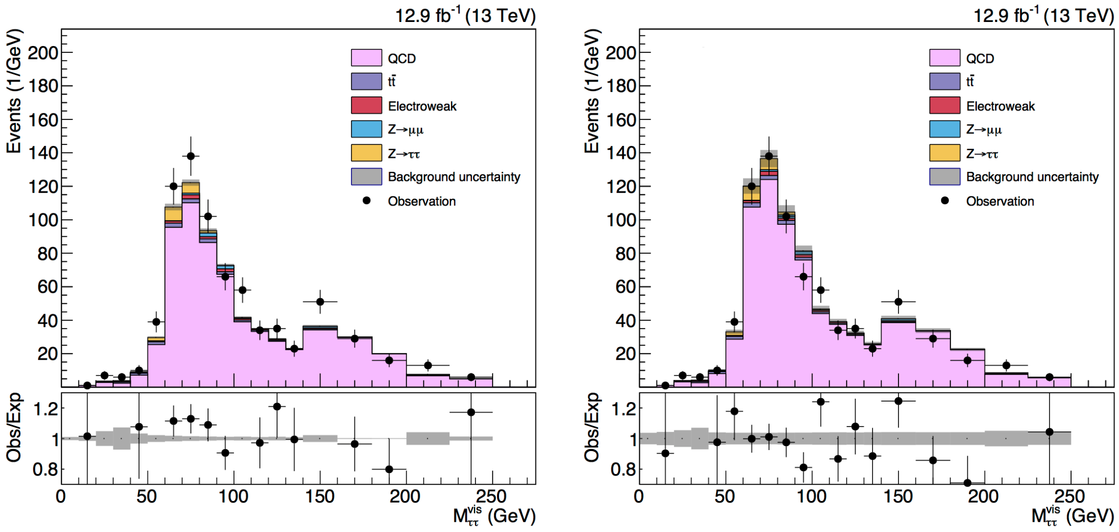

(a) Pre-fit distribution **(b)** Post-fit distribution

Figure 5.20: The visible mass distribution of the di-tau pair in the eτ_h channel for the sideband further away from the signal region, (a) before the maximum likelihood fit to $R_{\text{QCD}}^{\text{OS/SS}}$ and (b) after the fit. The resulting value of $R_{\text{QCD}}^{\text{OS/SS}}$ is 1.13 ± 0.05.

QCD normalisation

The QCD normalisation is estimated by inverting the opposite-sign requirement of the di-tau pair in the signal region. The yield is taken from this same-sign region with otherwise identical cuts to the opposite-sign region. The contributions from other backgrounds in this region are subtracted to give an estimate of the number of same-sign QCD events. For all backgrounds apart from W+jets the yields to subtract are estimated using simulation. The number of W+jets events expected in this region is given by

$$N_{\mathrm{W,SS\ low}\ m_{\mathrm{T}}} = \frac{N_{\mathrm{MC,SS\ low}\ m_{\mathrm{T}}}}{N_{\mathrm{MC,SS\ high}\ m_{\mathrm{T}}}} N_{\mathrm{W,SS\ high}\ m_{\mathrm{T}}}. \tag{5.8}$$

Because opposite-sign and same-sign QCD events do not necessarily appear in equal amounts the number of same-sign QCD events estimated as above is multiplied by $R_{\mathrm{QCD}}^{\mathrm{OS/SS}}$ to obtain an estimate of the number of QCD events in the signal region.

5.5.4 QCD in the $\tau_{\mathrm{h}}\tau_{\mathrm{h}}$ and eμ channels

This section describes the QCD background estimation in the $\tau_{\mathrm{h}}\tau_{\mathrm{h}}$ and eμ channels, which takes a slightly different form than in the $\mu\tau_{\mathrm{h}}$ and eτ_{h} channels.

$\tau_{\mathrm{h}}\tau_{\mathrm{h}}$ channel

In the $\tau_{\mathrm{h}}\tau_{\mathrm{h}}$ channel QCD events constitute by far the dominant background. The normalisation and shape of this background are estimated from a sideband with relaxed isolation requirements with respect to the signal region. In the no b-tag category the sideband used is defined by having the τ_{h} with highest p_{T} pass the tight working point of the tau isolation discriminator, as in the nominal selection. The other τ_{h} is required to fail the tight working point, but pass the medium working point. This sideband is chosen as it is as close to the signal region as possible, and this should minimise biases in the shape of the total transverse mass distribution. Other backgrounds in this sideband are subtracted from the observation to give the QCD estimate. Differences in normalisation due to the use of a loosened sideband are corrected for by the medium-to-tight isolation scale factor. This correction factor is measured as

$$R_{\mathrm{QCD}}^{\mathrm{medium}\rightarrow\mathrm{tight}} = \frac{N_{\mathrm{data}}^{SS,\mathrm{nominal\ isolation}} - N_{\mathrm{other\ bkgs}}^{SS,\mathrm{nominal\ isolation}}}{N_{\mathrm{data}}^{SS,\mathrm{loosened\ isolation}} - N_{\mathrm{other\ bkgs}}^{SS,\mathrm{loosened\ isolation}}}. \tag{5.9}$$

This correction factor takes the ratio between the background-subtracted data in regions equivalent to the signal region and the sideband with relaxed isolation, but with the charge requirement on the pair inverted.

The QCD estimate in the b-tag category is derived using an analogous method, however, the sideband as used for the no b-tag category does not contain enough events to provide a background estimate. Therefore a sideband where the highest p_T τ_h passes the tight working point of the tau isolation discriminator, and the other τ_h passes the loose working point of the discriminator, but not the tight working point, is used.

eμ channel

In the eμ channel the QCD background is estimated by inverting the charge requirement of the pair, considering the same-sign region with otherwise identical cuts to the signal region. Other backgrounds present in this region are subtracted. As for the eτ_h and $\mu\tau_\mathrm{h}$ channels, the number of QCD events with opposite-sign eμ pairs is not necessarily equal to the number of QCD events with same-sign eμ pairs and therefore the ratio of opposite-sign to same-sign pairs is measured by inverting the isolation requirements on the electron or muon. Both leptons need to satisfy $I_\mathrm{rel} < 0.4$ and at least one of them needs to fail the nominal isolation requirement. The OS/SS ratio is parameterised in terms of lepton kinematics and the separation in ΔR between the two leptons. These ratios are then applied to events in the same-sign region to give an estimate in the signal region. The statistical uncertainty in the measurement is 13%. Cross-checking the measurement using QCD simulation, it is observed that there is a 19% difference between the OS/SS ratio in the signal region and the sideband, the two uncertainties are added in quadrature. The OS/SS ratios are measured before applying the categorisation, and because studies of simulated events suggest that the OS/SS ratio is different in the b-tag category than in the no b-tag category, an extra scale factor of 0.66 ± 0.16 is applied to the QCD estimate in the b-tag category. This is the ratio between the OS/SS ratio as measured in the b-tag category and the measurement made before categorisation. The uncertainty is added in quadrature to the statistical and systematic uncertainties already described.

5.5.5 $\mathrm{t\bar{t}}$

The $\mathrm{t\bar{t}}$ shape and normalisation are estimated from simulation and are checked against data in a control region with a $\mathrm{t\bar{t}}$ purity of 91%. This control region is defined as $D_\zeta < -20\,\mathrm{GeV}$ and $E_\mathrm{T}^\mathrm{miss} > 80\,\mathrm{GeV}$ in the eμ channel, and it is shown in figure 5.12b.

Because the 6% $\mathrm{t\bar{t}}$ normalisation uncertainty covers the observed discrepancy between data and simulation, no scale factor is applied. In the $\mu\tau_\mathrm{h}$, $\mathrm{e}\tau_\mathrm{h}$ and $\tau_\mathrm{h}\tau_\mathrm{h}$ channels the $\mathrm{t\bar{t}}$ contribution is split into two components, one with real hadronic taus and one without, for fitting purposes. The component with real hadronic taus is composed of $\mathrm{t\bar{t}}$ events in which the hadronic tau is matched to a simulated hadronic tau. In the fully hadronic channel both hadronic taus need to be matched to simulated hadronic taus.

5.5.6 Other backgrounds

For all channels the di-boson and single-top backgrounds are small. Both normalisation and shape are estimated from simulation. For the $\mathrm{e}\tau_\mathrm{h}$, $\mu\tau_\mathrm{h}$ and $\tau_\mathrm{h}\tau_\mathrm{h}$ channels this background contribution is split into a component where the hadronically decaying tau originates from a real hadronic tau, and one where it does not. This is done in a similar way as for the $\mathrm{t\bar{t}}$ background. In the $\tau_\mathrm{h}\tau_\mathrm{h}$ and $\mathrm{e}\mu$ channels the W+jets background is less important than in the $\mathrm{e}\tau_\mathrm{h}$ and $\mu\tau_\mathrm{h}$ channels, and both its shape and normalisation are estimated from simulation. In the $\mathrm{e}\mu$ channel the W+γ background is also added to the W+jets background component.

5.6 Systematic uncertainties

As for the H → hh → $\mathrm{bb}\tau\tau$ analysis two types of systematic uncertainty are considered. Normalisation uncertainties only affect the yield of a process while shape uncertainties affect both the process normalisation and the shape of the $m_\mathrm{T}^\mathrm{tot}$ distribution. The uncertainties are taken into account in the final result as described in section 4.8.1.

Overview tables of the systematic uncertainties per category of each channel can be found in appendix B. The correlations between the different channels and categories for these uncertainties are also indicated.

5.6.1 Normalisation uncertainties

Luminosity uncertainty

The uncertainty in the luminosity measurement amounts to 6.2% for data collected during 2016 [142], and it is applied to all processes for which the normalisation is estimated using simulation.

Identification, isolation and trigger efficiencies

The combined uncertainty in the electron and muon identification, isolation, and trigger efficiencies amounts to 2%. For hadronic taus the identification and isolation uncertainty amounts to 6% per τ_h in the $\mathrm{e}\tau_\mathrm{h}$, $\mu\tau_\mathrm{h}$ and $\tau_\mathrm{h}\tau_\mathrm{h}$ channels, with an additional 7% uncertainty in the tau trigger efficiency added in quadrature for the $\tau_\mathrm{h}\tau_\mathrm{h}$ channel. This uncertainty is split between a part that is correlated between the channels and a part that is not. The correlated part amounts to a 5% (10%) uncertainty in the $\mathrm{e}\tau_\mathrm{h}$ and $\mu\tau_\mathrm{h}$ ($\tau_\mathrm{h}\tau_\mathrm{h}$) channels. The uncorrelated part amounts to 3% (9.2%) for the $\mathrm{e}\tau_\mathrm{h}$ and $\mu\tau_\mathrm{h}$ ($\tau_\mathrm{h}\tau_\mathrm{h}$) channels. The uncertainties on lepton and hadronic tau identification, isolation and trigger efficiency are applied to all processes for which the normalisation is estimated using simulation.

jet → τ_h fake rate

The uncertainty in the jet → τ_h fake rate measurement is 20% [119]. This uncertainty is applied to those backgrounds where the normalisation is estimated using simulation and where the hadronic taus are faked by jets, that is the $\mathrm{Z}/\gamma^* \to \ell\ell$ background with a jet faking a hadronic tau, the W+jets background in the fully hadronic channel, and the $\mathrm{t\bar{t}}$ background without real hadronic taus.

e → τ_h and $\mu \to \tau_\mathrm{h}$ fake rates

The e → τ_h fake rate uncertainty ranges from 10–30% depending on the anti-electron discriminator used [119]. This uncertainty is applied to the $\mathrm{Z}/\gamma^* \to \ell\ell$ background in which the hadronic tau is faked by an electron. The $\mu \to \tau_\mathrm{h}$ fake rate uncertainty ranges from 20–30% depending on the anti-muon discriminator used. This uncertainty is applied to the $\mathrm{Z}/\gamma^* \to \ell\ell$ background in which the hadronic tau is faked by a muon.

Jet energy scale uncertainty

The uncertainty in the jet energy corrections is applied by shifting the jet energy up and down by a p_T- and η-dependent uncertainty, and evaluating the change in the process normalisation in each category. The uncertainty ranges from 0–10% depending on process and category.

b-Tag scale factors

Uncertainties in the b-tagging efficiency and light jet mis-tagging rates are given as a function of jet p_T and η for the medium working point of the CSVv2 discriminator [114].

The b-tagging scale factors are varied within these uncertainties and the overall change in normalisation for each process in each category is evaluated. The uncertainty varies from 0–5%.

$E_{\mathrm{T}}^{\mathrm{miss}}$ resolution and response

Uncertainties in the $E_{\mathrm{T}}^{\mathrm{miss}}$ resolution and response are estimated by varying the recoil correction parameters within their uncertainties and evaluating the effect on process normalisations. The uncertainty amounts to around 2%.

Background normalisation uncertainties

- $\mathrm{Z}/\gamma^* \rightarrow \tau\tau$: As the $\mathrm{Z}/\gamma^* \rightarrow \mu\mu$ control region is included in the simultaneous fit with the signal region to correct the $\mathrm{Z}/\gamma^* \rightarrow \tau\tau$ normalisation, the Drell-Yan cross section uncertainty is not applied. In the no b-tag (b-tag) category a 3% (5%) extrapolation uncertainty from the kinematic phase space of the $\mathrm{Z}/\gamma^* \rightarrow \mu\mu$ to the $\mathrm{Z}/\gamma^* \rightarrow \tau\tau$ selection is applied.
- $\mathrm{Z}/\gamma^* \rightarrow \ell\ell$: The uncertainty in the Drell-Yan cross section is 4% [143].
- $\mathrm{t\bar{t}}$: The uncertainty in the $\mathrm{t\bar{t}}$ production cross section amounts to 6% [144].
- Di-boson and single-top: The combined uncertainty in the di-boson and single-top production cross sections amounts to 5% [145–147].
- W+jets: In the $\mu\tau_{\mathrm{h}}$ and $\mathrm{e}\tau_{\mathrm{h}}$ channels the statistical uncertainties in the observed data and subtracted backgrounds in the control regions are taken into account by the inclusion of these control regions in the fit. The statistical uncertainty in $R_{\mathrm{W}}^{\mathrm{OS/SS}}$ amounts to 2% in the no b-tag category in both the $\mathrm{e}\tau_{\mathrm{h}}$ and $\mu\tau_{\mathrm{h}}$ channels, and 11% (14%) in the b-tag category of the $\mu\tau_{\mathrm{h}}$ ($\mathrm{e}\tau_{\mathrm{h}}$) channel. The systematic uncertainty in this ratio amounts to 8% (10%) in the no b-tag (b-tag) category of both channels. The statistical uncertainty in the low-m_{T} to high-m_{T} ratio is 2% in the no b-tag category of both channels and 14% (17%) in the b-tag category of the $\mu\tau_{\mathrm{h}}$ ($\mathrm{e}\tau_{\mathrm{h}}$) channel. The systematic uncertainty in this ratio amounts to 20%. As the W+jets background in the $\tau_{\mathrm{h}}\tau_{\mathrm{h}}$ and $\mathrm{e}\mu$ channels is estimated from simulation a 4% theoretical production cross section uncertainty is applied [143].
- QCD: In the $\mathrm{e}\mu$ channel the uncertainty in the QCD estimate is taken as the uncertainty on the measured opposite-sign to same-sign ratio, which is 23% in the no b-tag category and 34% in the b-tag category. In the $\tau_{\mathrm{h}}\tau_{\mathrm{h}}$ channel the statistical uncertainty in the QCD estimate is derived from the uncertainties in

the observations and subtracted backgrounds in the sidebands used to derive the estimate. This uncertainty amounts to 3% in the no b-tag category and 20% in the b-tag category. An additional systematic uncertainty in the extrapolation factor from the anti-isolated sideband into the signal region is found to be 12% in the no b-tag category and 14% in the b-tag category. For the $e\tau_h$ and $\mu\tau_h$ channels the statistical uncertainties in the observation and subtracted backgrounds in the control regions used to derive the QCD estimate is accounted for by the inclusion of these control regions in the fit. The uncertainty in the opposite-sign to same-sign ratio, based on the studies described in section 5.5.3 is found to be 4% (60%) in the no b-tag (b-tag) category of the $\mu\tau_h$ channel, and 12% (60%) in the no b-tag (b-tag) category of the $e\tau_h$ channel.

Signal theory uncertainties

For interpretations of the results in MSSM benchmark scenarios, theory uncertainties in the SM and MSSM Higgs boson cross section predictions are taken into account. The uncertainties for the SM signal processes are described in more detail in reference [32]. Uncertainties due to different renormalisation and factorisation scales amount to 3.9% for gluon fusion, 0.4% for VBF, 2.8% for ZH and 0.5% for WH. The uncertainties due to different choices of pdf set and α_s amount to 3.2% for gluon fusion, 2.1% for VBF, 1.6% for ZH and 1.9% for WH. For the MSSM Higgs boson cross sections used in the models, the uncertainties due to different choices of factorisation and renormalisation scale and the choice of pdf set are computed, separately for each m_A-$\tan\beta$ point, following the prescription in references [148, 149].

5.6.2 Shape uncertainties

τ_h energy scale

The energy of hadronic taus is varied up and down by 3%, affecting the shape of the total transverse mass distribution. The uncertainty is applied to the signals and to backgrounds containing real hadronic taus in the $e\tau_h$, $\mu\tau_h$, and $\tau_h\tau_h$ channels, namely $Z/\gamma^* \to \tau\tau$, and the components of the $t\bar{t}$, single-top and di-boson backgrounds with real hadronic taus.

Electron energy scale

The energy of electrons is varied by 1% in the barrel and by 2.5% in the endcaps. This uncertainty is applied to the signals and to the $Z/\gamma^* \to \tau\tau$ background in the $e\mu$ channel.

High-p_T τ_h identification efficiency

An additional τ_h identification uncertainty of $\frac{20\%\times p_\mathrm{T}}{\mathrm{TeV}}$ is applied to account for the extrapolation from the tau ID efficiency measurement, which mostly uses di-tau events close to the Z peak, to taus with higher transverse momenta. This uncertainty is applied to signals and backgrounds with real taus in the $\mathrm{e}\tau_\mathrm{h}$, $\mu\tau_\mathrm{h}$ and $\tau_\mathrm{h}\tau_\mathrm{h}$ channels. The shape difference between the nominal, up and down shapes for this uncertainty in the no b-tag category of the $\tau_\mathrm{h}\tau_\mathrm{h}$ channel can be seen for a high-mass signal sample in figure 5.21a and for the $\mathrm{Z}/\gamma^* \rightarrow \tau\tau$ background in figure 5.21b. Because the $\mathrm{Z}/\gamma^* \rightarrow \tau\tau$ background has much softer hadronic taus than the high-mass signal sample, the impact of this uncertainty on the shape is much smaller.

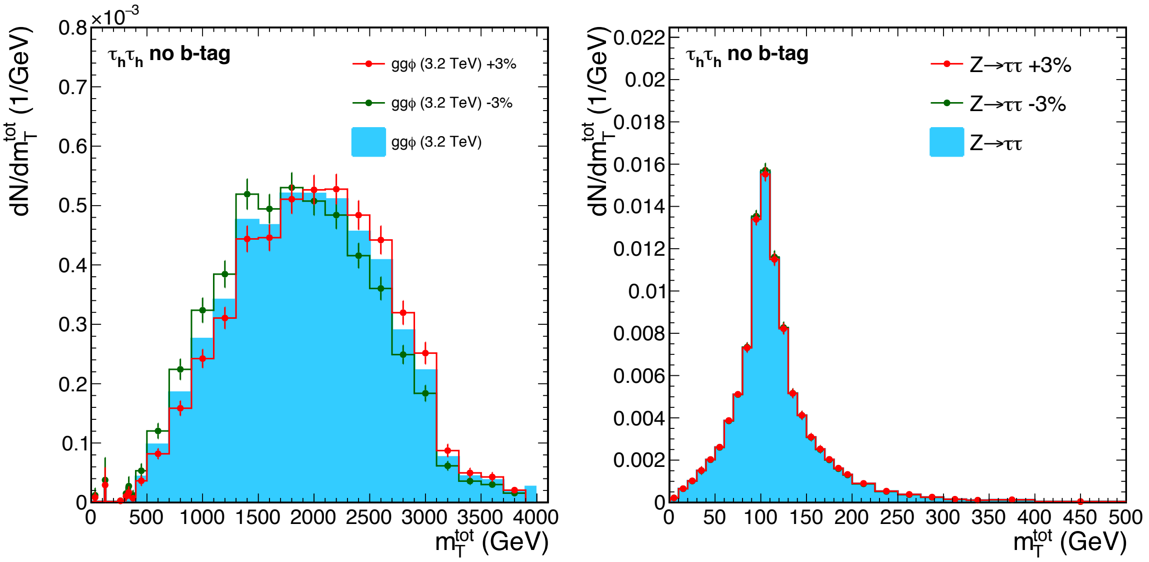

(a) ggϕ signal at $m_\phi = 3.2\,\mathrm{TeV}$ **(b)** $\mathrm{Z}/\gamma^* \rightarrow \tau\tau$ background

Figure 5.21: Impact of the high-p_T tau ID uncertainty in the no b-tag category of the $\tau_\mathrm{h}\tau_\mathrm{h}$ channel for (a) a high-mass signal sample and (b) the $\mathrm{Z}/\gamma^* \rightarrow \tau\tau$ background. The effect on the shape is larger in the high-mass signal sample, which contains hadronically decaying taus with much higher p_T than the $\mathrm{Z}/\gamma^* \rightarrow \tau\tau$ sample.

Top quark p_T reweighting

To account for the uncertainty in the derivation of the top-quark p_T reweighting, a shape uncertainty is applied to the $\mathrm{t\bar{t}}$ background. This uncertainty amounts to a 100% variation of the correction, that is the difference between applying the correction twice and not applying the correction at all.

Drell-Yan shape reweighting

An uncertainty in the Drell-Yan shape reweighting based on $Z/\gamma^* \rightarrow \mu\mu$ events is applied as 100% of the correction to the $Z/\gamma^* \rightarrow \tau\tau$ background.

Jet → τ_h fake rate shape reweighting

On the W+jets background in the $e\tau_h$ and $\mu\tau_h$ channels a shape uncertainty of $\frac{20\% \times p_T}{\text{GeV}}$ is applied. This uncertainty is derived from variations in the data to simulation ratio for the jet → τ_h fake rate as a function of jet p_T in W+jets events.

5.7 Signal extraction

The total transverse mass m_T^{tot} is used as the discriminating variable for signal extraction in this analysis. Binned distributions of this variable are used to perform a shape analysis. The general statistical methods, including the incorporation of nuisance parameters in the fit, were described in section 4.8.1. Some additional methods are used for this analysis, and they will be discussed in this section.

5.7.1 Inclusion of control regions in the fit

The control regions used for the estimation of the W+jets and QCD background contributions in the signal regions are included in the fit. They are added to the likelihood as single-bin counting experiments. In a given category of one of the channels, the W+jets normalisation is fully correlated between the three control regions and the signal region. One common, unconstrained, nuisance parameter controls the W+jets normalisation in all four regions. The QCD normalisation is fully correlated between the opposite-sign and same-sign low-m_T regions. The same is true for the QCD normalisation in the opposite-sign and same-sign high-m_T regions. This means there are two unconstrained nuisance parameters that govern the QCD normalisation: one that controls the normalisation in the two low-m_T regions, and one that controls it in the two high-m_T regions.

The $Z/\gamma^* \rightarrow \mu\mu$ control regions mentioned in section 5.5.2 are also included in the likelihood as single-bin counting experiments. The $Z/\gamma^* \rightarrow \mu\mu$ control region in the no b-tag category is tied to the $Z/\gamma^* \rightarrow \tau\tau$ normalisation in the no b-tag categories of all four channels, again being controlled by an unconstrained nuisance parameter. The same is true for the $Z/\gamma^* \rightarrow \mu\mu$ control region in the b-tag category and the $Z/\gamma^* \rightarrow \tau\tau$ normalisation in the b-tag categories of all four channels.

5.7.2 Signal process profiling and 2D likelihood scans

Because the analysis targets the two main MSSM production modes, gluon fusion and b-associated production, limits are set on these two signal processes. As discussed in section 5.2.6 the two signals cannot be fully separated by means of the categorisation used. However, in the upper limits on $\sigma\times\mathcal{B}$ for the ggϕ process no assumptions should be made about the presence or lack of the bbϕ process and vice versa. Therefore, when calculating the upper limits on the ggϕ (bbϕ) process, the contribution of the bbϕ (ggϕ) process is profiled. This means it is allowed to vary freely in the fit like a nuisance parameter.

Because the analysis targets these two signal processes, it is possible to redefine the likelihood as a function of both the ggϕ and bbϕ signals:

$$\mathcal{L}(\text{data}|\mu_{\text{gg}\phi}, \mu_{\text{bb}\phi}, \theta) = \mathcal{L}(\text{data}|\mu_{\text{gg}\phi}\cdot s_{\text{gg}\phi}(\theta) + \mu_{\text{bb}\phi}\cdot s_{\text{bb}\phi}(\theta) + b(\theta)), \tag{5.10}$$

where $s_{\text{gg}\phi}$ and $s_{\text{bb}\phi}$ are the signal expectations of the two production processes and the signal strength modifiers $\mu_{\text{gg}\phi}$ and $\mu_{\text{bb}\phi}$ now represent the $\sigma\times\mathcal{B}$ of the two processes. Using this definition a likelihood scan in two dimensions can be performed. First a 2D grid in $\mu_{\text{gg}\phi}$ and $\mu_{\text{bb}\phi}$, both required to be greater than or equal to zero, is constructed. The negative log-likelihood,

$$\text{NLL} = -\ln\,\mathcal{L}(\text{data}|\mu_{gg\phi}, \mu_{bb\phi}, \theta), \tag{5.11}$$

is then evaluated at each point. The point in the 2D grid where the NLL reaches its lowest value gives the best fit values for $\mu_{\text{gg}\phi}$ and $\mu_{\text{bb}\phi}$. The 68% and 95% confidence level regions are constructed as the values $\mu_{\text{gg}\phi}^{N\%}$ and $\mu_{\text{bb}\phi}^{N\%}$ for which:

$$\begin{aligned}\Delta(\text{NLL})_{68\%} &= \text{NLL}(\mu_{\text{gg}\phi}^{68\%}, \mu_{\text{bb}\phi}^{68\%}) - \text{NLL}(\text{best fit}) = 1.14,\\ \Delta(\text{NLL})_{95\%} &= \text{NLL}(\mu_{\text{gg}\phi}^{95\%}, \mu_{\text{bb}\phi}^{95\%}) - \text{NLL}(\text{best fit}) = 3.00.\end{aligned} \tag{5.12}$$

5.7.3 MSSM vs SM hypothesis testing

The results of the search are interpreted in MSSM benchmark scenarios, with the interpretation made in the m_{A}-$\tan\beta$ plane. At each point in the m_{A}-$\tan\beta$ plane each MSSM scenario predicts a production cross section, and a corresponding branching ratio into $\tau\tau$, for each of the three neutral Higgs bosons. The masses of the light h and the scalar H are also given as a function of m_{A} and $\tan\beta$. To interpret the results of this search in a particular scenario, the predicted signal from the three neutral Higgs bosons is combined into a single signal template[1]. In this way the compatibility of the data with all three Higgs bosons, not just a single one, is tested.

Simply comparing a three-Higgs-signal-plus-background hypothesis with a background-only hypothesis to determine the exclusion power of the search in a particular model is not strictly correct. Due to the existence of a Higgs boson with a mass of 125 GeV, all MSSM benchmark scenarios must include a light Higgs boson with very similar properties to the boson discovered during Run 1 of the LHC. Therefore a test that distinguishes between a three-Higgs-signal-plus-background hypothesis, and a standard model Higgs-signal-plus-background hypothesis, should be performed.

This means the likelihood function defined in equation 4.12 must be modified. Instead of testing for the compatibility of the data with a signal-plus-background expectation modified by the signal strength modifier μ as $\mu \cdot s(\theta) + b(\theta)$, a likelihood should be constructed as:

$$\mathcal{L}(\mathrm{data}|\mu,\theta) = \mathcal{L}(\mathrm{data}|\mu \cdot s_{\mathrm{MSSM}}(\theta) + (1-\mu)\cdot s_{\mathrm{SM}}(\theta) + b(\theta)), \tag{5.13}$$

where $s_{\mathrm{MSSM}}(\theta)$ corresponds to the MSSM signal expectation, that is the three-Higgs-signal, and $s_{\mathrm{SM}}(\theta)$ corresponds to the SM signal expectation. The signal strength modifier μ takes the role of distinguishing between the two hypotheses in this case. The model must not allow for the non-physical coexistence of the SM and MSSM hypotheses; the MSSM hypothesis ($\mu = 1$) has to be tested against the SM hypothesis ($\mu = 0$).

The modification of the likelihood function means it is no longer possible to use the profile likelihood ratio of equation 4.14: a test of $\mu = 1$ against $\mu = 0$ has to be made, and $\hat{\mu}$ in the denominator of equation 4.14 is in general not zero. A solution to this problem can be found in the test statistic used at the Tevatron [23, 131],

$$q_{\mu} = -2\ln\frac{\mathcal{L}(\mathrm{data}|\mu,\hat{\theta}_{\mu})}{\mathcal{L}(\mathrm{data}|0,\hat{\theta}_{0})} \text{ with } 0 \leq \mu. \tag{5.14}$$

---

[1] Examples of what such a combined signal profile might look like are given in figures 5.23–5.26, which give the $m_{\mathrm{T}}^{\mathrm{tot}}$ distributions for all channels and categories with an example three-Higgs boson signal overlaid.

In this test statistic a positive value of μ is tested against $\mu = 0$, thus the desired 'MSSMvsSM' test statistic can be defined, using $\mu = 1$, as,

$$q_{\mathrm{MSSMvsSM}} = -2\ln \frac{\mathcal{L}(\mathrm{data}|s_{\mathrm{MSSM}}(\theta) + b(\theta))}{\mathcal{L}(\mathrm{data}|s_{\mathrm{SM}}(\theta) + b(\theta))}. \tag{5.15}$$

The asymptotic approximation, discussed in section 4.8.1, cannot be applied to this test statistic, and therefore the probability density functions need to be generated with toy datasets. Using these probability density functions, $\mathrm{CL}_s(\mu = 1)$ can be calculated as defined in equation 4.17. If $\mathrm{CL}_s < 0.05$, the MSSM hypothesis is excluded at the 95% CL. The generation of toy datasets and calculation of corresponding CL_s values is performed for many points in a grid in the m_{A}-$\tan\beta$ plane, with interpolation between grid points performed to obtain a smooth exclusion contour. The probability distribution functions for the SM and MSSM hypotheses, as well as the resulting CL_s values, are given for three illustrative m_{A}-$\tan\beta$ points in figure 5.22. In figure 5.22a there is no separation between the MSSM and SM distributions, and so this point cannot be excluded. The separation between the distributions in figure 5.22b is much improved, and the observation is most compatible with the SM hypothesis. This point is on the edge of being excluded. Finally the distributions in figure 5.22c are very well separated, and the observation is compatible with the SM hypothesis, meaning this point of the parameter space is excluded.

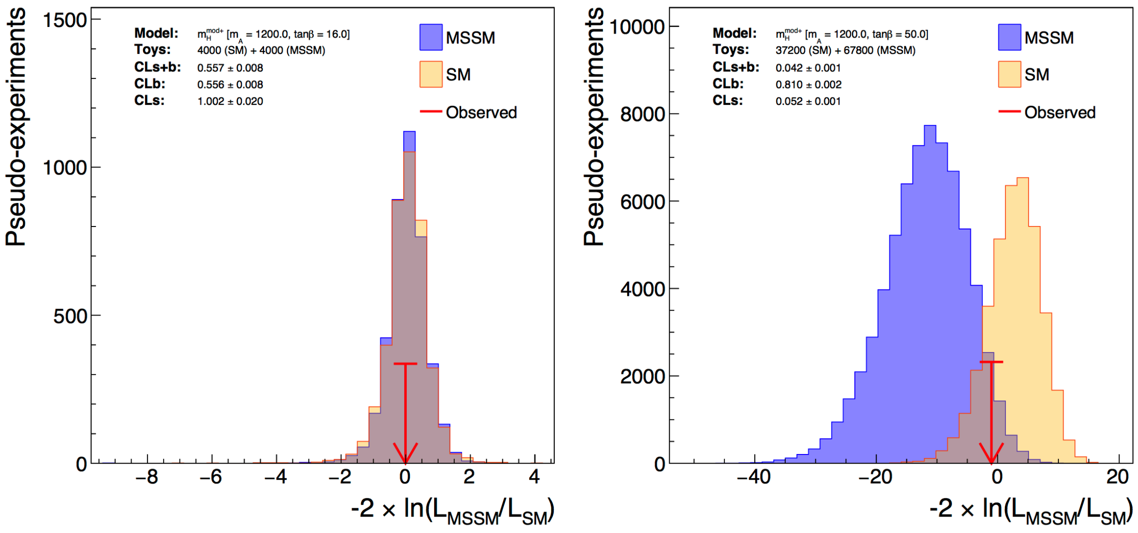

(a) $m_{\mathrm{A}} = 1.2\,\mathrm{TeV}$, $\tan\beta = 16$ **(b)** $m_{\mathrm{A}} = 1.2\,\mathrm{TeV}$, $\tan\beta = 50$

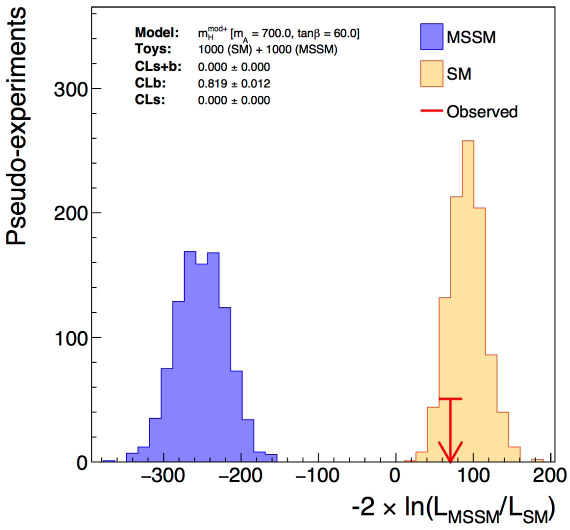

(c) $m_{\mathrm{A}} = 700\,\mathrm{GeV}$, $\tan\beta = 60$

Figure 5.22: Distributions of the test statistic, obtained by generating a large number of toy datasets, for the SM and MSSM hypotheses at three different points in the $m_{\mathrm{h}}^{\mathrm{mod+}}$ scenario, each with different levels of separation between the MSSM and SM distributions.

5.8 Results

5.8.1 Model-independent results

The $m_{\mathrm{T}}^{\mathrm{tot}}$ distributions in the no b-tag and b-tag categories of all channels, after the fit to the observed data has been performed, are shown in figures 5.23–5.26. The signal of the three neutral Higgs bosons at $m_{\mathrm{A}} = 1\,\mathrm{TeV}$ and $\tan\beta = 50$ in the $m_{\mathrm{h}}^{\mathrm{mod+}}$ scenario is overlaid on the total transverse mass distributions. The signal peaks twice due to the presence of a light Higgs boson with mass compatible with 125 GeV in this model, which is necessary to incorporate the Higgs boson observed at 125 GeV. The numbers of observed events, compared with the background expectation, are given in appendix C.

Out of the 400 nuisance parameters in this analysis, in the fit to data 14 are pulled by more than one standard deviation and none by more than two standard deviations. It is reasonable for a small fraction of the pulls to be greater than one standard deviation. In the low-mass region the dominant systematic uncertainties are the uncertainty related to the Drell-Yan shape reweighting, the QCD OS/SS ratio uncertainties, the τ_{h} identification efficiency uncertainty, and the high-m_{T} to low-m_{T} extrapolation uncertainty for the W+jets background. Above around 800 GeV the analysis becomes more statistically limited. In this region dominant uncertainties are due to the limited numbers of available simulated events in the background templates, the Drell-Yan shape reweighting uncertainty, the high-p_{T} τ_{h} identification efficiency uncertainty and the τ_{h} energy scale uncertainty.

None of these distributions show a significant excess of observed events over the background expectation. The 95% CL upper limits on $\sigma\times\mathcal{B}$ are shown in figure 5.27a for gluon fusion and in figure 5.27b for b-associated production. All channels and categories are combined.

A comparison of the expected limits per channel is shown in figure 5.28a for ggϕ production and in figure 5.28b for bbϕ production. These figures show that the $\mu\tau_{\mathrm{h}}$ channel is the most sensitive at masses up to 200 GeV, beyond which the $\tau_{\mathrm{h}}\tau_{\mathrm{h}}$ channel becomes more sensitive. The eτ_{h} channel is always slightly less sensitive than the $\mu\tau_{\mathrm{h}}$ channel. The eμ channel is the least sensitive over a large part of the mass range, until it overtakes the eτ_{h} channel in sensitivity at 1.6 TeV and is slightly more sensitive than the $\mu\tau_{\mathrm{h}}$ channel at 3.2 TeV. The eμ channel becomes more sensitive than the other channels at higher masses as a narrower binning of the $m_{\mathrm{T}}^{\mathrm{tot}}$ distribution is possible than for the other channels. The $m_{\mathrm{T}}^{\mathrm{tot}}$ distribution for the high mass signals is therefore wide enough to span more than the highest $m_{\mathrm{T}}^{\mathrm{tot}}$ bin used in the fit. This means at high mass this channel benefits more from the shape discrimination between signal and backgrounds than the other channels.

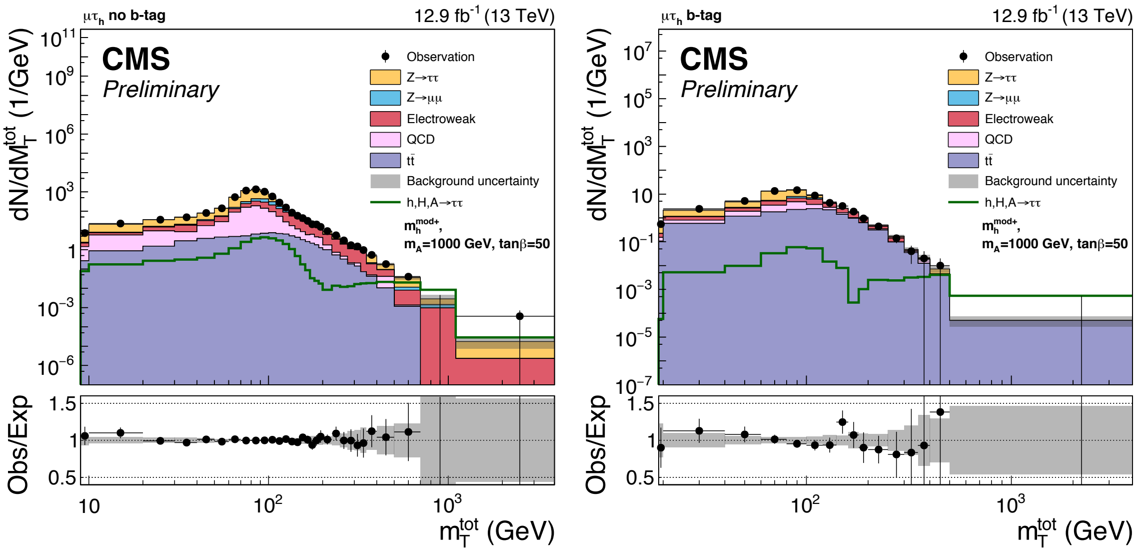

(a) No b-tag **(b)** B-tag

Figure 5.23: Distributions of $m_{\mathrm{T}}^{\mathrm{tot}}$ in the (a) no b-tag and (b) b-tag categories of the $\mu\tau_{\mathrm{h}}$ channel. The signal of the three neutral Higgs bosons at $m_{\mathrm{A}} = 1\,\mathrm{TeV}$ and $\tan\beta = 50$ in the $m_{\mathrm{h}}^{\mathrm{mod+}}$ scenario is overlaid. Note that, to incorporate the observed Higgs boson at 125 GeV, the $m_{\mathrm{h}}^{\mathrm{mod+}}$ scenario includes an h boson at around 125 GeV with a much larger $\sigma\times\mathcal{B}$ than the 1 TeV H and A bosons, and this is the reason for the doubly-peaking shape of the overlaid signal [2].

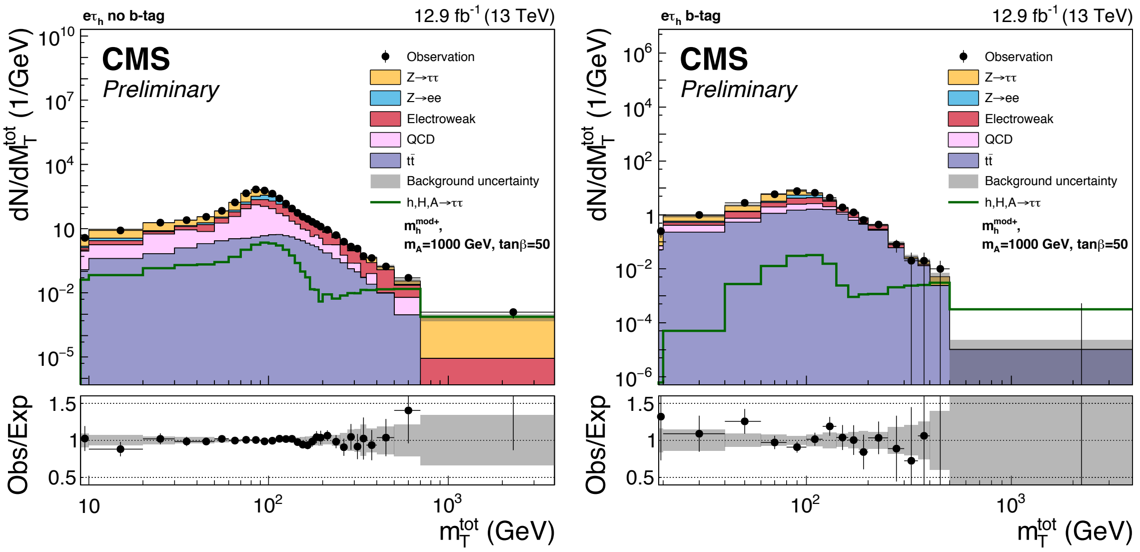

(a) No b-tag **(b)** B-tag

Figure 5.24: Distributions of $m_{\mathrm{T}}^{\mathrm{tot}}$ in the (a) no b-tag and (b) b-tag categories of the $\mathrm{e}\tau_{\mathrm{h}}$ channel. The signal of the three neutral Higgs bosons at $m_{\mathrm{A}} = 1\,\mathrm{TeV}$ and $\tan\beta = 50$ in the $m_{\mathrm{h}}^{\mathrm{mod+}}$ scenario is overlaid [2].

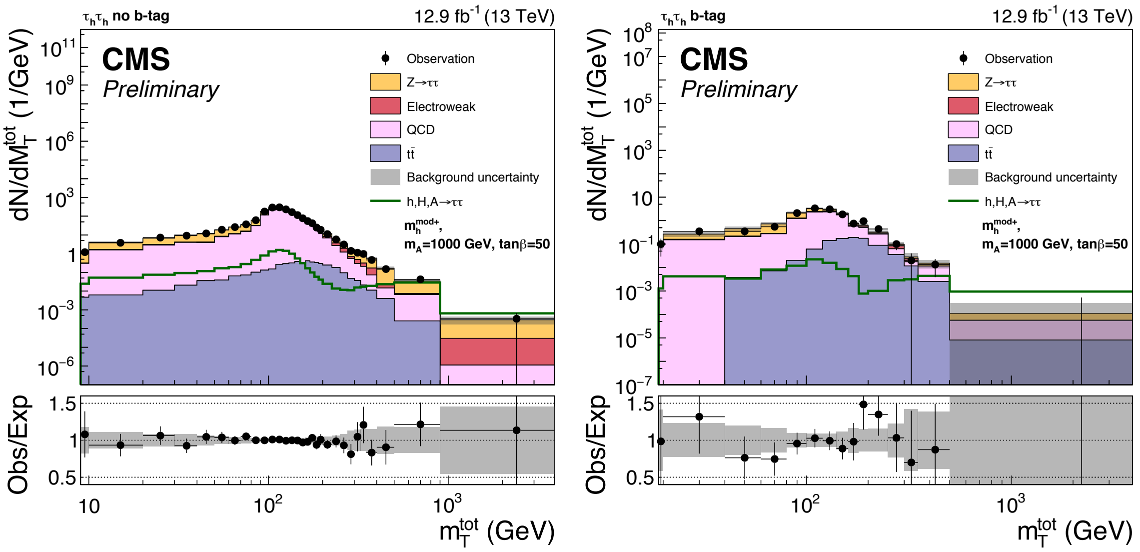

(a) No b-tag **(b)** B-tag

Figure 5.25: Distributions of $m_{\mathrm{T}}^{\mathrm{tot}}$ in the (a) no b-tag and (b) b-tag categories of the $\tau_{\mathrm{h}}\tau_{\mathrm{h}}$ channel. The signal of the three neutral Higgs bosons at $m_{\mathrm{A}} = 1\,\mathrm{TeV}$ and $\tan\beta = 50$ in the $m_{\mathrm{h}}^{\mathrm{mod+}}$ scenario is overlaid [2].

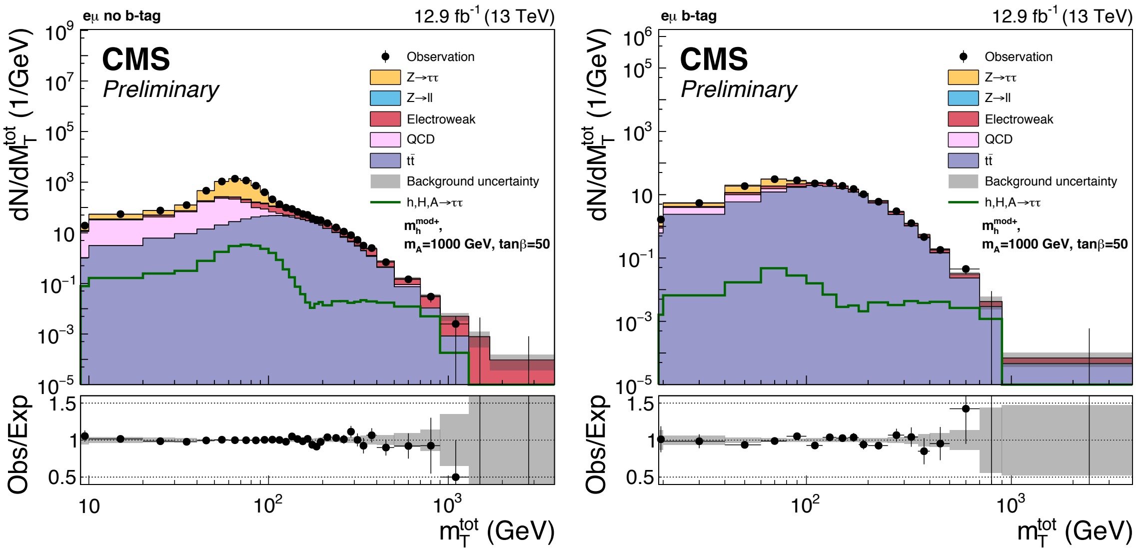

(a) No b-tag **(b)** B-tag

Figure 5.26: Distributions of $m_{\mathrm{T}}^{\mathrm{tot}}$ in the (a) no b-tag and (b) b-tag categories of the eμ channel. The signal of the three neutral Higgs bosons at $m_{\mathrm{A}} = 1\,\mathrm{TeV}$ and $\tan\beta = 50$ in the $m_{\mathrm{h}}^{\mathrm{mod+}}$ scenario is overlaid [2].

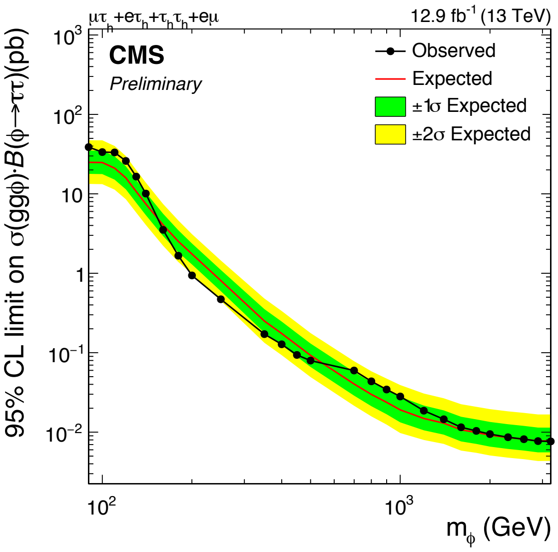

(a) ggϕ **(b)** bbϕ

Figure 5.27: Upper limits at the 95% CL for (a) the gluon fusion production process and (b) the b-associated production process. All four final states and all categories are combined for these limits. The green and yellow bands indicate the $\pm 1\sigma$ and $\pm 2\sigma$ probability intervals on the expected limit [2].

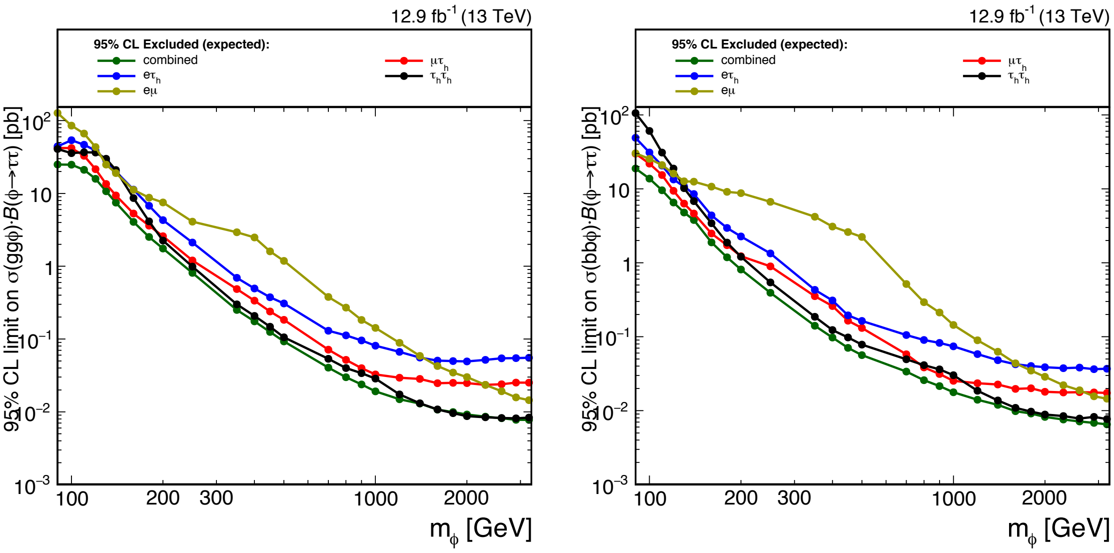

(a) ggϕ **(b)** bbϕ

Figure 5.28: Expected upper limits at the 95% CL for (a) gluon fusion and (b) b-associated production, comparing the combination of all channels (green) with the $\mu\tau_\mathrm{h}$ (red), $e\tau_\mathrm{h}$ (blue), $\tau_\mathrm{h}\tau_\mathrm{h}$ (black) and $e\mu$ (gold) channels.

5.8.2 Sensitivity to the SM Higgs boson

As limits are set on MSSM Higgs boson production down to masses of 90 GeV it is important to consider possible sensitivity to the 125 GeV SM Higgs boson. As the $\sigma\times\mathcal{B}$ for gluon fusion production of the 125 GeV Higgs boson in the SM, with decay into $\tau\tau$, is 3.05 pb [32] and the expected limit on $\sigma\times\mathcal{B}$ for MSSM ggϕ production at 125 GeV is around 20 pb the analysis is not yet sensitive to the SM Higgs boson. The limits shown in figure 5.29, which include the SM Higgs boson as part of the background, are almost exactly the same as those shown in figure 5.27, which also indicates the current lack of sensitivity to the SM Higgs boson.

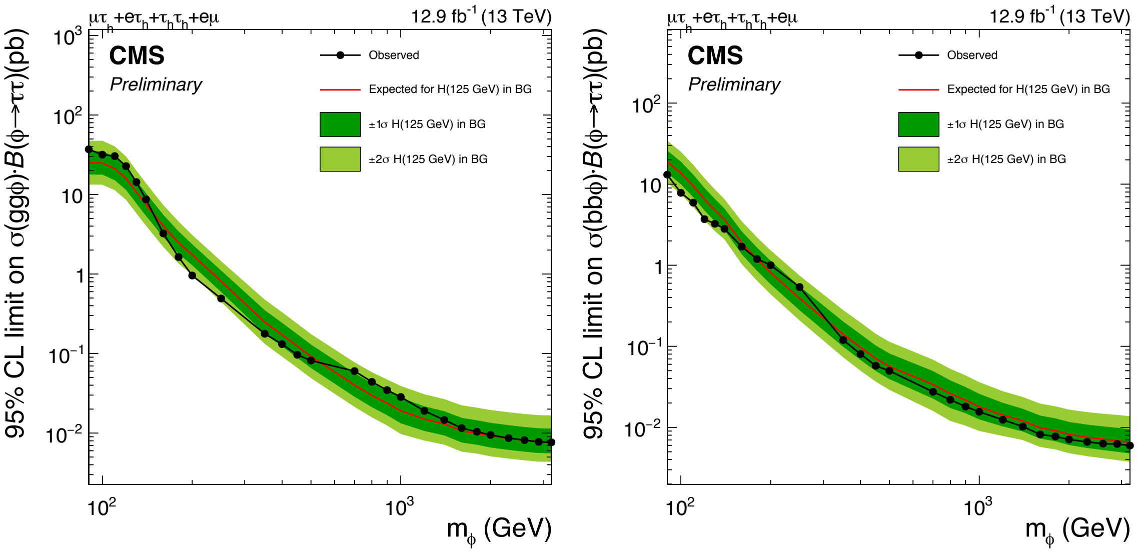

(a) ggϕ **(b)** bbϕ

Figure 5.29: Upper limits at the 95% CL for (a) the gluon fusion production process and (b) the b-associated production process. The 125 GeV SM Higgs boson is included as one of the backgrounds. All four final states and all categories are combined for these limits. The dark and light green bands indicate the $\pm1\sigma$ and $\pm2\sigma$ probability intervals on the expected limit [141].

5.8.3 2D likelihood scans

The 2D likelihood scans, as described in section 5.7.2, are shown in figure 5.30 for four mass points ranging from 100 GeV to 3.2 TeV. The black cross indicates the best-fit value, with the red diamond showing the expected best-fit value in the presence of the 125 GeV SM Higgs boson. The dark and light purple contours indicate the 68% and 95% confidence level regions, respectively. From the shape of the contours the correlation between the ggϕ and bbϕ processes is visible, illustrating the fact that the two processes are not fully disentangled by the chosen categorisation.

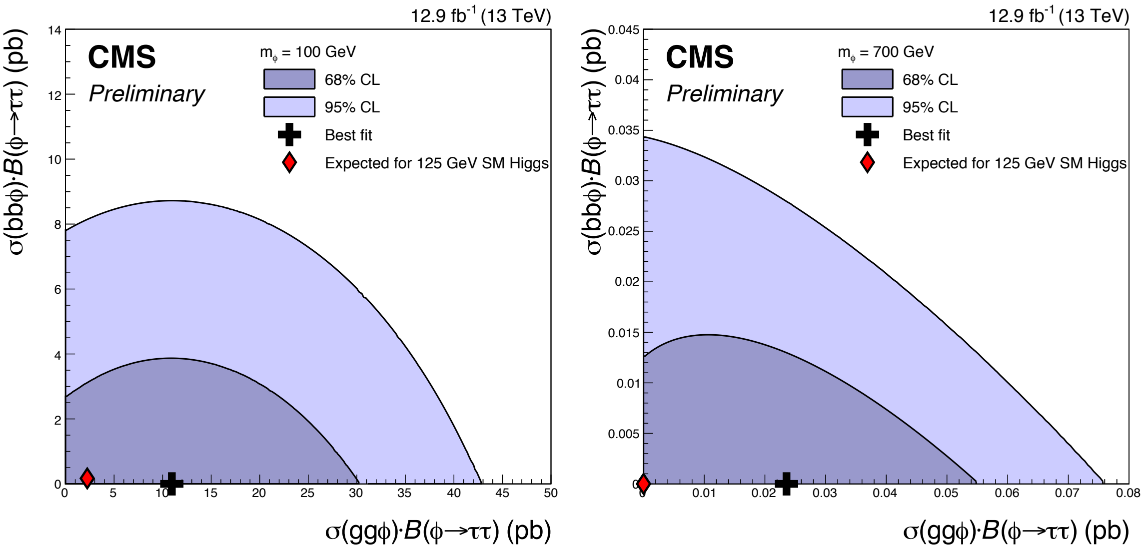

(a) $m_\phi = 100\,\mathrm{GeV}$ **(b)** $m_\phi = 700\,\mathrm{GeV}$

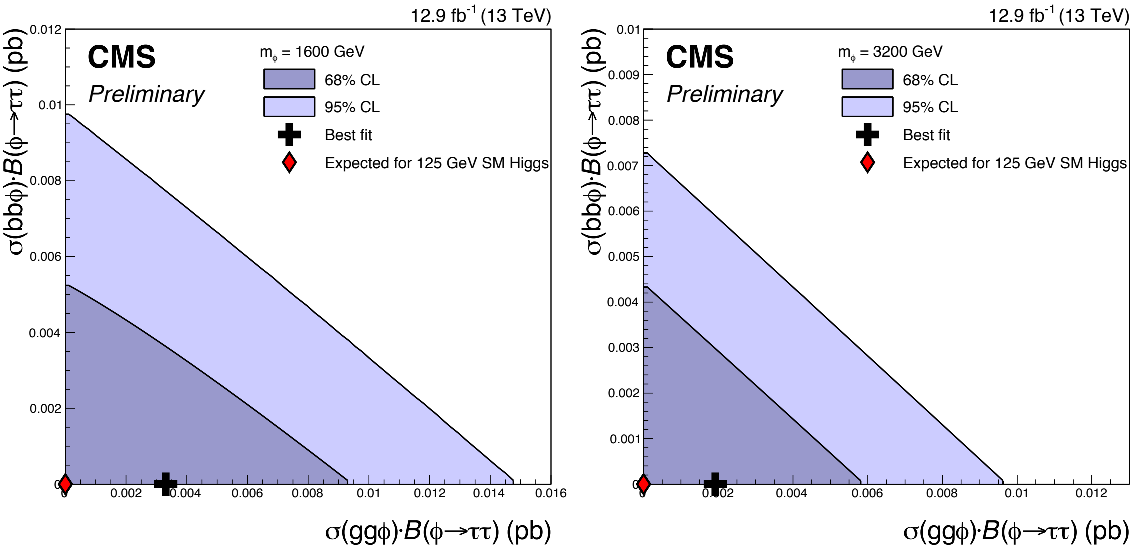

(c) $m_\phi = 1.6\,\mathrm{TeV}$ **(d)** $m_\phi = 3.2\,\mathrm{TeV}$

Figure 5.30: 2D likelihood scans showing the best-fit value (black cross) for $\sigma \times \mathcal{B}$ of both the gluon fusion (x axis) and b-associated production (y axis) processes. The red diamond indicates the expected best-fit point for the presence of a 125 GeV SM Higgs boson, and the purple bands indicate the 68% and 95% confidence level regions [2].

5.8.4 Interpretations in MSSM benchmark scenarios

The results are interpreted in two MSSM benchmark scenarios: the $m_{\mathrm{h}}^{\mathrm{mod+}}$ scenario and the hMSSM scenario. Both scenarios are described in chapter 1.

Figure 5.31a shows the expected and observed exclusions of the search presented in this chapter in the m_{A}-$\tan\beta$ parameter space of the $m_{\mathrm{h}}^{\mathrm{mod+}}$ scenario. The red shaded band indicates the area that is excluded due to the lack of a light Higgs boson with a mass compatible with 125 GeV in the model. Compared with the most sensitive limits set during Run 1 of the LHC these limits at high $\tan\beta$ have been significantly improved, by around 300 GeV for a given $\tan\beta$ value.

Figure 5.31b shows the expected and observed exclusions in the m_{A}-$\tan\beta$ plane of the hMSSM scenario. It should be noted again that this model, although defined for $\tan\beta$ values upwards of ten, is only strictly valid for $\tan\beta$ below ten. A small additional excluded area around $m_{\mathrm{A}} = 200\,\mathrm{GeV}$ is visible. It is caused by the $\sigma\times\mathcal{B}$ in the model, which is driven by two effects as already discussed in section 1.3.1. On the one hand the branching ratio into taus decreases with decreasing $\tan\beta$, while on the other hand a negative top-bottom interference effect increases the gluon fusion cross section with decreasing $\tan\beta$. Therefore the combined $\sigma\times\mathcal{B}$ decreases with decreasing $\tan\beta$, until it increases again from a low value of $\tan\beta \sim 3$ down to $\tan\beta{=}1$. The feature is thus expected to grow with more data.

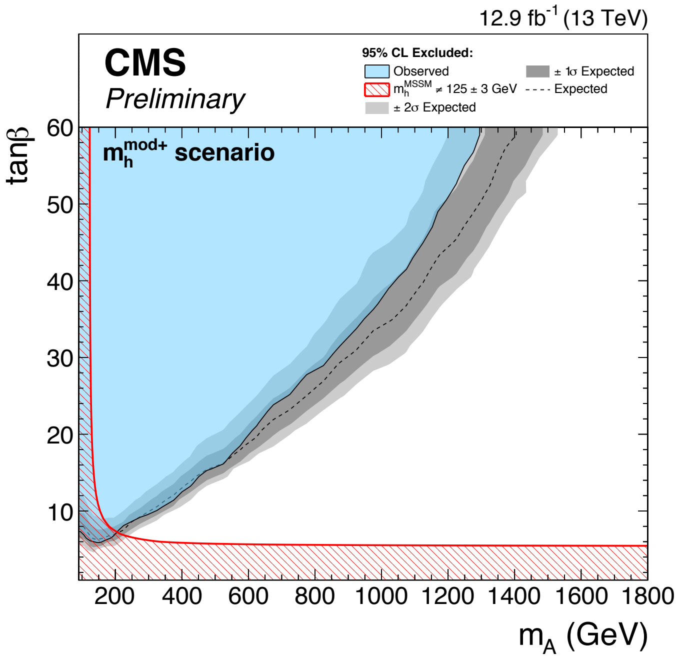

(a) $m_{\rm h}^{\rm mod+}$ scenario

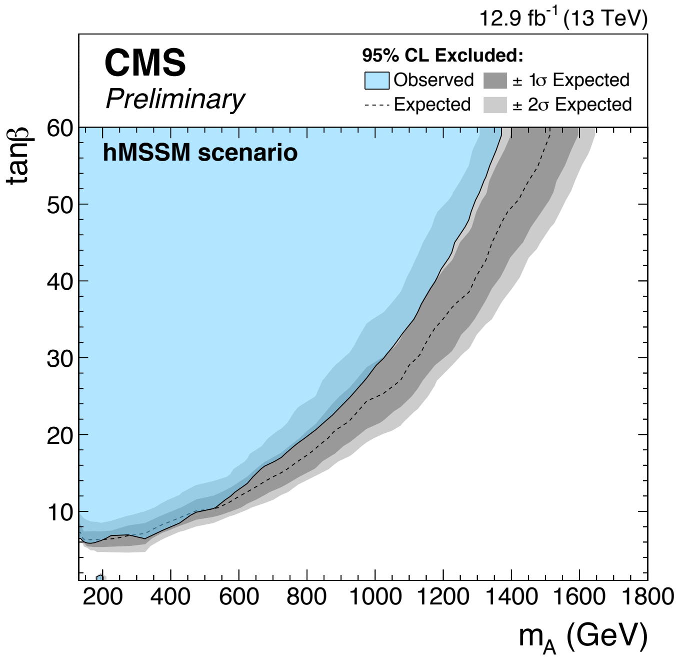

(b) hMSSM scenario

Figure 5.31: Exclusions in (a) the $m_{\rm h}^{\rm mod+}$ scenario and (b) the hMSSM scenario obtained by the combination of all channels. The blue shaded area bounded by the solid black line is the observed exclusion, with the dashed black line the expected exclusion. The light and dark grey bands indicate the $\pm 1\sigma$ and $\pm 2\sigma$ probability intervals on the expected exclusion under the SM hypothesis. The red shaded area in the $m_{\rm h}^{\rm mod+}$ figure is excluded by the lack of a light Higgs boson with mass compatible with 125 GeV in the model [2].

Chapter 6

Combination of MSSM analyses

The results of the search for neutral Higgs bosons decaying to di-tau pairs in the MSSM, using a dataset corresponding to an integrated luminosity of $12.9\,\mathrm{fb}^{-1}$, collected during the first half of 2016 and thus referred to as the '2016 analysis', can be combined with a previous search. This previous analysis was performed on a dataset corresponding to an integrated luminosity of $2.3\,\mathrm{fb}^{-1}$ collected during 2015 (the '2015 analysis'), and is detailed in reference [3]. By combining the two analyses it should be possible to set the most stringent limits, at the time of writing, on the two MSSM production modes, and in the m_{A}-$\tan\beta$ plane of MSSM benchmark scenarios. It is also a first step on the way to combining this $\mathrm{A/H} \rightarrow \tau\tau$ analysis with searches for charged Higgs bosons or heavy neutral Higgs bosons in other final states.

The 2015 analysis uses the same channels, categories, and very similar background estimation methods as the 2016 analysis and so it is not described in detail. The results of the analysis will be presented, and key differences with the more recent result highlighted where needed.

6.1 Results from the 2015 analysis

As for the analysis presented in chapter 5 a shape analysis is performed, however a different discriminating variable is used. The variable used is the transverse component of the di-tau mass as reconstructed using the `SVFit` algorithm, denoted $m_{\mathrm{T},\tau\tau}$. The transverse di-tau mass distributions for the signal region categories of the four channels are shown in figures 6.1–6.4.

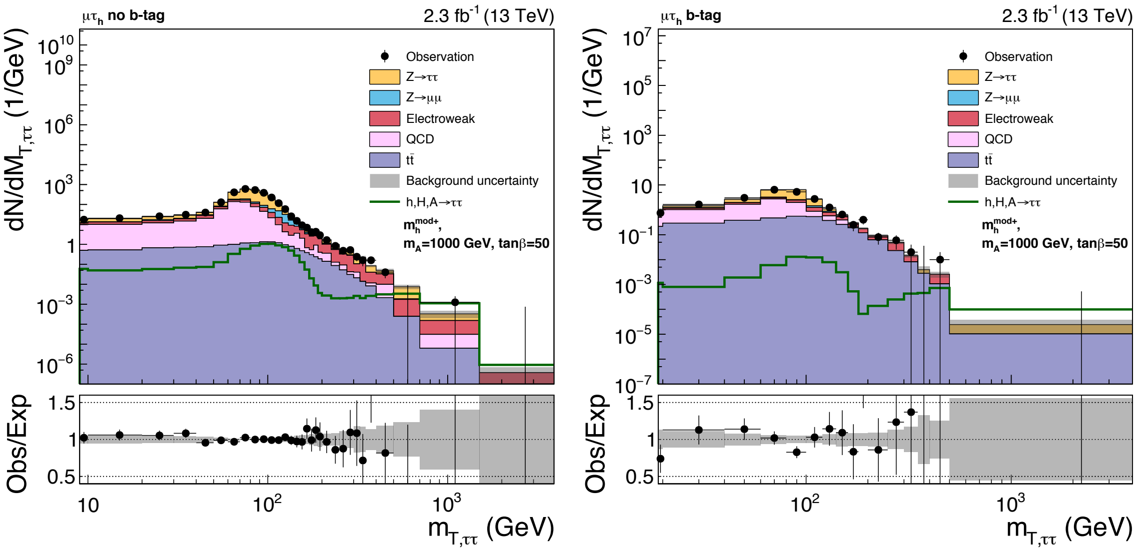

(a) No b-tag **(b)** B-tag

Figure 6.1: Transverse component of the di-tau mass for the expected backgrounds and observed events in the (a) no b-tag and (b) b-tag categories of the $\mu\tau_{\mathrm{h}}$ channel. The signal overlaid corresponds to the signal of the three Higgs bosons at $m_{\mathrm{A}} = 1\,\mathrm{TeV}$ and $\tan\beta = 50$ in the $m_{\mathrm{h}}^{\mathrm{mod}+}$ scenario, and so it peaks once at low mass, for the light Higgs boson, and once at higher mass, for the heavy H and A bosons.

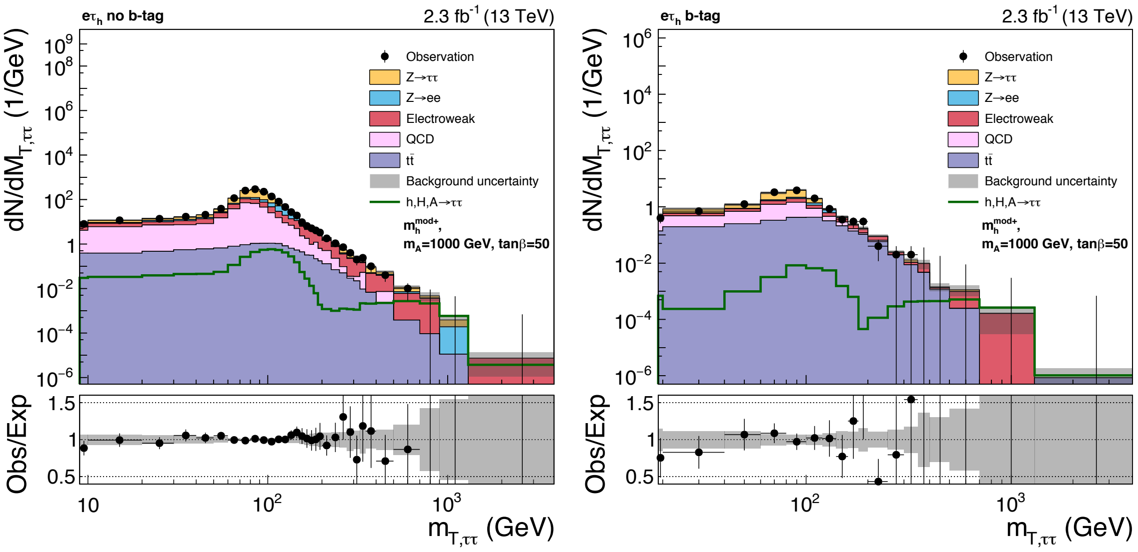

(a) No b-tag **(b)** B-tag

Figure 6.2: Transverse component of the di-tau mass for the expected backgrounds and observed events in the (a) no b-tag and (b) b-tag categories of the $e\tau_{\mathrm{h}}$ channel.

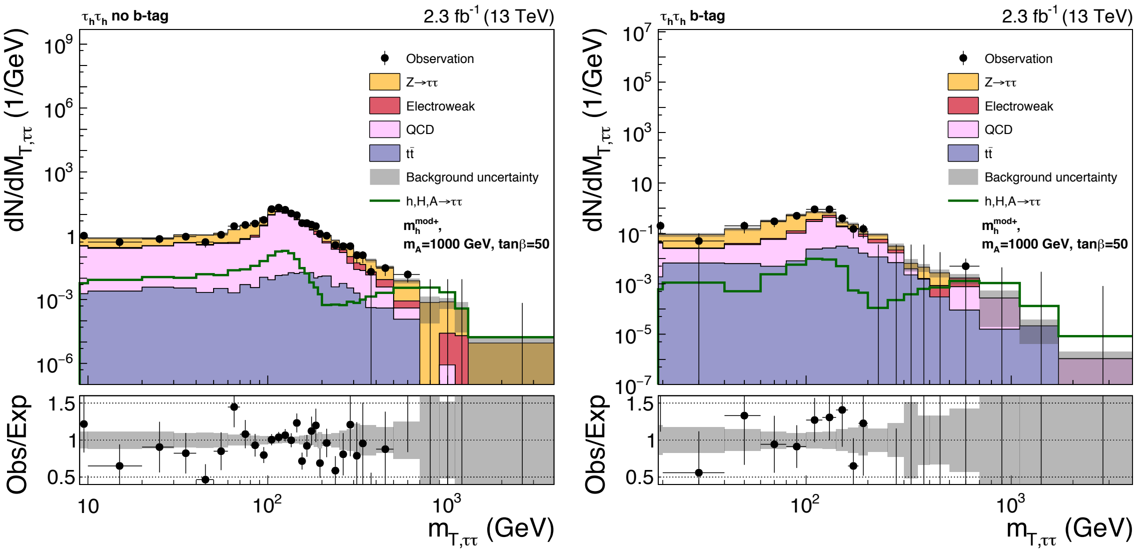

(a) No b-tag **(b)** B-tag

Figure 6.3: Transverse component of the di-tau mass for the expected backgrounds and observed events in the (a) no b-tag and (b) b-tag categories of the $\tau_h\tau_h$ channel.

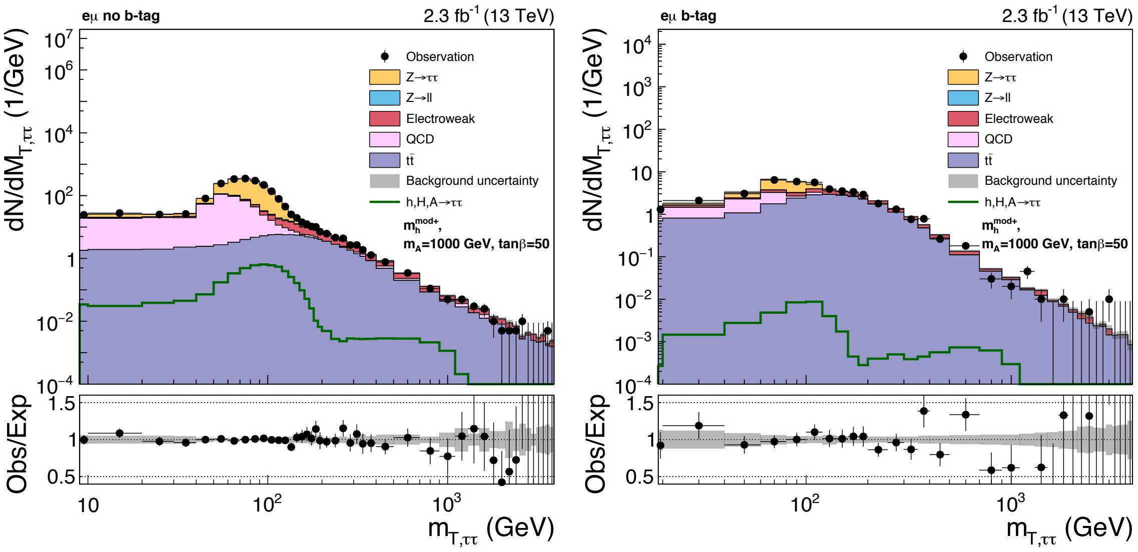

(a) No b-tag **(b)** B-tag

Figure 6.4: Transverse component of the di-tau mass for the expected backgrounds and observed events in the (a) no b-tag and (b) b-tag categories of the eμ channel.

These distributions do not show any significant excesses of observed events over the background expectation. The upper limits on $\sigma \times \mathcal{B}$ for the gluon fusion and b-associated production processes are shown in figure 6.5a and 6.5b, respectively. All channels and categories are combined. A comparison of the expected limits per channel is given in figure 6.6. These follow a similar pattern to those given in figure 5.28. Notice however that the eμ channel remains the least sensitive even at very high mass, as the transverse component of the di-tau mass exhibits a sizeable $t\bar{t}$ tail in the eμ channel. The total transverse mass collapses events from the tail into lower regions of the distribution, thus reducing the backgrounds at higher mass.

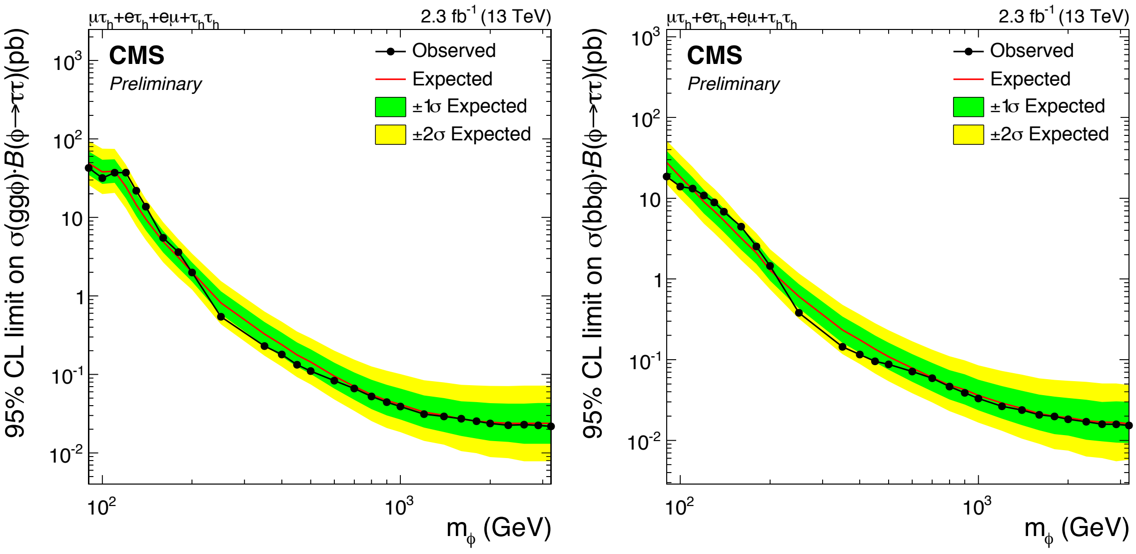

(a) ggϕ **(b)** bbϕ

Figure 6.5: Upper limits at the 95% CL for (a) the gluon fusion production process and (b) the b-associated production process. All four final states and all categories of the 2015 analysis are combined for these limits. The green and yellow bands indicate the $\pm 1\sigma$ and $\pm 2\sigma$ probability intervals on the expected limit [3].

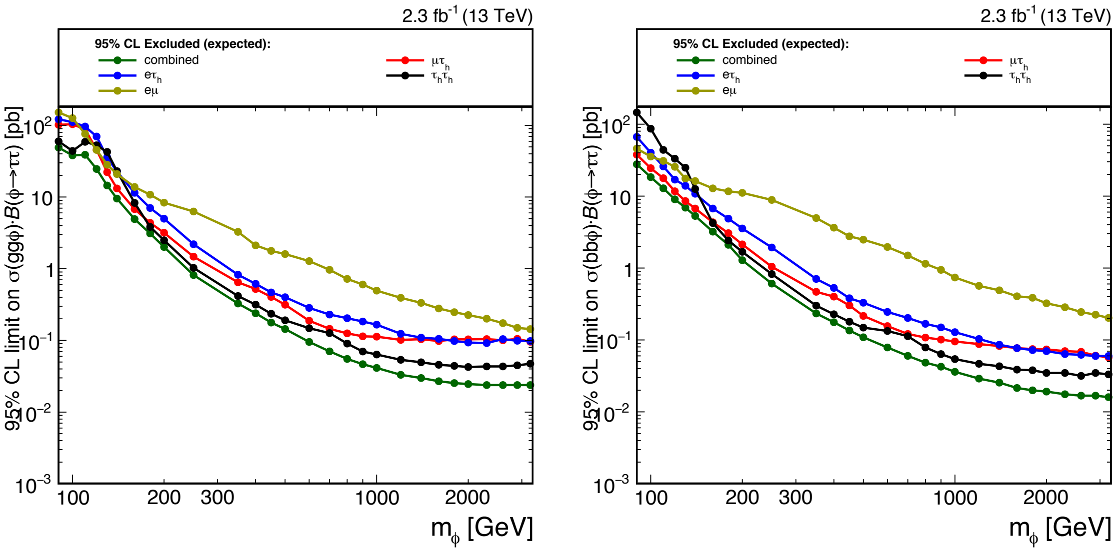

(a) ggϕ **(b)** bbϕ

Figure 6.6: Expected upper limits at the 95% CL for (a) gluon fusion and (b) b-associated production, comparing the combination of all channels (green) with the $\mu\tau_{\mathrm{h}}$ (red), eτ_{h} (blue), $\tau_{\mathrm{h}}\tau_{\mathrm{h}}$ (black) and eμ (gold) channels. For masses below 200 GeV the $\mu\tau_{\mathrm{h}}$ channel is the most sensitive, while the $\tau_{\mathrm{h}}\tau_{\mathrm{h}}$ channel dominates for higher masses. The eτ_{h} channel is always slightly less sensitive than the $\mu\tau_{\mathrm{h}}$ channel. The eμ channel is the least sensitive.

6.2 Combination procedure

The procedure for combining the two analyses is to combine the individual likelihoods to improve the analysis sensitivity and physics reach. To do this correctly the correlations between nuisance parameters in the 2015 and 2016 analyses need to be taken into account.

The correlation scheme is chosen based on the procedure used for the ATLAS and CMS Higgs combinations [28, 29]. This means uncertainties are either considered 100% (anti-)correlated or fully uncorrelated. Partial correlations are not taken into account, with a small number of exceptions. The correlations used for this combination are given in table 6.1, with the motivation for the chosen correlation given in the third column of the table. The chosen correlation scheme is motivated by carefully considering the differences between the two analyses and the conditions under which they were performed.

Table 6.1: Correlations between nuisance parameters in the 2015 and 2016 analyses.

Nuisance	**Correlation**	**Motivation**
Luminosity	Partially correlated	CMS-internal recommendation based on dedicated studies.
Jet energy scale	Fully correlated	CMS-internal recommendation based on dedicated studies.
b-Tagging	Uncorrelated	Scale factors used in the 2015 and 2016 analyses measured via different methods.
Mis-tagging	Partially correlated	CMS-internal recommendation based on dedicated studies.
Muon ID/isolation/trigger	Uncorrelated	The 2015 and 2016 analyses use different muon ID and isolation working points, and the L1 trigger was replaced completely between 2015 and 2016.
Electron ID/isolation/trigger	Uncorrelated	The L1 trigger was completely replaced between 2015 and 2016.
Tau ID/isolation/trigger	Uncorrelated	The L1 trigger was replaced between 2015 and 2016. The analyses received different tau ID scale factors, implying different behaviour of the hadronic tau selection criteria.
High-p_{T} tau ID efficiency	Correlated	This should not be affected by the difference of tau ID scale factor and covers the same underlying issue in both analyses.
Tau energy scale	Correlated	There is no reason to expect a different energy scale between 2015 and 2016 as the tau energy reconstruction remained the same.
Electron energy scale	Correlated	There is no reason to expect a different energy scale between 2015 and 2016.
Drell-Yan shape	Correlated	The same simulated samples are used in 2015 and 2016 to derive the correction. The weights derived for the 2015 analysis and the 2016 analysis are very similar.
W jet → τ_{h} fake rate shape	Uncorrelated	Correction not applied in the 2016 dataset while it was applied for the 2015 analysis. The uncertainties have a different functional form, possibly due to different jet → τ_{h} fake rates as a result of the use of a different tau isolation working point.
MET uncertainties	Correlated	The same MVA $E_{\mathrm{T}}^{\mathrm{miss}}$BDT training was used both for 2015 and 2016.
Top quark p_{T} reweighting	Correlated	The same corrections were applied to the 2015 and 2016 analyses.
Drell-Yan σ	Correlated	The same recommended cross sections were used in 2015 and 2016.
Di-boson and single-top σ	Correlated	The same recommended cross sections were used in 2015 and 2016.
$\mathrm{t\bar{t}}$ σ	Correlated	The same recommended cross sections were used in 2015 and 2016.
W+jets σ	Correlated	The same recommended cross section was used in 2015 and 2016..
SM signal theory uncertainties	Correlated	The same recommended cross sections were used in 2015 and 2016.

$Z/\gamma^* \rightarrow \tau\tau$ acceptance	N/A	Uncertainty only exists in the 2015 analysis as no fits to the $Z/\gamma^* \rightarrow \mu\mu$ control region were included.
$Z/\gamma^* \rightarrow \tau\tau$ extrapolation	N/A	Uncertainty only exists in 2016 analysis as fits to the $Z/\gamma^* \rightarrow \mu\mu$ control regions were included and this uncertainty should cover only the extrapolation from $Z/\gamma^* \rightarrow \mu\mu$ to $Z/\gamma^* \rightarrow \tau\tau$, not the full acceptance.
$e \rightarrow \tau_h$ fake rate	Correlated	Expected to behave the same in the 2015 and 2016 datasets, the same anti-electron discriminator was used and the uncertainty on the fake rate should not be affected by the use of a different hadronic tau ID discriminator working point.
$\mu \rightarrow \tau_h$ fake rate	Uncorrelated	Measurement had not been made at time of 2015 analysis and so no scale factors were applied yet, while this had changed for the 2016 analysis.
jet $\rightarrow \tau_h$ fake rate	Correlated	Uncertainty on the jet $\rightarrow \tau_h$ fake rate should not be affected by changes in hadronic tau isolation working point.
QCD extrapolation uncertainty ($e\mu$ channel)	Uncorrelated	Use of different anti-isolated sidebands in 2015 and 2016 analyses.
QCD normalisation uncertainty ($\tau_h\tau_h$ channel)	Uncorrelated	Use of different anti-isolated sidebands.
Parameters tying control regions to signal region normalisations	Uncorrelated	2016 control region fits should not influence the 2015 signal region and vice versa.
Statistical uncertainty in W opposite-sign to same-sign ratio ($e\tau_h$ and $\mu\tau_h$)	Uncorrelated	Statistical uncertainties should not be correlated.
Systematic uncertainty in W opposite-sign to same-sign ratio ($e\tau_h$ and $\mu\tau_h$)	Uncorrelated	Uncertainty based on high m_T region with anti-isolated τ_h, but because of the tau p_T cuts being different in the 2015 and 2016 analyses a different event composition can be expected in this region.
Statistical uncertainty in W low/high-m_T ratio ($e\tau_h$ and $\mu\tau_h$)	Uncorrelated	Statistical uncertainties should not be correlated.
Systematic uncertainty in W low/high-m_T ratio ($e\tau_h$ and $\mu\tau_h$)	Uncorrelated	Different m_T selections were used in the 2015 and 2016 analyses.
QCD OS/SS ratio statistical uncertainty ($e\tau_h$ and $\mu\tau_h$)	Uncorrelated	Statistical uncertainties should not be correlated.
QCD OS/SS ratio systematic uncertainty ($e\tau_h$ and $\mu\tau_h$)	Uncorrelated	The ratios were measured in different anti-isolated sidebands, and with different τ_h p_T selections, in the two analyses. Same comments about the correlations between channels and categories within the individual analyses as for the W systematic uncertainties apply.
bin-by-bin uncertainties for templates with low numbers of events	Uncorrelated	These are statistically independent.

6.3 Results

The expected and observed upper limits on $\sigma\times\mathcal{B}$ for the combination of the 2015 and 2016 analyses are shown in figure 6.7. These limits exhibit similar trends as the individual 2015 and 2016 limits.

To get a better picture of how the sensitivity of the individual analyses compares with the combination, the comparison of expected limits in figure 6.8 should be considered. The gluon fusion limits in figure 6.8a show that at higher masses the sensitivity is only very slightly improved with respect to the analysis of the 12.9 fb^{-1} dataset alone. However, for masses between 200 and 800 GeV there is a larger improvement in sensitivity from combining the two analyses. This behaviour is expected since the 2016 analysis used a different selection that made the analysis more optimal at masses above 800 GeV, and slightly less optimal below this mass. This effect is less visible on the b-associated production limits shown in figure 6.8b.

Figure 6.9a shows the exclusion obtained in the $m_{\mathrm{h}}^{\mathrm{mod+}}$ scenario by combining the 2015 and 2016 analyses. Figure 6.9b shows this exclusion in the hMSSM scenario. On both figures the expected and observed exclusions from the 2016 analysis only are overlaid, which shows how the combination increases the size of the excluded area. In the hMSSM scenario the feature already visible in figure 5.31b has grown by combining the two datasets. Future analyses using even more data will be able to fully close the gap between the two excluded regions.

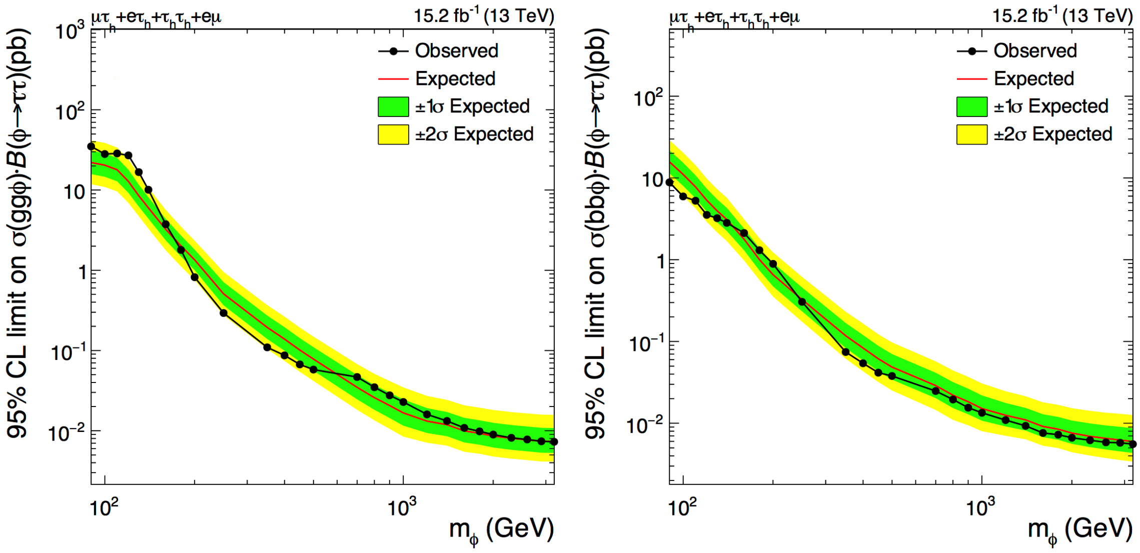

(a) ggϕ **(b)** bbϕ

Figure 6.7: Upper limits at the 95% CL for (a) the gluon fusion production process and (b) the b-associated production process. These results combine all categories and all four final states from both the 2015 and the 2016 analyses. The green and yellow bands indicate the $\pm 1\sigma$ and $\pm 2\sigma$ probability intervals on the expected limit.

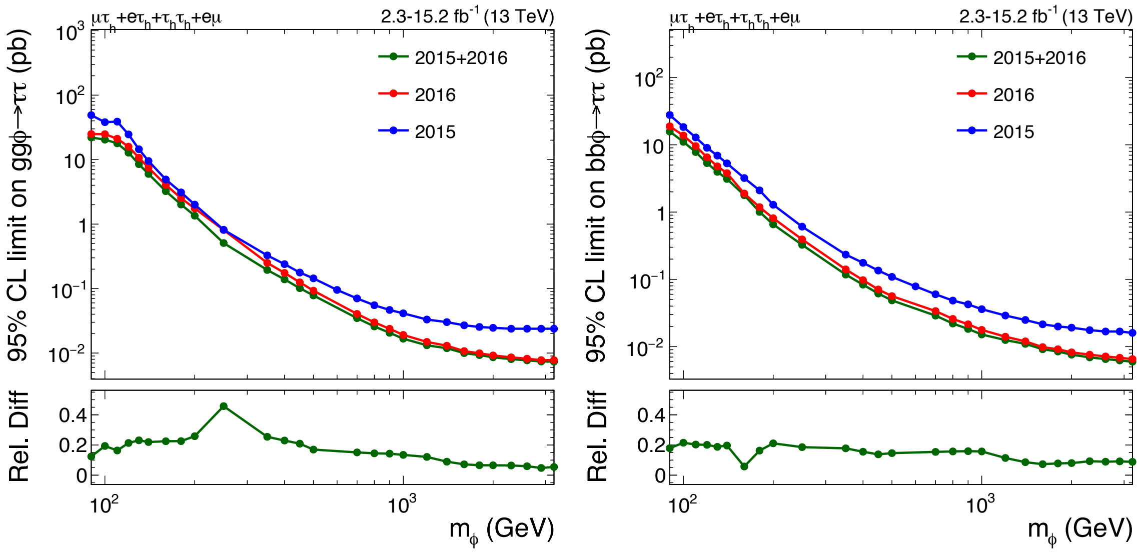

(a) ggϕ **(b)** bbϕ

Figure 6.8: Comparison of the expected upper limits at the 95% CL for (a) the gluon fusion production process and (b) the b-associated production process. The green curve shows the results from combining the 2015 and 2016 analyses, with the red line indicating the limits from the 2016 analysis only and the blue line indicating the limits from the 2015 analysis only. The relative difference is shown with respect to the limits from the 2016 analysis.

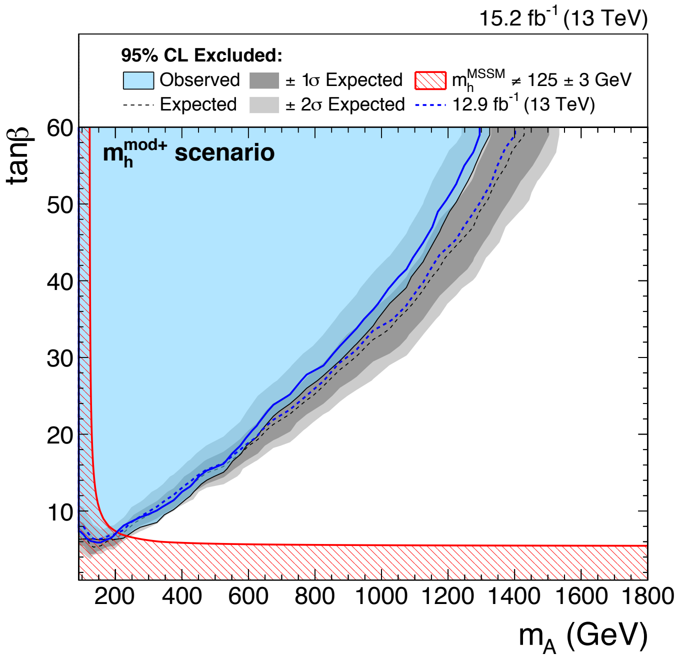

(a) $m_{\mathrm{h}}^{\mathrm{mod+}}$ scenario

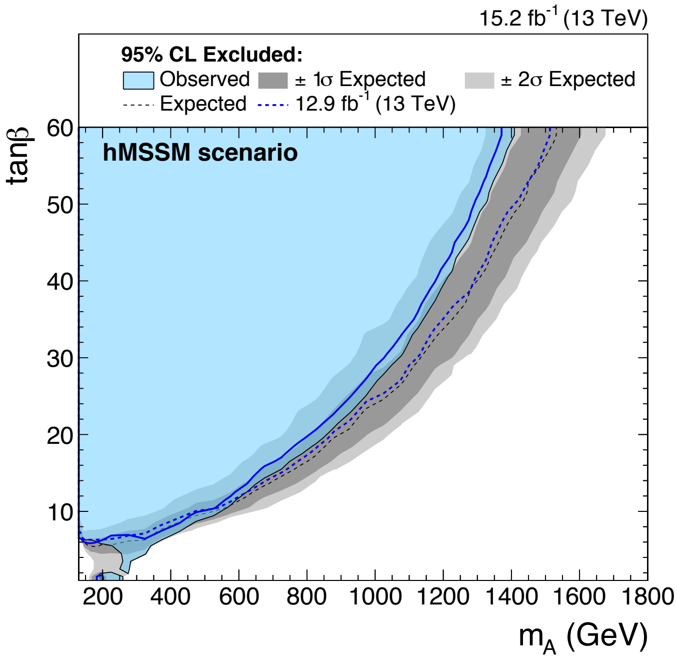

(b) hMSSM scenario

Figure 6.9: Exclusions in (a) the $m_{\mathrm{h}}^{\mathrm{mod+}}$ scenario and (b) the hMSSM scenario obtained by the combination of all channels of the 2015 and 2016 $\mathrm{A/H} \to \tau\tau$ analyses. The blue shaded area bounded by the solid black line is the observed exclusion, with the dashed black line the expected exclusion. The light and dark grey bands indicate the $\pm 1\sigma$ and $\pm 2\sigma$ probability intervals on the expected exclusion under the SM hypothesis. The red shaded area in the $m_{\mathrm{h}}^{\mathrm{mod+}}$ figure is excluded by the lack of a light Higgs boson with mass compatible with 125 GeV in the model. The dashed (solid) blue lines indicate the expected (observed) exclusion from the 2016 analysis alone.

Chapter 7

Conclusions and outlook

In this thesis analyses of proton-proton collisions recorded by the CMS detector during Run 1 and Run 2 of the LHC have been presented. The focus of these analyses is the search for BSM Higgs bosons with tau leptons in the final state.

The search for a heavy Higgs boson decaying to a final state of $\mathrm{bb}\tau\tau$ via two 125 GeV Higgs bosons was performed using $19.7\,\mathrm{fb}^{-1}$ of data collected at a centre-of-mass energy of 8 TeV during the 2012 LHC data-taking period. Such a final state can access areas of the MSSM parameter space not easily accessible via other channels. To separate more signal-like and more background-like events, a categorisation based on the number of b-tagged jets is used. To further increase the sensitivity to the signal, cuts on the di-tau and di-jet mass in a window around 125 GeV are used in combination with a kinematic fitting technique for the reconstruction of the four-body mass. The resulting mass variable provides good separation between the signal and the dominant $\mathrm{t\bar{t}}$ background, and is thus used as the variable for signal extraction. The results of this search are upper limits on production cross section times branching ratio, in a mass range of $260 < m_{\mathrm{H}} < 350\,\mathrm{GeV}$. A combination with a search for $\mathrm{A} \rightarrow \mathrm{Zh} \rightarrow \ell\ell\tau\tau$ yields exclusion in the lowest $\tan\beta$ region of the low-$\tan\beta$ MSSM scenario, as well as several areas of the $\cos(\beta-\alpha)$-$\tan\beta$ plane in a 2HDM scenario [1].

Searches for heavy neutral Higgs bosons decaying into pairs of tau leptons were performed using $2.3\,\mathrm{fb}^{-1}$ of data recorded during the 2015 data-taking period of the LHC, and using $12.9\,\mathrm{fb}^{-1}$ of data recorded during the first half of the 2016 data-taking period. The branching ratio of heavy neutral Higgs bosons into di-tau pairs is enhanced at high $\tan\beta$ in the MSSM, making this one of the most sensitive search channels for such particles. Both analyses use a categorisation based on the presence of b-tagged jets to separate the gluon fusion and b-associated Higgs boson production modes in the MSSM.

The hadronic tau isolation working point and the topological selection on the transverse mass between the electron or muon and the missing transverse energy are chosen to optimise the search sensitivity for signal masses of around 1 TeV. The sensitivity is maximised by using the total transverse mass for signal extraction. This variable, which is the combination of the transverse mass between the two legs of the di-tau candidate and the transverse masses between each of the legs of the di-tau candidate and the missing transverse energy, separates the dominant backgrounds and the high-mass signal well. No significant excess is observed in these searches, and so these analyses set limits on the production cross section times branching ratio of both the gluon fusion and b-associated production processes. The results are also interpreted in MSSM benchmark scenarios, where the analyses exclude large areas of the m_{A}-$\tan\beta$ plane, with significant improvement with respect to the most sensitive results obtained in Run 1 [2, 3]. A combination of the 2015 and 2016 analyses is also performed. This combination improves on the results of the 2016 analysis alone, thus setting the most stringent limits on A/H production to date.

As more data are collected during the remainder of Run 2, and in the future, searches for MSSM Higgs bosons in the di-tau final state will continue. If no such Higgs bosons are found, these searches will be able to exclude even more of the m_{A}-$\tan\beta$ plane in specific MSSM benchmark scenarios, although not all of the m_{A}-$\tan\beta$ plane will become accessible. A projection of the results of the 2015 MSSM analysis to integrated luminosities of $300\,\mathrm{fb}^{-1}$ and $3000\,\mathrm{fb}^{-1}$ [150] is shown in figure 7.1. Even with an integrated luminosity of $3000\,\mathrm{fb}^{-1}$ it is not possible to exclude the full m_{A}-$\tan\beta$ plane of this scenario, as the branching ratio of A/H into di-tau pairs is very low in the high-m_{A} and low-$\tan\beta$ corner. This region can be accessed via searches for the $\mathrm{A/H} \rightarrow \mathrm{t\bar{t}}$ decay, which has an enhanced branching ratio in this region. To fully cover this parameter space it will therefore start to become more and more important to combine searches for heavy Higgs bosons in different final states. Doing this will give the best sensitivity to possible heavy Higgs bosons, or in the absence of these particles exclusion of the scenarios that predict them.

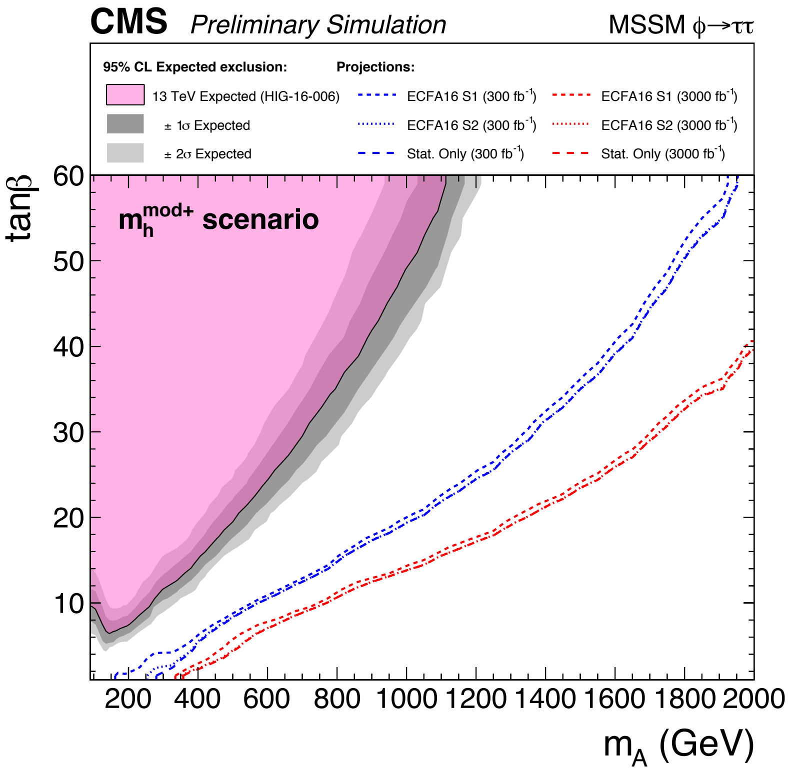

Figure 7.1: The expected exclusion in the $m_{\mathrm{h}}^{\mathrm{mod+}}$ scenario at the 95% CL of the 2015 MSSM analysis (pink) projected to integrated luminosities of $300\,\mathrm{fb}^{-1}$ (blue) and $3000\,\mathrm{fb}^{-1}$ (red) under several assumptions of how the systematic uncertainties scale. In scenario "S1" all systematic uncertainties are kept constant with integrated luminosity, while in scenario "S2" the theoretial uncertainties are scaled down by a factor $\frac{1}{2}$ and experimental systematic uncertainties scaled down by the square root of the integrated luminosity until they reach a lower limit. In the "Stat. Only" scenario all systematic uncertainties are neglected. Even with an integrated luminosity of $3000\,\mathrm{fb}^{-1}$ it is not possible to exclude the entire m_{A}-$\tan\beta$ plane in this MSSM benchmark scenario using this analysis alone [150].

Bibliography

[1] CMS Collaboration, "Searches for a heavy scalar boson H decaying to a pair of 125 GeV Higgs bosons hh or for a heavy pseudoscalar boson A decaying to Zh in the final states with h→ $\tau\tau$", *Phys. Lett.* **B755** (2016) 217, `doi:10.1016/j.physletb.2016.01.056`, `arXiv:1510.01181`.

[2] CMS Collaboration, "Search for a neutral MSSM Higgs boson decaying into $\tau\tau$ with 12.9 fb^{-1} of data at $\sqrt{s} = 13$ TeV", *CMS Physics Analysis Summary* **CMS-PAS-HIG-16-037** (2016).

[3] CMS Collaboration, "Search for a neutral MSSM Higgs boson decaying into $\tau\tau$ at 13 TeV", *CMS Physics Analysis Summary* **CMS-PAS-HIG-16-006** (2016).

[4] D. J. Gross and F. Wilczek, "Ultraviolet Behavior of Nonabelian Gauge Theories", *Phys. Rev. Lett.* **30** (1973) 1343–1346, `doi:10.1103/PhysRevLett.30.1343`.

[5] H. D. Politzer, "Reliable Perturbative Results for Strong Interactions?", *Phys. Rev. Lett.* **30** (1973) 1346–1349, `doi:10.1103/PhysRevLett.30.1346`.

[6] D. Griffiths, "Introduction to elementary particle physics". Wiley-VCH, 2nd edition, 2008.

[7] S. L. Glashow, "Partial-symmetries of weak interactions", *Nucl. Phys.* **22** (1961) 579–588, `doi:10.1016/0029-5582(61)90469-2`.

[8] S. Weinberg, "A Model of Leptons", *Phys. Rev. Lett.* **19** (1967) 1264–1266, `doi:10.1103/PhysRevLett.19.1264`.

[9] A. Salam, "Weak and electromagnetic interactions", *Elementary particle physics: relativistic groups and analyticity* **Proceedings of the eighth Nobel symposium** (1968) 367.

[10] Gargamelle Neutrino Collaboration, "Observation of neutrino-like interactions without muon or electron in the gargamelle neutrino experiment", *Phys. Lett.* **B46** (1973) 138–140, `doi:10.1016/0370-2693(73)90499-1`.

[11] UA1 Collaboration, "Experimental Observation of Isolated Large Transverse Energy Electrons with Associated Missing Energy at $\sqrt{s} = 540$ GeV", *Phys. Lett.* **B122** (1983) 103–116, `doi:10.1016/0370-2693(83)91177-2`.

[12] UA2 Collaboration, "Observation of Single Isolated Electrons of High Transverse Momentum in Events with Missing Transverse Energy at the CERN anti-p p Collider", *Phys. Lett.* **B122** (1983) 476–485, `doi:10.1016/0370-2693(83)91605-2`.

[13] UA1 Collaboration, "Experimental Observation of Lepton Pairs of Invariant Mass Around 95 GeV/c^2 at the CERN SPS Collider", *Phys. Lett.* **B126** (1983) 398–410, `doi:10.1016/0370-2693(83)90188-0`.

[14] UA2 Collaboration, "Evidence for $\mathrm{Z}^0 \to \mathrm{e}^+\mathrm{e}^-$ at the CERN anti-p p Collider", *Phys. Lett.* **B129** (1983) 130–140, `doi:10.1016/0370-2693(83)90744-X`.

[15] F. Englert and R. Brout, "Broken symmetry and the mass of gauge vector mesons", *Phys. Rev. Lett.* **13** (1964) 321, `doi:10.1103/PhysRevLett.13.321`.

[16] P. W. Higgs, "Broken symmetries and the masses of gauge bosons", *Phys. Rev. Lett.* **13** (1964) 508, `doi:10.1103/PhysRevLett.13.508`.

[17] P. W. Higgs, "Broken symmetries, massless particles and gauge fields", *Phys. Lett.* **12** (1964) 132–133, `doi:10.1016/0031-9163(64)91136-9`.

[18] P. W. Higgs, "Spontaneous symmetry breakdown without massless bosons", *Phys. Rev.* **145** (1966) 1156–1163, `doi:10.1103/PhysRev.145.1156`.

[19] G. S. Guralnik, C. R. Hagen, and T. W. B. Kibble, "Global conservation laws and massless particles", *Phys. Rev. Lett.* **13** (1964) 585–587, `doi:10.1103/PhysRevLett.13.585`.

[20] J. Goldstone, "Field Theories with Superconductor Solutions", *Nuovo Cim.* **19** (1961) 154–164, `doi:10.1007/BF02812722`.

[21] J. Goldstone, A. Salam, and S. Weinberg, “Broken Symmetries”, *Phys. Rev.* **127** (1962) 965, `doi:10.1103/PhysRev.127.965`.

[22] ALEPH, DELPHI, L3 and OPAL Collaborations, “Search for the standard model Higgs boson at LEP”, *Phys. Lett. B* **565** (2003) 61–75, `doi:10.1016/S0370-2693(03)00614-2`, `arXiv:hep-ex/0306033`.

[23] CDF and D0 Collaborations, “Higgs Boson Studies at the Tevatron”, *Phys. Rev.* **D88** (2013) 052014, `doi:10.1103/PhysRevD.88.052014`, `arXiv:1303.6346`.

[24] ATLAS Collaboration, “Observation of a New Particle in the Search for the Standard Model Higgs Boson with the ATLAS Detector at the LHC”, *Phys. Lett.* **B716** (2012) 1–29, `doi:10.1016/j.physletb.2012.08.020`, `arXiv:1207.7214`.

[25] CMS Collaboration, “Observation of a new boson at a mass of 125 GeV with the CMS experiment at the LHC”, *Phys. Lett.* **B716** (2012) 30, `doi:10.1016/j.physletb.2012.08.021`, `arXiv:1207.7235`.

[26] ATLAS Collaboration, “Evidence for the spin-0 nature of the Higgs boson using ATLAS data”, *Phys. Lett.* **B726** (2013) 120, `doi:10.1016/j.physletb.2013.08.026`, `arXiv:1307.1432`.

[27] CMS Collaboration, “Observation of the diphoton decay of the Higgs boson and measurements of its properties”, *Eur. Phys. J.* **C74** (2014) 3076, `doi:10.1140/epjc/s10052-014-3076-z`, `arXiv:1407.0558`.

[28] ATLAS and CMS Collaborations, “Combined Measurement of the Higgs Boson Mass in pp Collisions at $\sqrt{s} = 7$ and 8 TeV with the ATLAS and CMS Experiments”, *Phys. Rev. Lett.* **114** (2015) 191803, `doi:10.1103/PhysRevLett.114.191803`, `arXiv:1503.07589`.

[29] ATLAS and CMS Collaborations, “Measurements of the Higgs boson production and decay rates and constraints on its couplings from a combined ATLAS and CMS analysis of the LHC pp collision data at $\sqrt{s} = 7$ and 8 TeV”, *JHEP* **08** (2016) 045, `doi:10.1007/JHEP08(2016)045`, `arXiv:1606.02266`.

[30] ATLAS Collaboration, “Evidence for the Higgs-boson Yukawa coupling to tau leptons with the ATLAS detector”, *JHEP* **04** (2015) 117,

`doi:10.1007/JHEP04(2015)117`, `arXiv:1501.04943`.

[31] CMS Collaboration, "Evidence for the 125 GeV Higgs boson decaying to a pair of τ leptons", *JHEP* **05** (2014) 104, `doi:10.1007/JHEP05(2014)104`, `arXiv:1401.5041`.

[32] The LHC Higgs Cross Section Working Group, "Handbook of LHC Higgs Cross Sections: 4. Deciphering the Nature of the Higgs Sector", `arXiv:1610.07922`.

[33] CMS Collaboration, "Updated measurements of Higgs boson production in the diphoton decay channel at $\sqrt{s} = 13$ TeV in pp collisions at CMS", *CMS Physics Analysis Summary* **CMS-PAS-HIG-16-020** (2016).

[34] ATLAS Collaboration, "Measurement of fiducial, differential and production cross sections in the $\mathrm{H} \rightarrow \gamma\gamma$ decay channel with 13.3 fb^{-1} of 13 TeV proton-proton collision data with the ATLAS detector", *ATLAS Note* **ATLAS-CONF-2016-067** (2016).

[35] CMS Collaboration, "Measurements of properties of the Higgs boson and search for an additional resonance in the four-lepton final state at $\sqrt{s} = 13$ TeV", *CMS Physics Analysis Summary* **CMS-PAS-HIG-16-033** (2016).

[36] ATLAS Collaboration, "Study of the Higgs boson properties and search for high-mass scalar resonances in the $\mathrm{H} \rightarrow \mathrm{ZZ}^{*} \rightarrow 4\ell$ decay channel at $\sqrt{s} = 13$ TeV with the ATLAS detector", *ATLAS Note* **ATLAS-CONF-2016-079** (2016).

[37] CMS Collaboration, "First results on Higgs to WW at $\sqrt{s} = 13$ TeV", *CMS Physics Analysis Summary* **CMS-PAS-HIG-15-003** (2016).

[38] ATLAS Collaboration, "Measurements of the Higgs boson production cross section via Vector Boson Fusion and associated WH production in the $\mathrm{WW}^{*} \rightarrow \ell\nu\ell\nu$ decay mode", *ATLAS Note* **ATLAS-CONF-2016-112** (2016).

[39] CMS Collaboration, "Search for the standard model Higgs boson produced through vector boson fusion and decaying to $\mathrm{b\overline{b}}$ with proton-proton collisions at $\sqrt{s} = 13$ TeV", *CMS Physics Analysis Summary* **CMS-PAS-HIG-16-003** (2016).

[40] ATLAS Collaboration, "Search for the Standard Model Higgs boson produced in

association with a vector boson and decaying to a $\mathrm{b\overline{b}}$ pair in *pp* collisions at 13 TeV using the ATLAS detector", *ATLAS Note* **ATLAS-CONF-2016-091** (2016).

[41] ATLAS Collaboration, "Search for Higgs bosons decaying into di-muon in pp collisions at $\sqrt{s} = 13$ TeV with the ATLAS detector", *ATLAS Note* **ATLAS-CONF-2016-041** (2016).

[42] CMS Collaboration, "Search for $\mathrm{t\overline{t}H}$ production in the $\mathrm{H} \to \mathrm{b\overline{b}}$ decay channel with 2016 pp collision data at $\sqrt{s} = 13$ TeV", *CMS Physics Analysis Summary* **CMS-PAS-HIG-16-038** (2016).

[43] CMS Collaboration, "Search for associated production of Higgs bosons and top quarks in multilepton final states at $\sqrt{s} = 13$ TeV", *CMS Physics Analysis Summary* **CMS-PAS-HIG-16-022** (2016).

[44] ATLAS Collaboration, "Search for the Standard Model Higgs boson produced in association with top quarks and decaying into a bb pair in pp collisions at $\sqrt{s} = 13$ TeV with the ATLAS detector", *ATLAS Note* **ATLAS-CONF-2016-080** (2016).

[45] ATLAS Collaboration, "Search for the Associated Production of a Higgs Boson and a Top Quark Pair in Multilepton Final States with the ATLAS Detector", *ATLAS Note* **ATLAS-CONF-2016-058** (2016).

[46] Particle Data Group Collaboration, "Review of particle physics", *Chin. Phys.* **C38** (2014).

[47] G. Bertone, D. Hooper, and J. Silk, "Particle dark matter: Evidence, candidates and constraints", *Phys. Rept.* **405** (2005) 279–390, `doi:10.1016/j.physrep.2004.08.031`, `arXiv:hep-ph/0404175`.

[48] U. Amaldi, W. de Boer, and H. Fürstenau, "Comparison of grand unified theories with electroweak and strong coupling constants measured at LEP", *Phys. Lett.* **B260** (1991) 447–455, `doi:10.1016/0370-2693(91)91641-8`.

[49] S. Carlip, "Quantum gravity: A Progress report", *Rept. Prog. Phys.* **64** (2001) 885, `doi:10.1088/0034-4885/64/8/301`, `arXiv:gr-qc/0108040`.

[50] S. P. Martin, "A Supersymmetry Primer", `doi:10.1142/9789812839657_0001`, `arXiv:hep-ph/9709356`.

[51] M. Carena and H. Haber, "Higgs Boson Theory and Phenomenology", *Prog. Part. Nucl. Phys.* **50** (2003) 63–152, `doi:10.1016/S0146-6410(02)00177-1`, `arXiv:hep-ph/0208209`.

[52] LHC Higgs Cross Section Working Group Collaboration, "MSSM neutral BR plots". `https://twiki.cern.ch/twiki/bin/view/LHCPhysics/LHCHXSWGCrossSectionsFigures#MSSM_neutral_BR_plots`, 2014.

[53] G. Branco, P. Ferreira, L. Lavoura et al., "Theory and phenomenology of two-Higgs-doublet models", *Phys. Rep.* **516** (July, 2012) 1–102, `doi:http://dx.doi.org/10.1016/j.physrep.2012.02.002`, `arXiv:1106.0034`.

[54] N. Craig, J. Galloway, and S. Thomas, "Searching for Signs of the Second Higgs Doublet", *RU-NHETC-2013-07* (2013) `arXiv:1305.2424`.

[55] M. Carena, S. Heinemeyer, O. Stal et al., "MSSM Higgs Boson Searches at the LHC: Benchmark Scenarios after the Discovery of a Higgs-like Particle", *Eur. Phys. J.* **C73** (2013) 2552, `doi:10.1140/epjc/s10052-013-2552-1`, `arXiv:1302.7033`.

[56] M. Carena, S. Heinemeyer, C. Wagner et al., "Suggestions for Improved Benchmark Scenarios for Higgs-Boson Searches at LEP2", `arXiv:hep-ph/9912223`.

[57] The LHC Higgs Cross Section Working Group, "Handbook of LHC Higgs Cross Sections: 3. Higgs Properties", `doi:10.5170/CERN-2013-004`, `arXiv:1307.1347`.

[58] A. Djouadi and J. Quevillon, "The MSSM Higgs sector at high M_{SUSY}: reopening the low $\tan\beta$ regime and heavy Higgs searches", *JHEP* **10** (2013) 028, `doi:10.1007/JHEP10(2013)028`, `arXiv:1304.1787`.

[59] S. Heinemeyer, "Benchmark Scenario for low $\tan\beta$ in the MSSM: First preliminary interim recommendation/suggestion". `https://twiki.cern.ch/twiki/pub/LHCPhysics/HXSWG3LowTanB/benchmark5-v0.pdf`.

[60] E. Bagnaschi et al., “Benchmark Scenarios for low tan β in the MSSM”, *LHC Higgs Cross Section Working Group Public Note* **LHCHXSWG-2015-002** (2015).

[61] A. Djouadi, L. Maiani, G. Moreau et al., “The post-Higgs MSSM scenario: Habemus MSSM?”, *Eur. Phys. J.* **C73** (2013) 2650, `doi:10.1140/epjc/s10052-013-2650-0`, `arXiv:1307.5205`.

[62] A. Djouadi, L. Maiani, A. Polosa et al., “Fully covering the MSSM Higgs sector at the LHC”, *JHEP* **06** (2015) 168, `doi:10.1007/JHEP06(2015)168`, `arXiv:1502.05653`.

[63] CMS Collaboration, “Summary results of high mass BSM Higgs searches using CMS run-I data”, *CMS Physics Analysis Summary* **CMS-PAS-HIG-16-007** (2016).

[64] ATLAS Collaboration, “Search for the Minimal Supersymmetric Standard Model Higgs bosons H/A in the $\tau\tau$ final state in up to 13.3 fb^{-1} of pp collision data at $\sqrt{s} = 13$ TeV with the ATLAS detector”, *ATLAS Note* **ATLAS-CONF-2016-085** (2016).

[65] ATLAS Collaboration, “Search for new phenomena in $\mathrm{t\bar{t}}$ final states with additional heavy-flavour jets in pp collisions at $\sqrt{s} = 13$ TeV with the ATLAS detector”, *ATLAS Note* **ATLAS-CONF-2016-104** (2016).

[66] ATLAS Collaboration, “Search for a high-mass Higgs boson decaying to a pair of W bosons in *pp* collisions at $\sqrt{s} = 13$ TeV with the ATLAS detector”, *ATLAS Note* **ATLAS-CONF-2016-074** (2016).

[67] ATLAS Collaboration, “Search for charged Higgs bosons in the τ+jets final state with 14.7 fb^{-1} of *pp* collision data recorded at $\sqrt{s} = 13$ TeV with the ATLAS experiment”, *ATLAS Note* **ATLAS-CONF-2016-088** (2016).

[68] ATLAS Collaboration, “Search for charged Higgs bosons in the $\mathrm{H}^{\pm} \to \mathrm{tb}$ channel in pp collisions at $\sqrt{s} = 13$ TeV using the ATLAS detector”, *ATLAS Note* **ATLAS-CONF-2016-089** (2016).

[69] CMS Collaboration, “Search for charged Higgs bosons with the $\mathrm{H}^{\pm} \to \tau\nu$ decay

channel in the fully hadronic final state at $\sqrt{s} = 13$ TeV", *CMS Physics Analysis Summary* **CMS-PAS-HIG-16-031** (2016).

[70] ATLAS Collaboration, "Search for Higgs boson pair production in the bb$\gamma\gamma$ final state using pp collision data $\sqrt{s} = 13$ TeV with the ATLAS detector", *ATLAS Note* **ATLAS-CONF-2016-004** (2016).

[71] ATLAS Collaboration, "Search for Higgs boson pair production in the final state of $\gamma\gamma WW^* \to l\nu jj$ using 13.3 fb^{-1} of pp collision data recorded at $\sqrt{s} = 13$ TeV with the ATLAS detector", *ATLAS Note* **ATLAS-CONF-2016-071** (2016).

[72] ATLAS Collaboration, "Search for pair production of Higgs bosons in the $\mathrm{b\overline{b}b\overline{b}}$ final state using proton-proton collisions at $\sqrt{s} = 13$ TeV with the ATLAS detector", *ATLAS Note* **ATLAS-CONF-2016-049** (2016).

[73] CMS Collaboration, "Search for $\mathrm{H(b\overline{b})H(\gamma\gamma)}$ decays at $\sqrt{s} = 13$ TeV", *CMS Physics Analysis Summary* **CMS-PAS-HIG-16-032** (2016).

[74] CMS Collaboration, "Search for resonant Higgs boson pair production in the $\mathrm{b\overline{b}}\tau^+\tau^-$ final state using 2016 data", *CMS Physics Analysis Summary* **CMS-PAS-HIG-16-028** (2016).

[75] CMS Collaboration, "Search for Higgs boson pair production in the $\mathrm{b\overline{b}}\ell\nu\ell\nu$ final state at $\sqrt{s} = 13$ TeV", *CMS Physics Analysis Summary* **CMS-PAS-HIG-16-024** (2016).

[76] L. Evans and P. Bryant, "The LHC Machine", *JINST* **3** (2008) S08001, `doi:10.1088/1748-0221/3/08/S08001`.

[77] LEP Injector Study Group, "LEP Design Report: Vol.2. The LEP Main Ring", *Technical Design Report* **CERN-LEP-84-01** (1984).

[78] "STFC public pages". `http://www.stfc.ac.uk/stfc/includes/themes/MuraSTFC/assets/legacy/LHCinteractive/LHC_default.jpg`.

[79] ATLAS Collaboration, "The ATLAS Experiment at the CERN Large Hadron Collider", *JINST* **3** (2008) `doi:10.1088/1748-0221/3/08/S08003`.

[80] CMS Collaboration, “The CMS experiment at the CERN LHC”, *JINST* **3** (2008) `doi:10.1088/1748-0221/3/08/S08004`.

[81] ALICE Collaboration, “The ALICE experiment at the CERN LHC”, *JINST* **3** (2008) `doi:10.1088/1748-0221/3/08/S08002`.

[82] LHCb Collaboration, “The LHCb Detector at the LHC”, *JINST* **3** (2008) `doi:10.1088/1748-0221/3/08/S08005`.

[83] W. Stirling. `http://www.hep.ph.ic.ac.uk/~wstirlin/plots/crosssections2013.jpg`.

[84] “CMS Luminosity public results”. `https://twiki.cern.ch/twiki/bin/view/CMSPublic/LumiPublicResults`.

[85] CMS Collaboration, “CMS Technical Design Report for the Pixel Detector Upgrade”, *Technical Design Report CMS* **CMS-TDR-11,CERN-LHCC-2012-016** (2012).

[86] CMS HCAL/ECAL Collaboration, “The CMS barrel calorimeter response to particle beams from 2 to 350 GeV/c”, *Eur. Phys. J.* **C60** (2009) 359–373, `doi:10.1140/epjc/s10052-009-0959-5`.

[87] CMS Collaboration, “CMS Technical Design Report for the Phase 1 Upgrade of the Hadron Calorimeter”, *Technical Design Report CMS* **CMS-TDR-010,CERN-LHCC-2012-015** (2012).

[88] CMS Collaboration, “Performance of Resistive Plate Chambers installed during the first long shutdown of the CMS experiment”, *JINST* **11** (2016) `arXiv:1605.06798`.

[89] CMS Collaboration, “The performance of the CMS muon detector in proton-proton collisions at $\sqrt{s} = 7\,\mathrm{TeV}$ at the LHC”, *JINST* **8** (2013) `doi:10.1088/1748-0221/8/11/P11002`, `arXiv:1306.6905`.

[90] CMS Collaboration, “The CMS Trigger system”, *Submitted to J. Instrum* (2016) `arXiv:1609.02336`.

[91] CMS Collaboration, "CMS Technical Design Report for the Level-1 Trigger Upgrade", *Technical Design Report CMS* **CERN-LHCC-2013-011,CMS-TDR-12** (2013).

[92] "Worldwide LHC Computing Grid". `http://wlcg-public.web.cern.ch`.

[93] CMS Collaboration, "Description and performance of track and primary-vertex reconstruction with the CMS tracker", *JINST* **9** (2014) `doi:10.1088/1748-0221/9/10/P10009`, `arXiv:1405.6569`.

[94] R. Frühwirth, "Application of Kalman Filtering to Track and Vertex Fitting", *Nuclear Instruments and Methods in Physics Research* **A262** (1987) `doi:10.1016/0168-9002(87)90887-4`.

[95] CMS Collaboration, "Measurement of Tracking Efficiency", *CMS Physics Analysis Summary* **CMS-PAS-TRK-10-002** (2010).

[96] K. Rose, "Deterministic Annealing for Clustering, Compression, Classification, Regression, and Related Optimization Problems", *Proceedings of the IEEE* **86** (1998) `doi:10.1109/5.726788`.

[97] R. Frühwirth, W. Waltenberger, and P. Vanlaer, "Adaptive Vertex Fitting", *J.Phys.* **G34** (2007) `doi:10.1088/0954-3899/34/12/N01`.

[98] CMS Collaboration, "Primary vertex resolution in 2016", *CMS Performance Note* **CMS-DP-2016-041** (2016).

[99] CMS Collaboration, "Performance of electron reconstruction and selection with the CMS detector in proton-proton collisions at $\sqrt{s} = 8\,\text{TeV}$", *JINST* **10** (2015) `doi:10.1088/1748-0221/10/06/P06005`, `arXiv:1502.02701`.

[100] W.Adam, R. Frühwirth, A. Strandlie et al., "Reconstruction of electrons with the Gaussian-sum filter in the CMS tracker at the LHC", *J. Phys.* **G31** (2005) `doi:10.1088/0954-3899/31/9/N01`.

[101] CMS Collaboration, "Commissioning of the Particle-Flow reconstruction in Minimum-Bias and Jet Events from pp Collisions at 7 TeV", *CMS Physics Analysis Summary* **CMS-PAS-PFT-10-002** (2010).

[102] CMS Collaboration, “Performance of CMS muon reconstruction in pp collision events at $\sqrt{s} = 7$ TeV”, *JINST* **7** (2012) `doi:10.1088/1748-0221/7/10/P10002`, `arXiv:1206.4071`.

[103] CMS Collaboration, “Performance of CMS Muon Reconstruction in Cosmic-Ray Events”, *JINST* **5** (2010) `doi:10.1088/1748-0221/5/03/T03022`, `arXiv:0911.4994`.

[104] CMS Collaboration, “Particle Flow Event Reconstruction in CMS and Performance for Jets, Taus and MET”, *CMS Physics Analysis Summary* **CMS PAS PFT-09-001** (2009).

[105] CMS Collaboration, “Commissioning of the Particle-flow Event Reconstruction with the first LHC collisions recorded in the CMS detector”, *CMS Physics Analysis Summary* **CMS-PAS-PFT-10-001** (2010).

[106] M. Cacciari, G. Salam, and G. Soyez, “The anti-k_{T} jet clustering algorithm”, *JHEP* **04** (2008) 063, `doi:10.1088/1126-6708/2008/04/063`, `arXiv:0802.1189`.

[107] M. Cacciari, G. P. Salam, and G. Soyez, “FastJet user manual”, *Eur. Phys. J.* **C72** (2012) 1896, `doi:10.1140/epjc/s10052-012-1896-2`, `arXiv:1111.6097`.

[108] CMS Collaboration, “Determination of Jet Energy Calibration and Transverse Momentum Resolution in CMS”, *JINST* **6** (2011) P11002, `doi:doi:10.1088/1748-0221/6/11/P11002`, `arXiv:1107.4277`.

[109] CMS Collaboration, “Jet algorithms performance in 13 TeV data”, *CMS Physics Analysis Summary* **CMS-PAS-JME-16-003** (2017).

[110] CMS Collaboration, “Jet Performance in pp Collisions at $\sqrt{s} = 7$ TeV”, *CMS Physics Analysis Summary* **CMS-PAS-JME-10-003** (2010).

[111] CMS Collaboration, “Pileup Jet Identification”, *CMS Physics Analysis Summary* **CMS-PAS-JME-13-005** (2013).

[112] M. Cacciari and G. P. Salam, “Pileup subtraction using jet areas”, *Phys. Lett.* **B659** (2007) `doi:10.1016/j.physletb.2007.09.077`.

[113] CMS Collaboration, "Identification of b-quark jets with the CMS experiment"", *JINST* **8** (2013) P04013, `doi:10.1088/1748-0221/8/04/P04013`, `arXiv:1211.4462`.

[114] CMS Collaboration, "Identification of b quark jets at the CMS Experiment in the LHC Run 2", *CMS Physics Analysis Summary* **CMS-PAS-BTV-15-001** (2016).

[115] CMS Collaboration, "Measurement of $B\bar{B}$ angular correlations based on secondary vertex reconstruction at $\sqrt{s} = 7$ TeV", *JHEP* **03** (2011) 136, `doi:10.1007/JHEP03(2011)136`, `arXiv:1102.3194`.

[116] CMS Collaboration, "Performance of the CMS missing transverse momentum reconstruction in pp data at $\sqrt{s} = 8$ TeV", *JINST* **10** (2015) P02006, `doi:10.1088/1748-0221/10/02/P02006`, `arXiv:1411.0511`.

[117] CMS Collaboration, "Multivariate Determination of the Missing Energy in the Transverse Plane ($E_{\mathrm{T}}^{\mathrm{miss}}$) at $\sqrt{s} = 13$ TeV", *CMS Performance Note* **CMS-DP-2015-042** (2015).

[118] CMS Collaboration, "Reconstruction and identification of τ lepton decays to hadrons and ν_τ at CMS", *JINST* **11** (2016) `doi:10.1088/1748-0221/11/01/P01019`.

[119] CMS Collaboration, "Performance of reconstruction and identification of τ leptons in their decays to hadrons and ν_τ in LHC Run-2", *CMS Physics Analysis Summary* **CMS PAS TAU-16-002** (2016).

[120] J. Alwall, M. Herquet, F. Maltoni et al., "MadGraph 5: Going Beyond", *JHEP* **06** (2011) 128, `doi:10.1007/JHEP06(2011)128`, `arXiv:1106.0522`.

[121] S. Frixione, P. Nason, and C. Oleari, "Matching NLO QCD computations with Parton Shower simulations: the POWHEG method", *JHEP* **11** (2007) 070, `doi:10.1088/1126-6708/2007/11/070`.

[122] S. Alioli, P. Nason, C. Oleari et al., "A general framework for implementing NLO calculations in shower Monte Carlo programs: the POWHEG BOX", *JHEP* **06** (2010) 043, `doi:10.1007/JHEP06(2010)043`.

[123] T. Sjöstrand, S. Mrenna, and P. Skands, "PYTHIA 6.4 Physics and Manual", *JHEP* **06** (2006), no. 05, 026, `doi:10.1088/1126-6708/2006/05/026`.

[124] S. Jadach, J. Kühn, and Z. Was, "TAUOLA: a library of Monte Carlo programs to simulate decays of polarized τ leptons", *Comput. Phys. Commun* **64** (1991) 275–299, `doi:10.1016/0010-4655(91)90038-M`.

[125] S. Agostinelli and et. al., "Geant4-a simulation toolkit", *Nuclear Instruments and Methods in Physics Research Section A: Accelerators, Spectrometers, Detectors and Associated Equipment* **506** (2003) 250–303, `doi:doi:10.1016/S0168-9002(03)01368-8`.

[126] CMS Collaboration, "Performance of b tagging at $\sqrt{s} = 8$ TeV in multijet, $\mathrm{t\bar{t}}$ and boosted topology events", *CMS Physics Analysis Summary* **CMS-PAS-BTV-13-001** (2013).

[127] L. Bianchini, J. Conway, E. K. Friis et al., "Reconstruction of the Higgs mass in $\mathrm{H} \to \tau\tau$ Events by Dynamical Likelihood techniques", *J.Phys.Conf.Ser* **513** (2014) 022035, `doi:10.1088/1742-6596/513/2/022035`.

[128] CMS Collaboration, "CMS Luminosity Based on Pixel Cluster Counting - Summer 2013 Update", *CMS Physics Analysis Summary* **CMS-PAS-LUM-13-001** (2013).

[129] CMS Collaboration, "Measurement of the $\mathrm{W^+W^-}$ and ZZ production cross sections in pp collisions at $\sqrt{s} = 8$ TeV", *Phys. Lett.* **B721** (2013) 190, `doi:10.1016/j.physletb.2013.03.027`, `arXiv:1301.4698`.

[130] CMS Collaboration, "Measurement of the single-top-quark t-channel cross section in pp collisions at $\sqrt{s} = 7$ TeV", *JHEP* **12** (2012) 035, `doi:10.1007/JHEP12(2012)035`, `arXiv:1209.4533`.

[131] ATLAS and CMS Collaborations, "Procedure for the LHC Higgs boson search combination in Summer 2011", *CMS Note-2011/005, ATL-PHYS-PUB-2011-11* (2011).

[132] J. Conway, "Incorporating Nuisance Parameters in Likelihoods for Multisource Spectra", *Proceedings of the PHYSTAT 2011 Workshop on Statistical Issues*

Related to Discovery Claims in Search Experiments and Unfolding **CERN-2011-006** (2011) 117.

[133] R. Barlow and C. Beeston, “Fitting using finite Monte Carlo samples”, *Comput. Phys. Commun* **77** (1993) 219–228, `doi:10.1016/0010-4655(93)90005-W`.

[134] A. Read, “Presentation of search results: the CLs technique”, *Journal of Physics G: Nuclear and Particle Physics* **28** (2002) 2693, `doi:10.1088/0954-3899/28/10/313`.

[135] G. Cowan, K. Cranmer, E. Gross et al., “Asymptotic formulae for likelihood-based tests of new physics”, *Eur. Phys. J.* **C71** (2011) 1–19, `doi:doi:10.1140/epjc/s10052-011-1554-0`.

[136] T. Sjöstrand, S. Mrenna, and P. Z. Skands, “A Brief Introduction to PYTHIA 8.1”, *Comput. Phys. Commun* **178** (2008) 8520867, `doi:10.1016/j.cpc.2008.01.036`, `arXiv:0710.3820`.

[137] S. Alioli, P. Nason, C. Oleari et al., “NLO single-top production matched with shower in POWHEG: s- and t- channel contributions”, *JHEP* **09** (2009) 111, `doi:10.1007/JHEP02(2010)011,10.1088/1126-6708/2009/09/111`, `arXiv:0907.4076`.

[138] J. Alwall et al., “The automated computation of tree-level and next-to-leading order differential cross sections, and their matching to parton shower simulations”, *JHEP* **07** (2014) 079, `doi:10.1007/JHEP07(2014)079`, `arXiv:1405.0301`.

[139] D. Jang, “Search for MSSM Higgs decaying to tau pairs in $p\bar{p}$ collision at $\sqrt{s} = 1.96$ TeV at CDF”, *PhD thesis, Rutgers University* **FERMILAB-THESIS-2006-11** (2006).

[140] CMS Collaboration, “Measurement of the differential cross section for top quark pair production in pp collisions at $\sqrt{s} = 8\,\mathrm{TeV}$”, *Eur. Phys. J.* **C75** (2015) 542, `doi:10.1140/epjc/s10052-015-3709-x`, `arXiv:1505.04480`.

[141] CMS Collaboration, “Search for a neutral MSSM Higgs boson decaying into $\tau\tau$ with 12.9 fb^{-1} of data at $\sqrt{s} = 13$ TeV (Additional material)”. `http://cms-results.web.cern.ch/cms-results/public-results/`

`preliminary-results/HIG-16-037/index.html`, 2016.

[142] CMS Collaboration, “CMS Luminosity Measurement for the 2015 Data Taking Period”, *CMS Physics Analysis Summary* **CMS-PAS-LUM-15-001** (2016).

[143] R. Gavin, Y. Li, F. Petriello et al., “FEWZ 3.1: A User’s Guide”. `http://www.hep.anl.gov/fpetriello/FEWZManual_3.1.pdf`, 2012.

[144] M. Czakon and A. Mitov, “Top++: a program for the calculation of the top-pair cross-section at hadron colliders”, *Comput. Phys. Commun* **185** (2014) 2930.

[145] J. M. Campbell, R. K. Ellis, and C. Williams, “Vector boson pair production at the LHC”, *JHEP* **07** (2011) 018, `doi:10.1007/JHEP07(2011)018`, `arXiv:1105.0020`.

[146] M. Aliev, H. Lacker, U. Langenfeld et al., “HATHOR - HAdronic Top and Heavy quarks crOss section calculatoR”, *Comput. Phys. Commun* **182** (2011) 1034–1046, `doi:10.1016/j.cpc.2010.12.040`, `arXiv:1007.1327`.

[147] P. Kant, O. M. Kind, T. Kintscher et al., “HATHOR for single top-quark prodution: Updated predictions and uncertainty estimates for single top-quark production in hadronic collisions”, *Comput. Phys. Commun* **191** (2015) 74–89, `doi:10.1016/j.cpc.2015.02.001`, `arXiv:1406.4403`.

[148] A. Martin, W. Stirling, and G. Watt, “Parton distributions for the LHC”, *Eur. Phys. J.* **C63** (2009) 1890285, `doi:10.1140/epjc/s10052-009-1072-5`, `arXiv:0901.0002`.

[149] A. Martin, W. Stirling, R. Thorne et al., “Uncertainties on alpha(S) in global PDF analyses and implications for predicted hadronic cross sections”, *Eur. Phys. J.* **C64** (2009) 653–680, `doi:10.1140/epjc/s10052-009-1164-2`, `arXiv:0905.3531`.

[150] CMS Collaboration, “Updates on Projections of Physics Reach with the Upgraded CMS Detector for High Luminosity LHC”, *CMS Performance Note* **CMS-DP-2016-064** (2016).

List of acronyms

2HDM two Higgs doublet model

BDT boosted decision tree

BSM beyond the standard model

CERN the European Organisation for Nuclear Research

CHS charged hadron subtraction

CL confidence level

CMS Compact Muon Solenoid

CSC cathode strip chamber

CSV combined secondary vertex

CTF combinatorial track finder

DA deterministic annealing

DAQ data acquisition

DT drift tube chamber

EB ECAL barrel

ECAL electromagnetic calorimeter

EE ECAL endcap

EM electromagnetic

GSF gaussian sum filter

HB hadron barrel calorimeter

HCAL hadron calorimeter

HE hadron endcap calorimeter

HF hadron forward calorimeter

HLT high-level trigger

HO hadron outer calorimeter

IVF inclusive vertex finder

KF Kalman filter

L1 level-1

LEP Large Electron-Positron

LHC Large Hadron Collider

LS1 Long Shutdown 1

MC Monte Carlo

MPF missing transverse energy projection fraction

MSSM minimal supersymmetric standard model

QCD quantum chromodynamics

PF particle flow

PS Proton Synchrotron

PSB Proton Synchrotron Booster

QFT quantum field theory

RF radio frequency

RPC resistive plate chamber

SM standard model

SPS Super Proton Synchrotron

SUSY supersymmetry

TEC tracker endcap

TIB tracker inner barrel

TID tracker inner disk

TOB tracker outer barrel

UE underlying event

VBF vector boson fusion

WLCG Worldwide LHC Computing Grid

Appendix A

Event yields in the H → hh → $\mathrm{bb}\tau\tau$ analysis

The numbers of observed and expected events in the H → hh → $\mathrm{bb}\tau\tau$ analysis (chapter 4) are given in table A.1 for the $\mu\tau_{\mathrm{h}}$ channel and in table A.2 for the $\mathrm{e}\tau_{\mathrm{h}}$ channel. The background expectations are given after the fit to data has been performed. The uncertainties also correspond to the values obtained after performing the fit to data, with the correlations between the different systematic uncertainties taken into account.

$\mu\tau_{\mathrm{h}}$ channel			
	$\sqrt{s} = 8$ TeV		
Process	2jet-0tag	2jet-1tag	2jet-2tag
QCD	207 ± 33	42 ± 13	4 ± 2
$\mathrm{t\bar{t}}$	89 ± 9	197 ± 16	109 ± 9
Di-bosons + single top	38 ± 7	17 ± 2	4 ± 0.6
W+jets	346 ± 32	54 ± 18	1 ± 7
$\mathrm{Z} \to \ell\ell$ (lepton/jet faking τ)	84 ± 15	6 ± 1	1 ± 0.6
$\mathrm{Z} \to \tau\tau$	865 ± 56	95 ± 10	12 ± 3
Total Background	1629 ± 40	410 ± 18	131 ± 14
$\mathrm{H} \to \mathrm{hh} \to \mathrm{bb}\tau\tau$	1 ± 0.2	5 ± 0.3	3 ± 0.2
Data	1622	405	134

Table A.1: Number of events observed in data in the 2jet-0tag, 2jet-1tag and 2jet-2tag categories in the $\mu\tau_{\mathrm{h}}$ channel, compared with the background expectation. The signal expectations at $m_{\mathrm{H}} = 300\,\mathrm{GeV}$, $\tan\beta = 2$ are given for comparison. The uncertainties correspond to the post-fit systematic uncerainties, taking into account correlations between them.

eτ_h channel			
	$\sqrt{s} = 8$ TeV		
Process	2jet-0tag	2jet-1tag	2jet-2tag
QCD	219 ± 33	24 ± 8	4 ± 5
$t\bar{t}$	46 ± 5	109 ± 9	59 ± 6
Di-bosons + single top	17 ± 3	8 ± 1	2 ± 0.4
W+jets	186 ± 16	35 ± 13	3 ± 3
Z → $\ell\ell$ (lepton/jet faking τ)	158 ± 26	15 ± 3	1 ± 0.5
Z → $\tau\tau$	393 ± 38	44 ± 5	4 ± 1
Total Background	1019 ± 31	236 ± 13	73 ± 7
H → hh → bb$\tau\tau$	1 ± 0.1	2 ± 0.1	2 ± 0.1
Data	1022	237	67

Table A.2: Number of events observed in data in the 2jet-0tag, 2jet-1tag and 2jet-2tag categories in the eτ_h channel, compared with the background expectation. The signal expectations at $m_H = 300\,\text{GeV}$, $\tan\beta = 2$ are given for comparison. The uncertainties correspond to the post-fit systematic uncerainties, taking into account correlations between them.

Appendix B

Systematic uncertainties in the MSSM A/H $\rightarrow \tau\tau$ analysis

An overview of the systematic uncertainties that are applied in the MSSM A/H $\rightarrow \tau\tau$ analysis (chapter 5) are summarised in this appendix. The uncertainties are given in table B.1 for the $\mu\tau_h$ channel, in table B.2 for the $e\tau_h$ channel, in table B.3 for the $\tau_h\tau_h$ channel and in table B.4 for the $e\mu$ channel. Additionally, the systematic uncertainties for the $Z \rightarrow \mu\mu$ control region are shown in table B.5. Correlations are also indicated. Some of the uncertainties are different for different processes, where this is the case ranges are given. Uncertainties marked "Fully correlated" are correlated between the different decay channels and event categories, those marked "Fully uncorrelated" are uncorrelated between the different decay channels and event categories. "Cats:C,chns:U" indicates that the uncertainty is correlated between categories but uncorrelated between the different decay channels. For brevity the backgrounds are denoted with shorthand notations. ‘ZTT’ indicates the Z/γ^* $\rightarrow \tau\tau$ component. ’ZJ’ is reserved for the Z/γ^* $\rightarrow \ell\ell$ background in which the tau is faked by a jet. The Z/γ^* $\rightarrow \ell\ell$ background in which the tau is faked by an electron or muon is indicated as ’ZL’. ‘W’ indicates the W+jets process. ‘TT’ denotes the t$\bar{\text{t}}$ background, with ‘TTT’ and ‘TTJ’ indicating the t$\bar{\text{t}}$ background with real hadronic taus and without real hadronic taus, respectively. The di-boson and single-top backgrounds are denoted ‘VV’, with ‘VVT’ and ‘VVJ’ indicating the di-boson plus single-top background with real hadronic taus and without real hadronic taus, respectively. The QCD multijet background is denoted ‘QCD’.

Table B.1: Systematic uncertainties that affect the estimated number of signal or background events in the $\mu\tau_{\mathrm{h}}$ channel.

	Event yield uncertainty by event category								
Process	**No b-tag**				**B-tag**				**Correlation**
	SR	OS high m_{T}	SS low m_{T}	SS high m_{T}	SR	OS high m_{T}	SS low m_{T}	SS high m_{T}	
Integrated luminosity 13 TeV									
All from MC	6.2%	6.2%	6.2%	6.2%	6.2%	6.2%	6.2%	6.2%	Fully correlated
Jet energy scale									
All from MC	0–1%	0–2%	0–1%	0–1%	0–12%	3–11%	0–15%	0–14%	Fully correlated
$E_{\mathrm{T}}^{\mathrm{miss}}$ **scale**									
ZTT,W	2%		2%		2%		2%		Corr. between chn/cat; TTT,TTJ, VVT,VVJ
TT(T/J),VV(T/J)	2%		2%		2%		2%		uncorr. from ZTT,W
$E_{\mathrm{T}}^{\mathrm{miss}}$ **resolution**									
ZTT,W	2%		2%		2%		2%		Corr. between chn/cat; TTT,TTJ,VVT,VVJ
TT(T/J),VV(T/J)	2%		2%		2%		2%		uncorr. from ZTT,W
Muon identification and trigger									
All from MC	2%	2%	2%	2%	2%	2%	2%	2%	Fully correlated
Tau-lepton identification									
ZTT,TTT,VVT, signal	5%	5%	5%	5%	5%	5%	5%	5%	Fully correlated
ZTT,TTT,VVT, signal	3%	3%	3%	3%	3%	3%	3%	3%	Cats:C,chns:U
b-Tagging efficiency									
All from MC	0–3%	0–3%	0–3%	0–2%	1–3%	0–3%	0–3%	0–3%	Fully correlated
W					4%	4%	6%	6%	Fully correlated
light jet mis-tagging rate									
All from MC					1–7%				Fully correlated
Tau-lepton energy scale									
ZTT,TTT,VVT, signal	shape	shape	shape	shape	shape	shape	shape	shape	Cats:C,chns:U
High-p_{T} τ_{h} ID efficiency									
ZTT,TTT,VVT, signal	shape	shape	shape	shape	shape	shape	shape	shape	Cats:C,chns:U
Top quark p_{T} reweighting									
TTT,TTJ	shape	shape	shape	shape	shape	shape	shape	shape	Fully correlated
Drell-Yan reweighting									
ZTT	shape	shape	shape	shape	shape	shape	shape	shape	Fully correlated
Jet $\rightarrow \tau_{\mathrm{h}}$ fake rate reweighting									
W	shape				shape				Fully correlated
Normalisation, Z production									
ZL,ZJ	4%	4%	4%	4%	4%	4%	4%	4%	Fully correlated
ZTT		4%	4%	4%		4%	4%	4%	Fully correlated
$Z \rightarrow \tau\tau$**:** $\boldsymbol{Z \rightarrow \tau\tau / Z \rightarrow \mu\mu}$ **extrapolation**									
ZTT	3%	3%	3%	3%	5%	5%	5%	5%	Fully uncorrelated
Normalisation, $\mathrm{t\bar{t}}$									
TTT,TTJ	6%	6%	6%	6%	6%	6%	6%	6%	Fully correlated
Normalisation, di-boson + single-top									
VVT,VVJ	5%	5%	5%	5%	5%	5%	5%	5%	Fully correlated
Normalisation, Z $\rightarrow \mu\mu$**:** μ **misidentified as** τ_{h}									
ZL	30%	30%	30%	30%	30%	30%	30%	30%	Cats:C,chns:U
Normalisation, Z**+jets : jet misidentified as** τ_{h}									
ZJ,TTJ	20%	20%	20%	20%	20%	20%	20%	20%	Cats:C,chns:U
W OS/SS ratio (stat)									
W	2%	2%			11%	11%			Fully uncorrelated
W OS/SS ratio (syst)									
W	8%	8%			10%	10%			Fully uncorrelated
W low/high m_T ratio (stat)									
W	2%		2 %		14%		14%		Fully uncorrelated
W low/high m_T ratio (syst)									
W	20%		20%		20%		20%		Fully uncorrelated
QCD OS/SS ratio (syst)									
QCD	4%	4%			60%	60%			Fully uncorrelated

Table B.2: Systematic uncertainties that affect the estimated number of signal or background events in the eτ_h channel.

	Event yield uncertainty by event category								
Process	**No b-tag**				**B-tag**				**Correlation**
	SR	OS high m_T	SS low m_T	SS high m_T	SR	OS high m_T	SS low m_T	SS high m_T	
Integrated luminosity 13 TeV									
All from MC	6.2%	6.2%	6.2%	6.2%	6.2%	6.2%	6.2%	6.2%	Fully correlated
Jet energy scale									
All from MC	0–1%	0–1%	0–2%	0–1%	1–14%	0–12%	0–15%	0–15%	Fully correlated
$E_\mathrm{T}^\mathrm{miss}$ **scale**									
ZTT,W	2%		2%		2%		2%		Corr. between chn/cat, TTT,TTJ,VVT,VVJ
TT(T/J),VV(T/J)	2%		2%		2%		2%		uncorr. from ZTT,W
$E_\mathrm{T}^\mathrm{miss}$ **resolution**									
ZTT,W	2%		2%		2%		2%		Corr. between chn/cat, TTT,TTJ,VVT,VVJ
TT(T/J),VV(T/J)	2%		2%		2%		2%		uncorr. from ZTT,W
Electron identification and trigger									
All from MC	2%	2%	2%	2%	2%	2%	2%	2%	Fully correlated
Tau-lepton identification									
ZTT,TTT,VVT, signal	5%	5%	5%	5%	5%	5%	5%	5%	Fully correlated
ZTT,TTT,VVT, signal	3%	3%	3%	3%	3%	3%	3%	3%	Cats:C,chns:U
b-Tagging efficiency									
All from MC	0–3%	0–3%	0–4%	0–4%	1–4%	0–2%	0–2%	0–2%	Fully correlated
W					5%	2%	10%	3%	Fully correlated
Light jet mis-tagging rate									
All from MC					0–3%				Fully correlated
Tau-lepton energy scale									
ZTT,TTT,VVT, signal	shape	shape	shape	shape	shape	shape	shape	shape	Cats:C,chns:U
High-p_T τ_h ID efficiency									
ZTT,TTT,VVT, signal	shape	shape	shape	shape	shape	shape	shape	shape	Cats:C,chns:U
Top quark p_T reweighting									
TTT,TTJ	shape	shape	shape	shape	shape	shape	shape	shape	Fully correlated
Drell-Yan reweighting									
ZTT	shape	shape	shape	shape	shape	shape	shape	shape	Fully correlated
Jet → τ_h fake rate reweighting									
W	shape				shape				Fully correlated
Normalisation, Z **production**									
ZL,ZJ	4%	4%	4%	4%	4%	4%	4%	4%	Fully correlated
ZTT		4%	4%	4%		4%	4%	4%	Fully correlated
$Z \to \tau\tau / Z \to \mu\mu$ **extrapolation**									
ZTT	3%	3%	3%	3%	5%	5%	5%	5%	Fully uncorrelated
Normalisation, $\mathrm{t\bar{t}}$									
TTT,TTJ	6%	6%	6%	6%	6%	6%	6%	6%	Fully correlated
Normalisation, di-boson + single-top									
VVT,VVJ	5%	5%	5%	5%	5%	5%	5%	5%	Fully correlated
Normalisation, Z → ee: e **misidentified as** τ_h									
ZL	30%	30%	30%	30%	30%	30%	30%	30%	Cats:C,chns:U
Normalisation, Z**+jets : jet misidentified as** τ_h									
ZJ,TTJ	20%	20%	20%	20%	20%	20%	20%	20%	Cats:C,chns:U
W OS/SS ratio (stat)									
W	2%	2%			14%	14%			Fully uncorrelated
W OS/SS ratio (syst)									
W	8%	8%			10%	10%			Fully uncorrelated
W low/high m_T ratio (stat)									
W	2%		2 %		17%		17%		Fully uncorrelated
W low/high m_T ratio (syst)									
W	20%		20%		20%		20%		Fully uncorrelated
QCD OS/SS ratio (syst)									
QCD	12%	12%			60%	60%			Fully uncorrelated

Table B.3: Systematic uncertainties that affect the estimated number of signal or background events in the $\tau_h\tau_h$ channel.

	Event yield uncertainty by event category		
Process	No b-tag	B-tag	Correlation
Integrated luminosity 13 TeV			
All from MC	6.2%	6.2%	Fully correlated
Jet energy scale			
All from MC	0–4%	0–9%	Fully correlated
E_T^{miss} **scale**			
ZTT,W	2%	2%	Correlated between chn/cat,
TTT,TTJ,VVT,VVJ	2%	2%	ZTT/W uncorrelated from TTT,TTJ,VVT,VVJ
E_T^{miss} **resolution**			
ZTT,W	2%	2%	Correlated between chn/cat,
TTT,TTJ,VVT,VVJ	2%	2%	ZTT/W uncorrelated from TTT,TTJ,VVT,VVJ
Tau-lepton identification and trigger			
ZTT,TTT,VVT, signal	10%	10%	Fully correlated
ZTT,TTT,VVT, signal	9.2%	9.2%	Correlated between categories, uncorrelated between channels
b-Tagging efficiency			
All from MC	0–4%	0–11%	Fully correlated
Light jet mis-tagging rate			
All from MC	0–1%	0–12%	Fully correlated
Tau-lepton energy scale			
ZTT,TTT,VVT, signal	shape	shape	Correlated between categories, uncorrelated between channels
High-p_T τ_h **ID efficiency**			
ZTT,TTT,VVT, signal	shape	shape	Correlated between categories, uncorrelated between channels
Drell-Yan reweighting			
ZTT	shape	shape	Fully correlated
Top quark p_T **reweighting**			
TTT,TTJ	shape	shape	Fully correlated
Normalisation, Z **production**			
ZL,ZJ	4%	4%	Fully correlated
$Z \to \tau\tau / Z \to \mu\mu$: **extrapolation**			
ZTT	3%	5%	Fully uncorrelated
Normalisation, $t\bar{t}$			
TTT,TTJ	6%	6%	Fully correlated
Normalisation, di-boson + single-top			
VVT,VVJ	5%	5%	Fully correlated
Normalisation, Z → ee: e **misidentified as** τ_h			
ZL	10%	10%	Correlated between categories, uncorrelated between channels
Normalisation, Z**+jets : jet misidentified as** τ_h			
ZJ,W,TTJ	20%	20%	Correlated bewteen categories, uncorrelated between channels
Normalisation, QCD multijet (stat)			
QCD	2%	20%	Fully uncorrelated
Normalisation, QCD multijet (syst)			
QCD	12%	14%	Fully uncorrelated
Normalisation, W+jets			
W	4%	4%	Fully correlated

Table B.4: Systematic uncertainties that affect the estimated number of signal or background events in the eμ channel.

	Event yield uncertainty by event category		
Process	**No b-tag**	**B-tag**	**Correlation**
Integrated luminosity 13 TeV			
All from MC	6.2%	6.2%	Fully correlated
Jet energy scale			
All from MC	0–1%	1–69%	Fully correlated
$E_{\mathrm{T}}^{\mathrm{miss}}$ scale			
ZTT,W	2%	2%	Correlated between chn/cat,
TT,VV	2%	2%	ZTT,W uncorrelated from TT,VV
$E_{\mathrm{T}}^{\mathrm{miss}}$ resolution			
ZTT,W	2 %	2%	Correlated between chn/cat,
TT,VV	2%	2%	ZTT,W uncorrelated from TT,VV
Electron identification and trigger			
All from MC	2%	2%	Fully correlated
Muon identification and trigger			
All from MC	2%	2%	Fully correlated
b-Tagging efficiency			
All from MC	0–3%	1–3%	Fully correlated
Light jet mis-tagging rate			
All from MC		0–10%	Fully correlated
Electron energy scale			
ZTT,signal	shape	shape	Fully correlated
Drell-Yan reweighting			
ZTT	shape	shape	Fully correlated
Top quark p_{T} reweighting			
TT	shape	shape	Fully correlated
Normalisation, Z production			
ZLL	4%	4%	Fully correlated
$Z \to \tau\tau / Z \to \mu\mu$: extrapolation			
ZTT	3%	5%	Fully uncorrelated
Normalisation, $\mathrm{t\bar{t}}$			
TT	6%	6%	Fully correlated
Normalisation, di-boson + single-top			
VV	5%	5%	Fully correlated
Normalisation, QCD multijet			
QCD	23%	34%	Fully uncorrelated
Normalisation, W+jets			
W+jets	4%	4%	Fully correlated

Table B.5: Systematic uncertainties that affect the estimated number of background events in the Z → $\mu\mu$ channel.

	Event yield uncertainty by event category		
Process	**No b-tag**	**B-tag**	**Correlation**
Integrated luminosity 13 TeV			
All from MC (not ZL)	6.2%	6.2%	Fully correlated
Jet energy scale			
All from MC	0–1%	1–69%	Fully correlated
$E_{\mathrm{T}}^{\mathrm{miss}}$ **scale**			
ZTT,W	2%	2%	Correlated between chn/cat,
TT,VV	2%	2%	ZTT,W uncorrelated from TT,VV
$E_{\mathrm{T}}^{\mathrm{miss}}$ **resolution**			
ZTT,W	2 %	2%	Correlated between chn/cat,
TT,VV	2%	2%	ZTT,W uncorrelated from TT,VV
Muon identification and trigger			
All from MC	2–4%	2–4%	Fully correlated
b-Tagging efficiency			
All from MC	0–3%	1–3%	Fully correlated
Light jet mis-tagging rate			
All from MC		0–10%	Fully correlated
Normalisation, $\mathrm{t\bar{t}}$			
TT	6%	6%	Fully correlated
Normalisation, di-boson + single-top			
VV	5%	5%	Fully correlated
Normalisation, W+jets			
W+jets	4%	4%	Fully correlated

Appendix C

Event yields in the MSSM A/H $\rightarrow \tau\tau$ analysis

The numbers of observed and expected events in the MSSM A/H $\rightarrow \tau\tau$ analysis (chapter 5) are given in table C.1 for the $\mu\tau_\mathrm{h}$ channel, in table C.2 for the $\mathrm{e}\tau_\mathrm{h}$ channel, in table C.3 for the $\tau_\mathrm{h}\tau_\mathrm{h}$ channel and in table C.4 for the $\mathrm{e}\mu$ channel. The background expectations are given after the fit to data has been performed. The uncertainties also correspond to the values obtained after performing the fit to data, with the correlations between the different systematic uncertainties taken into account.

$\mu\tau_\mathrm{h}$ channel		
	$\sqrt{s} = 13$ TeV	
Process	No b-tag	B-tag
QCD	8019 ± 492	146 ± 43
$\mathrm{t\bar{t}}$ (jet faking τ_h)	406 ± 73	83 ± 15
$\mathrm{t\bar{t}}$ (genuine τ_h)	447 ± 21	212 ± 9
Di-bosons + single top (jet faking τ_h)	245 ± 13	37 ± 2
Di-bosons + single top (genuine τ_h)	352 ± 23	63 ± 4
W+jets	8506 ± 616	116 ± 43
Z+jets (jet faking τ_h)	961 ± 189	12 ± 2
Z+jets (l faking τ_h)	4138 ± 888	41 ± 9
$\mathrm{Z} \rightarrow \tau\tau$	34467 ± 896	437 ± 25
Total Background	57541 ± 301	1146 ± 36
A/H→ $\tau\tau$	259 ± 27	6 ± 0.5
Data	57564	1136

Table C.1: Number of events observed in data in the b-tag and no b-tag categories in the $\mu\tau_\mathrm{h}$ compared with the background expectation. The signal expectation, for $m_\mathrm{A} = 1\,\mathrm{TeV}$ and $\tan\beta = 50$ in the $m_\mathrm{h}^\mathrm{mod+}$ scenario, is also shown. The uncertainties correspond to the post-fit systematic uncerainties, taking into account correlations between them.

$\mathrm{e}\tau_\mathrm{h}$ channel		
	$\sqrt{s} = 13$ TeV	
Process	No b-tag	B-tag
QCD	5963 ± 734	82 ± 42
$\mathrm{t\bar{t}}$ (jet faking τ_h)	262 ± 48	45 ± 8
$\mathrm{t\bar{t}}$ (genuine τ_h)	317 ± 17	150 ± 7
Di-bosons + single top (jet faking τ_h)	166 ± 9	24 ± 1
Di-bosons + single top (genuine τ_h)	238 ± 15	38 ± 2
W+jets	6778 ± 639	88 ± 47
Z+jets (jet faking τ_h)	734 ± 128	9 ± 2
Z+jets (l faking τ_h)	4517 ± 733	54 ± 8
$\mathrm{Z} \rightarrow \tau_\mathrm{h}\tau_\mathrm{h}$	12907 ± 631	174 ± 13
Total Background	31883 ± 239	664 ± 30
A/H→ $\tau\tau$	130 ± 13	4 ± 0.3
Data	31907	675

Table C.2: Number of events observed in data in the b-tag and no b-tag categories in the $\mathrm{e}\tau_\mathrm{h}$ channel, compared with the background expectation. The signal expectation, for $m_\mathrm{A} = 1\,\mathrm{TeV}$ and $\tan\beta = 50$ in the $m_\mathrm{h}^\mathrm{mod+}$ scenario, is also shown. The uncertainties correspond to the post-fit systematic uncerainties, taking into account correlations between them.

$\tau_h\tau_h$ channel		
	$\sqrt{s} = 13$ TeV	
Process	No b-tag	B-tag
QCD multijet	12489 ± 368	186 ± 18
$t\bar{t}$ (jet faking τ_h)	20 ± 3	6 ± 0.9
$t\bar{t}$ (genuine τ_h)	33 ± 3	17 ± 1
Di-bosons + single top (jet faking τ_h)	16 ± 0.9	3 ± 0.2
Di-bosons + single top (genuine τ_h)	51 ± 5	6 ± 0.6
W+jets	409 ± 63	4 ± 0.7
Z+jets (jet faking τ_h)	52 ± 9	1 ± 0.2
Z+jets (l faking τ_h)	124 ± 27	2 ± 0.5
Z → $\tau\tau$	4127 ± 359	72 ± 7
Total Background	17321 ± 132	297 ± 16
A/H→ $\tau\tau$	107 ± 12	6 ± 0.6
Data	17314	298

Table C.3: Number of events observed in data in the b-tag and no b-tag categories in the $\tau_h\tau_h$ channel, compared with the background expectation. The signal expectation, for $m_A = 1\,\text{TeV}$ and $\tan\beta = 50$ in the $m_h^{\text{mod+}}$ scenario, is also shown. The uncertainties correspond to the post-fit systematic uncerainties, taking into account correlations between them.

eμ channel		
	$\sqrt{s} = 13$ TeV	
Process	No b-tag	B-tag
QCD multijet	9511 ± 653	205 ± 35
$t\bar{t}$	6709 ± 210	2733 ± 65
Di-bosons + single top	3798 ± 200	550 ± 30
W+jets	1675 ± 98	29 ± 2
Z → $\ell\ell$	560 ± 32	11 ± 2
Z → $\tau\tau$	42463 ± 627	583 ± 29
Total Background	64717 ± 264	4112 ± 62
A/H→ $\tau\tau$	192 ± 20	5 ± 0.3
Data	64743	4081

Table C.4: Number of events observed in data in the b-tag and no b-tag categories in the and eμ channel, compared with the background expectation. The signal expectation, for $m_A = 1\,\text{TeV}$ and $\tan\beta = 50$ in the $m_h^{\text{mod+}}$ scenario, is also shown. The uncertainties correspond to the post-fit systematic uncerainties, taking into account correlations between them.